THE UNIVERSITY
of ADELAIDE

Performance Enhancement of Submerged Ocean Wave Energy Converter using Nonlinear Stiffness

BENJAMIN W. SCHUBERT

School of Mechanical Engineering
The University of Adelaide
South Australia 5005
Australia

Thesis submitted in partial fulfillment of the requirements for the degree of Ph. D. in Engineering on July 31, 2021.

Ph. D. Thesis

July 31, 2021

School of Mechanical Engineering
The University of Adelaide
South Australia 5005
Australia

Typeset by the author using LaTeX.
Printed in Australia.

Abstract

Ocean waves are a source of renewable energy with an enormous potential to augment current renewable energy markets. Historically, the levelised cost of wave energy has been higher than conventional renewable energy sources such as wind or solar. While significant progress has been made in improving the economic viability of wave energy, a robust control system for wave energy converters is an important step to progress their technology readiness level. Utility scale wave energy systems typically require large capital investment. Therefore, tools are required to accurately and reliably model systems to predict the dynamic response and performance of potential control systems.

This thesis presents a passive control system in the form of a nonlinear stiffness to improve the robustness of wave energy systems in situ as the ocean wave conditions change over time. In the preceding work in the literature, two common shortcomings, which may undermine the investigations, are: (i) the lack of comparisons against optimal conditions; and, (ii) the simplistic representation of hydrodynamic forces in fluid-structure interactions. These two gaps underpin the purpose of each chapter of this thesis and are systematically addressed in the context of a submerged point absorbing wave energy converter.

Many differing designs of wave energy converters have been proposed in literature, with fundamentally different modes of operation. This thesis initially compares the application of a passive control system to point absorbing wave energy devices in both floating and submerged contexts. It was found that the application of nonlinear stiffness did not improve upon a system controlled by an optimised linear stiffness in both floating and submerged scenarios for regular wave excitation. Since many floating point absorbers experience a large hydrostatic stiffness, mechanisms to provide large negative stiffness are required for tuning purposes. The nonlinear stiffness — which can provide negative stiffness — offers a notable improvement in power production capacity compared to the scenario with no control stiffness in floating systems. For a submerged system, a position-dependent force is inherently required to counteract the constant buoyancy force, so the system may be optimally tuned by a linear stiffness. For irregular waves, which are more representative of ocean conditions, a floating system without an optimised linear stiffness experiences a significant benefit, while systems with optimal

i

linear parameters do not benefit in terms of the power converted. However, as ocean conditions change in terms of significant wave height, energy period, and wave phase relationships, the addition of a nonlinear stiffness mechanism provides an improvement by enhancing the robustness to changing ocean conditions and by desensitising the system to wave phasing.

The fidelity of simulations involving nonlinear stiffness may be improved by extending the model to three degrees of freedom to capture geometric nonlinearities and dynamic coupling between different degrees of freedom. In this work, the nonlinear stiffness was parametrised and varied to demonstrate how and why the system responds either positively or negatively depending on particular wave conditions. It was shown that when the system is optimally tuned for a regular wave, the nonlinear stiffness is not able to improve the amount of power generated. For irregular waves, the optimal performance is observed when the system is tuned with a linear stiffness to give a particular natural frequency—depending on wave condition. However, the same performance is also achieved with a nonlinear stiffness augmentation when the system is oscillating about any equilibrium point if the position dependent natural frequency is close to the optimal natural frequency. A consistent beneficial trend is seen under different irregular wave excitations. The nonlinear stiffness exposes the system to a changing effective resonance frequency varying with position. As a result, performance improvements over the linear system are observed when the system is tuned for one irregular wave and excited by a different irregular wave. Therefore, the primary benefit of a nonlinear augmentation is the improvement to robustness of such systems for varying sea conditions.

The hydrodynamic modelling of the fluid-structure interaction of a submerged wave energy device is often achieved using linear potential flow theory. This limitation is explored by comparing both linear and nonlinear hydrodynamic models (using a validated computational fluid dynamics simulation) with a novel pseudo-nonlinear model, which extends the linear model to incorporate pose-dependent hydrodynamic parameters during simulation through pre-calculated values. The results showed that linear hydrodynamics do not adequately represent all the important nonlinear effects. The trends in motion also indicates the presence of frequency dependent fluid-structure interactions associated with the resonance of body of water above the buoy. It is not possible to represent such phenomena using standard linear potential flow methods. Therefore, higher fidelity models should be employed to obtain more reliable indications of performance.

The three degrees of freedom model was further extended by including nonlinear stiffness into the validated computational fluid dynamics model. It was shown that inclusion of nonlinear hydrodynamics shifts the optimal natural frequency of the system. For regular waves, the nonlinear stiffness did not provide a consistent improvement. Under irregular conditions, a small amount of nonlinear stiffness was shown to provide a 5.5%

improvement. The nonlinear stiffness was parametrised relative to the potential energy of the incident wave, leading to the observation that the peak in time-averaged power generation occurred when the nonlinear stiffness potential at the nominal equilibrium position was around 25% of the potential energy of the incident wave.

While the trend in power results between the models using linear and nonlinear hydrodynamics with the nonlinear stiffness were reasonably similar, in the nonlinear hydrodynamics model, the nonlinear stiffness more rapidly detunes the system than in the linear model. This finding indicates that a nonlinear stiffness mechanism may be an effective method to detune the device to protect components from extreme operating conditions.

Declaration

I certify that this work contains no material which has been accepted for the award of any other degree or diploma in my name, in any university or other tertiary institution and, to the best of my knowledge and belief, contains no material previously published or written by another person, except where due reference has been made in the text. In addition, I certify that no part of this work will, in the future, be used in a submission in my name, for any other degree or diploma in any university or other tertiary institution without the prior approval of the University of Adelaide and where applicable, any partner institution responsible for the joint-award of this degree.

I acknowledge that copyright of published works contained within this thesis resides with the copyright holder(s) of those works.

I also give permission for the digital version of my thesis to be made available on the web, via the University's digital research repository, the Library Search and also through web search engines, unless permission has been granted by the University to restrict access for a period of time.

I acknowledge the support I have received for my research through the provision of an Australian Government Research Training Program Scholarship.

_____

Benjamin W. Schubert

Acknowledgements

I would like to thank my principle supervisor Dr Will Robertson for his kind support and patient direction. The insightful conversations, though often drifting off topic, have helped me immensely over the course of this research journey. I deeply appreciate the care and respect he gives in all his interactions which inspires me support and encourage others.

I also offer my sincere gratitude to my co-supervisors Professor Benjamin Cazzolato, Dr Nataliia Sergiienko, and Dr Mergen Ghayesh for their unique contributions over my candidature. The expansive experience and knowledge provided by Professor Benjamin Cazzolato in seemingly any field has been invaluable, both in the creation of this thesis, and in my future career. A special thanks goes to Dr Nataliia Sergiienko for helping develop a firm foundational understanding at the start of this journey, and for joining my supervisory team by offering encouragement, thoughtful opinions, and sharing of her own experiences. I also thank Dr Mergen Ghayesh for his energetic encouragement and inspiration in cultivating technical understanding.

I also wish to acknowledge my fellow PhD candidates, colleagues, and members of the wave energy group. The endless banter, stimulating discussions, and words of support have made this journey truly joyful and provided motivation during difficult times. I thank the Fabien Voisin and the Phoenix team for providing above and beyond support in high performance computing challenges, and Ashkan Rafiee and Richard Jones for providing pertinent technical computational fluid dynamics advice.

I owe huge thanks to my wife, Zoe, for partnering with me along this adventure through the challenges and triumphs. I am also grateful to my family and friends for bearing with me through these years and always checking in with how I'm going.

Finally, and most importantly, I thank God for his abundant provision, graciousness, guidance, support, wisdom, challenges, and love. It is only by his far reaching love and mercy that I may complete this research. Thank you gracious heavenly father for the wisdom, endurance, peace of mind, and good health I've needed on this path. I'm inspired by the beauty of the world you've given, and humbled by the means you've provided to understand it.

Contents

Chapter 1

Introduction

1.1 Wave energy prospect

World energy generation is shifting from a once fossil-fuel dominated market, to more renewable sources. In 2019, 41% of growth in primary energy was from renewable sources [1]. The renewable energy market is predominantly composed of hydro, solar, and wind [2]. One form of renewable energy that is largely underutilised is ocean energy. Ocean renewable energy generation may be categorised into four major technologies — ocean thermal energy conversion, salinity gradient, tidal, and wave. The largest resource potential of these is ocean thermal energy conversion with an estimated 44,000 TWh/y available, followed by wave energy with a potential of 29,500 TWh/y [3]. The global electricity demand was 25,814 TWh in 2019 [4]. Therefore, wave energy alone presents a resource of comparable potential to the global energy demand.

Ocean wave energy, as a technology, has been developing for over two centuries [5], but has yet to reach commercial viability. While significant advances have been made in progressing the technology over this time, further developments are needed to reduce the levelised cost of energy (LCOE) and the overall competitiveness with other forms of renewable energy generation. One key advantage ocean energy has is the increased predictability and low variability compared to solar PV and wind generated electricity [3]. So the addition of wave energy into renewable energy markets would provide a less variable base load renewable alternative to fossil fuels. Another advantage is the application to remote areas where wind or solar are not suitable, or as a component in a hybrid offshore wind and wave system.

1.2 State of technology

The current wave energy industry has not settled on an ideal device, with many different wave energy converters (WEC) having been proposed over several decades with funda-

mentally different modes of operation [6]. Most WECs can be broadly categorised into three main types: terminators, attenuators, or point absorbers (PA) [7]. Each category can be further decomposed into subgroups, such as quasi-PA, which are too large to be considered a point, but exhibit similar operational modes as PA devices. There are other WEC devices which do not fit under these classifications such as overtopping devices. As wave energy technologies have not seen a convergence towards a standard system and research efforts continue to investigate alternative designs, it is challenging to form general conclusion around best practices. It would be beyond the scope of a single project to thoroughly investigate all modes of operation proposed.

The scope of this thesis will pertain to PA WECs which are small relative to the incident wavelength, and are therefore relatively insensitive to direction. Two significant PA WEC currently under development and have relevance to the work in this thesis are (Figure 1.1) the C5 from CorPower Ocean [8] and the CETO from Carnegie Clean Energy [9]. The C5 is a floating PA WEC which employs a negative stiffness component for passive phase matching, and CorPower Ocean are on track to move the technology readiness level of their device to TRL8 over the next two years through the demonstration and certification of a pilot array of three full scale WECs. This milestone, if successful, will place CorPower at the forefront of the wave energy industry. The CETO device is a submerged three tether system, which allows the device to capture energy in three degrees of freedom (DOF) [10]. The company has experienced significant funding difficulty in recent years, but continues to progress the CETO system through development of innovative wave prediction tools to assist in intelligent controller design [9].

The lack of funding for commercialisation has been a consistent theme over the global wave energy industry [3], in part due to the high upfront cost, but also due to the high LCOE compared to other renewable energies. The LCOE for wave energy is currently predicted to be between \$0.37–1.22/kWh, whereas the average LCOE for solar photovoltaic in 2018 was \$0.085/kWh [11]. Overall, alternative energy sources, such as wind and solar, are estimated to cost between \$0.03/kWh to \$0.22/kWh [12] while offshore wind projects have been estimated to cost \$0.17/kWh [13]. To achieve an economic advantage, it has been estimated that wave energy projects must reach a LCOE of \$0.30/kWh [12]. In addition to the continued reduction of capital and operational expenses, one key aspect to achieve this LCOE is to improve the capability of wave energy devices to generate power by employing control strategies to optimise for local and variable wave conditions either through active or passive means [14]. While active control can require sophisticated models, complex concepts, and predictions of various forces, passive control may be used to achieve good performance and potentially reduce the dependence on active components, as is the case with the C5 device by CorPower. The nonlinear stiffness approach has received increased attention from research communities over the past few years [15], but has not been extended to submerged PA WECs in a high fidelity numerical modelling or experimental approach. The application of nonlinear

(a) The C5 WEC from CorPower Ocean [8].

(b) The CETO 6 from Carnegie Clean Energy [9].
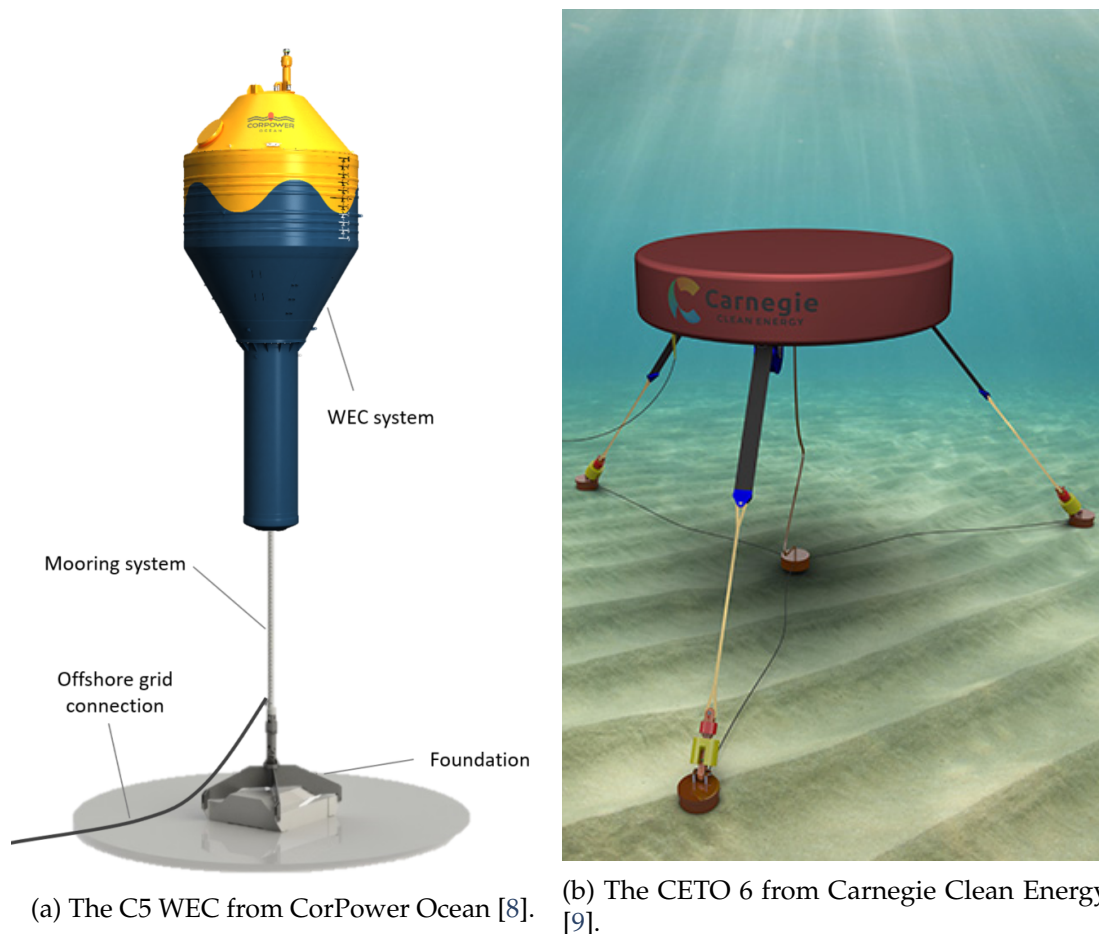
Figure 1.1: Indicative floating and submerged PA WEC currently under development by industry.

stiffness to submerged PA WECs is a research opportunity that will be explored in this thesis.

1.3 Thesis

1.3.1 Thesis aims and scope

The need to reduce the LCOE of wave energy requires the formulation of cost effective control strategies which maximise the amount of power generated. This thesis is an in-depth investigation of a passive control strategy which introduces a nonlinear stiffness mechanism to a submerged PA WEC in a high fidelity hydrodynamic scenario. The investigation involves: understanding different application of nonlinear stiffness between floating and submerged PA WECs, determining the mechanisms behind why

the nonlinear stiffness provides a benefit, extending the model to incorporate other non-linear hydrodynamic influences, and combining the high fidelity hydrodynamic model with the nonlinear stiffness passive control system to estimate the realistic potential benefit. The key research questions that will be answered are:

1. Under what conditions does a passive control system using nonlinear stiffness provide a benefit to the performance of a floating or submerged device?

2. How do nonlinear stiffness mechanisms provide a performance enhancement in submerged wave energy devices if geometric nonlinearities are included?

3. What impact do the nonlinear hydrodynamic effects have on a submerged quasi-PA WEC, and is the linear potential flow hydrodynamic representations suitable for representative simulations?

4. How does a nonlinear stiffness mechanism affect the system performance of a submerged WEC under high fidelity hydrodynamic fluid-structure interactions in three degrees of freedom?

This systematic approach allows for clear discernment between the impact of the non-linear stiffness, the nonlinear hydrodynamic or geometric effects, and a representative assessment of the possible application of such a passive control system.

1.3.2 Outline

This thesis is arranged as a collection of four manuscripts that have been published or are currently under review. Additional conference and journal publications are included as appendices to further elaborate on the methodologies employed and the key findings. Chapter 2 provides an overview of the pertinent literature related to PA WECs, hydrody-namics, and nonlinear stiffness passive control systems. The foundational background and theory of these devices is presented in Chapter 3. The specific literature and theory relevant to each research question is presented in the substantive Chapters 4–7.

An initial comparison between the application of nonlinear stiffness in the floating and submerged contexts is presented in Chapter 4. The impact of nonlinear stiffness is investigated by introducing a nonlinear stiffness force into three distinct scenarios: floating with no linear control stiffness, floating with an optimised linear control stiffness, and submerged with an optimised linear control stiffness. This comparison demonstrates why floating systems may benefit more substantially than submerged systems from nonlinear stiffness. However, submerged systems still experience a benefit in the form of enhanced robustness to changing ocean conditions.

The model fidelity of the submerged scenario is enhanced in Chapter 5 by expanding the model from one DOF to three DOFs. This model captures coupling between each DOF,

and includes geometric nonlinearity which may interact with the nonlinear stiffness. For sufficient nonlinear stiffness conditions, two stable regions may form. This bistable condition is varied in both regular and irregular wave excitation to explore how such a mechanism may improve the submerged system.

The influence of the nonlinear hydrodynamic effects is investigated in Chapter 6 by comparing four different representations of hydrodynamic forces acting on the submerged WEC. This chapter shows that the linear potential flow hydrodynamic model employed in the preceding chapters is not capable of fully representing all the important nonlinear hydrodynamic effects and a validated higher fidelity computational fluid dynamics (CFD) model should be used instead.

Chapter 7 combines a nonlinear stiffness representation into a validated high fidelity nonlinear hydrodynamic simulations for both regular and irregular wave conditions. This chapter assesses the most representative potential benefit of nonlinear stiffness for the submerged PA WEC system and shows that with the nonlinear hydrodynamic influences, the nonlinear stiffness can improve upon an optimised linear system.

The final conclusions, unique contributions to the research field, and potential future work are documented in Chapter 8.

1.3.3 Publications arising from this project

The publications which constitute the thesis include:

Chap. 4   Schubert, B.W., Sergiienko, N.Y., Cazzolato, B.S., Robertson, W.S.P. and Ghayesh, M.H., 2020. The true potential of nonlinear stiffness for wave energy converters. Submitted to *Ocean Engineering*.

Chap. 5   Schubert, B.W., Robertson, W.S.P., Cazzolato, B.S., Ghayesh, M.H. and Sergiienko, N.Y., 2020. Performance enhancement of submerged wave energy device using bistability. *Ocean Engineering*, 213, p.107816.

Chap. 6   Schubert, B.W., Robertson, W.S.P., Cazzolato, B.S. and Ghayesh, M.H., 2020. Linear and nonlinear hydrodynamic models for dynamics of a submerged point absorber wave energy converter. *Ocean Engineering*, 197, p.106828.

Chap. 7   Schubert, B.W., Robertson, W.S.P., Cazzolato, B.S., Sergiienko, N.Y. and Ghayesh, M.H., 2020. Nonlinear stiffness enhancement of submerged wave energy device in high fidelity model. Submitted to *Renewable Energy*.

These journal papers have been reproduced as published or submitted, with the exception of formatting, which has been changed to accommodate the thesis format. Additional studies related to this work, but do not form part of this thesis include:

App. A Schubert, B. W., Robertson, W.S.P., Cazzolato, B. S. and Ghayesh, M. H., 2020. Enhancement of a 3-DOF submerged wave energy device using bistability. In: *International Marine Energy Journal*, 3, pp.73–82. DOI: 10.36688/imej.3.73-82.

App. B Schubert, B. W., Meng, F., Sergiienko, N. Y., Robertson, W.S.P., Cazzolato, B. S., Ghayesh, M. H., Rafiee, A., Ding, B. and Arjomandi, M., 2018. Pseudo-nonlinear hydrodynamic coefficients for modelling point absorber wave energy converters. In: *The 4th Asian Wave and Tidal Energy Conference (AWTEC)*. Taipei, Taiwan.

References

[1]   BP. *Statistical Review of World Energy*. Tech. rep. 2020.

[2]   IRENA. *Renewable Capacity Statistics*. Tech. rep. 2020.

[3]   IRENA. *Innovation outlook ocean energy technologies*. Tech. rep. 2020.

[4]   Ember. *Global Electricity Review*. Tech. rep. Mar. 2020.

[5]   J. Cruz. *Ocean Wave Energy*. 1st ed. Springer-Verlag Berlin Heidelberg, 2008. DOI: `10.1007/978-3-540-74895-3`.

[6]   A. F. de O. Falcão. "Wave energy utilization: A review of the technologies". In: *Renewable and Sustainable Energy Reviews* 14.3 (Apr. 2010), pp. 899–918. DOI: `10.1016/j.rser.2009.11.003`.

[7]   B. Drew, A. R. Plummer, and M. N. Sahinkaya. "A review of wave energy converter technology". In: *Proceedings of the Institution of Mechanical Engineers, Part A: Journal of Power and Energy* 223.8 (2009), pp. 887–902. DOI: `10.1243/09576509JPE782`. eprint: `http://dx.doi.org/10.1243/09576509JPE782`.

[8]   *CorPower's Wave Energy Concept*. Accessed: December 2020. URL: `https://www.corpowerocean.com/technology/`.

[9]   *CETO Next Generation*. Accessed: December 2020. URL: `https://www.carnegiece.com/portfolio/ceto-next-generation/`.

[10] N. Sergiienko et al. "Feasibility study of the three-tether axisymmetric wave energy converter". In: *Ocean Engineering* 150 (Feb. 2018), pp. 221–233. DOI: `10.1016/j.oceaneng.2017.12.055`.

[11] IRENA. "Renewable power generation costs in 2018". In: *Report, International Renewable Energy Agency, Abu Dhabi* (2019).

[12] G. Chang et al. "A comprehensive evaluation of factors affecting the levelized cost of wave energy conversion projects". In: *Renewable Energy* 127 (Nov. 2018), pp. 344–354. DOI: `10.1016/j.renene.2018.04.071`.

[13] R. Wiser et al. *Forecasting wind energy costs and cost drivers: the views of the world's leading experts*. Tech. rep. Lawrence Berkeley National Laboratory, 2016.

[14] J. V. Ringwood, G. Bacelli, and F. Fusco. "Energy-maximizing control of wave-energy converters: the development of control system technology to optimize their operation". In: *IEEE Transactions on Control Systems* 34.5 (Oct. 2014), pp. 30–55. DOI: 10.1109/MCS.2014.2333253.

[15] H. Zhao et al. "Enhancing efficiency of a point absorber bistable wave energy converter under low wave excitations". In: *Energy* 212 (Dec. 2020), p. 118671. DOI: 10.1016/j.energy.2020.118671.

Chapter 2

Literature review

The focus of this thesis is on the application of nonlinear stiffness to enhance the performance of WECs. This chapter provides an overview of the current literature pertaining to WECs, the hydrodynamic models used to simulate the WECs, and control techniques employed to improve the amount of power generated from WECs. Additionally, the recent studies on including a nonlinear stiffness force into WEC systems as an alternative passive control technique are also reviewed. This chapter provides the framework and motivation behind the research conducted for this thesis.

2.1   Wave energy devices

Throughout the two centuries of attempts to harness the energy of ocean waves [1], WEC designs have not converged to a unique solution. Broad classifications have emerged based on the WEC size, orientation relative to the direction of an incident wave, and the mode of generating electrical power from the kinetic energy in ocean waves [2–4]. These classifications were introduced in Chapter 1 as terminators, attenuators, and PA and are conceptually presented in Figure 2.1. Terminators are long in the direction of the wavefront, attenuators are long in the wave direction, whereas PA are devices that are small relative to the wavelength, which means that such devices are less sensitive to wave direction. As an extension of the PA, a quasi-PA is an axisymmetric device that have relatively large dimensions compared to the incident wavelength. Additional WEC classifications which do not strictly fit into these classifications include:

- oscillating water columns, which use the wave elevation to compress air to drive a turbine [5];

- oscillating wave surge converters, which use the horizontal particle velocity of the wave [6];

- overtopping devices, which concentrate incident waves to store a reservoir of water above the sea level and use the gravitational potential to drive a turbine [2]; or

- submerged pressure differential devices, which use the oscillation in wave pressure differential over a structure or membrane [7] to generate electricity [8].
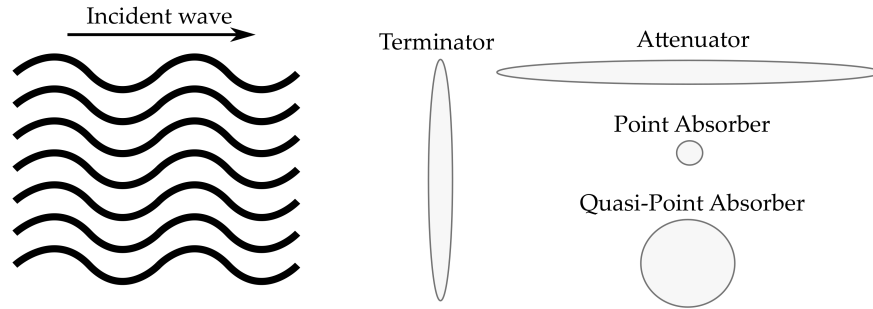
Figure 2.1: Generalised classifications of WEC which are defined based on the size and orientation relative to the direction of an incident wave.

Each broad classification of WECs have fundamentally different modes of operating and require unique modelling techniques to represent the fluid-structure dynamics [9], and to control such devices [1]. Furthermore, different devices may be more suited to particular environments. For example, a PA would be well suited to environmental conditions in which the direction of the wave changes significantly over time, due to its insensitivity to wave direction. Additionally, there are numerous differences between floating and submerged PA WEC. Fully submerged PA WECs generally absorb less power than floating PA WECs of equal volume, but are able to better absorb power from multiple DOF [10]. Furthermore, submerged devices are less exposed to extreme weather conditions and have reduced visual impact compared to floating systems. Most studies on PA WECs are conducted on floating devices, which indicates that many dynamical features of submerged systems have not been explored in great detail. Hence, the work in this thesis will focus primarily on submerged quasi-PA WECs. The following sections will present the current literature around the relevant hydrodynamic and control considerations for this type of device.

2.2 Hydrodynamics

The fluid-structure interactions in many offshore situations can be modelled using a range of different methods, ranging from linear potential flow models [11], to fully

nonlinear CFD simulations. There are several different techniques which aim to capture the nonlinearities associated with different aspects of the hydrodynamic features, which are outlined in this Section. For context, the main hydrodynamic effects which influence WECs are [9]:

- the Froude-Krylov force — the induced load as a result of the dynamic pressure distribution over the device in an undisturbed wave,

- the diffraction force — the force associated with disturbing an incident wave,

- the radiation force — the force linked to the radiated waves due to the motion of the buoy,

- the viscous force — the force opposing the motion relative to the fluid due to the effects of viscosity, and

- nonlinear effects due to water displacement such as slamming or sloshing.

Since the Froude-Krylov and diffraction forces are both associated with an incident wave, and is therefore commonly combined into a single force termed the excitation force.

2.2.1 Wave Models

Numerous models to represent water waves have been proposed, with the most simple representation being Airy wave theory [12]. This simple representation makes many assumptions of the behaviour of water, but is widely used in engineering applications to provide indicative results [13]. The primary assumptions are:

- the fluid is continuous, homogeneous, incompressible, and inviscid,

- the Coriolis forces and surface tensions may be neglected,

- the pressure at the free surface is constant,

- the flow is irrotational,

- the bottom is fixed, and

- the height of the wave relative to the water column is small.

This theory uses a potential function and the dispersion relationship to determine the surface elevations, η, and fluid velocity fields. The dispersion relationship is [14]

$$\omega^2 = gk \tanh(kh) \,, \tag{2.1}$$

11

where ω, g, k, and h represent the wave frequency, acceleration of gravity, wavenumber, and depth of the wave column, respectively. The wave elevation is given by [13]

$$\eta = \frac{H}{2}\cos(kx - \omega t) \,, \tag{2.2}$$

where H represents the wave height, x is the horizontal position, and t represents time. While the theory can be used to calculate the fluid velocity in all directions, for simplicity, only the vertical velocity, $\dot{z}_f$, is provided here and may be calculated as

$$\dot{z}_f = \frac{H}{2}\omega\frac{\sinh(kz)}{\sinh(kh)}\sin(kx - \omega t) \,, \tag{2.3}$$

where z is the vertical position with respect to the surface with up as positive [15]. This representation of a wave is also known as a Stokes I wave. If any of the assumptions are violated, the theory breaks down and, consequently, is not representation of a realistic wave. However, a second order term may be included through the iterative solving of the dispersion relationship [13]. This second order wave representation is known as a Stokes II wave and has a wave elevation of [13]

$$\eta = \frac{H}{2}\cos(kx - \omega t) + k\frac{H^2(3 - \sigma^2)}{16\sigma^3}\cos(2(kx - \omega t)) \,, \tag{2.4}$$

where

$$\sigma = \tanh(kh) \,. \tag{2.5}$$

Similar additional terms may be seen in the velocity components of the fluid. If wave conditions are even more extreme such as for shallow water waves or high frequency waves, higher order wave theories exist such as Stokes III, Stokes IV, Stokes V, cnoidal, and streamfunction waves. The applicability of the different wave theories available is presented in Figure 2.2. The relevant quantities should be calculated for a given wave scenario to determine which wave theory should be used to represent the physical water wave.

2.2.2 Linear methods

Simple methods to quantify the hydrodynamics involve using linear potential flow models — often solved using the boundary element method (BEM) — to quantify the Froude-Krylov, diffraction, and radiation forces at a given wave frequency for a given buoy [17]. The pressures acting on the surface of a buoy due to various sources may be superimposed to find the total pressure, p, represented by

$$p = p_s + p_d + p_{Di} + p_r \,, \tag{2.6}$$

where p_s, p_d, p_{Di}, and p_r represent the pressures associated with the static, dynamic, diffraction, and radiation loadings, respectively. The dynamic pressure, p_d, in this case,
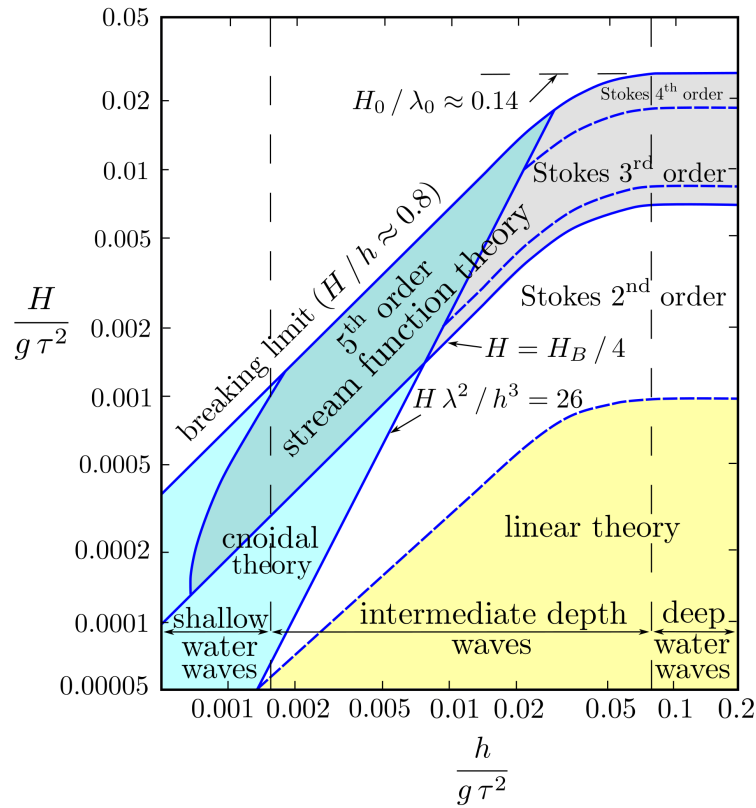
Figure 2.2: The applicable regions for different wave theories to apply [16]. This figure was sourced from `https://commons.wikimedia.org/wiki/File:Water_wave_theories.svg`, CC BY-SA 3.0.

is related to the Froude-Krylov force and is the pressure acting on the device due to an undisturbed wave. The associated forces may then be quantified by integrating over the surface of the buoy. This approach has the advantage of being able to be precalculated for frequency domain models, and may be implemented into time domain simulations using some assumptions, which may result in fast models. However, this method linearises the pressures and calculates these hydrodynamic parameters about a single position, and therefore ignores all second order hydrodynamics [17]. Linear BEM solvers have demonstrated reduced accuracy for scenarios in which the buoy deviates significantly from the nominal position [18].

Linear BEM solvers operate by using Green's Theorem in which the velocity potential of the fluid is specified by specifying the conditions at the boundary surfaces [19]. This approach leads to solving an integral equation over the surface of the buoy. To numerically solve this problem, the surface of the buoy is approximated by a number of

quadrilateral panels. The velocity potential at the centroid of each panel is evaluated and used to quantify the pressure acting on the panel [19]. The pressure is then integrated over the body to quantify the required forces and moments.

Typical solvers which are used to find the linearised hydrodynamic parameters are NEMOH (L'École Centrale De Nantes, Nantes, France), WAMIT (WAMIT, Inc., Chestnut Hill MA, USA), and AQWA (ANSYS, Inc., Canonsburg PA, USA). While WAMIT may be considered the standard in literature of such approaches, NEMOH provides almost identical results for submerged PA WEC [11], and is open source. The AQWA software may be used for PA, but is more often used in other applications. These potential flow BEM solvers provide a computationally efficient method of quantifying hydrodynamic characteristics, but neglect any nonlinear hydrodynamic properties.

2.2.3 Partially nonlinear

Depending on the mode of operation of a given device, particular nonlinear hydrodynamic features may be more influential, and therefore more complex models may be required. For example, the most influential nonlinearity related to hydrodynamic forces for small heaving PA WECs is known to be the Froude-Krylov force due to the change of position, as the radiation and diffraction effects are typically smaller [20]. An extension to the linearised model which has been proposed is to recalculate the Froude-Krylov force at each time step for the instantaneous wetted surface [21, 22]. Similar attempts to increase the fidelity of models based on the potential flow method include: extending the linear potential flow to a nonlinear potential flow [23]; partially extending the hydrodynamic forces to a second order approximation [21]; applying Wheeler's stretching method of Airy's linear wave theory [24]; and precalculating the hydrodynamic parameters for a range of poses and applying a gain scheduling method [25]. Such extensions are termed partially nonlinear within literature but are often only suited to niche situations. For small buoys, modelling the nonlinearity in the Froude-Krylov force is influential as it is larger than other force components. However, for larger buoys, diffraction forces are more significant and would require different approaches to incorporate into a linear model. As BEM solvers calculate hydrodynamic properties for a given position, for small oscillations the system is predisposed to linear conditions and therefore give similar results to models using nonlinear hydrodynamics, but rapidly lose accuracy as the system deviates from a nominal position [18].

An extension of potential flow models is the weak-scatter approach which uses potential flow theory to solve for the diffracted and radiated waves and treats the incident wave as a forcing term. For a submerged buoy, such an approach has been shown to agree with results found using a linear model for linear wave conditions, and show substantial deviations under nonlinear wave conditions [26].

2.2.4 Fully nonlinear

A common fully nonlinear method to model hydrodynamics is CFD, which can quantify the fluid forces based on the numerical implementation of the Navier-Stokes equations [9]. The prevalence of CFD and numerical wave tanks (NWT) in literature has been increasing with the rise of available computational power [27]. Such approaches are both time and computationally intensive to develop and execute but offer increased fidelity and are more representative simulations for assessing device performance if experimentally validated [27]. For the context of wave energy, there are a number of important considerations in the application of fully nonlinear hydrodynamic models, including: the fluid foundational theory, the discretisation of the numerical domain, the flow characteristics of the fluid, the generation and absorption of waves, and the dynamic behaviour of the buoy and discretised mesh.

2.2.4.1 Theory

The Navier-Stokes equations are a set of fundamental equations which describe the relationship between momentum, energy, and mass and are [9]

$$\frac{\partial \rho}{\partial t} + \nabla(\rho \mathbf{u}) = 0 \,, \tag{2.7}$$

$$\frac{\partial \mathbf{u}}{\partial t} + (\mathbf{u}\nabla)\mathbf{u} = -\frac{1}{\rho}\nabla \mathbf{p} + \mathbf{F}_{\text{ext}} + \frac{\mu}{\rho}\nabla^2 \mathbf{u} \,, \tag{2.8}$$

$$\rho\left(\frac{\partial \epsilon}{\partial t} + \mathbf{u}\nabla\epsilon\right) - \nabla(K_H \nabla T) + \rho\nabla \mathbf{u} = 0 \,, \tag{2.9}$$

where $\mathbf{u}$, ρ, and μ are the fluid velocity, density, and viscosity, respectively. The pressure field and external forces are denoted by $\mathbf{p}$ and $\mathbf{F}_{\text{ext}}$, respectively. The internal energy, heat conduction coefficient, and temperature are represented by ϵ, K_H, and T, respectively. If implemented appropriately, using software such as OpenFOAM, an open source CFD package, the fully nonlinear behaviour of the fluid-buoy interactions may be numerically quantified. In practice, for the ocean wave energy context, the themal properties of the fluid are less consequential and are often not included in relevant OpenFOAM solvers. Due to the complexity of such an approach, for the results to have meaning, the model should be validated and the most reliable method of validation is a comparison against experimental data [9].

For some contexts, the Navier-Stokes equations may be simplified by assuming the fluid is inviscid and incompressible. These assumptions result in the Euler equations

$$\nabla(\mathbf{u}) = 0 \,, \tag{2.10}$$

$$\frac{\partial \mathbf{u}}{\partial t} + (\mathbf{u}\nabla)\mathbf{u} = -\frac{1}{\rho}\nabla \mathbf{p} + \mathbf{F}_{\text{ext}} \,. \tag{2.11}$$

Table 2.1: The distribution of CFD software in the wave energy research field in 2018 [27].

Software	Percentage used
OpenFOAM	39%
Fluent	20%
STAR-CCM+	13%
CFX	11%
In-house	10%
Flow-3D	7%

This simplification reduces the computational intensity of the equations solved, but assumes the fluid has no viscosity. In cases where the interaction between a fluid and a structure that is fixed or undergoes forced oscillations, neglecting viscosity to reduce the computational burden does not significantly change the result [28]. However, when viscous effects are influential, such as for PA dynamics in multiple degrees of freedom [27], the full Navier-Stokes equations should be used, or the drag associated with viscosity must be accounted for by added adhoc damping.

Computational fluid dynamics programs can numerically solve the Navier-Stokes equations by discretising temporally and spatially. This discretisation forms a set of linear algebraic equations to be solved. The domain is subdivided or meshed to appropriately represent the required physical arrangement. Then, each time-step is iteratively solved to achieve convergence in the final calculated values. Methods of meshing, solving, and interpolating vary between different software packages. The most common CFD software used within WEC analysis is OpenFOAM [27]. The distribution of CFD software usage within the wave energy research field is presented in Table 2.1

The specific applications of CFD to WEC include the evaluation of viscous influences [29–34], performance evaluation and optimisation [35–38], load estimation [28, 31, 39–41], and control [42–46]. These applications span a range of devices and contexts.

Another fully nonlinear approach is known as smooth-particles hydrodynamics, which uses an approach developed for astrophysics applications [47]. This technique considers the domain to be a set of discrete points which represent a continuous field and may be used to interpolate. In the wave energy context, SPH are often used [48–51] to simulate extreme scenarios where alternative hydrodynamic models are either too low fidelity, or too computationally expensive [9].

2.2.4.2 Discretisation

In any application of CFD to model offshore fluid-structure interactions, one of the key considerations is the mesh discretisation, both temporal and spatial. For wave energy, this discretisation influences how a wave is generated, propagated, and absorbed. Common

metrics used to quantify spatial discretisation include the number of cells per waveheight (in the vertical direction), and the number of cells per wavelength (in the direction of wave propagation) [52, 53]. A meshed computational domain for generating waves is often referred to as a numerical wave tank (NWT). The temporal discretisation is achieved either through variable or fixed time steps. A common metric employed to ensure appropriate time steps is the Courant number Co [27], which is a measure of how fast information travels across the mesh in a unit of time. This metric is defined as

$$Co = \frac{u\Delta t}{\Delta x} \,,$$
(2.12)

where u is the velocity of the fluid, Δt is length of the time step, and Δx is the characteristic length of the meshed cell. This metric may be analysed or applied in all three spatial directions and is often used to calculate the appropriate variable time step. A common rule of thumb used within literature is that $Co < 0.5$.

2.2.4.3 Flow characterisation

Depending on the assumptions made, the flow of the fluid may be calculated using the Navier-Stokes or Euler equations, depending on whether the fluid is assumed to have viscosity. If the fluid has viscosity, which is more representative of real fluids, the flow may be laminar or turbulent. If it is assumed that the fluid does not interact with adjacent fluid layers, a laminar regime may be considered [54]. Without this assumption, the flow can become turbulent, which may be computationally intensive but more physically representative [27]. The most common method of implementing the Navier-Stokes equations to account for turbulent effects is the Reynolds Averaged Navier Stokes (RANS) equations. These equations combine the Navier-Stokes equations with additional equations to describe turbulence. The additional equations describe the transport of kinetic turbulent energy and the dissipation rate of kinetic energy [27]. As an extension of the RANS equations, the volume averaged RANS have been proposed to better represent momentum transport at interfaces between porous media [13]. Further information on turbulence models is well documented in literature [13, 27].

To determine if a laminar or turbulent flow regime should be employed, two dimensionless numbers may be used: the Reynolds number, Re, and the Keulegan-Carpenter number KC, given by [55]

$$Re = \frac{uL}{\nu} \,,$$
(2.13)

$$KC = \frac{u_m T}{L} \,,$$
(2.14)

where u is the fluid velocity, L is the characteristic length, ν is the kinematic viscosity, T is the wave period, and u_m is the amplitude of the flow velocity. If these two quantities

are sufficiently low, the flow over an object may be assumed to be laminar. For PA WECs, CFD scenarios in literature indicate that laminar flow is often a sufficient flow regime to use. One study on a floating PA assumes laminar flow [56] and validates the model against experimental data. Similarly, another study models a submerged cylindrical WEC [57], assumes laminar flow, and finds the values $Re < 10^4$ and $KC < 1$, which ensures the flow is laminar [55]. While there are further cases which affirm the validity of laminar flow conditions for PA WECs, such assumptions should be assessed for each scenario. The general approximate rule of thumb for a CFD model to be considered validated is to be with 10% of the reference data, either experimental results or data attained from another validated CFD scenario.

2.2.4.4 Wave generation and absorption

Within a NWT, it is critically important to computationally generate and absorb a desired wave to represent a physical scenario. The three main methods of generating water waves in a NWT are: internal wave generation, static boundary wave generation, and moving boundary wave generation [58].

The internal wave generation approach effectively adds or removes momentum in the form of additional mass or velocity according to a predefined function. As the generated waves propagate throughout the computational domain, absorption zones must also be included to dissipate the added momentum and energy. The addition or removal of momentum can take place over a region, known as a relaxation zone, rather than at a boundary to avoid rapid changes, discontinuities, and numerical instabilities [13]. The disadvantage of this approach is that it requires a larger domain size to allow for these relaxation zones. For RANS models, there have been a number of examples in literature of internal wave generation employed in a 2D [59, 60] and 3D [61] context. Other examples of this approach include but are not limited to [42, 62, 63].

Static boundary wave generation specifies the boundary conditions based on a given wave theory. These wave theories specify the boundary conditions, free surface elevation, and fluid state over the NWT. The boundary conditions from the wave theory may be applied to the boundaries of the computational domain, which causes the required fluid motion. One advantage of this technique is that these operations are computed at the boundaries, which reduces the need for larger computational domains observed in internal wave generation. However, since the boundary conditions are specified throughout the duration of the simulation, there may be a disparity between volume of fluid moving in and out of the boundaries at wave crests compared to troughs, which can lead to a net increase in water level over each wave period. Therefore, static boundary wave generation must have some form of active wave absorption to compensate for this imbalance [13]. Examples of this approach for a range of devices and contexts include [64–67].

18

Dynamic boundary wave generation mimics the action of physical wave generators by moving the boundaries to form or absorb the required wave. While there are different approaches within dynamic boundary wave generation identified in literature [13], the general approach is to either apply a force on an immersed body in the computational domain, or by deforming the mesh at the boundaries to displace the fluid in a required way. The computational cost associated with a dynamic or deforming mesh can increase the simulation times by over 30% [13]. Accordingly, dynamic boundary approaches are not as common as other wave generating techniques for CFD scenarios, but are well suited to meshless tools such as SPH [49].

The absorption of a generated wave is a necessary component to ensure that waves are not reflected back into the simulated region of interest. Wave absorption, similar to wave generation, has different approaches, but can be classified as either passive or active. Passive approaches aim to replicate the wave dissipation techniques used in experimental setups such as beaches [68] or perforated mesh screens [69]. Active wave absorption, which is derived from early attempts to experimentally absorb waves [70], aims to actively generate a wave/particle velocity at the boundary to act in the opposite direction to the generated wave. There have been many approaches which achieve this experimentally and in a NWT [13]. For OpenFOAM, a package known as *olaFlow* [71] has been constructed which implements both static boundary wave generation, and active wave absorption, which eliminates the need for long relaxation zones [52]. The principle advantage of active absorption over passive is the reduced domain size, and therefore computational requirements.

2.2.4.5 Motion

For wave energy devices, the structure the fluid is interacting with is often not fixed. This implies that the way the fluid interacts with the structure or object depends on the motion of the object, and consequently coupling between the fluid solver and motion solver forms part of the computational problem. In CFD software, the motion of object and mesh may be performed by the following process at each time step [27]:

1. update position,

2. evaluate forces,

3. determine acceleration,

4. move object, and

5. move (or slide, interpolate, and deform) mesh.

While these steps provide a general process, the specific algorithms depend on the CFD software used. For OpenFOAM, a review of the implicit motion solver has been conducted [72]. The degree to which the mesh is deformable, as well as the specific regions and the algorithm to use may be specified in the development of the CFD scenario. Mesh motion and structure are often crucially important in the stability of the simulation and is the most significant limitation of dynamic meshes [73]. The development of the mesh structure, computational domain and deformation algorithm is an iterative process heavily dependent on individual scenarios. The specific approaches taken in this thesis will be discussed in Section 3.4.

2.2.5 Concluding remarks for hydrodynamics

There are numerous approaches taken in literature to model PA WECs with varying degrees of fidelity. While potential flow models provide a computationally efficient solution and an indicative result in simple linear circumstances, many hydrodynamic nonlinearities are not captured. Therefore, to properly quantify the fluid-structure interaction and assess the performance of a WEC, nonlinear hydrodynamic models must be employed. Such nonlinear hydrodynamic models use appropriate mathematical foundation for the particular wave conditions, be sufficiently discretised in space and time, have adequate mesh structure and deformation algorithms, and have appropriate conditions to generate and absorb waves. Such a model should be validated against experimental data to provide confidence in using the NWT as an analysis tool to assess device performance.

2.3 Control approaches

One key priority of wave energy is the development of a suitable control system to improve the economic viability of WECs [74, 75]. The theoretical optimal control strategy that is presented in literature relies upon matching the intrinsic impedance of a system [76]. For this optimal control strategy to work for more than a simplistic regular wave case, future knowledge of the wave is required due to the non-causal relationship between an incident wave and the force exerted by an incident wave [77]. In practice, it may infeasible to employ such optimal control, so a number of suboptimal control schemes have been proposed as alternatives. These control systems may be described as [76]:

- constant damping control,

- time-varying damping control,

- reactive control,

- latching/unlatching (or declutching), and

- model predictive control (MPC).

These control techniques (except constant damping) are examples of active control, or require some actuation, which rely on estimating a control force to apply at a given time. While there are other control strategies that have been proposed which do not fit into these categories, these are main control approaches which have been utilised WECs. For further information on different active control strategies, see [2, 76, 78].

2.3.1   Optimal control

Optimal control strategies in literature attempt to match the stiffness and damping of a device to force resonant absorption [79]. For a heaving 1 DOF PA in regular waves, the complex amplitude of the device velocity, $\hat{u}$, can be derived to be [79]

$$\hat{u} = \frac{\hat{F}_e}{B_m + B_\omega + i[\omega(m_m + m_\omega) - K_m/\omega]} \,, \tag{2.15}$$

where $\hat{F}_e$ is the frequency domain representation of the excitation force; B_m and K_m represent the mechanical damping and stiffness, respectively; B_ω and m_ω are the hydrodynamic damping and added mass, respectively; and m_m is the mass of the PA WEC device. The average mechanical power absorbed by the device in a regular wave, P_a is

$$P_a = \frac{B_m}{2}|\hat{u}|^2 = \frac{(B_m/2)|\hat{F}_e|^2}{(B_m + B_\omega)^2 + (\omega m_m + \omega m_\omega - K_m/\omega)^2} \,. \tag{2.16}$$

The maximum absorbed power may be found when the condition

$$\frac{\partial P_a}{\partial B_m} = 0 \tag{2.17}$$

is satisfied. This condition is met if the mechanical damping parameter is

$$B_m = \sqrt{B_\omega^2 + (\omega m_m + \omega m_\omega - K_m/\omega)^2} \,. \tag{2.18}$$

For an arbitrary system, the stiffness may be selected based on design requirements. By further examining Equation (2.16), the power may be maximised if the denominator is at a minimum. As the stiffness may be selected as required, the second term in the denominator can become

$$\omega m_m + \omega m_\omega - K_m/\omega = 0 \,, \tag{2.19}$$

if the stiffness is

$$K_m = \omega^2(m_m + m_\omega) \,. \tag{2.20}$$

This stiffness is the combined mechanical stiffness in the WEC and can include the hydrostatic stiffness if the WEC is a floating device. Enforcing this condition on the combined stiffness reduces the optimal damping in Equation (2.18) to

$$B_m = B_\omega \, . \tag{2.21}$$

Therefore, by substituting these terms into Equation (2.15) it can be seen than an optimal control system removes the influence of inertial terms and matches the phase of the velocity and the excitation force, leading to the device resonating. This condition is achieved by matching the intrinsic impedance (stiffness and damping) of the system, which is the guiding principle of theoretical optimal control of WEC systems.

2.3.2 Damping control

Constant damping control applies a constant load on the device proportional to the instantaneous speed. The simplicity of implementation of such a control system makes it common in prototype devices and may be optimised for regular (sinusoidal) waves [79]. However, real ocean conditions are irregular by nature. Irregular waves contain many frequency components, are described by spectra, and change over time. This complexity necessitates that the optimal value for damping (and stiffness) changes over time [78]. Therefore, the constant damping approach offers a comparatively small amount of power generation compared to other control strategies [76]. Various approaches to determine the optimal instanteous linear damping parameter have been investigated [78]. One such approach uses a Hilbert-Huang transform [80] to instantaneously tune based on the excitation force frequency.

2.3.3 Reactive control

Unlike damping control, reactive control utilises a displacement-dependent force as well as a velocity-dependent force to control the WEC system, thereby giving the system linear stiffness and damping parameters [76]. This type of control aims to determine optimal values for these parameters [81], which may be calculated offline or during operation. Different approaches for calculating or selecting these parameters include using fuzzy logic [82], Pontryagin's maximum principle [83], and evolutionary algorithms [84].

Reactive control strategies operate storing and releasing energy to cause the WEC to oscillate beneficially in the wave [85]. The storage mechanism varies with design by may be applied by hydraulic, pneumatic, mechanical, electrical, or magnetic means [76]. While optimal values may be calculated for a given ocean condition or wave, as with damping control, the optimal requirement change depending on the excitation conditions. The most significant disadvantage of these strategies is the losses associated with the reactive energy exchange and the cyclic switching between motor and generator

of a potential active control system [76]. Passive mechanisms may help reduce losses but are less robust to changing conditions.

2.3.4 Latching and unlatching

Latching control aims to match the phase of the velocity and excitation force by fixing the WEC during a portion of the oscillation [86]. This suboptimal approach approximates resonance operation while including the losses of reactive control [1]. The duration of the latching is essential for this system to provide an improvement [2]. To determine this timing, numerous techniques have been employed. One study uses genetic algorithms on a simulation to quantify the latching periods [87]. Three different approaches to timing have been compared in [86]. While all approaches demonstrated improvements upon an uncontrolled system, the study highlighted the need for predicting future excitation force to further enhance the performance of the systems. Unlatching control, or declutching control, the opposite of latching control, involves allowing the system to freely move for a portion of the oscillation [2] with the same aim of matching the phase of the velocity and excitation force. The algorithms for unlatching control are subject to the same prediction and timing limitations.

2.3.5 Model predictive control

The approach of MPC is to simulate the system in an attempt to predict the ideal control parameters to maximize the energy absorption over time. The benefit of MPC approaches is that the simulations may included nonlinearities and system constraints, such as motion or PTO force limits, making it a versatile approach that is widely adopted in industry [88]. For such a system to be an optimal control solution, the excitation force must be predicted in advance due to the non-causality of the impulse response functions of propagating water waves [77, 89]. Using the excitation force prediction, the instantaneous optimal force may be applied at each time step. This prediction is a complicated prospect due to the nonlinear fluid-structure interactions and stochastic nature of ocean waves. Some predictive strategies use neural networks and machine learning [90, 91], another approach uses an autoregressive model and Kalman Filter to estimate the force of a given sea state [92]. These approaches often require significant amounts of data to train or are specific to an individual ocean condition, so further developments are required. While MPC does not improve the amount of absorbed power compared to an optimised reactive controller, it can enhance the robustness and ability to deal with variations in wave conditions.

2.4   Nonlinear stiffness passive control

As an alternative to active control, passive elements could be included to supplement the active elements. Such hybrid control may provide advantages over actively controlled systems which require power to augment the system dynamics using electrical or mechanical inputs [93]. One form of this passive control strategy which is a current research topic is the addition of a nonlinear control stiffness force as a means to passively enhance the WEC.

The application of a nonlinear stiffness force has been explored for numerous purposes [94]. Within the context of energy harvesting, a number of demonstrated benefits exist which occur as a result of such nonlinear mechanisms [94]. Such benefits include stochastic resonance, which exploit the statistical nature of some energy sources to convert low amplitude oscillations of broadband excitation into larger amplitude oscillations. The literature on vibration energy harvesting using a nonlinear stiffness mechanism [95–99] provides a strong foundation to build upon to extend this approach into the wave energy field.

The implementation of this nonlinear stiffness force to the wave energy context varies throughout literature but has been explored using a general representation in the form of a polynomial of displacement and velocity [100], or through a set of adjacent springs [93, 101–105] or magnets [106, 107]. A common approach is to increase the nonlinearity of the stiffness force to create an negative effective stiffness, which often forms two or more stable regions. Arrangements with exactly two stable regions are referred to as bistable and may provide some benefit for stochastic systems [94]. The consensus in literature is that these nonlinear stiffness systems can be employed to improve the amount of power generated. However, the most common type of PA WEC presented in this literature is on floating rather than submerged devices. Floating devices typically have a large hydrostatic stiffness and therefore require some form of negative stiffness to shift the natural frequency of the WEC to the excitation frequency.

Instead of aiming to counteract the hydrostatic stiffness, in some of the studies on passive nonlinear stiffness control only the damping parameter is optimised [102, 103, 107], another study does not include a linear control stiffness [101], while others neglect to optimise the linear control parameters [100, 105]. Under these assumptions, the cases studied in literature result in comparing a system with nonlinear stiffness to another suboptimal system, which does not provide a true representation of the potential benefit of the passive control system approach.

When these nonlinear stiffness passive systems are implemented in simulations, the PA WEC is often restricted to a single DOF [93, 102, 103, 106, 108]. This simplification restricts the potential for modelling coupled dynamics between multiple DOF, which, for submerged PA WEC can be significant [10, 109, 110]. Furthermore, in some studies, the systems were only excited by regular waves, which are not indicative of ocean conditions

but do give a broad picture of the frequency response [93, 103, 104, 106].

A further review of literature pertaining to nonlinear stiffness control techniques may be found in Chapters 4 and 5.

2.5   Concluding remarks

This chapter provided an overview of the different types of WECs and the common tools used to quantify the hydrodynamic features of PA WECs. The techniques commonly used to control wave energy devices were reviewed along with the current literature involving passive control approaches using nonlinear stiffness.

While there are many different classifications of WECs based on their size relative to an incoming wave and mode of operation, the focus of this thesis was selected to be the PA (and quasi-PA) due to the axisymmetric design and the consequential insensitivity to wave direction. Specifically, the primary focus is submerged quasi-PA, due to the fewer studies on submerged PA systems and the potential benefit of absorbing more energy from multiple DOF.

There have been many different control strategies developed for floating and submerged PA WECs, each with advantages in terms of improvement to the total absorbed power, and disadvantages in terms of complexity, robustness, and efficiency. As an alternative to active control systems, passive systems using nonlinear stiffness mechanisms, which may offer some improvement to performance, have been simulated in simplistic circumstances and compared to suboptimally controlled systems. To address this gap, Chapter 4 explores this concept by modelling a simplified PA in both submerged and floating contexts with both regular and irregular wave conditions with nonlinear stiffness and comparing the results to a system with an optimally tuned linear stiffness. Then, in Chapter 5 the fidelity of the submerged system was increased by modelling the device in three degrees of freedom. The nonlinear stiffness mechanism was included for an optimally tuned and suboptimally tuned system to determine if the benefit observed in literature is consistent as the fidelity increases.

The different hydrodynamic considerations relevant to the PA type WECs were identified. The methodologies employed to quantify the hydrodynamic interaction of these WECs include linear, partially nonlinear, and fully nonlinear simulations. The most influential hydrodynamic nonlinearity for small heaving PA type WECs is known to be the excitation force. While there have been attempts to include this nonlinearity into fast-solving models, many approaches are device specific. So for larger PAs, which are submerged and operating in multiple degrees of freedom, different hydrodynamic modelling tools should be compared with experimental data to determine if low fidelity simulations are adequate representations of important hydrodynamic influences. This topic is investigated in Chapter 6 by incorporating pose-dependence as an extension

of linear hydrodynamic models and then comparing results of the simulations against a validated CFD model. The results from the simulations under different operating conditions, such as wave heights and submergence depths, are compared to identify the influence of different hydrodynamics features in different scenarios.

The benefit due to nonlinear stiffness discussed in the current literature is observed for suboptimally tuned systems at low fidelity hydrodynamic simulations. Therefore, the validated fully nonlinear hydrodynamic tool was used to model a system with a nonlinear stiffness in three degrees of freedom in Chapter 7. Such high fidelity simulations to capture the nonlinear dynamics between the hydrodynamic features and nonlinear stiffness is not observed in present work, and addresses a significant gap in current literature to advance this research field.

These gaps identified in literature and the methods outlined to address these shortcomings form the fundamental key research questions to be answered throughout the thesis, which are presented in Section 1.3.1. Literature specific to these research questions are reviewed in more detail in the substantive Chapters 4 − 7.

References

[1]   J. Cruz. *Ocean Wave Energy*. 1st ed. Springer-Verlag Berlin Heidelberg, 2008. DOI: 10.1007/978-3-540-74895-3.

[2]   B. Drew, A. R. Plummer, and M. N. Sahinkaya. "A review of wave energy converter technology". In: *Proceedings of the Institution of Mechanical Engineers, Part A: Journal of Power and Energy* 223.8 (2009), pp. 887–902. DOI: 10.1243/09576509JPE782. eprint: http://dx.doi.org/10.1243/09576509JPE782.

[3]   A. F. de O. Falcão. "Wave energy utilization: A review of the technologies". In: *Renewable and Sustainable Energy Reviews* 14.3 (Apr. 2010), pp. 899–918. DOI: 10.1016/j.rser.2009.11.003.

[4]   A. Babarit. *Ocean wave energy conversion*. 2018.

[5]   P. Hardy et al. "A maximum capture width tracking controller for ocean wave energy converters in irregular waves". In: *Ocean Engineering* 121 (2016), pp. 516–529. DOI: http://dx.doi.org/10.1016/j.oceaneng.2016.05.045.

[6]   D. J. Crooks. "Nonlinear hydrodynamic modelling of an oscillating wave surge converter". PhD thesis. Queen's University Belfast, 2017.

[7]   C. Algie, S. Ryan, and A. Fleming. "Predicted power performance of a submerged membrane pressure-differential wave energy converter". In: *International journal of marine energy* 20 (2017), pp. 125–134.

[8]   IRENA. *Innovation outlook ocean energy technologies*. Tech. rep. 2020.

[9] M. Penalba, G. Giorgi, and J. V. Ringwood. "Mathematical modelling of wave energy converters: A review of nonlinear approaches". In: *Renewable and Sustainable Energy Reviews* 78 (Oct. 2017), pp. 1188–1207. DOI: `10.1016/j.rser.2016.11.137`.

[10] N. Y. Sergiienko et al. "Performance comparison of the floating and fully submerged quasi-point absorber wave energy converters". In: *Renewable Energy* 108 (Aug. 2017), pp. 425–437. DOI: `10.1016/j.renene.2017.03.002`.

[11] M. Penalba, T. Kelly, and J. V. Ringwood. "Using NEMOH for modelling wave energy converters: a comparative study with WAMIT". In: *Centre for Ocean Energy Research (COER), Maynooth University, Co. Kildare, Ireland* (2017).

[12] G. B. Airy. *Tides and waves*. B. Fellowes, 1845.

[13] P. Higuera. "Application of computational fluid dynamics to wave action on structures". In: *PhD. Universidade de Cantabria* (2015).

[14] M. W. Dingemans. *Water wave propagation over uneven bottoms*. Vol. 13. World Scientific, 1997.

[15] R. Salmon. "Introduction to ocean waves". In: *Scripps Institution of Oceanography, University of California, San Diego* (2008).

[16] B. Le Méhauté. "An introduction to water waves". In: *An Introduction to Hydrodynamics and Water Waves*. Springer, 1976, pp. 197–211.

[17] M. Penalba et al. "Influence of nonlinear Froude–Krylov forces on the performance of two wave energy points absorbers". In: *Journal of Ocean Engineering and Marine Energy* 3.3 (June 2017), pp. 209–220. DOI: `10.1007/s40722-017-0082-x`.

[18] J. Davidson, S. Giorgi, and J. V. Ringwood. "Linear parametric hydrodynamic models for ocean wave energy converters identified from numerical wave tank experiments". In: *Ocean Engineering* 103 (2015), pp. 31–39. DOI: `http://dx.doi.org/10.1016/j.oceaneng.2015.04.056`.

[19] C.-H. Lee and J. N. Newman. "Computation of wave effects using the panel method". In: *WIT Transactions on State-of-the-art in Science and Engineering* 18 (2005).

[20] G. Giorgi and J. V. Ringwood. "Comparing nonlinear hydrodynamic forces in heaving point absorbers and oscillating wave surge converters". In: *Journal of Ocean Engineering and Marine Energy* 4.1 (Aug. 2017), pp. 25–35. DOI: `10.1007/s40722-017-0098-2`.

[21] A. Merigaud, J.-C. Gilloteaux, and J. V. Ringwood. "A nonlinear extension for linear boundary element methods in wave energy device modelling". In: *Volume 4: Offshore Geotechnics; Ronald W. Yeung Honoring Symposium on Offshore and Ship Hydrodynamics*. ASME, July 2012. DOI: `10.1115/omae2012-83581`.

[22] H. A. Wolgamot and C. J. Fitzgerald. "Nonlinear hydrodynamic and real fluid effects on wave energy converters". In: *Proceedings of the Institution of Mechanical Engineers, Part A: Journal of Power and Energy* 229.7 (2015), pp. 772–794.

[23] E. Guerber et al. "A fully nonlinear implicit model for wave interactions with submerged structures in forced or free motion". In: *Engineering Analysis with Boundary Elements* 36.7 (July 2012), pp. 1151–1163. DOI: `10.1016/j.enganabound.2012.02.005`.

[24] G. Giorgi and J. V. Ringwood. "A compact 6-DoF nonlinear wave energy device model for power assessment and control investigations". In: *IEEE Transactions on Sustainable Energy* 10.1 (Jan. 2019), pp. 119–126. DOI: `10.1109/tste.2018.2826578`.

[25] A. McCabe, G. A. Aggidis, and T. Stallard. "A time-varying parameter model of a body oscillating in pitch". In: *Applied Ocean Research* 28.6 (2006), pp. 359–370.

[26] L. Letournel et al. "Weakly nonlinear modeling of submerged wave energy converters". In: *Applied Ocean Research* 75 (June 2018), pp. 201–222. DOI: `10.1016/j.apor.2018.03.014`.

[27] C. Windt, J. Davidson, and J. V. Ringwood. "High-fidelity numerical modelling of ocean wave energy systems: A review of computational fluid dynamics-based numerical wave tanks". In: *Renewable and Sustainable Energy Reviews* 93 (Oct. 2018), pp. 610–630. DOI: `10.1016/j.rser.2018.05.020`.

[28] J. Westphalen et al. "Investigation of wave-structure interaction using state of the art CFD techniques". In: *Open Journal of Fluid Dynamics* 4.01 (2014), p. 18.

[29] M. A. Bhinder et al. "Assessment of viscous damping via 3D-CFD modelling of a floating wave energy device". In: *Proceedings of the 9th European Wave and Tidal Energy Conference, Southampton, UK*. 2011, pp. 5–9.

[30] M. A. Bhinder et al. "Effect of viscous forces on the performance of a surging wave energy converter". In: *The Twenty-second International Offshore and Polar Engineering Conference*. International Society of Offshore and Polar Engineers. 2012.

[31] A. Rafiee and J. Fiévez. "Numerical prediction of extreme loads on the CETO wave energy converter". In: *Proceedings of the 11th European Wave and Tidal Energy Conference, Nantes, France*. 2015.

[32] H. Asmuth et al. "Determination of non-linear damping coefficients of bottom-hinged oscillating wave surge converters using numerical free decay tests". In: *Proceedings of the 1st International Conference on Renewable Energies Offshore, Lisbon, Portugal*. 2014, pp. 24–26.

[33] M. A. Bhinder et al. "Potential time domain model with viscous correction and CFD analysis of a generic surging floating wave energy converter". In: *International Journal of Marine Energy* 10 (2015), pp. 70–96.

[34] A. Nematbakhsh et al. "Comparison of experimental data of a moored multibody wave energy device with a hybrid CFD and BIEM numerical analysis framework". In: *International Conference on Offshore Mechanics and Arctic Engineering*. Vol. 56574. American Society of Mechanical Engineers. 2015, V009T09A002.

[35] E. B. Agamloh, A. K. Wallace, and A. Von Jouanne. "Application of fluid–structure interaction simulation of an ocean wave energy extraction device". In: *Renewable Energy* 33.4 (2008), pp. 748–757. DOI: https://doi.org/10.1016/j.renene.2007.04.010.

[36] A. Ghasemi et al. "A nonlinear computational modeling of wave energy converters: A tethered point absorber and a bottom-hinged flap device". In: *Renewable energy* 103 (2017), pp. 774–785. DOI: https://doi.org/10.1016/j.renene.2016.11.011.

[37] Y. Yu and Y. Li. *Preliminary results of a RANS simulation for a floating point absorber wave energy system under extreme wave conditions*. Tech. rep. National Renewable Energy Lab.(NREL), Golden, CO (United States), 2011.

[38] Y.-H. Yu and Y. Li. "Reynolds-Averaged Navier–Stokes simulation of the heave performance of a two-body floating-point absorber wave energy system". In: *Computers & Fluids* 73 (2013), pp. 104–114. DOI: https://doi.org/10.1016/j.compfluid.2012.10.007.

[39] J. Westphalen et al. "Extreme wave loading on offshore wave energy devices using CFD: a hierarchical team approach". In: *Proceedings of the 8th European Wave and Tidal Energy Conference*. 2009, pp. 500–508.

[40] J. Westphalen et al. "Numerical simulation of a floating body in multible degrees of freedom". In: *Marine Renewable and Offshore Wind Energy*. The Royal Institution of Naval Architects. 2010, pp. 81–88.

[41] Z. Z. Hu et al. "Numerical simulation of floating bodies in extreme free surface waves". In: *Natural Hazards and Earth System Sciences* 11.2 (2011), pp. 519–527.

[42] G. Giorgi and J. V. Ringwood. "Implementation of latching control in a numerical wave tank with regular waves". In: *Journal of Ocean Engineering and Marine Energy* 2.2 (2016), pp. 211–226.

[43] J. Davidson et al. "Evaluation of Energy Maximising Control Systems for Wave Energy Converters Using OpenFOAM". In: *OpenFOAM ® : Selected Papers of the 11th Workshop*. Ed. by J. M. Nóbrega and H. Jasak. Cham: Springer International Publishing, 2019, pp. 157–171. DOI: `10.1007/978-3-319-60846-4_12`.

[44] G. Giorgi, M. Penalba, and J. Ringwood. "Nonlinear hydrodynamic models for heaving buoy wave energy converters". In: *Asian Wave and Tidal Energy Conference*. 2016.

[45] W. Chen et al. "Numerical modelling of a point-absorbing wave energy converter in irregular and extreme waves". In: *Applied Ocean Research* 63 (Feb. 2017), pp. 90–105. DOI: `10.1016/j.apor.2017.01.004`.

[46] W. Wang et al. "Estimation of numerical uncertainty in computational fluid dynamics simulations of a passively controlled wave energy converter". In: *Proceedings of the Institution of Mechanical Engineers, Part M: Journal of Engineering for the Maritime Environment* 232.1 (Feb. 2018), pp. 71–84. DOI: `10.1177/1475090217726884`.

[47] R. A. Gingold and J. J. Monaghan. "Smoothed particle hydrodynamics: theory and application to non-spherical stars". In: *Monthly Notices of the Royal Astronomical Society* 181.3 (1977), pp. 375–389.

[48] A. Henry et al. "The characteristics of wave impacts on an oscillating wave surge converter". In: *The Twenty-third International Offshore and Polar Engineering Conference*. International Society of Offshore and Polar Engineers. 2013.

[49] B. Edge et al. "Application of GPUSPH to design of wave energy". In: *Proceedings of the 9th International SPHERIC Workshop, Paris, France*. 2014, pp. 342–347.

[50] S. Yeylaghi et al. "SPH modeling of hydrodynamic loads on a point absorber wave energy converter hull". In: *Proceedings of the 11th European Wave and Tidal Energy Conference (EWTEC2015), Nantes, France*. 2015.

[51] S. Yeylaghi et al. "ISPH modelling of an oscillating wave surge converter using an OpenMP-based parallel approach". In: *Journal of Ocean Engineering and Marine Energy* 2.3 (2016), pp. 301–312. DOI: `https://doi.org/10.1007/s40722-016-0053-7`.

[52] F. Meng et al. "Nonlinear hydrodynamics analysis of a submerged spherical point absorber with asymmetric mass distribution". In: *Renewable Energy* 147 (2020), pp. 1895–1908. DOI: `https://doi.org/10.1016/j.renene.2019.09.101`.

[53] A. Bharath et al. "Nonlinear hydrodynamic effects on a generic spherical wave energy converter". In: *Renewable Energy* 118 (Apr. 2018), pp. 56–70. DOI: `10.1016/j.renene.2017.10.078`.

[54] H. K. Versteeg and W. Malalasekera. *An introduction to computational fluid dynamics: the finite volume method*. Pearson Education, 2007.

[55] B. M. Sumer and J. Fredsøe. *Hydrodynamics around cylindrical structures*. Vol. 26. World scientific, 2006.

[56] B. Devolder, P. Rauwoens, and P. Troch. "Numerical simulation of a single floating point absorber wave energy converter using OpenFOAM®". In: *Progress in Renewable Energies Offshore; CRC Press: Boca Raton, FL, USA* (2016), pp. 197–205.

[57] M. Anbarsooz, M. Passandideh-Fard, and M. Moghiman. "Numerical simulation of a submerged cylindrical wave energy converter". In: *Renewable Energy* 64 (Apr. 2014), pp. 132–143. DOI: 10.1016/j.renene.2013.11.008.

[58] P. Higuera, I. J. Losada, and J. L. Lara. "Three-dimensional numerical wave generation with moving boundaries". In: *Coastal Engineering* 101 (July 2015), pp. 35–47. DOI: 10.1016/j.coastaleng.2015.04.003.

[59] P. Lin and P. L.-F. Liu. "Internal wave-maker for Navier-Stokes equations models". In: *Journal of waterway, port, coastal, and ocean engineering* 125.4 (1999), pp. 207–215. DOI: https://doi.org/10.1061/(ASCE)0733-950X(1999)125:4(207).

[60] N. G. Jacobsen, D. R. Fuhrman, and J. Fredsøe. "A wave generation toolbox for the open-source CFD library: OpenFoam". In: *International Journal for numerical methods in fluids* 70.9 (2012), pp. 1073–1088. DOI: https://doi.org/10.1002/fld.2726.

[61] T. Ha, P. Lin, and Y.-S. Cho. "Generation of 3D regular and irregular waves using Navier–Stokes equations model with an internal wave maker". In: *Coastal Engineering* 76 (2013), pp. 55–67. DOI: https://doi.org/10.1016/j.coastaleng.2013.01.013.

[62] L. Li, M. Tan, and J. Blake. "OpenFOAM simulation of regular wave and wave load on cylinder". In: *Proceedings of the 15th Numerical Towing Tank Symposium*. 2012, pp. 146–151.

[63] P. Schmitt et al. "The opportunities and limitations of using CFD in the development of wave energy converters". In: *Marine & Offshore Renewable Energy* (2012), pp. 89–97.

[64] G. F. Clauss, C. E. Schmittner, and R. Stuck. "Numerical wave tank: Simulation of extreme waves for the investigation of structural responses". In: *International Conference on Offshore Mechanics and Arctic Engineering*. Vol. 41979. 2005, pp. 785–792. DOI: https://doi.org/10.1115/OMAE2005-67048.

[65] C. Lifen et al. "Numerical study of roll motion of a 2-D floating structure in viscous flow". In: *Journal of Hydrodynamics* 28.4 (2016), pp. 544–563. DOI: https://doi.org/10.1016/S1001-6058(16)60659-5.

31

[66] Y. Luo et al. "Nonlinear 2D analysis of the efficiency of fixed oscillating water column wave energy converters". In: *Renewable energy* 64 (2014), pp. 255–265. DOI: https://doi.org/10.1016/j.renene.2013.11.007.

[67] J. L. Lara, A. Ruju, and I. J. Losada. "Reynolds averaged Navier–Stokes modelling of long waves induced by a transient wave group on a beach". In: *Proceedings of the Royal Society A: Mathematical, Physical and Engineering Sciences* 467.2129 (2011), pp. 1215–1242. DOI: https://doi.org/10.1098/rspa.2010.0331.

[68] Y. Ouellet and I. Datta. "A survey of wave absorbers". In: *Journal of Hydraulic Research* 24.4 (1986), pp. 265–280.

[69] C. Klinghammer, P. Lomónaco Tonda, P. Higuera Caubilla, et al. "Design optimization for a passive mesh screen wave absorber for the CCOB". In: *Coastal Engineering Proceedings*. Vol. 1. 33. Coastal Engineering Research Council, 2012.

[70] H. A. Schäffer and G. Klopman. "Review of multidirectional active wave absorption methods". In: *Journal of Waterway, Port, Coastal, and Ocean Engineering* 126.2 (2000), pp. 88–97.

[71] P. Higuera, J. L. Lara, and I. J. Losada. "Realistic wave generation and active wave absorption for Navier–Stokes models: Application to OpenFOAM®". In: *Coastal Engineering* 71 (2013), pp. 102–118.

[72] B. Devolder et al. "A review of the implicit motion solver algorithm in OpenFOAM to simulate a heaving buoy". In: *18th Numerical Towing Tank Symposium*. 2015.

[73] D. M. Causon et al. "Calculation of shallow water flows using a cartesian cut cell approach". In: *Advances in Water Resources* 23.5 (2000), pp. 545–562.

[74] D. Greaves and G. Iglesias. *Wave and Tidal Energy*. John Wiley & Sons, 2018.

[75] N. Y. Sergiienko et al. "Design Optimisation of a Multi-Mode Wave Energy Converter". In: *39th International Conference on Ocean, Offshore and Arctic Engineering*. American Society of Mechanical Engineers, Aug. 2020. DOI: 10.1115/omae2020-19266.

[76] A. Maria-Arenas et al. "Control strategies applied to wave energy converters: State of the art". In: *Energies* 12.16 (2019), p. 3115.

[77] J. Falnes. "On non-causal impulse response functions related to propagating water waves". In: *Applied Ocean Research* 17.6 (Dec. 1995), pp. 379–389. DOI: 10.1016/S0141-1187(96)00007-7.

[78]   J. V. Ringwood, G. Bacelli, and F. Fusco. "Energy-maximizing control of wave-energy converters: the development of control system technology to optimize their operation". In: *IEEE Transactions on Control Systems* 34.5 (Oct. 2014), pp. 30–55. DOI: 10.1109/MCS.2014.2333253.

[79]   J. Falnes. *Ocean waves and oscillating systems: Linear interactions including wave-energy extraction*. Cambridge University Press, 2002.

[80]   P. B. Garcia-Rosa et al. "Real-time passive control of wave energy converters using the Hilbert-Huang Transform". In: *20th IFAC World Congress* 50.1 (July 2017), pp. 14705–14710. DOI: 10.1016/j.ifacol.2017.08.2502.

[81]   P. Jin et al. "Performance optimization of a coaxial-cylinder wave energy converter". In: *Energy* 174 (May 2019), pp. 450–459. DOI: 10.1016/j.energy.2019.02.189.

[82]   M. P. Schoen, J. Hals, and T. Moan. "Wave prediction and fuzzy logic control of wave energy converters in irregular waves". In: *2008 16th Mediterranean Conference on Control and Automation*. IEEE, June 2008. DOI: 10.1109/med.2008.4602036.

[83]   J. Cândido, P. A. Justino, et al. "Stochastics, time domain models and pontryagin maximum priciple for a two body wave power device". In: *8th European Wave and Tidal Energy Conference*. 2009.

[84]   K. Gunn, C. J. Taylor, and C. Lingwood. "Evolutionary algorithms for the development and optimisation of wave energy converter control systems". In: *Proc. of the 8th Euro. Wave and Tidal Energy Conf., Uppsala, Sweden*. 2009.

[85]   N. Sergiienko et al. "Considerations on the control design for a three-tether wave energy converter". In: *Ocean Engineering* 183 (July 2019), pp. 469–477. DOI: 10.1016/j.oceaneng.2019.04.053.

[86]   A. Babarit, G. Duclos, and A. H. Clément. "Comparison of latching control strategies for a heaving wave energy device in random sea". In: *Applied Ocean Research* 26.5 (2004), pp. 227–238.

[87]   T. Mundon, A. Murray, and R. Wallace. "Toward a biologically inspired, neural control mechanism for multiple degree of freedom wave energy converters". In: *Proc. 9th European Wave Tidal Energy Conf.* 2011, pp. 1–7.

[88]   N. Faedo, S. Olaya, and J. Ringwood. "Optimal Control, MPC and MPC-Like Algorithms for Wave Energy Systems: An Overview". In: *IFAC Journal of Systems and Control* (July 2017).

[89]   S. Naito and S. Nakamura. "Wave energy absorption in irregular waves by feedforward control system". In: *Hydrodynamics of ocean wave-energy utilization*. Springer, 1986, pp. 269–280.

[90] E. Anderlini et al. "Reactive control of a wave energy converter using artificial neural networks". In: *International Journal of Marine Energy* 19 (2017), pp. 207–220.

[91] L. Li, Z. Yuan, and Y. Gao. "Maximization of energy absorption for a wave energy converter using the deep machine learning". In: *Energy* 165 (2018), pp. 340–349.

[92] Z. Shahroozi. "Force Prediction and Estimation for Point Absorber Wave Energy Converter". MA thesis. Uppsala University, 2019.

[93] Z. Wu, C. Levi, and S. F. Estefen. "Wave energy harvesting using nonlinear stiffness system". In: *Applied Ocean Research* 74 (May 2018), pp. 102–116. DOI: 10.1016/j.apor.2018.02.009.

[94] R. L. Harne and K.-W. Wang. *Harnessing bistable structural dynamics: For vibration control, energy harvesting and sensing*. John Wiley & Sons, 2017.

[95] M. Masoumi and Y. Wang. "Repulsive magnetic levitation-based ocean wave energy harvester with variable resonance: Modeling, simulation and experiment". In: *Journal of Sound and Vibration* 381 (Oct. 2016), pp. 192–205. DOI: http://dx.doi.org/10.1016/j.jsv.2016.06.024.

[96] S. Palagummi and F. Yuan. "A bi-stable horizontal diamagnetic levitation based low frequency vibration energy harvester". In: *Sensors and Actuators A: Physical* 279 (Aug. 2018), pp. 743–752. DOI: 10.1016/j.sna.2018.07.001.

[97] N. Stephen. "On energy harvesting from ambient vibration". In: *Journal of Sound and Vibration* 293.1–2 (2006), pp. 409–425. DOI: http://dx.doi.org/10.1016/j.jsv.2005.10.003.

[98] R. L. Harne and K. W. Wang. "A review of the recent research on vibration energy harvesting via bistable systems". In: *Smart Materials and Structures* 22.2 (Jan. 2013), p. 023001. DOI: 10.1088/0964-1726/22/2/023001.

[99] B. Mann and B. Owens. "Investigations of a nonlinear energy harvester with a bistable potential well". In: *Journal of Sound and Vibration* 329.9 (2010), pp. 1215–1226. DOI: https://doi.org/10.1016/j.jsv.2009.11.034.

[100] O. Abdelkhalik and S. Darani. "Optimization of nonlinear wave energy converters". In: *Ocean Engineering* 162 (Aug. 2018), pp. 187–195. DOI: 10.1016/j.oceaneng.2018.05.023.

[101] L. Wang, H. Tang, and Y. Wu. "On a submerged wave energy converter with snap-through power take-off". In: *Applied Ocean Research* 80 (Nov. 2018), pp. 24–36. DOI: 10.1016/j.apor.2018.08.005.

[102] D. Younesian and M.-R. Alam. "Multi-stable mechanisms for high-efficiency and broadband ocean wave energy harvesting". In: *Applied Energy* 197 (2017), pp. 292–302. DOI: http://dx.doi.org/10.1016/j.apenergy.2017.04.019.

[103] X.-T. Zhang, J.-M. Yang, and L.-F. Xiao. "An oscillating wave energy converter with nonlinear snap-through Power-Take-Off systems in regular waves". In: *China Ocean Engineering* 30.4 (July 2016), pp. 565–580. DOI: 10.1007/s13344-016-0035-5.

[104] X. Zhang et al. "Mechanism and sensitivity for broadband energy harvesting of an adaptive bistable point absorber wave energy converter". In: *Energy* 188 (Dec. 2019), p. 115984. DOI: 10.1016/j.energy.2019.115984.

[105] Z. Wu, C. Levi, and S. F. Estefen. "Practical considerations on nonlinear stiffness system for wave energy converter". In: *Applied Ocean Research* 92 (Nov. 2019), p. 101935. DOI: 10.1016/j.apor.2019.101935.

[106] X. Xiao, L. Xiao, and T. Peng. "Comparative study on power capture performance of oscillating-body wave energy converters with three novel power take-off systems". In: *Renewable Energy* 103 (Apr. 2017), pp. 94–105. DOI: 10.1016/j.renene.2016.11.030.

[107] H. Zhang et al. "Efficiency enhancement of a point wave energy converter with a magnetic bistable mechanism". In: *Energy* 181 (Aug. 2019), pp. 1152–1165. DOI: 10.1016/j.energy.2019.06.008.

[108] X. Zhang et al. "Application of an adaptive bistable power capture mechanism to a point absorber wave energy converter". In: *Applied Energy* 228 (Oct. 2018), pp. 450–467. DOI: 10.1016/j.apenergy.2018.06.100.

[109] N. Tran et al. "The impact of pitch-surge coupling on the performance of a submerged cylindrical wave energy converter". In: *Applied Ocean Research* 104 (Nov. 2020), p. 102377. DOI: 10.1016/j.apor.2020.102377.

[110] N. Tran et al. "The effect of nonlinear pitch-surge coupling on the performance of multi-DOF submerged WECs". In: *The Thirtieth (2020) International Ocean and Polar Engineering Conference*. Oct. 2020.

Chapter 3

Background theory

The purpose of this chapter is to present the fundamental concepts that are used throughout the thesis. A generic submerged spherical buoy is used as an example. More specific background theory is provided in the relevant Chapters 4–7.

3.1 Dynamics of submerged wave energy converters

A submerged PA WEC, as shown in Figure 3.1, may be modelled by first quantifying all the forces influencing the system. For simplicity, restricting the motion to a single DOF, using Equation 2.6 and applying Newton's 2nd law, the following governing equation may be derived:

$$M\ddot{z} = F_{\mathrm{e}} + F_{\mathrm{rad}} + F_{\mathrm{D}} + F_{\mathrm{hs}} + F_{\mathrm{PTO}} + F_{\mathrm{n}} \, , \qquad (3.1)$$

where M is the mass of the system, $\ddot{z}$ is the vertical acceleration of the buoy, F_{e} is the excitation force, F_{rad} is the radiation force, F_{D} is the drag force, F_{hs} is the hydrostatic force, F_{PTO} is the force from the power take off unit (PTO), and F_{n} is a potential nonlinear stiffness force. The representation and quantification of each of these forces may change depending on the arrangement of the device, the DOFs, the hydrodynamic model, and geometry. However, the conceptual origin of each force is distinct.

3.1.1 Excitation force

The excitation force is the force acting on the buoy due to an incident wave. This force is composed of two components, the Froude-Krylov force and the diffraction force, as introduced in Section 2.2. The Froude-Krylov component is the force due to the dynamic pressure due to the incident wave over the surface of the device, and the diffraction force is due to the wave diffracting as a result of the presence of the buoy. It is common in literature to combine the components into the excitation force as these are the forces associated with an incident excitation wave [1]. For regular waves, the incident wave
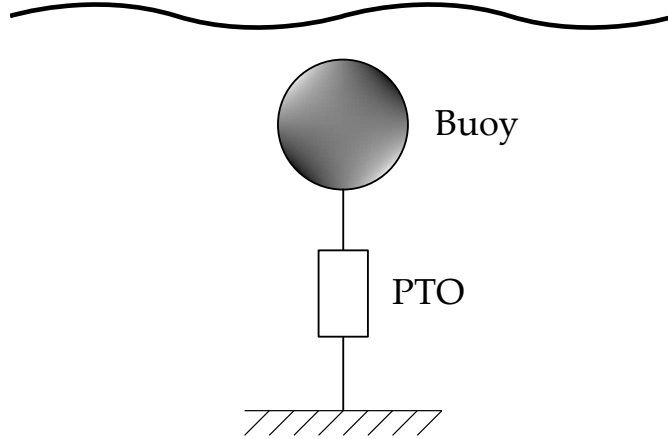
Figure 3.1: A heuristic submerged PA WEC device with a spherical buoy.

elevation, η, and the excitation force, F_e, may be represented as

$$\eta = A_w \cos(-\omega t) , \tag{3.2}$$

$$F_e = A_w F_{e,amp} \cos(\phi - \omega t) , \tag{3.3}$$

where the excitation wave amplitude and frequency are given by A_w and ω, respectively, and the parameter t is the time. The wave amplitude is half of the wave height, H, introduced in Equation 2.2. The amplitude and phase of the excitation force are represented as $F_{e,amp}$ and ϕ, respectively. This force amplitude and phase may be quantified by linear potential flow BEM solver such as NEMOH [2].

3.1.2 Radiation force

As a buoy oscillates in the water, it radiates waves. The force associated with these radiated waves is termed the radiation force. Throughout literature, a common way of representing this force is through Cummins' equation [3]

$$F_{rad} = -A_\infty \ddot{z} - \int_0^t K(t - t')\dot{z}dt' , \tag{3.4}$$

with the added mass at infinite frequency given as A_∞ (this can be considered the additional inertia due to the surrounding fluid), the buoy velocity is $\dot{z}$, and the influence of the fluid over time is introduced through the convolution integral. The impulse response function, K, describes the transient force of the fluid on the buoy during motion. The added mass at infinite frequency is included in the impulse response function, but taken out of the integral to avoid the integral diverging. So by integrating from an initial time, the fluid memory is incorporated into the model. In practice, this integral may be computationally expensive even for moderate time durations. Therefore, this integral is

conventionally represented by an appropriate state-space equation which takes velocity as an input. The state-space equation may be quantified via a parametric identification method [4] as

$$\dot{\mathbf{p}}(t) = \mathbf{A}_r \mathbf{p}(t) + \mathbf{B}_r \dot{z}(t)$$

$$\int_0^t K(t - t')\dot{z}dt' = \mathbf{C}_r \mathbf{p}(t) \,, \tag{3.5}$$

where the state space matrices, $\mathbf{A}_r$, $\mathbf{B}_r$, and $\mathbf{C}_r$, have coefficients found using the Matlab MSS FDI toolbox [5], and the intermediate state vector is $\mathbf{p}(t)$.

The radiation force can also be considered the composition of additional inertia and damping terms, and can be represented in the frequency domain as

$$\hat{F}_{\text{rad}} = -A_\omega \hat{a} - B_\omega \hat{u} \,, \tag{3.6}$$

where the frequency dependent added mass and damping parameter are represented as A_ω and B_ω, respectively. The acceleration and velocity of the system are represented as a and u, respectively. The notation $\hat{f}$ represents the complex amplitude of the signal $f(t)$. The hydrodynamic added mass and damping terms may be quantified using linear potential flow BEM.

3.1.3 Drag force

The viscous drag force may be quantified using the Morison drag formulations [6]

$$F_{\text{D}} = -\frac{1}{2}\rho C_{\text{d}} A_{\text{d}} |\dot{z} - \dot{z}_{\text{f}}| (\dot{z} - \dot{z}_{\text{f}}) \,, \tag{3.7}$$

where the density of water, coefficient of drag, and characteristic area are represented by ρ, C_{d}, and A_{d}, respectively. The fluid velocity, given by $\dot{z}_{\text{f}}$ may be quantified using linear wave theory as [7]

$$\dot{z}_{\text{f}} = A_{\text{w}}\omega \frac{\sinh(k(h + z - d_s))}{\sinh(kh)} \sin(-\omega t) \,, \tag{3.8}$$

where the wavenumber, water column depth, and submergence depth of the buoy are represented by k, h, and d_s, respectively.

3.1.4 Hydrostatic force and PTO force

For a submerged buoy, the volume of displaced water and the gravitational forces acting on the buoy are constant. The net result of these forces is the effective hydrostatic force acting on the buoy and may be calculated to be

$$F_{\text{hs}} = (\rho V - M)g, \tag{3.9}$$

where V represents the volume of the buoy, and g represents the acceleration of gravity. If the density of the buoy is less than the water, then the effective hydrostatic force is upward. This net force requires that some pretension is included in the control mechanism to counteract the hydrostatic force and ensure the system operates at a submerged nominal position. This pretension is combined into the PTO system along with control stiffness, k_{PTO}, and damping, b_{PTO}, parameters and may be described as

$$F_{\text{PTO}} = -k_{\text{PTO}}z - b_{\text{PTO}}\dot{z} - F_{\text{hs}}. \tag{3.10}$$

A representation of a WEC with PTO composed of a linear spring and damper is presented in Figure 3.2. The approximate optimal values for simple linear hydrodynamic models are well known in literature [8], but do not guarantee optimality in the presence of nonlinear effects such as drag, nonlinear hydrodynamics, or multiple DOF systems. The method of quantifying these control parameters is outlined in the following chapters when required.
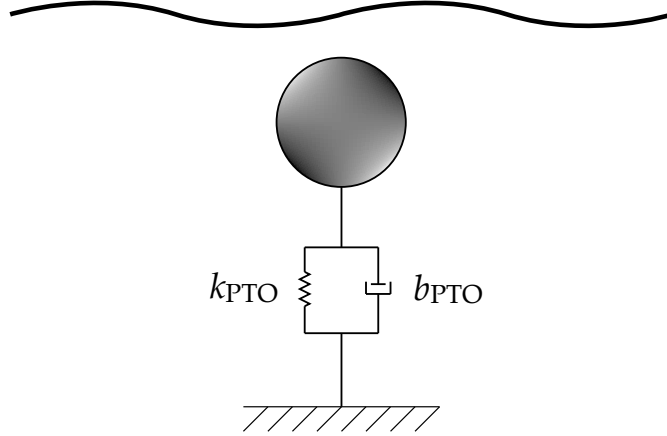
Figure 3.2: A submerged PA WEC device with a spherical buoy using a simple linear spring damper PTO configuration.

3.2 Nonlinear stiffness

The nonlinear stiffness force in this work is a force for which the effective stiffness changes depending on position. This force may be achieved using various different methods such as magnetic sources, adjacent springs (see Figure 3.3), or through actively controlling a device. In the work presented in this thesis, the force is constructed using the magnetic dipole model [9] to give a simplified analytic nonlinear stiffness which is indicative of magnetic trends. The force between two magnetic dipoles can be derived from [10]

$$\mathbf{F}_{\text{n}} = \nabla\left(\mathbf{m}_{\text{d},1} \cdot \mathbf{B}_{\text{d},2}\right), \tag{3.11}$$

where $\mathbf{m}_{d,1}$ is the dipole moment of the first dipole, and $\mathbf{B}_{d,2}$ is the magnetic field of the second dipole at the location of the first dipole. Assuming magnetisation in the z direction, the dipole moments are given by

$$\mathbf{m}_d = (0, 0, V_m M_m),\tag{3.12}$$

where V_m is the volume of the magnet, and M_m is the magnetisation field per unit volume. The magnetic field for a dipole is given by [9]

$$\mathbf{B}_{d,2} = -\frac{\mu_0}{4\pi}\nabla\frac{\mathbf{m}_{d,1}\cdot\mathbf{r}_d}{r_d^3}\tag{3.13}$$

where $\mathbf{r}_d$ is the displacement between the dipoles, r_d is the distance between the dipoles, and μ_0 is the permeability of free space. Using these equations, the vertical force between the two dipoles may be derived as

$$F_n = \frac{\mu_0 M_1 V_1 M_2 V_2}{4\pi}\left(\frac{9z}{(r_0^2 + z^2)^{\frac{5}{2}}} - \frac{15z^3}{(r_0^2 + z^2)^{\frac{7}{2}}}\right),\tag{3.14}$$

where r_0 is the horizontal distance between dipoles. By representing the constants and material properties as a lumped parameter C, the equation for the nonlinear stiffness force is

$$F_n = C\left[\frac{9z}{(r_0^2 + z^2)^{\frac{5}{2}}} - \frac{15z^3}{(r_0^2 + z^2)^{\frac{7}{2}}}\right],\tag{3.15}$$

and the related nonlinear stiffness, k_n is

$$k_n = \frac{\partial F_n}{\partial z} = C\left[\frac{-9}{(r_0^2 + z^2)^{\frac{5}{2}}} + \frac{90z^2}{(r_0^2 + z^2)^{\frac{7}{2}}} - \frac{105z^4}{(r_0^2 + z^2)^{\frac{9}{2}}}\right].\tag{3.16}$$

This magnetic representation is not a perfect description of realistic magnetic system, however it captures the trend of similar magnetic systems and will be used to determine what features of nonlinear forces and stiffnesses are useful.

To vary this nonlinear stiffness force for the wave energy application, the C parameter is varied in relation to the potential energy of the incident wave. The C parameter is a lumped parameter which depends on magnetisation and volume, which, in principle, may be designed as needed. Therefore, for the purposes of this study, this lumped parameter is considered suitably variable to achieve a large range of nonlinear stiffness and potential energy profiles. Therefore, to generalise the system, the nondimensional potential energy, γ, is used to parameterise the mechanism. This nondimensional potential energy is the ratio between the potential energy due to the effective stiffness at the nominal position of the device, $U_{n,z=0}$, to the average potential energy of the incident wave for the buoy, U_w, or

$$\gamma = \frac{U_{n,z=0}}{U_w}.\tag{3.17}$$
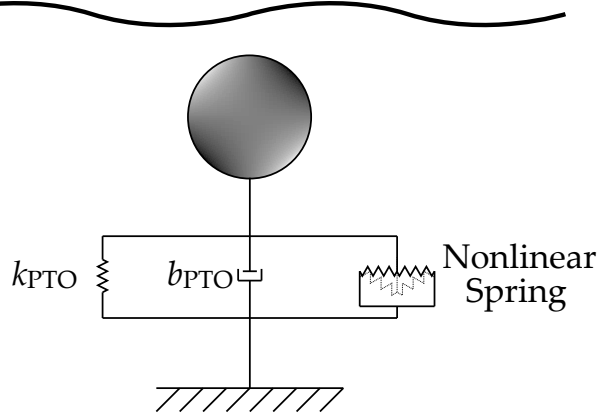
Figure 3.3: A submerged PA WEC device with a spherical buoy using a linear spring and damper, as well as a nonlinear spring mechanism.

Using the magnetic dipole representation, the potential energy of the between two dipoles may be derived as [10]

$$U_n = -\mathbf{m}_{d,1} \cdot \mathbf{B}_{d,2} \, , \tag{3.18}$$

and by substituting the dipole moment and magnetic field into this equation, the potential energy for the nonlinear force may be described as

$$U_n = C \left[\frac{-1}{(r_0^2 + z^2)^{\frac{3}{2}}} + \frac{3z^2}{(r_0^2 + z^2)^{\frac{5}{2}}} \right] . \tag{3.19}$$

For deep water regular waves, the average potential energy per unit area may be described as [11]

$$\hat{U}_w = \frac{1}{4} \rho g A_w^2 \, , \tag{3.20}$$

and therefore, the total potential energy of the wave for the buoy can be quantified by multiplying be the horizontal area, which, for a spherical or cylindrical buoy, becomes

$$U_w = \frac{1}{4} \rho g A_w^2 \pi r^2 \, , \tag{3.21}$$

where r represents the radius of the axisymmetric buoy. This approach allows for intuitive interpretation of γ, that is, when $\gamma = 1$ the potential energy of the nonlinear force system is equal in magnitude to the potential energy of the wave, and therefore would be the sufficient condition to overcome the potential barrier in a bistable scenario. By varying both γ and r_0 a large range of nonlinear conditions may be sampled. Depictions of the total potential energy curves of a system with linear and nonlinear stiffnesses are presented in Figure 3.4.
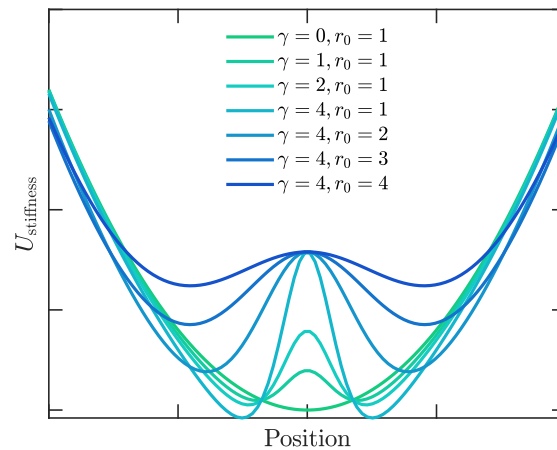
Figure 3.4: Representative potential energies of a system with linear and nonlinear stiffness for varying values of γ and r_0. The system with $\gamma = 0$ has no nonlinear stiffness component. As γ increases, a bistable condition may occur. As r_0 increases, the location of the stable regions moves further out, and the rate of change of potential energy generally reduces. This image is repeated in Chapter 7.

As a heuristic example of how a bistable condition may change the dynamic behaviour of a system, a bistable simulation is presented in Figure 3.5a. This graph shows the same system with different amplitudes of excitation oscillation. If the excitation is sufficient to overcome the central potential barrier, the bistable system can increase the amplitude of oscillation by forcing oscillations between the two stable potential wells (interwell motion) and excite additional harmonics which may beneficially shift low frequency oscillations into higher frequency oscillations for energy generation [12]. If the excitation is insufficient to overcome the central barrier, it is restricted to one side (intrawell motion), and is effectively a monostable system. For stochastic systems, the motion may occasionally cross the central barrier as a result of a random noise, as shown in Figure 3.5b. This beneficially exploits small random motions to cause larger amplitudes of motions and is known as stochastic resonance [12]. Further information and representations are provided in the modelling descriptions in each relevant chapter.

3.3   Wave modelling

A simplistic approach to modelling ocean waves involves assuming the conditions are monochromatic sinusoidal waves. Such regular waves are useful in describing the frequency response of a WEC, however, do not fully represent ocean conditions. Instead, irregular waves may be used to excite the system to model a more realistic response.
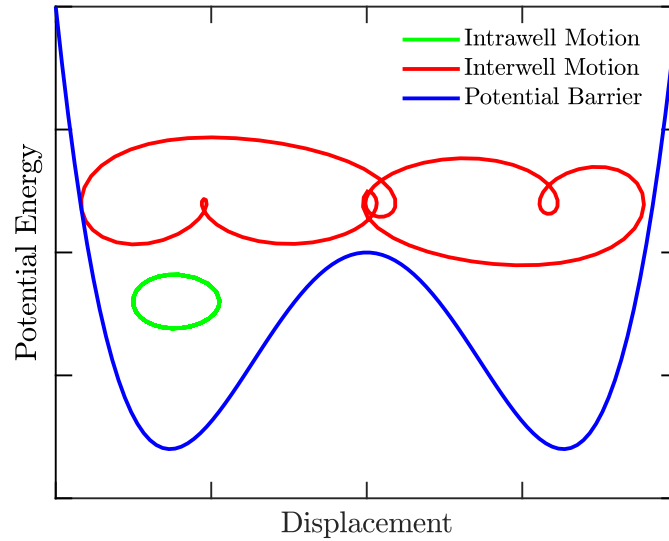
(a) A heuristic bistable system with a low and high amplitude excitation force, which results in intrawell and interwell oscillations, respectively.
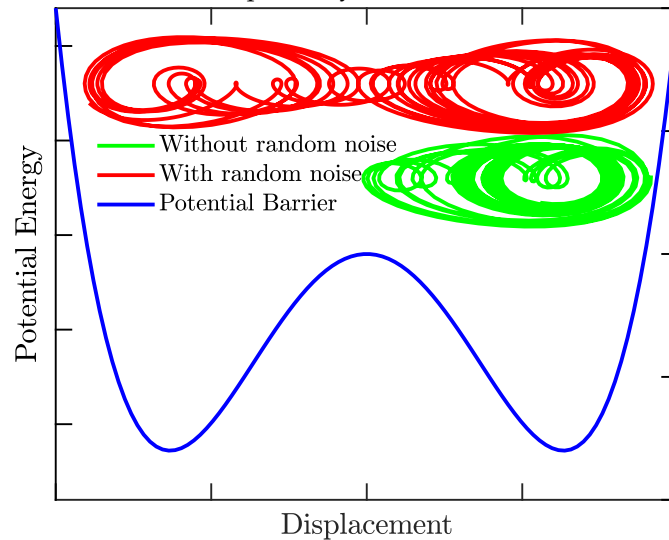
(b) A heuristic bistable system excited by a common amplitude excitation. This graph shows the motion response for a system with and without an additional Gaussian noise. The scenario with noise occasionally crosses the central potential barrier and snaps through to other stable location. This effectively shifts the oscillation frequency and increases the amplitude of motion. This phenomenon is called stochastic resonance, and is a beneficial feature of bistable systems.

Figure 3.5: Two heuristic bistable systems with different interwell and intrawell motions depending on the form of excitation. The vertical coordinate only relates to the potential energy barrier provided on each plot. The resultant motions are vertically displaced on the plots for clarity.

Irregular waves may be modelled as the superposition of many different sinusoidal waves of different frequencies. The weighting of each regular wave component may be related to a spectrum. A prevalent approach in literature to represent an irregular wave spectrum is the Pierson-Moskowitz spectrum [13], which is

$$S(f) = \frac{A_{\text{PM}}}{f^5} \exp\left(-\frac{B_{\text{PM}}}{f^4}\right) , \tag{3.22}$$

where f represents the excitation frequencies in Hz, and the coefficients A_{PM} and B_{PM} are [13]

$$A_{\text{PM}} = \frac{5H_{\text{s}}^2 f_{\text{p}}^4}{16} , \quad B_{\text{PM}} = \frac{5f_{\text{p}}^4}{4} , \tag{3.23}$$

where f_{p} is the peak frequency in the spectrum, and H_{s} is the significant wave height. The peak frequency for these spectrums may be quantified using the energy period T_{e} of the irregular wave through the relationship [13]

$$f_{\text{p}} = \frac{0.858}{T_{\text{e}}} . \tag{3.24}$$

Therefore, the irregular wave spectrum may be formed if H_{s} and T_{e} are known. These two parameters may be found using measured experimental data in the form of an energy density spectra by using [14].

$$T_{\text{e}} = 2\pi \frac{m_{-1}}{m_0} , \quad H_{\text{s}} = 4\sqrt{m_0} , \tag{3.25}$$

where the nth spectral moment is defined as

$$m_n = \int_0^\infty S(\omega)\omega^n d\omega . \tag{3.26}$$

Using this model of an irregular wave, the amplitude of each regular wave component is

$$A_{\text{w},j} = \sqrt{2S(\omega_j)\Delta\omega_j} . \tag{3.27}$$

The superposition of regular wave components with a random phase offset gives the elevation of the incident irregular wave, and impacts both the excitation force and the fluid velocity. Therefore, the wave elevation of an irregular wave, η_{irr}, may be expressed as

$$\eta_{\text{irr}} = \sum_{j=1}^N A_{\text{w},j} \cos(\epsilon_j - \omega_j t) , \tag{3.28}$$

where ϵ_j is the random phase offset applied at each frequency, and N is the number of frequencies. The excitation force from an irregular wave, $F_{\text{e,irr}}$, is

$$F_{\text{e,irr}} = \sum_{j=1}^N A_{\text{w},j} F_{\text{e,amp},j} \cos(\phi_j - \omega_j t + \epsilon_j) . \tag{3.29}$$

The fluid velocity may be calculated by

$$\dot{z}_{\text{f,irr}} = \sum_{j=1}^{N} A_{\text{w},j}\omega_{\text{e},j}\frac{\sinh(k_j(h+z-d_s))}{\sinh(k_j h)}\sin(\epsilon_j - \omega_{\text{e},j}t)\,. \tag{3.30}$$

Similarly, it also follows that the potential energy per horizontal area for an irregular wave may be expressed as a superposition of the amplitudes in the following form

$$\hat{U}_{\text{w}} = \frac{1}{4}\rho g \sum_{j=1}^{N} A_{\text{w},j}^{2}\,. \tag{3.31}$$

To demonstrate the variation of irregular waves, a map of the wave climate at the Torbay site in Western Australia between the 5th of March and 14th of October 2019, characterised by the significant wave height and energy period, is presented in Figure 3.6. The data used to construct this figure is available at `https://wawaves.org/` and is also presented in the analysis in Chapter 4.
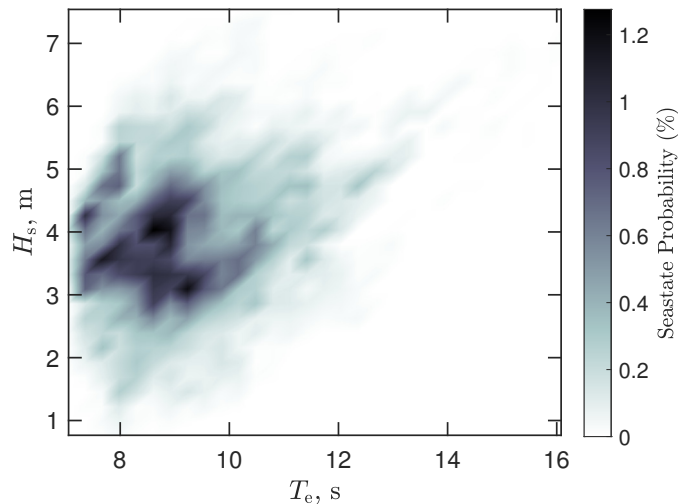
Figure 3.6: The wave climate at the Torbay site characterised as the probability of finding an irregular wave with a particular significant wave height and energy period. To form this map, the sea state probability wave determined by subdividing both the data of H_{s} and T_{e} into 30 bins, which means the provided sea state probability is only a relative indication rather than a true probability of observing a particular wave condition.

To demonstrate the influence of these parameters, three different irregular spectra and corresponding wave elevations are presented in Figure 3.7. The wave elevation shows significant variation over time. The variation means that when modelling irregular waves, the scenarios must be simulated long enough for the irregular wave to be well represented and any variance estimates to converge to their true values. In practice, this varies depending on the system. The resulting wave elevation spectra may be compared

to the desired spectra, or the scenario may be simulated for a long enough time until results converge [15, 16].
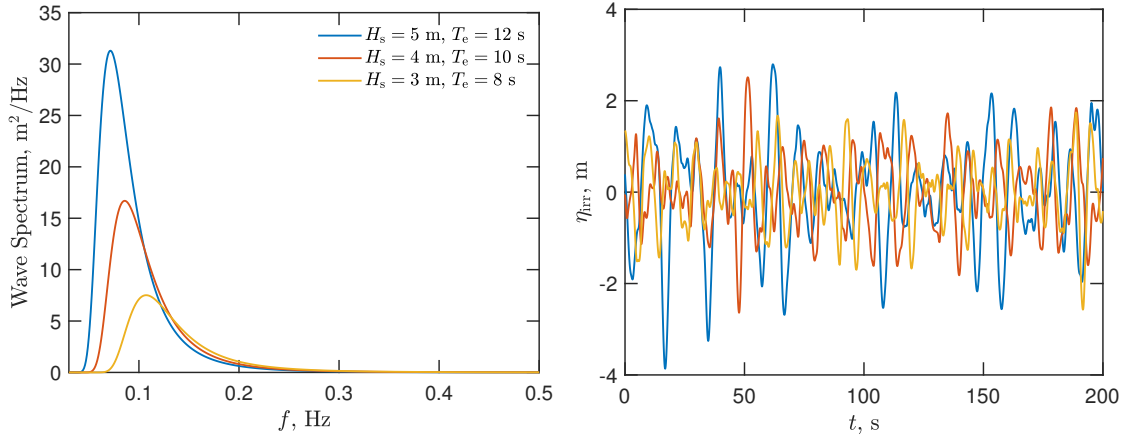
(a) The spectra of three different irregular waves.

(b) The wave elevation of three different irregular waves.

Figure 3.7: Three indicative irregular waves are presented in the form of both a spectra and wave elevation. Due to the random phase offset, the wave elevations vary significantly and so irregular waves should be modelled using long simulation times.

3.4 Computational fluid dynamics

To simulate the nonlinear hydrodynamic features of the ocean waves acting on the PA, a NWT was built in the open source CFD software OpenFOAM (version 7). The following section is intended to provide a broad overview of the approach taken in the development and validation of the model. This discussion is not intended to be a comprehensive example of the use of OpenFOAM or CFD, but instead, provide a conceptual outline of the steps involved in the research presented in this thesis.

3.4.1 Mesh

An example of the code required to run an OpenFOAM simulation of a submerged quasi-PA WEC is available at `https://github.com/AUMAG/SubmergedCETO`. OpenFOAM requires a specific file structure to operate, which is not presented in this thesis. Arguably the most important component to CFD simulations is the construction of the computational domain and the structure of the mesh. The CFD software OpenFOAM has a number of packages to aid in building an appropriate mesh of an object. Namely, the application *snappyHexMesh* was used to undertake a number of steps in forming and

47

refining the mesh used in the NWT. The general steps that were taken may be described as:

1. background mesh,

2. geometry,

3. castellation,

4. snapping,

5. layering, and

6. assessing.

The background mesh step consists of specifying the raw numerical domain. Using the OpenFOAM tool *blockMesh*, the vertices of the boundary of the computational domain may be specified. The type and number of cells in each direction was then selected to form the meshed domain.

The geometry of the floating object was included by first constructing an STL file of the required geometry, and then using the *surfaceFeatureExtract* application within OpenFOAM. This application specifies the edges of the object, which will be used when snapping the vertices of the computational domain to the geometry of the object.

The castellation, snapping, and layering steps are executed using the *snappyHexMesh* application. Firstly, the cells in particular regions of interest may be refined. In this case, the more important fluid features occur close to the water-air interface, so this region should have a higher resolution mesh than the fluid near the bottom of the domain. Futhermore, since the fluid-structure interaction is of interest, the region around the object may be refined further. The geometry of the object may then be included in the mesh by superimposing the geometry into the three dimensional meshed grid, and removing the points within the geometry of the floating object. This process is known as castellation. Since this step leaves the mesh jagged and is a poor representation of smooth surfaces, the snapping step attempts to snap the points near the surface of the object to the edges found using the *surfaceFeatureExtract* tool. This step is often performed iteratively and undergoes some relaxation to avoid poorly conditioned cells which would lead to numerical instability. If the features of the object are not adequately captured by the resolution of the mesh, additional layers on the surface of the object may be introduced. This step is again an iterative process and attempts to smooth out mesh immediately around the object. It is also important to avoid having low resolution meshed cells connected to much higher resolution meshed cells, which can cause numerical instability. Fortunately, the *snappyHexMesh* utility allows the user to specify a minimum number of cells between different levels of resolutions.

At each step, the quality of the mesh is assessed based on a range of characteristics specified by the user. It is difficult to provide general guidelines for any specific quantities in these steps because each circumstance and scenarios is drastically different. However, throughout this process, each metric may be varied and assessed to determine how much influence it has on the final mesh. The *snappyHexMeshDict* in the provided example at https://github.com/AUMAG/SubmergedCETO under the folder *system*, may give a useful starting point for mesh quality controls, castellation mesh controls, and mesh refinement and snapping parameters. The final result depicting a CETO-shaped submerged buoy in a NWT is given in Figure 3.8.
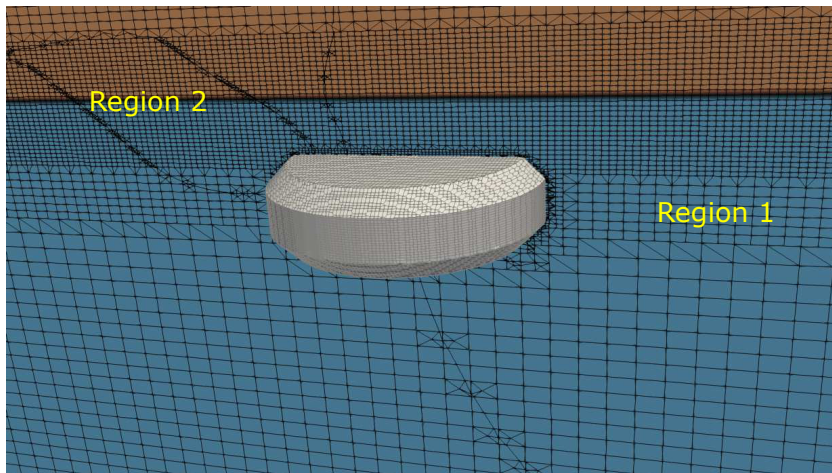
Figure 3.8: An example of the mesh in a NWT with a CETO-shaped submerged quasi PA. Region 1 and 2 are near the surface of the water and have double and quadruple the resolution of the background mesh, respectively. The surface of the floating object is higher resolution again, and is deformed and smoothed to better fit the surface of the floating object. Furthermore, additional layers immediately around the surface have been included to better capture the fluid-structure interaction at these critical areas. The stray lines passing through the mesh are merely a result of rendering the mesh rather than a feature of the structure and therefore have no influence on the simulation. This image is repeated in Chapter 7.

3.4.2 Wave

The solver *olaFlow*, allows the generation of a wave using a static boundary approach, and active wave absorption, as outlined in Section 2.2.4.4. The wave theory, direction, height, period, and phase may be specified. If the mesh is sufficient, this wave will be adequately generated and propagate down the NWT.

3.4.3 Motion

As the floating object is excited by the wave, the object moves. Therefore, the mesh describing the object must also deform. The OpenFOAM solver *dynamicMotionSolverFvMesh* was employed to specify the dynamic features of both the floating object and the mesh. These include the mass/moment of inertia, the control force acting on the object, any constraints around DOFs, and also the size of the mesh surrounding the floating object that is permitted to deform. One consideration here which proved difficult was that if the deformable region was too small, the motion of the floating object would cause meshed cells to be deformed to extreme aspect ratios and cause the simulation to go unstable. Alternatively, if the deformation region was too large and included the boundary of the computational domain, the mesh would again be poorly deformed and cause the simulation to fail. In many cases, poorly structured mesh may cause issues during motion and deformation steps and, in this research, were the main obstacle to reliable CFD simulations.

3.4.4 Control

The control system was implemented into the OpenFOAM simulation by modifying an existing restraint function. The *linearSpringDamper* restraint was modified to include an optional nonlinear stiffness following the magnetic dipole representation outlined in Section 3.2. This modified code is also provided in the example case presented at `https://github.com/AUMAG/SubmergedCETO` under the folder *modifiedBistableSpring*.

Additional background information of the different modelling approaches are introduced in each relevant chapter. Furthermore, the notation of the various terms introduced in this chapter is not necessarily consistent throughout the substantive chapters since they were written as journal papers. However, each chapter contains all the relevant definitions required for clarity and outlines the modelling approaches employed for each distinct finding.

References

[1]   M. Penalba, T. Kelly, and J. V. Ringwood. "Using NEMOH for modelling wave energy converters: a comparative study with WAMIT". In: *Centre for Ocean Energy Research (COER), Maynooth University, Co. Kildare, Ireland* (2017).

[2]   A. Babarit. *NEMOH user manual*. Ecole Centrale de Nantes. Jan. 2014.

[3]   W. Cummins. *The impulse response function and ship motions*. Tech. rep. David Taylor Model Basin, Washington DC, 1962.

[4]   T. Perez and T. I. Fossen. "Joint identification of infinite-frequency added mass and fluid-memory models of marine structures". In: *Modeling, Identification and Control* 29.3 (2008), pp. 93–102. DOI: `10.4173/mic.2008.3.2`.

[5]   T. Perez and T. I. Fossen. "A Matlab toolbox for parametric identification of radiation-force models of ships and offshore structures". In: *Modeling, Identification and Control: A Norwegian Research Bulletin* 30.1 (2009), pp. 1–15. DOI: `10.4173/mic.2009.1.1`.

[6]   N. Sergiienko et al. "Feasibility study of the three-tether axisymmetric wave energy converter". In: *Ocean Engineering* 150 (Feb. 2018), pp. 221–233. DOI: `10.1016/j.oceaneng.2017.12.055`.

[7]   R. Salmon. "Introduction to ocean waves". In: *Scripps Institution of Oceanography, University of California, San Diego* (2008).

[8]   J. Falnes. *Ocean waves and oscillating systems: Linear interactions including wave-energy extraction*. Cambridge University Press, 2002.

[9]   K. W. Yung, P. B. Landecker, and D. D. Villani. "An analytic solution for the force between two magnetic dipoles". In: *Physical Separation in Science and Engineering* 9.1 (1998), pp. 39–52.

[10]   D. Griffiths. *Introduction to Electrodynamics*. Pearson Education, 2014.

[11]   S. Gran. "A Course in Ocean Engineering (Developments in Marine Technology)". In: Elsevier Science Ltd, 1992. Chap. 2, pp. 187–199.

[12]   R. L. Harne and K.-W. Wang. *Harnessing bistable structural dynamics: For vibration control, energy harvesting and sensing*. John Wiley & Sons, 2017.

[13]   C. Stansberg et al. "The specialist committee on waves final report and recommendations to the 23rd ITTC". In: *Proceedings of the 23rd ITTC* 2 (2002), pp. 505–551.

[14]   W. Sheng and H. Li. "A method for energy and resource assessment of waves in finite water depths". In: *Energies* 10.4 (Apr. 2017), p. 460. DOI: `10.3390/en10040460`.

[15]   P. Hardy et al. "A maximum capture width tracking controller for ocean wave energy converters in irregular waves". In: *Ocean Engineering* 121 (2016), pp. 516–529. DOI: `http://dx.doi.org/10.1016/j.oceaneng.2016.05.045`.

[16]   B. Ding et al. "Sea-state based maximum power point tracking damping control of a fully submerged oscillating buoy". In: *Ocean Engineering* 126 (Nov. 2016), pp. 299–312. DOI: `http://dx.doi.org/10.1016/j.oceaneng.2016.09.020`.

Chapter 4

The true potential of nonlinear stiffness for wave energy converters

This thesis focuses on exploring the benefit of a nonlinear stiffness mechanism to submerged point absorbing WECs. To first contextualise submerged PAs, both floating and submerged systems are compared. The dynamical behaviour of floating and submerged systems are substantially different, which is in part due to the large hydrostatic stiffness acting on floating buoys. This chapter highlights the different requirements for a linear control system between the floating and submerged contexts, and applies a nonlinear stiffness to show under what conditions a benefit may occur. The research question this chapter addresses is: *Under what conditions does a passive control system with nonlinear stiffness provide a benefit to the performance of a floating or submerged device?*

   This section consists of the submitted journal article:

Schubert, B.W., Robertson, W.S., Cazzolato, B.S., Ghayesh, M.H. and Sergiienko, N.Y., 2020. The true potential of nonlinear stiffness for wave energy converters. Submitted to *Ocean Engineering*.

Statement of Authorship

Title of Paper	The true potential of nonlinear stiffness for wave energy converters
Publication Status	☐ Published ☐ Accepted for Publication ☑ Submitted for Publication ☐ Unpublished and Unsubmitted work written in manuscript style
Publication Details	Schubert, B.W., Robertson, W.S., Cazzolato, B.S., Ghayesh, M.H. and Sergiienko, N.Y., 2021. The true potential of nonlinear stiffness for wave energy converters. Submitted to Ocean Engineering.

Principal Author

Name of Principal Author (Candidate)	Benjamin Schubert
Contribution to the Paper	Developed ideas and concepts • Conducted a comprehensive literature review • Outlined the concepts of the paper to address the gaps in literature based on knowledge of the field Performed the modelling • Developed a model of a spherical buoy to estimate the hydrodynamic parameters using the potential flow solver NEMOH in both fully submerged and floating contexts • Developed a simulation in Simulink to predict the dynamic behaviour of a spherical wave energy converter in both floating and submerged contexts • Varied the control system of the dynamic simulations emphasise different performances • Optimised control parameters for the relevant floating and submerged contexts • Parameterised nonlinear stiffness force and implemented into dynamic model Interpreted results • Collected and stored data from simulation results • Post processed the data using Matlab • Performed spectral analysis of time domain results • Interpreted results between different scenarios • Calculated limits on performance and compared to results Writing • Solely developed the first full draft of the manuscript • Applied comments provided by all co-authors • Acting as corresponding author.
Overall percentage (%)	80%
Certification:	This paper reports on original research I conducted during the period of my Higher Degree by Research candidature and is not subject to any obligations or contractual agreements with a third party that would constrain its inclusion in this thesis. I am the primary author of this paper.
Signature		Date	2/2/2021

Co-Author Contributions

By signing the Statement of Authorship, each author certifies that:

    i.   the candidate's stated contribution to the publication is accurate (as detailed above);

    ii.   permission is granted for the candidate in include the publication in the thesis; and

    iii.   the sum of all co-author contributions is equal to 100% less the candidate's stated contribution.

Name of Co-Author	William Robertson		
Contribution to the Paper	Participated in developing the ideas and concepts, assisted in analysing and interpreting the obtained results, and provided revision of manuscript. Provided expertise and advice on the magnetic concepts and code employed in the development of this paper.		
Signature		Date	15/02/2021

Name of Co-Author	Benjamin Cazzolato		
Contribution to the Paper	Participated in developing the ideas and concepts, assisted in analysing and interpreting the obtained results, and provided revision of manuscript. Provided critical understanding of signal processing techniques employed in the development of this manuscript.		
Signature		Date	15/02/2021

Name of Co-Author	Mergen Ghayesh		
Contribution to the Paper	Participated in developing the ideas and concepts, assisted in analysing and interpreting the obtained results, and provided revision of manuscript.		
Signature		Date	18/02/2021

Name of Co-Author	Nataliia Sergiienko		
Contribution to the Paper	Participated in developing the ideas and concepts, assisted in analysing and interpreting the obtained results, and provided revision of manuscript. Provided insight to context of research and shaped direction of the manuscript. Provided a code template related to using the linear hydrodynamics tool NEMOH. Also provided code to analytically quantify hydrodynamics of a sphere to assist in verifying results and data.		
Signature		Date	15/02/2021

Please cut and paste additional co-author panels here as required.

The true potential of nonlinear stiffness for wave energy converters

B. W. Schubert, N. Y. Sergiienko, B. S. Cazzolato, W. S. P. Robertson, M. H. Ghayesh

Abstract

A spherical point absorbing wave energy converter was simulated in floating and submerged conditions for regular and irregular waves. A nonlinear stiffness was included to augment a linear stiffness and damper control system. The linear control parameters were optimised for each regular and irregular wave condition. The optimal linear control stiffness for the floating system was negative to counteract the hydrostatic stiffness. The nonlinear stiffness was shown to increase the converted power if no linear control stiffness was used, and reduce the converted power if optimal linear control parameters were used for regular waves. Similarly, for irregular conditions, nonlinear stiffness degrades the performance of the system when compared to optimised parameters, but enhances the robustness of the system to changing sea states. Therefore, a nonlinear stiffness mechanism may improve the power output for poorly tuned control systems arising from plant uncertainty.

4.1   Introduction

Ocean wave energy is a largely untapped source of renewable energy. While this form of potential energy is not currently economically competitive to harness compared with other renewable sources, it may offer a potential base-load or less intermittent renewable energy source. Several fundamentally different WECs have been explored which can be broadly categorised as PAs, attenuators, or terminators [1].

To improve the efficiency, and therefore the cost of energy generation of WECs, numerous active and passive control strategies have been proposed within literature [2]. Many studies use a linear stiffness and damper as a control force. One form of control strategy, which has been the focus of many recent studies, uses a nonlinear stiffness control force, sometimes called a snap-through mechanism, to enhance the performance of floating or submerged PA WECs. This mechanism can have two points of stability and can cause a system to possess multiple possible dynamic modes of motion [3] which may be beneficial for WECs.

The mechanism and implementation of the nonlinear force throughout literature varies from using a general representation in the form of a polynomial of displacement

and velocity proportional forces [4], to more physically realisable systems involving springs [5–10], magnetic systems [11, 12], or pneumatic systems such as those proposed by CorPower Ocean [13]. These studies generally confirm that this nonlinearity in the control force may be employed to improve the power production capacity of the system under certain conditions. The addition of this bistable mechanism can increase the power generated of a system (compared to a baseline control system) by up to 157% [5], around 100–200% [10], and by factor of 10 or more [8].

It is well-known that a linear model of a WEC can absorb maximum power in regular waves with just a linear spring-damper controller [14]. So proper tuning of linear parameters can theoretically provide the absolute maximum in generated power. Therefore, the mechanisms behind the significant improvements seen in current literature should be explored.

Most of previous studies are for floating WECs which typically have significant hydrostatic stiffnesses. These large stiffnesses give the system a natural frequency higher than the frequency of typical excitation waves. This limitation on the natural frequency leads to comparisons to suboptimal conditions, which in turn, lead to an exaggeration of the possible improvement of passive nonlinear control systems. A closer investigation of current literature reveals that all papers compare a nonlinear stiffness controller to a system with a non-optimised controller. Specific shortcomings within literature which lead to this suboptimal comparison involve:

- optimising only the damping parameter [7, 8, 12],

- excluding a linear stiffness component within the control force [5]

- not optimising linear control parameters [4, 10],

- sampling a limited range of parameters which may not find optimal linear parameters [6, 11], and

- considering only regular wave scenarios which are not representative of real ocean conditions [6, 8, 9, 11].

While these contributions made important steps in understanding the application of nonlinear stiffnesses to wave energy devices, the benchmarking to **sub-optimal** conditions reduces the confidence in the conclusions of enhanced performance. This paper aims to reveal the true potential benefit of adding nonlinear stiffness to wave energy devices compared to an **optimised** system.

In contrast to most other studies, a recent study by the present authors on a submerged quasi-PA WEC found that nonlinear stiffness could not improve upon a system with optimised linear stiffness and damping [15]. However, the nonlinear feature was able to improve the robustness of the system and was capable of generating near-optimal

power generation. Furthermore, this study was limited to the submerged scenario which
did not have the large hydrodynamic stiffness influence. So the current study will extend
this work to the floating WEC context and discuss why this discrepancy in literature
exists.

The clear gap in the current research is whether a nonlinear stiffness force can
enhance power production capability for a floating system compared to a system with
optimised linear stiffness and damping parameters. To have a fair comparison with
existing literature, the WEC was modelled as a linear system with linear hydrodynamic
forces, linear hydrostatic stiffness, and the only nonlinear force is the viscous drag.
Furthermore, this paper considered both the regular and irregular excitation of a single
tether spherical buoy operating in both floating and submerged conditions. To address a
common shortcoming within literature, the scenarios with and without a linear stiffness
in the passive control force were also analysed. The scenarios are graphically depicted in
Figure 4.1.
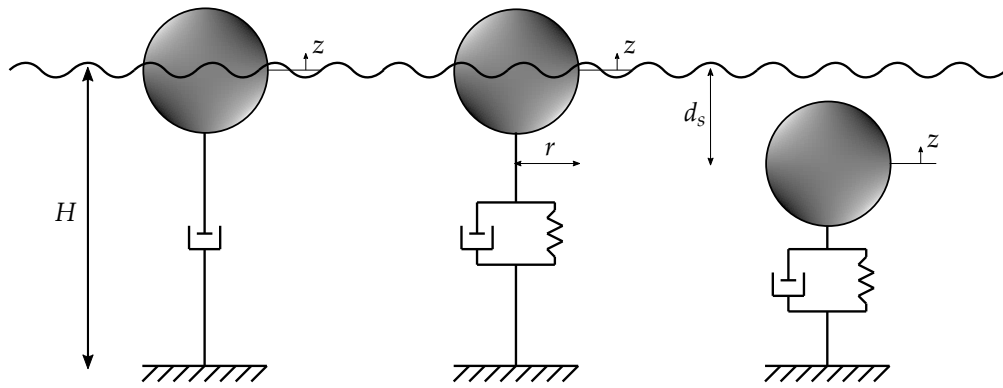
Figure 4.1: A depiction of the spherical PA WEC systems analysed in this study. The
leftmost representation depicts a floating WEC with only linear damping, the center
shows a floating WEC with linear stiffness as well, and the rightmost representation
depicts a submerged system with both. Note that in all cases, the control parameters
are optimised and allow for the linear control stiffness to be negative. The origin of the
coordinate systems are shown, as well as the water depth, submersion depth, and radius,
as given in Table 4.1

.

This work aims to unify the seemingly contradictory research within this field to
contextualise the applicable benefit of passive nonlinear stiffness control systems. Ac-
cordingly, the 1 degree of freedom (DOF) scenario was deemed a sufficient representation
of such PA WEC systems, as much of the significant dynamical features are associated
with vertical oscillations. The wave-structure interaction was modelled using linear
potential flow theory from the boundary element method (BEM) solver NEMOH [16].
For such buoys, linear hydrodynamic representations capture much of the significant

dynamics. A partially nonlinear method is preferable where a linear BEM method is used to represent the radiation force, and an instantaneous Froude-Krylov force is calculated [17]. However, for this benchmarking exercise, a linear hydrodynamic model was deemed sufficient for the 1 DOF model, as underlying trends are indicative when compared to higher fidelity models [18]. Additionally, most of the previous literature involving nonlinear stiffness control systems uses methods based on linear hydrodynamic to quantify fluid-structure interaction [4, 5, 7–10, 12].

The linear stiffness and damping parameters were optimised using time domain modelling to create a consistent benchmark for comparison. One key difference between the present work and recent literature is that the optimised linear stiffness parameter is allowed to be a negative value, such that it may counteract the large hydrostatic stiffness in the floating scenario. Negative stiffness is realisable either through active control, or using passive nonlinear stiffness mechanisms such as buckling beams, inclined springs, or permanent magnetic systems in attraction [19].

A nonlinear stiffness force, generated using a magnetic dipole model, was then incorporated into the control force and the power generated was quantified for each regular and irregular scenario. The variation of sea states over time was considered by subjecting the system to different irregular wave conditions while it was tuned for another. Furthermore, the dependency of the system performance on wave phase was explored by randomising the phase relationships between the components constituting a common irregular wave.

In both of these irregular wave extension scenarios, the nonlinear stiffness was varied to demonstrate the robustness arising from the nonlinear stiffness mechanism. In reality, regular and consistent irregular waves do not exist and consequently, perfect optimisation is not currently feasible. Therefore, enhanced robustness over a range of common sea states in a particular wave climate is of tangible benefit to the power generation capability of a WEC.

The mathematical model used in this study to represent the PA WEC system is given in Section 4.2 with the quantification of the nonlinear stiffness force presented in Section 4.2.7. The various parameters pertaining to both the geometric arrangement and simulation of the WEC model are given in Section 4.3. The results are presented and discussed in Section 4.4, limitations and possible extensions to the present work are identified in Section 4.5, with the final conclusions summarised in Section 4.6.

4.2 Mathematical models

The spherical PA WEC system may be represented using the following model

$$M\ddot{z} = F_e + F_{rad} + F_D + F_{hs} + F_{PTO} + F_n \, , \tag{4.1}$$

where M and $\ddot{z}$ are the mass and acceleration of the device, respectively. The total force
acting on the spherical buoy may be decomposed into the force due to: the excitation
F_e, the radiation F_{rad}, viscous drag effects F_D, the hydrostatic or buoyancy effect F_{hs}, the
linear power take off (PTO) unit F_{PTO}, and the nonlinear stiffness force F_n. While the
nonlinear stiffness force may be considered an addition of the PTO force, it was formu-
lated separately in the following model to emphasise the importance of benchmarking
the performance against a scenario with an optimally tuned PTO force. The spherical
PA WEC system with a magnetic nonlinear stiffness is represented in Figure 4.2. The
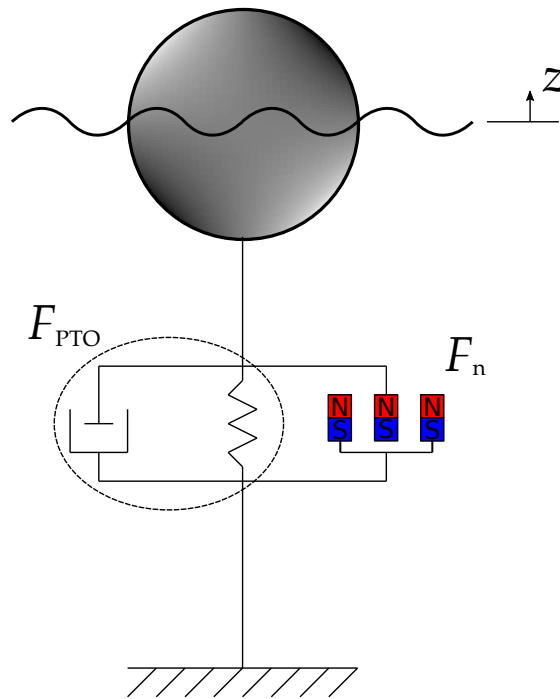
Figure 4.2: A depiction of the spherical PA WEC system with the magnetic nonlinear
stiffness. The system is shown floating and with a stiffness in this model, although
the configurations considered include a submerged buoy, or a system with no linear
stiffness. The PTO force and nonlinear stiffness force are indicated on the diagram, and
the mathematical representation is discussed in Section 4.2.7.

formulation of each force component depends on the configuration of the system. This
study considers three configurations which may be summarised into the following

1. floating device with only optimal linear damping — referred to as *Floating no
   stiffness*,

2. floating device with linear optimal stiffness and damping — referred to as Floating,
   and

3. submerged device with optimal linear stiffness and damping — referred to as Submerged.

For each of the above scenarios, both the regular and irregular wave conditions are considered in order to quantify the real potential improvement due to the nonlinear stiffness addition. Each force component is described in the following subsection for each of the scenarios.

4.2.1 Excitation force

The excitation force may be considered the force acting on the buoy due to the wave. This force, for a monochromatic wave, may be represented as

$$F_\text{e} = A_\text{w} F_\text{e,amp} \cos(\phi - \omega t) \, , \tag{4.2}$$

where the wave amplitude, time, and wave frequency is represented by A_w, t, and ω, respectively. The force amplitude and phase with respect to an incident wave, given by $F_\text{e,amp}$ and ϕ, respectively, may be quantified using the linear potential flow BEM solver, NEMOH [16]. This force is the superposition of the Froude-Krylov and diffraction forces acting on the buoy, and is effectively a function of geometry, depth, wave amplitude, and frequency. This representation of the hydrodynamic excitation force is common in literature [20]. To allow for the assumption of deep water conditions, a depth of 50 m was selected. Ocean waves with periods less than approximately 8 s with this depth have wavelengths larger than twice the depth, meaning such waves are not strictly deep water waves. However, the hydrodynamic parameters quantified in NEMOH do not assume deep water waves. The assumption of deep water conditions is used in this study to compare against theoretical optimal conditions and for relative comparison, rather than in direct simulation of WECs.

4.2.2 Radiation force

The radiation force is the force acting on the buoy as it moves through the fluid and radiates waves, and can be represented as [21]

$$F_\text{rad} = -A_\infty \ddot{z} - \int_0^t K(t - t') \dot{z} dt' \, , \tag{4.3}$$

where A_∞, K, and $\dot{z}$ represent the infinite frequency added mass, the impulse response function, and the buoy velocity, respectively. The added mass may be considered the additional inertia due to the fluid surrounding the buoy, which is dependent on the frequency at which the buoy is oscillating. The infinite frequency added mass is the constant to which the added mass converges to as the frequency of oscillation is increased.

The convolution of the impulse response function captures the impact of the fluid over time and is often termed the "fluid memory effect". In practice, this integral may be computationally expensive to quantify in time domain simulations. So, this integral is conventionally represented using a state-space function with the buoy velocity as an input via a parametric identification method [22]. This method requires knowledge of the frequency dependent added mass, A_ω, and radiation damping B_ω. In this study, these hydrodynamic coefficients were calculated using NEMOH. The number of panels describing the buoy was increased until convergence was observed in the hydrodynamic coefficients of each case. An assumption of this representation is that the device does not deviate significantly from a nominal position, about which these parameters were calculated.

4.2.3 Drag force

The viscous drag force may be approximated as a quadratic function of the buoy velocity relative to the fluid velocity using a Morison drag formulation [23]. The drag force is represented as

$$ F_\mathrm{D} = -\frac{1}{2}\rho C_\mathrm{d} A_\mathrm{d} |\dot{z} - \dot{z}_\mathrm{f}|(\dot{z} - \dot{z}_\mathrm{f}) \,, \tag{4.4} $$

where ρ, C_d, A_d, and $\dot{z}_\mathrm{f}$ represent the density of water, coefficient of drag, characteristic area, and surround fluid velocity, respectively. Given that PA WECs are, by definition, small with respect to the wave length, it is therefore reasonable to assume the surrounding fluid velocity to be constant and approximately equal to the fluid velocity at the geometric centre of the submerged buoy, and on the surface for the floating buoy. The vertical velocity of the fluid may be calculated using linear wave theory as [24]

$$ \dot{z}_\mathrm{f} = A_\mathrm{w}\omega \frac{\sinh(k(h + z - d_s))}{\sinh(kh)} \sin(-\omega t) \,, \tag{4.5} $$

where k, h, and d_s represent the wavenumber, water column depth, and submergence depth of the buoy, respectively. The origin of the coordinate system here is defined at the nominal free surface and the positive direction is up.

4.2.4 Irregular wave adjustments

Regular waves are simplistic representations of ocean waves and can provide insight into the frequency dependence of given systems. However, more realistic representations of ocean conditions, such as irregular waves, may be employed to better understand how a device will perform in situ. Irregular waves may be represented as the superposition of sinusoids of many different frequencies, each weighted based on a desired spectrum. One common way to model energy distribution across frequency is the Pierson-Moskowitz

spectrum, described by [25]

$$S(f) = \frac{A_{\text{PM}}}{f^5} \exp\left(-\frac{B_{\text{PM}}}{f^4}\right), \tag{4.6}$$

where the excitation frequencies in Hz are represented by f, and the coefficients A_{PM} and B_{PM} are

$$A_{\text{PM}} = \frac{5H_{\text{s}}^2 f_{\text{p}}^4}{16}, \quad B_{\text{PM}} = \frac{5f_{\text{p}}^4}{4}, \tag{4.7}$$

where f_{p} is the peak frequency in the spectrum, and H_{s} is the significant wave height. This peak frequency may be approximated from the energy period T_e as [25]

$$f_{\text{p}} = \frac{0.858}{T_e}. \tag{4.8}$$

Therefore, a spectrum may be constructed by the two parameters H_{s} and T_e. These two parameters may be calculated using measured data in the form of an energy density spectra by using [26].

$$T_{\text{e}} = 2\pi \frac{m_{-1}}{m_0}, \quad H_{\text{s}} = 4\sqrt{m_0}, \tag{4.9}$$

where the nth spectral moment is defined as

$$m_n = \int_0^\infty S(\omega)\omega^n d\omega, \tag{4.10}$$

where ω is the frequencies in the spectrum in rad/s. Data for the wave climate at the Torbay site, Western Australia between the 5th of March 2019 and 14th of October 2019 is available online at https://wawaves.org/. The depth at this location is estimated to be approximately 30 m. A map depicting the probability of finding an irregular wave with any given H_{s} and T_e is presented in Figure 4.3. For the purposes of this paper, the irregular wave parameters selected were around the most common parameters observed at the Torbay site: $H_{\text{s}} = 3.75$ m and $T_e = 8.8$ s. The wave amplitude of each frequency component, $A_{\text{w},j}$, may be calculated as

$$A_{\text{w},j} = \sqrt{2S(\omega_j)\Delta\omega_j}. \tag{4.11}$$

Therefore, the excitation force due to an irregular wave, $F_{\text{e,irr}}$, takes the form

$$F_{\text{e,irr}} = \sum_{j=1}^N A_{\text{w},j} F_{\text{e,amp},j} \cos(\phi_j - \omega_j t + \epsilon_j), \tag{4.12}$$

where ϵ_j is a random phase offset normally distributed between 0 and 2π radians applied at each frequency, and N is the number of frequencies. In this study, the irregular wave was composed of 1024 linearly spaced frequencies in the range $0.03 - 1$ Hz, resulting
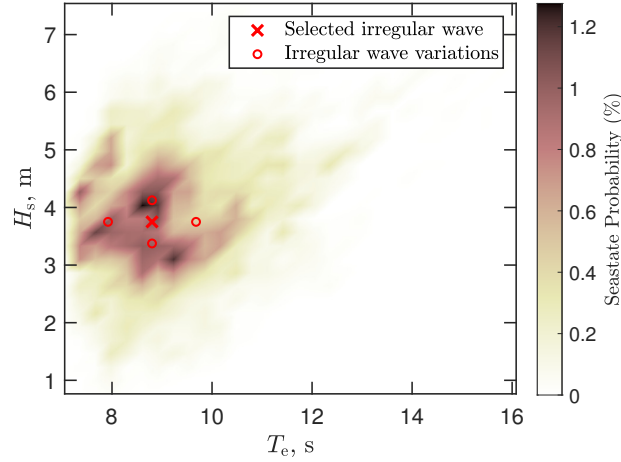
Figure 4.3: The wave climate at the Torbay site depicted as a joint probability distribution of H_s and T_e. The red cross indicates the irregular wave properties selected for modelling in this study, and the red circles indicate variations relevant to Section 4.4.4. The sea state probability was found by subdividing the available data into 30 bins for both H_s and T_e, so this probability only provides a relative indication rather than a true probability of observing a given sea state.

in a frequency spacing of approximately 0.0095. The fluid velocity is also a similar summation of the regular wave components given by

$$\dot{z}_{\text{f,irr}} = \sum_{j=1}^{N} A_{\text{w},j} \omega_j \frac{\sinh(k_j(h + z - d_s))}{\sinh(k_j h)} \sin(\epsilon_j - \omega_j t) \,. \tag{4.13}$$

The Pierson-Moskowitz spectral shape has been used in this study as the gathered data has coarse and nonuniform frequency spacings. Therefore, to better capture the stochastic nature of waves, more frequency components were used with random phase offsets. The measured data covers the winter half of a year, which would mean the seasonal variability in the Albany wave climate would skew the most probable sea state to more severe conditions than if long term data was used. While the generated spectrum may differ from the measured spectrum or the true spectrum due to seasonal variability, it does provide a basis for modelling the WEC in a semi-realistic wave climate and provides a sufficient test case for the 1 DOF WEC modelled in this study.

4.2.5 Hydrostatic force

The hydrostatic force represents the net force acting on the buoy due to gravity and the displaced fluid. If the buoy is submerged, the net hydrostatic force is constant and may be described as

$$F_{\text{hs,sub}} = (\rho V - M)g \,, \tag{4.14}$$

where g and V represent the acceleration of gravity and the volume of the buoy, respectively. If the buoy is floating, the hydrostatic force varies with the submergence depth. For a sphere, this variation is nonlinear. However, for small oscillations about the nominally half-submerged position (where $M = \rho V / 2$ to balance the gravitational force), the hydrostatic force may be described as

$$F_{\text{hs,float}} = -k_{\text{hs}}z \, , \tag{4.15}$$

where z is the vertical heave position, and k_{hs} is the linearised effective hydrodynamic stiffness, given by

$$k_{\text{hs}} = \rho g \pi r^2 \, , \tag{4.16}$$

where r is the radius of the sphere. This equation assumes the change in submerged volume varies linearly with heave, and is also valid only for small oscillations. Therefore the motion is restricted to 3 m amplitude for regular waves and 4 m in irregular waves. For context, the radius of the buoy is 5 m. While these are relatively large motions for the given assumptions, linear hydrodynamics are fundamentally limited in the representation of fluid-structure interactions, and for most of the operating range in the regular and irregular wave excitations, the hydrostatic stiffness remains approximately linear. This assumption will be justified in the discussion. Therefore, with these assumptions, the simulations provided indicative results useful for inferring the impact of the nonlinear stiffness mechanism.

4.2.6 PTO force and optimisation

The force due to the PTO is a combined stiffness and damping force and may be represented as

$$F_{\text{PTO}} = -k_{\text{PTO}}z - b_{\text{PTO}}\dot{z} - F_{\text{pre}} \, , \tag{4.17}$$

where k_{PTO} is the linear stiffness coefficient, b_{PTO} is the linear damping coefficient, and F_{pre} is the pretension force required to submerge the buoy to the desired equilibrium position. The mass is selected to be half the mass of displaced fluid when fully submerged, so no pretension force is required for the floating buoy. For the submerged buoy, the pretension force is equal in magnitude to the hydrostatic force given in Equation (4.14). The linear stiffness and damping is often selected from well known approximate optimal values [14]. However, due to the influence of drag, larger amplitudes of excitation, and irregular wave excitation, both the linear stiffness and damping were calculated using constrained nonlinear optimisation (Matlab function *fmincon*) with motion amplitude constraints of 3 m for regular waves and 4 m for irregular waves. The optimisation was performed for each regular wave excitation frequency and for the irregular wave scenarios. The optimisation metric was the time-averaged power and is discussed in Section 4.2.8. Each of the operating conditions — floating without linear stiffness (with

optimised damping), floating with stiffness (with optimised stiffness and damping), and submerged (with optimised stiffness and damping) — were optimised separately to ensure the best linear conditions were used for each specific scenario.

4.2.7 Nonlinear stiffness force

The nonlinear stiffness force in this work is described using the magnetic dipole model. While there exist other sources of nonlinear stiffness, this approach allows for significant variation of force profiles. The nonlinear stiffness force between two dipoles can be represented by [15].

$$F_{\mathrm{n}} = C \left[\frac{9z}{(r_0^2 + z^2)^{\frac{5}{2}}} - \frac{15z^3}{(r_0^2 + z^2)^{\frac{7}{2}}} \right] , \tag{4.18}$$

where C represents a combination of constants and material properties, and r_0 is the horizontal distance between two dipoles moving vertically. The parameter C is not an intuitive representation of the nonlinear force. To generalise the nonlinear force, it is instead parameterised by γ, which is ratio of the potential energy of the nonlinear stiffness at the nominal position, $U_{\mathrm{nl},z=0}$, to the potential energy of the incident wave, U_{w}, or

$$\gamma = \frac{U_{\mathrm{nl},z=0}}{U_{\mathrm{w}}} . \tag{4.19}$$

The potential energy of the nonlinear stiffness force is

$$U_{\mathrm{nl}} = C \left[\frac{-1}{(r_0^2 + z^2)^{\frac{3}{2}}} + \frac{3z^2}{(r_0^2 + z^2)^{\frac{5}{2}}} \right] , \tag{4.20}$$

which, when evaluated at $z = 0$ and $r_0 = 1$m, reduces to $U_{\mathrm{nl},z=0} = C$. The time-averaged potential energy of deep water waves per horizontal unit area, $\overline{U}_{\mathrm{w}}$, can be described as [27]

$$\overline{U}_{\mathrm{w}} = \frac{1}{4} \rho g A_{\mathrm{w}}^2 . \tag{4.21}$$

There, the time-average potential energy of the wave, U_{w}, can by quantified multiplying $\overline{U}_{\mathrm{w}}$ by the horizontal area of the buoy, which becomes

$$U_{\mathrm{w}} = \frac{1}{4} \rho g A_{\mathrm{w}}^2 \pi r^2 , \tag{4.22}$$

where r represents the radius of the spherical buoy. By parameterising the nonlinear stiffness force in this way, it is non-dimensionalised against a given wave condition. The total potential energy of the stiffness forces, $U_{\mathrm{s,total}}$, is

$$U_{\mathrm{s,total}} = U_{\mathrm{lin}} + U_{\mathrm{nl}} , \tag{4.23}$$

where U_{lin} is the potential energy associated with the linear spring. The potential energy profile for various γ is provided in Figure 4.4 for conceptual purposes. The corresponding total restoring force, $F_{\text{r,total}}$, which is composed of both the linear and nonlinear stiffness forces, is also provided in Figure 4.4. As expected, the occurrences of zero net restoring force correspond to the equilibria in the potential energy profiles.

4.2.8 Performance metrics

To analyse the potential performance benefit of each system, the time-averaged power, P_{avg}, is calculated using the following formula

$$P_{\text{avg}} = \frac{1}{T} \sum_{j=1}^{n_t} b_{\text{PTO}} \dot{z}^2 \Delta t_j \,, \tag{4.24}$$

where Δt_j is the jth time step and T is the length of the simulation. This metric provides a benchmark to compare the performance of each regular and irregular wave situation. For regular waves, there exist an upper limit on the absorbed power at both lower frequencies and higher frequencies [28]. Assuming deep water conditions and a small body relative to an incident wave, the upper bound at lower wave frequencies for floating buoys, known as the Budal limit, is given by [29]

$$P < \rho g \omega V \frac{A_{\text{w}}}{4} \,, \tag{4.25}$$

and for submerged buoys is [29]

$$P < \rho e^{-kd_s} z_{\text{max}} V A_{\text{w}} \omega^3, \tag{4.26}$$

where z_{max} is the maximum heave displacement. This is a general result for a heaving body and not specific to a spherical device. The upper limit at higher wave frequencies is based on the assumption of optimum destructive interference and deep water conditions, sometimes referred to as the radiation limit, [28] and is given by

$$P < \rho g^3 V \frac{A_{\text{w}}^2}{4\omega^3} \,. \tag{4.27}$$

These two limits should be included in understanding any potential improvement to power, relative to the maximum possible power and is included in the results for regular wave excitation in both the floating and submerged cases.

4.3 Simulation conditions

The parameters specifying the physical and geometric features of the system are presented in Table 4.1. The wave conditions are provided in Table 4.2. The optimised linear
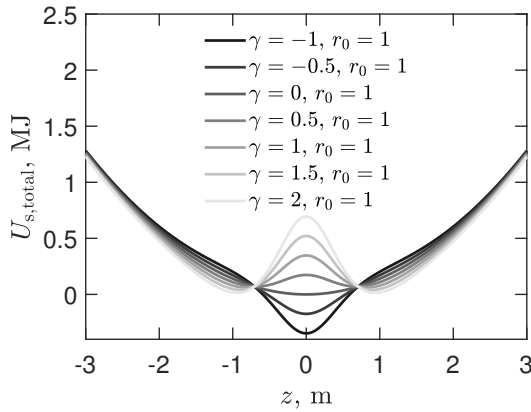
(a) The total potential energy associated with the stiffness forces acting on the WEC for various dimensionless potentials represented by γ, and a constant r_0.

(b) The total restoring force acting on the WEC for various dimensionless potentials represented by γ, and a constant r_0. The forces correspond to the cases and legend presented in (a).
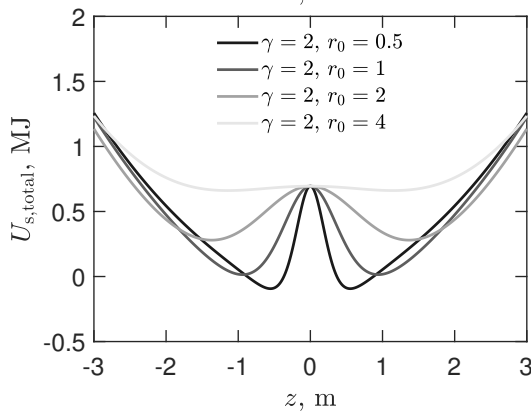
(c) The total potential energy associated with the stiffness forces acting on the WEC for various dipole spacings represented by r_0, and a constant γ.
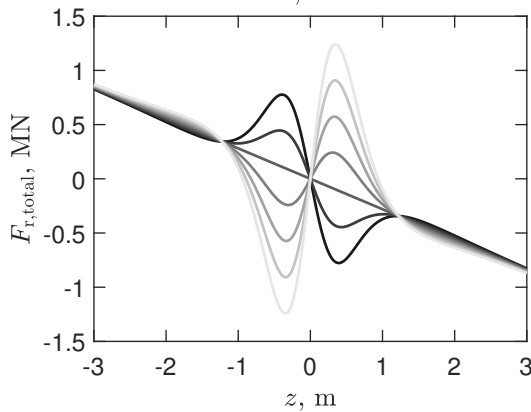
Figure 4.4: The total potential energy associated with the stiffness forces, and the total restoring forces acting on the WEC. As the nondimensional potential term γ increase, the height of the central peak increases. As the geometric parameter r_0 increases, the stable equilibrium shifts outward and for sufficiently large values, the system converges to a monostable scenario. The occurrences of zero net stiffness force in (b) correspond to the equilibria on the potential energy profiles in (a). The stiffness and wave potential energy in the presented data are from the selected irregular wave.

control parameters for the irregular wave in each of the operating conditions are given in Table 4.3, and the optimised linear control stiffnesses of the regular wave conditions are included as part of the discussion of results. These parameters were combined into a Matlab and Simulink simulation using the variable time step solver *ode45*.

Table 4.1: Physical and geometric parameters of the buoy

Parameter	Value	Units
Water depth, H	50	m
Submersion depth (buoy center), d_s	9	m
Sphere radius, r	5	m
Water density, ρ	1025	kg/m^3
Buoy density, ρ_{buoy}	0.5ρ	kg/m^3
Acceleration due to gravity, g	9.81	m/s^2
Coefficient of drag [30], D_d	0.5	-
Characteristic area, A_d	πr^2	m^2

Table 4.2: Regular and irregular wave conditions

Parameter	Value	Units
Regular wave frequency range	$0.1 - 2$	rad/s
Regular wave simulation length, T_{reg}	2000	s
Regular wave amplitude, A_w	0.5	m
Irregular wave energy period, T_e	8.8	s
Irregular wave significant height, H_s	3.75	m
Irregular wave frequency range	$0.03 - 1$	Hz
Number of frequencies in irregular wave, N	1024	-
Irregular wave simulation length, T_{irr}	10000	s
Maximum displacement (regular wave), z_{max}	3	m
Maximum displacement (irregular wave), z_{max}	4	m

4.4 Results and discussion

4.4.1 Regular waves

The resultant time-averaged powers for the regular wave excitation under the floating condition with and without linear stiffness in the control force are presented in Figures 4.5a and 4.5b, respectively. The results shown are for various levels of γ, but have a

Table 4.3: Optimal linear stiffness and damping irregular waves scenarios

Scenario parameter	Value	Units
Floating (no stiffness), b_{PTO}	762	kN/m
Floating, k_{PTO}	-622	kN/m
Floating, b_{PTO}	521	kNs/m
Submerged, k_{PTO}	281	kN/m
Submerged, b_{PTO}	139	kNs/m

constant value of $r_0 = 1$m. For the case with no control stiffness, the additional nonlinear
stiffness increases the converted power for low levels of γ, but after $\gamma = 2$, acts to reduce
the performance. The improvement seen is dependent on frequency and can significantly
improve the system performance at some frequencies. However, even after the best
nonlinear stiffness addition, the converted power is well below the maximum possible
power. If an optimised linear stiffness is included in the control force, the converted
power is closer to the theoretical maximum. However, any additional nonlinear stiffness
only acts to reduce the performance of the floating spherical buoy.

A similar previous study, [31] demonstrates that for a semi-submerged heaving
sphere, optimal reactive control (optimised PTO coefficients) outperforms simple pas-
sive control (damping coefficient). The previous study calculates the reactive parameters
using the intrinsic parameters of the WEC, whereas the PTO parameters were numeri-
cally optimised in the present study. The present findings match the previous literature
in that passive WEC systems with optimised damping may be improved by including
some form of appropriately selected restoring force.

As an alternative representation of the floating scenario without stiffness, a colour
map depicting the time-averaged power for each frequency and γ combination is pre-
sented in Figure 4.6. This demonstrates that the frequencies that experience the greatest
benefit from the nonlinear stiffness are around 0.6 rad/s and that for frequencies and γ
levels away from this position, the time-averaged power reduces significantly. This is an
outcome of the larger maximum possible power at this frequency, as indicated by the
limits displayed on Figure 4.5a, and the additional nonlinear stiffness at the nominal
position counteracting the large hydrostatic stiffness resulting in a more adequately
tuned device. This concept will be explored further in the context of all three scenarios.

In the submerged case (Figure 4.7) a similar result is observed relative to the theoreti-
cal maxima. The energy density of ocean waves reduce exponentially with submergence
depth for deep water conditions. Therefore, the maximum possible power is less than
that of the floating case. The additional nonlinear stiffness acts again to detune the sys-
tem and reduce the performance compared to optimised linear control conditions. There
are also significant spikes and jumps in these results, which demonstrates the sensitivity
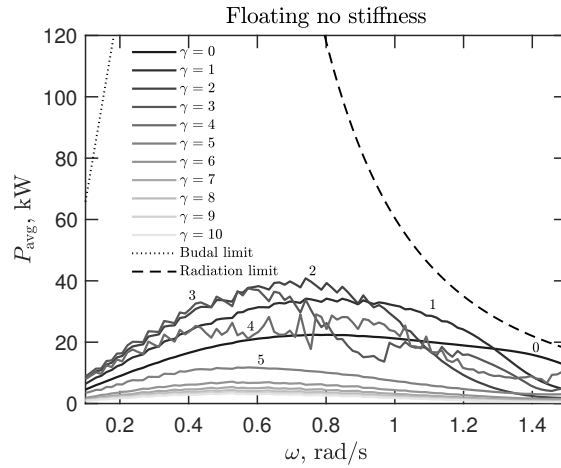
(a) The time-averaged power for each frequency of regular wave excitation of the floating WEC with only damping control at various levels of nonlinear stiffness. The curves associated with $\gamma \leq 5$ are annotated with the corresponding γ for clarity. As the nonlinear stiffness potential, γ, increases, the power converted is improved around at some frequencies. However, for $\gamma > 2$, the nonlinear stiffness acts to reduce the power converted.
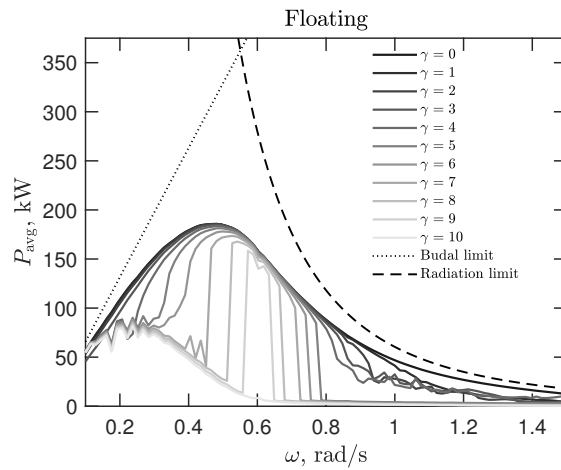
(b) The time-averaged power for each frequency of regular wave excitation of the floating WEC with optimised linear control parameters at various levels of nonlinear stiffness. As the nonlinear stiffness potential γ increases, the power converted is monotonically reducing. Therefore the nonlinear stiffness only acts to detune the system from optimal linear conditions.

Figure 4.5: Floating WEC regular wave simulation time-averaged powers. The scenario with no linear control stiffness may benefit from a nonlinear stiffness. However, the time-averaged power is well below the limits and is far from optimal. The scenario with an optimised linear control stiffness follows the trend of the low and high frequency limits on power. In these scenarios, r_0 was selected to be 1 m.
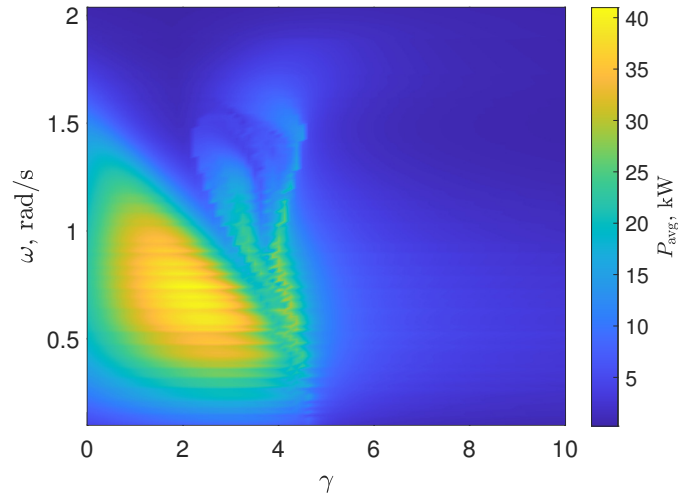
Figure 4.6: A map depicting the time-averaged power at each frequency, at each nonlinear stiffness potential γ for the floating WEC with no linear control stiffness.

of such nonlinear stiffness mechanisms. If the excitation energy in insufficient to overcome the potential energy barrier, the system may oscillate about an local equilibrium which may not be tuned for the excitation frequency. Such behaviour leads to distinct spikes and jumps in power when the excitation frequency matches or is near the natural frequency at the local equilibrium. Additionally, the variability at higher frequencies may be interpreted as the occasions where there is sufficient energy to overcome the potential barrier and oscillate over both stable equilibria. These findings show that for regular waves, nonlinear stiffness can provide no improvement in converted power unless the system does not have the capacity to provide an appropriate linear stiffness.

The geometric parameter r_0 is another variable which adjusts the potential energy profile, and therefore, the stiffness. The influence of r_0 is shown in Figure 4.8 by holding γ constant and varying r_0. These figures show that for all cases, increasing r_0 acts to reduce the variation over different frequencies, and moves the result towards the optimised linear condition ($\gamma = 0$). This implies that the nonlinear contribution to the stiffness reduces as r_0 increases. Therefore, neither γ nor r_0 were the most important factor to consider. It was the combination of both which adjust the shape of the potential energy curve, and therefore the effective stiffness, that is influential. So, for simplicity, in future calculations for irregular waves r_0 was selected to be 1 m as this represents a reasonable point to illustrate the process with no loss of generality. This selection allows for both near linear conditions for smaller values of γ, and negative effective stiffness and bistability for larger values of γ, and therefore simulating a large variety of nonlinear stiffnesses.

The linear stiffness components in each case at each excitation frequency for the
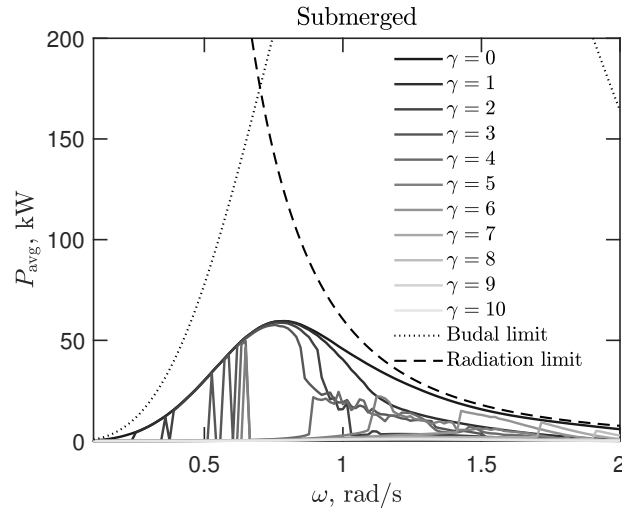
Figure 4.7: The time-averaged power for the submerged scenario with optimised control parameters at each regular wave frequency. The magnitude of power converted is lower than the floating counterpart due to the reduced upper and lower frequency limits on power. In this scenario, r_0 was selected to be 1 m.

floating and submerged cases, denoted as k_{lin} with specific stiffnesses identified in the legend, are given in Figure 4.9. For comparison, the linearised optimal linear stiffnesses k_{theory} for the floating and submerged cases, calculated from [14]

$$k_{theory} = \omega_e^2(M + A_\omega) \,, \tag{4.28}$$

is also provided. This plot shows a similar trend between the stiffnesses of the floating and submerged scenarios, but with an offset in the floating scenario. The offset and negative value of the optimal control stiffness for the floating scenario is an outcome of compensating for the hydrostatic stiffness to tune to the frequency.

The natural frequency of the system, ω_n depends on the stiffness and hydrodynamic added mass, which depends on the excitation frequency, and may be derived as [15]

$$\omega_n = \sqrt{\frac{k_{PTO} + k_{hs}}{m + A_\omega}} \,. \tag{4.29}$$

The natural frequency of the floating and submerged systems at each regular wave frequency, with optimal linear stiffness, are given in Figure 4.10. The hydrostatic stiffness in the floating system is not present in the submerged system as the pretension force compensates for the combined buoyancy and gravitational force, and because there is no intersection with the free surface. In the floating system, the hydrostatic stiffness is very large due to the cross-sectional area of the buoy at the free surface. Therefore, a negative stiffness is required to better tune the system to the incident excitation wave.
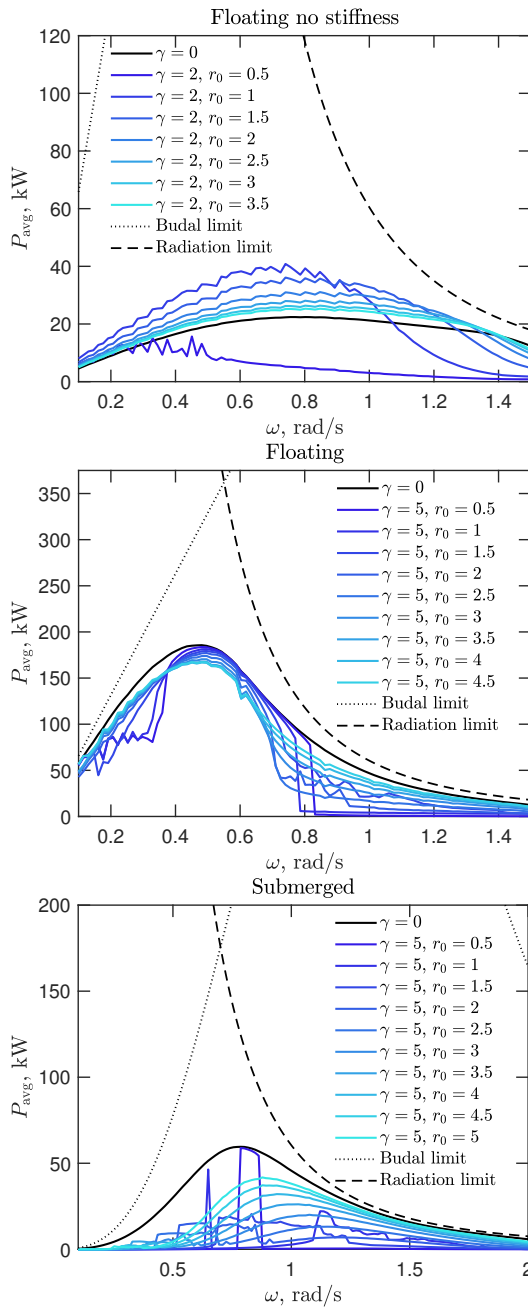
(a) The time-averaged power for the regular wave excitation simulations of the floating WEC, with no linear control stiffness for a constant γ at varying levels of r_0 (in m).

(b) The time-averaged power for the regular wave excitation simulations of the floating WEC, with optimised linear control stiffnesses at each frequency, for a constant γ at varying levels of r_0 (in m).

(c) The time-averaged power for the submerged scenario with optimised control parameters at each regular wave frequency, for a constant γ at varying levels of r_0 (in units of m).

Figure 4.8: The converted power for each frequency for a constant γ and a varying r_0 in each scenario. All results indicate that an increasing r_0 reduces the influence of the nonlinear stiffness. As r_0 increases, the power converted curve is smoothed and the system converges to optimal linear conditions. A single γ is presented for each scenario, however, the same trend is observed at other levels of dimensionless potentials.
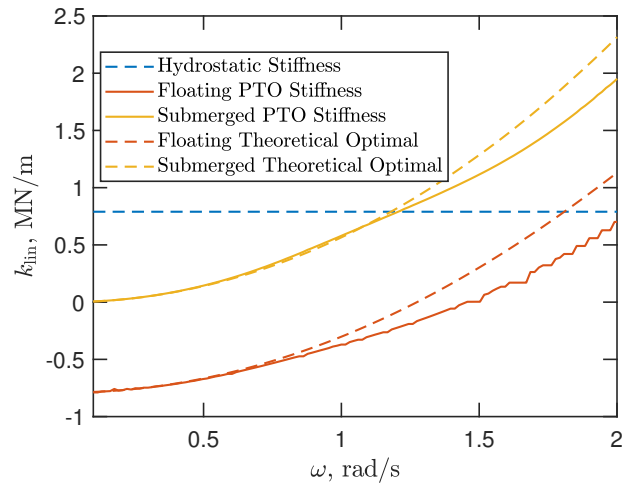
Figure 4.9: The optimised stiffnesses in the floating and submerged scenarios. In the floating scenario, the linear stiffness must compensate for the hydrostatic stiffness (also shown). As a result, the optimal stiffness becomes negative. The rough curve of the floating optimal linear stiffness is the result of the limitation of the motion amplitude of, in this case, 3m. The optimised stiffnesses for both floating and submerged cases follow the linearised theoretical optimal stiffnesses at lower frequencies, but deviate slightly at higher frequencies.

The optimal natural frequencies of each system indicate that the best performance occurs when the natural frequency of the WEC matches the excitation frequency, which explains the reduced performance of the system with no linear control stiffness.

The effective natural frequency of the WEC with a nonlinear stiffness depends on both frequency and position. Hence, the natural frequency deviates from the optimal value during operation leading to suboptimal performance. The key finding is that to obtain the best performance, the natural frequency around the operating condition should approximate the incident wave frequency, which matches intuition. In some cases, this necessitates negative stiffness to compensate for the hydrostatic stiffness. So, in theory, the nonlinear stiffness mechanism could be used to produce the necessary negative stiffness about the nominal position for the required regular wave conditions.

An alternative approach to the presented investigation in this study was to set the net stiffness at the nominal position as the optimal linear stiffness and vary the nonlinear and linear components. This has also been undertaken by the authors but did not provide any further insight upon what has been discussed in this study and has therefore not been included in this paper.
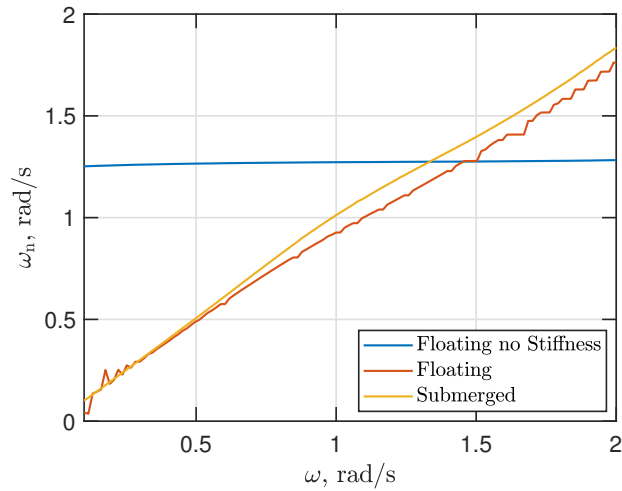
Figure 4.10: The natural frequency of the optimised scenarios. The trend indicates that
the optimal condition is when the natural frequency of the device at each excitation
frequency is approximately equivalent to the excitation frequency. The natural frequency
of the system without a linear control stiffness is generally away from the excitation
frequency. The theoretical relationship, which is not presented for clarity, follows a simi-
lar trend with slope of 1 for the floating and submerged cases. However the theoretical
value is derived by ignoring nonlinear drag.

4.4.2 Irregular wave scenarios

Irregular waves, which are more representative of ocean conditions, are composed
of many frequencies, which cause the plant to interact differently with the nonlinear
stiffness mechanisms as the position changes. The time-averaged power of each of the
three WEC control scenarios detailed in Section 4.2 over a range of nonlinear stiffness
potentials are presented in Figure 4.11.

The scenario involving the floating system without linear stiffness benefits from
the nonlinear stiffness when the potential energy of the nonlinear stiffness is less than
the potential energy of the incident wave. This scenario has an optimised damping
parameter, but can be improved by 27% in this case if the nonlinear potential is selected
to be $\gamma = 0.6$. This finding suggested that if it is not feasible to include a negative linear
stiffness, a WEC system may be improved by including a nonlinear mechanism. Whereas
the floating and submerged scenarios with an optimised linear control stiffness do not
experience a benefit for any γ. In the floating scenario, the converted power with an
optimised linear stiffness is substantially greater than the scenario with no linear control
stiffness. This is because the linear control system is tuned for the particular irregular
wave. Therefore, the nonlinear stiffness does not provide a significant improvement to
the generated power when the linear PTO conditions are optimal (or near optimal) for
a given irregular wave. Importantly, the optimal stiffness in this scenario was found
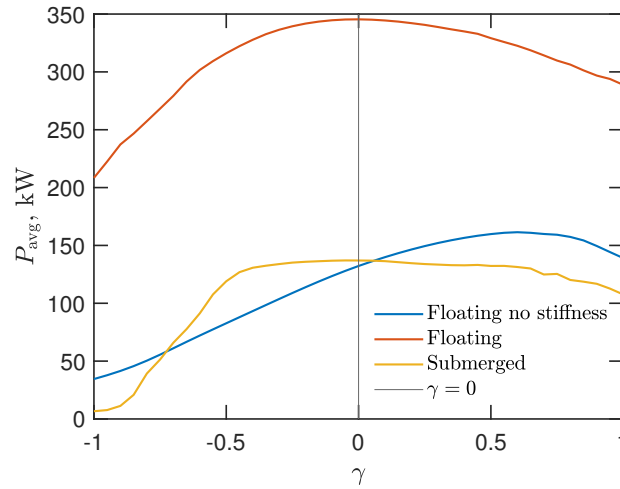
Figure 4.11: The time-averaged power for each of the three control scenarios under irregular wave excitation. The floating scenario without stiffness experiences a benefit from the nonlinearity with a peak around $\gamma = 0.6$. The floating and submerged scenarios with optimised linear stiffness and damping do not show an improvement upon linear control ($\gamma = 0$) for any γ, demonstrating that the nonlinear stiffness acts to reduce the power converted.

to be a large negative value to counteract the large hydrostatic stiffness. Meaning that some mechanism would be required to provide this negative stiffness. In practise, the nonlinear mechanism could be designed to provide an adequate negative stiffness about the nominal position for tuning purposes of a floating WEC. For the submerged WEC, the optimal linear control stiffness is positive and any additional nonlinear stiffness degrades the performance.

4.4.3 Justification of hydrostatic stiffness

In Section 4.2.5, the hydrostatic stiffness of the floating spherical buoy is assumed to be linear. The analytical nonlinear hydrostatic force relative to the half submerged equilibrium position (to cancel with the mass of the buoy) was derived by integrating over the submerged volume of the sphere to give

$$F_{\text{hs,float,n}} = \frac{\rho g \pi (R - z)^2}{3}(2r + z) - F_{\text{hs,0}} \tag{4.30}$$

where $F_{\text{hs,0}}$ is the hydrostatic force about the equilibrium position, which cancels with the weight of the buoy, is represented as

$$F_{\text{hs,0}} = \frac{2\rho g \pi r^3}{3} . \tag{4.31}$$

The linear and nonlinear representation of the hydrostatic force for the floating buoy are presented in Figure 4.12. This comparison indicates that for amplitudes of motion up to 3 m, the linear approximation of the hydrostatic is a good representation. The regular waves were optimised in scenarios allowing for 3 m oscillations, and therefore do not exceed this range. The irregular wave scenarios were optimised in scenarios allowing 4 m oscillations. However, the distribution of position of the buoy over the irregular wave scenarios under both floating control conditions are provided in Figure 4.13. These data sets indicate that the system rarely exceeds the 3 m bound, so the linear approximation of the hydrostatic stiffness is justified given the typical operating range of the floating device under these conditions.
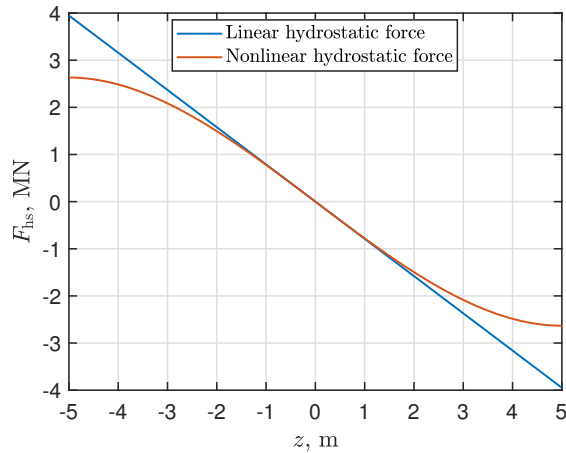
Figure 4.12: The linear and nonlinear representation of the hydrostatic force acting on the sphere relative to equilibrium position. In the range -3 to 3 m there is not a significant difference between the linear and nonlinear representations the hydrostatic force.

4.4.4 Changing irregular waves

During operation, wave conditions change over time, as implied by the sea state probability distribution shown in Figure 4.3. Therefore, for a system controlled through passive means, it is important to consider how robust the system would be if the irregular wave was to change. To understand how the changing irregular wave conditions and the nonlinear stiffness mechanism may interact, the energy period and significant wave height wave was varied by 10%, giving an additional 4 separate scenarios. Each irregular wave was generated with five distinct random phase realisations. The scenarios were subjected to the adjusted wave conditions and the resulting time-averaged powers from each realisation were averaged. The adjusted energy period ($T_{e,irr}$) and significant wave height ($H_{s,irr}$) are presented in Table 4.4. The percentage improvement upon the time-
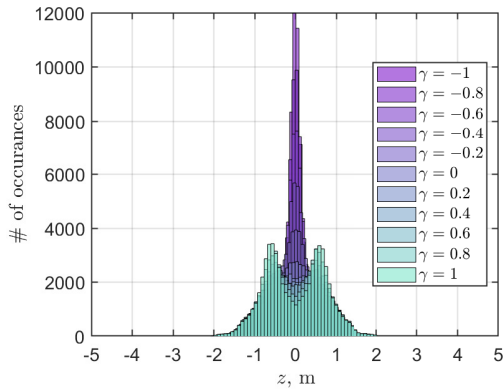
(a) The number of occurrences in the simulation of the floating system with optimised damping no control stiffness that the buoy was at a given position.
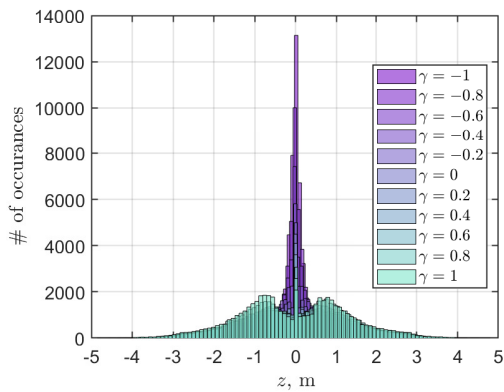
(b) The number of occurrences in the simulation of the floating system with optimised linear stiffness and damping that the buoy was at a given position.

Figure 4.13: The distribution of positions during the time domain simulations of the floating WEC irregular wave scenarios with and without and optimal control stiffness. In both cases, for all levels of nonlinear stiffness examined, the displacement rarely exceeds 3 m, which justifies the approximation of linear hydrostatic stiffness for the sphere in these scenarios.

averaged power of the floating with no stiffness scenario and the submerged scenario using the previously found optimal linear control parameters are presented in Figure 4.14.

Table 4.4: Irregular wave variations

Units	$T_{e,irr}$ (s)	$H_{s,irr}$ (m)
Irregular wave 1	$0.9T_e$	H_s
Irregular wave 2	$1.1T_e$	H_s
Irregular wave 3	T_e	$0.9H_s$
Irregular wave 4	T_e	$1.1H_s$

The percentage improvement is not consistent over all the nonlinear stiffnesses

(a) The percentage improvement in the time-averaged power of the floating WEC with no stiffness, relative to the case with optimised linear damping control. This trend demonstrates the improvement observed in the floating case with no linear stiffness is reasonably consistent as the irregular wave changes over time.

(b) The percentage improvement in the time-averaged power of the submerged WEC with nonlinear stiffness relative to the case with optimised linear control stiffness. This optimal stiffness was found using the baseline irregular wave parameters. This trend demonstrates that as the energy period increase, the time-averaged power is improved if γ is increased. Whereas if the energy period decreases, the time-averaged power is improved if γ is reduced.

Figure 4.14: The percentage improvement in the time-averaged power of the floating WEC with no linear stiffness and the submerged WEC scenarios. The floating WEC with optimised linear stiffness showed the same trend as the submerged case and so has not been presented here.

for both Floating as Submerged scenarios considered. However, if the energy period increases, the system benefits from slightly higher levels of γ and if the energy period decreases, the system benefits from lower levels of γ. The impact of H_s is less pronounced, indicating that the energy period of an irregular wave is more consequential than the significant wave height. Therefore, the nonlinear stiffness may be used in some cases to improve the robustness of the WEC control system to changing irregular waves. Wave energy systems are known to be reasonably phase dependent [32]. Since the irregular wave components have an associated random phase, ϵ_j, the influence of different random phases realisations on WEC performance should be considered. The submerged WEC was excited with 5 irregular waves with identical wave conditions (the originally selected irregular wave) with a randomised phase. The resulting time-averaged power is given

in Figure 4.15b. The variation shows that the time-averaged power from each realisation should be averaged to attain a more representative indication of performance for a particular irregular wave.

(a) The time-averaged power of the floating WEC with no linear control stiffness excited by a consistent irregular wave with different random phases.

(b) The time-averaged power of the submerged WEC excited by a consistent irregular wave with different random phases.
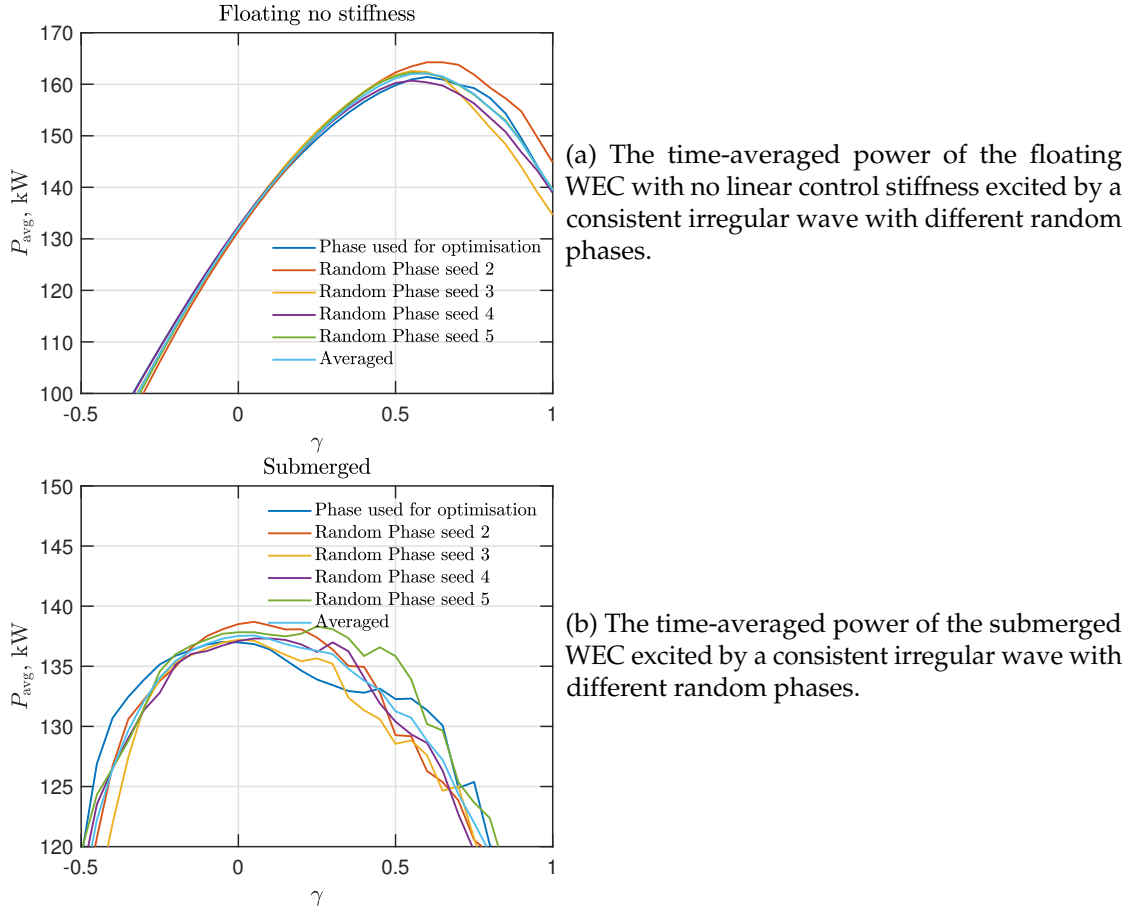
Figure 4.15: The time-averaged power of the floating with no stiffness and the submerged WEC scenarios derived from different realisations of the same underlying sea state. As the optimal linear conditions were obtained for the original irregular wave phase, the nonlinear stiffness potential γ offers some improvement to waves with different random phases. The average time-averaged power over the different realisations are presented.

The random phase is shown to influence the time-averaged power of the WEC, even for many cycles and many discrete frequencies. The random phase introduces some uncertainty in the results, which indicates the need for averaging the results of different realisations. For the five realisations presented, the corresponding mean over the results for $-0.5 < \gamma < 0.5$. The mean of the standard deviation was found to be 1.1% and 0.8% of the mean time-averaged power for the submerged and floating with no linear control stiffness cases, respectively. This indicates that for the floating with no linear

control stiffness, the improvement for a changing irregular wave is clear, but for the submerged system, the standard deviation is around the same order of improvement identifies. Therefore, further investigation is needed to provide more confidence around the performance of the submerged WEC subject to irregular wave phases.

4.5   Limitations and future work

This work shows that for a simplified 1 DOF PA WEC that is either floating or submerged, a nonlinear stiffness mechanism does not directly increase the amount of converted power if the linear stiffness and damping are optimised. This model uses a linear hydrodynamic representation, is constrained to 1 DOF, and represents the hydrostatic stiffness as linear. Therefore, these additional nonlinearities should be included for more general conclusions of nonlinear stiffness.

The study only considers a nonlinear stiffness in the form of a magnetic dipole. While the approach provides a large range of the potential energy curves, which influences the effective stiffness at each point, other representations of nonlinear stiffnesses could be considered. Although it is not anticipated that findings using other nonlinear stiffness representations would deviate from the findings presented in this study, more physically or economically feasible variations should be investigated.

The optimised linear damping and stiffness in this study were found using the case without nonlinear stiffness. An algorithm to optimise the parameters defining the nonlinear stiffness while holding the optimised linear PTO parameters constant for a single frequency was also conducted by the authors, but not presented or discussed. This optimisation routine reduced the nonlinear stiffness to zero or near zero in an effort to maximise power, however this investigation of optimising the nonlinear parameters could be further explored in future work to determine if this is a general finding, or specific to the individual frequency case.

As shown in the above results, the primary purpose of included nonlinear stiffness into a floating WEC is to counteract the hydrostatic stiffness. However, as the floating WEC heaves relative to the local instantaneous free surface elevation, the simplified constant linear hydrostatic stiffness about a nominal position may not adequately represent the effective stiffness force. The submerged case does not have this additional consideration due to having no hydrostatic stiffness. Therefore, in higher fidelity scenarios, the nonlinear stiffness may offer some additional benefit by counteracting the nonlinear hydrostatic stiffness to produce a net stiffness near the optimal condition.

4.6 Conclusion

The application of a nonlinear stiffness mechanism was applied to both floating and submerged spherical PA WECs which are restricted to 1 DOF. The performance was analysed compared to optimised linear control systems. For the floating WEC, the scenarios with and without a linear control stiffness were considered, while for the submerged buoy, only the scenario with a linear stiffness control force was considered. The control stiffness and damping parameters were optimised in the time domain to maximise the converted power. The nonlinear stiffness was parameterised by a nondimensionalised potential energy term based on the incident wave energy.

The regular wave results show that in the scenario with no linear control stiffness, the system experiences a benefit when the nonlinear stiffness potential energy is less than twice the average potential energy of the incident wave. However, the overall time-averaged power is small compared to the scenario in which an optimal linear control stiffness is included. If optimal control parameters are used in either floating or submerged scenarios, for regular waves, the nonlinear stiffness monotonically reduces the time-averaged power and effectively detunes the system. The optimal linear control stiffness in the floating case is negative to counteract the significant hydrostatic stiffness. Therefore, in practice, the nonlinear stiffness may be used to generate the required negative stiffness about the operating position for significant benefit. For the submerged regular wave case, no benefit was observed as the optimal stiffness is positive because no hydrostatic stiffness is present.

In irregular waves, the nonlinear stiffness improved performance in the floating scenario with no linear control stiffness, and reduced the performance in the floating and submerged scenarios with optimised control parameters. However, as irregular waves vary over time and are stochastic in nature, the impact of the nonlinear stiffness was investigated for the situations in which the irregular wave parameters vary, and the phase between the components constituting the irregular wave was varied. It was shown that the nonlinear stiffness can improve the performance when the irregular wave parameters drift over time, and that this improvement is consistent for different irregular wave phase realisations, thereby improving the robustness of the system in ocean conditions. However, it should be noted that the standard deviation of the time-averaged power between all the realisations of the irregular waves is comparable to the improvement due to the nonlinear stiffness. Therefore, further investigation is needed to clarify the degree of improvement in higher fidelity contexts.

Acknowledgment

References

[1] J. Cruz. *Ocean Wave Energy*. 1st ed. Springer-Verlag Berlin Heidelberg, 2008. DOI: 10.1007/978-3-540-74895-3.

[2] B. Drew, A. R. Plummer, and M. N. Sahinkaya. "A review of wave energy converter technology". In: *Proceedings of the Institution of Mechanical Engineers, Part A: Journal of Power and Energy* 223.8 (2009), pp. 887–902. DOI: 10.1243/09576509JPE782. eprint: http://dx.doi.org/10.1243/09576509JPE782.

[3] R. L. Harne and K.-W. Wang. *Harnessing bistable structural dynamics: For vibration control, energy harvesting and sensing*. John Wiley & Sons, 2017.

[4] O. Abdelkhalik and S. Darani. "Optimization of nonlinear wave energy converters". In: *Ocean Engineering* 162 (Aug. 2018), pp. 187–195. DOI: 10.1016/j.oceaneng.2018.05.023.

[5] L. Wang, H. Tang, and Y. Wu. "On a submerged wave energy converter with snap-through power take-off". In: *Applied Ocean Research* 80 (Nov. 2018), pp. 24–36. DOI: 10.1016/j.apor.2018.08.005.

[6] Z. Wu, C. Levi, and S. F. Estefen. "Wave energy harvesting using nonlinear stiffness system". In: *Applied Ocean Research* 74 (May 2018), pp. 102–116. DOI: 10.1016/j.apor.2018.02.009.

[7] D. Younesian and M.-R. Alam. "Multi-stable mechanisms for high-efficiency and broadband ocean wave energy harvesting". In: *Applied Energy* 197 (2017), pp. 292–302. DOI: http://dx.doi.org/10.1016/j.apenergy.2017.04.019.

[8] X.-T. Zhang, J.-M. Yang, and L.-F. Xiao. "An oscillating wave energy converter with nonlinear snap-through Power-Take-Off systems in regular waves". In: *China Ocean Engineering* 30.4 (July 2016), pp. 565–580. DOI: 10.1007/s13344-016-0035-5.

[9] X. Zhang et al. "Mechanism and sensitivity for broadband energy harvesting of an adaptive bistable point absorber wave energy converter". In: *Energy* 188 (Dec. 2019), p. 115984. DOI: 10.1016/j.energy.2019.115984.

[10] Z. Wu, C. Levi, and S. F. Estefen. "Practical considerations on nonlinear stiffness system for wave energy converter". In: *Applied Ocean Research* 92 (Nov. 2019), p. 101935. DOI: 10.1016/j.apor.2019.101935.

[11] X. Xiao, L. Xiao, and T. Peng. "Comparative study on power capture performance of oscillating-body wave energy converters with three novel power take-off systems". In: *Renewable Energy* 103 (Apr. 2017), pp. 94–105. DOI: 10.1016/j.renene.2016.11.030.

[12] H. Zhang et al. "Efficiency enhancement of a point wave energy converter with a magnetic bistable mechanism". In: *Energy* 181 (Aug. 2019), pp. 1152–1165. DOI: 10.1016/j.energy.2019.06.008.

[13] J. H. Todalshaug et al. "Tank testing of an inherently phase-controlled wave energy converter". In: *International Journal of Marine Energy* 15 (Sept. 2016), pp. 68–84. DOI: 10.1016/j.ijome.2016.04.007.

[14] J. Falnes. *Ocean waves and oscillating systems: Linear interactions including wave-energy extraction*. Cambridge University Press, 2002.

[15] B. W. Schubert et al. "Performance enhancement of submerged wave energy device using bistability". In: *Ocean Engineering* 213 (Oct. 2020), p. 107816. DOI: 10.1016/j.oceaneng.2020.107816.

[16] A. Babarit. *NEMOH user manual*. Ecole Centrale de Nantes. Jan. 2014.

[17] M. Penalba, G. Giorgi, and J. V. Ringwood. "Mathematical modelling of wave energy converters: A review of nonlinear approaches". In: *Renewable and Sustainable Energy Reviews* 78 (Oct. 2017), pp. 1188–1207. DOI: 10.1016/j.rser.2016.11.137.

[18] B. W. Schubert et al. "Linear and nonlinear hydrodynamic models for dynamics of a submerged point absorber wave energy converter". In: *Ocean Engineering* 197 (Feb. 2020), p. 106828. DOI: 10.1016/j.oceaneng.2019.106828.

[19] R. Ibrahim. "Recent advances in nonlinear passive vibration isolators". In: *Journal of Sound and Vibration* 314.3-5 (July 2008), pp. 371–452. DOI: 10.1016/j.jsv.2008.01.014.

[20] M. Penalba, T. Kelly, and J. V. Ringwood. "Using NEMOH for modelling wave energy converters: a comparative study with WAMIT". In: *Centre for Ocean Energy Research (COER), Maynooth University, Co. Kildare, Ireland* (2017).

[21] W. Cummins. *The impulse response function and ship motions*. Tech. rep. David Taylor Model Basin, Washington DC, 1962.

[22] T. Perez and T. I. Fossen. "A Matlab toolbox for parametric identification of radiation-force models of ships and offshore structures". In: *Modeling, Identification and Control: A Norwegian Research Bulletin* 30.1 (2009), pp. 1–15. DOI: 10.4173/mic.2009.1.1.

[23]   N. Sergiienko et al. "Feasibility study of the three-tether axisymmetric wave energy converter". In: *Ocean Engineering* 150 (Feb. 2018), pp. 221–233. DOI: 10.1016/j.oceaneng.2017.12.055.

[24]   R. Salmon. "Introduction to ocean waves". In: *Scripps Institution of Oceanography, University of California, San Diego* (2008).

[25]   C. Stansberg et al. "The specialist committee on waves final report and recommendations to the 23rd ITTC". In: *Proceedings of the 23rd ITTC* 2 (2002), pp. 505–551.

[26]   W. Sheng and H. Li. "A method for energy and resource assessment of waves in finite water depths". In: *Energies* 10.4 (Apr. 2017), p. 460. DOI: 10.3390/en10040460.

[27]   S. Gran. "A Course in Ocean Engineering (Developments in Marine Technology)". In: Elsevier Science Ltd, 1992. Chap. 2, pp. 187–199.

[28]   J. Falnes. "A review of wave-energy extraction". In: *Marine Structures* 20.4 (Oct. 2007), pp. 185–201. DOI: 10.1016/j.marstruc.2007.09.001.

[29]   N. Y. Sergiienko et al. "Performance comparison of the floating and fully submerged quasi-point absorber wave energy converters". In: *Renewable Energy* 108 (Aug. 2017), pp. 425–437. DOI: 10.1016/j.renene.2017.03.002.

[30]   N. Y. Sergiienko et al. "Three-tether axisymmetric wave energy converter: Estimation of energy delivery". In: *Proceedings of the 3rd Asian Wave and Tidal Energy Conference, Singapore*. 2016, pp. 163–171.

[31]   J. Hals, T. Bjarte-Larsson, and J. Falnes. "Optimum reactive control and control by latching of a wave-absorbing semisubmerged heaving sphere". In: *International Conference on Offshore Mechanics and Arctic Engineering*. Vol. 36142. 2002, pp. 415–423.

[32]   B. Ding et al. "Sea-state based maximum power point tracking damping control of a fully submerged oscillating buoy". In: *Ocean Engineering* 126 (Nov. 2016), pp. 299–312. DOI: http://dx.doi.org/10.1016/j.oceaneng.2016.09.020.

Chapter 5

Performance enhancement of submerged wave energy device using bistability

The potential benefits of a nonlinear stiffness mechanism was highlighted for both a floating and submerged spherical WEC in the previous chapter. This chapter further explores the application of a nonlinear stiffness mechanism to a submerged wave energy device. As the previous representation restricted the system to a single DOF, the cross coupling between each DOF was neglected. This may influence the benefit of a nonlinear stiffness mechanism. Therefore, to further assess the potential benefit of the proposed nonlinear passive control system, a more realistic buoy geometry is employed and the simulation is expanded to three DOF. This introduces more complex geometric nonlinearities multi-DOF coupling. The following chapter addresses the research question: *How do nonlinear stiffness mechanisms provide a performance enhancement in submerged wave energy devices if geometric nonlinearities are included?*

Additional analysis on the enhancement of a submerged WEC in terms of a passive phase matching property may be found in Appendix A. This auxiliary study demonstrates that bistability may be used to enhance non-optimally tuned systems by exciting multiple frequencies and matching the phase of the excitation force and velocity. However, bistability does not improve upon a system with an optimally tuned linear power take off.

This section consists of the published journal article:
Schubert, B.W., Robertson, W.S., Cazzolato, B.S., Ghayesh, M.H. and Sergiienko, N.Y., 2020. Performance enhancement of submerged wave energy device using bistability. *Ocean Engineering*, **213, p.107816.**

The article in its published format is available at `https://doi.org/10.1016/j.oceaneng.2020.107816`.

Statement of Authorship

Title of Paper	Performance enhancement of submerged wave energy device using bistability
Publication Status	☑ Published ☐ Accepted for Publication ☐ Submitted for Publication ☐ Unpublished and Unsubmitted work written in manuscript style
Publication Details	Schubert, B.W., Robertson, W.S., Cazzolato, B.S., Ghayesh, M.H. and Sergiienko, N.Y., 2020. Performance enhancement of submerged wave energy device using bistability. Ocean Engineering, 213, p.107816.

Principal Author

Name of Principal Author (Candidate)	Benjamin Schubert

Contribution to the Paper	Developed ideas and concepts • Conducted a comprehensive literature review • Outlined the concepts of the paper to address the gaps in literature based on knowledge of the field Performed the modelling • Developed a model of a spherical buoy to estimate the hydrodynamic parameters using the potential flow solver NEMOH • Developed a simulation in Simulink to predict the dynamic behaviour of a CETO-shaped wave energy converter for regular and irregular waves • Conducted an analysis of varying natural frequencies in each degree of freedom • Optimised control parameters for the relevant contexts • Parameterised nonlinear stiffness force and implemented into dynamic model • Developed the framework to vary the linear and nonlinear control parameters and excitation waves in model Interpreted results • Collected and stored data from simulation results • Post processed the data using Matlab • Performed spectral analysis of time domain results • Interpreted results between different scenarios • Compared the results of simulations with the analysis of the natural frequencies of different degrees of freedom Writing • Solely developed the first full draft of the manuscript • Applied comments provided by all co-authors • Acted as corresponding author. • Responsible for revising the manuscript after review
Overall percentage (%)	80%
Certification:	This paper reports on original research I conducted during the period of my Higher Degree by Research candidature and is not subject to any obligations or contractual agreements with a third party that would constrain its inclusion in this thesis. I am the primary author of this paper.

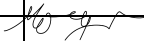| Signature		Date	2/2/2021
	✔		

Co-Author Contributions

By signing the Statement of Authorship, each author certifies that:

 i. the candidate's stated contribution to the publication is accurate (as detailed above);

 ii. permission is granted for the candidate in include the publication in the thesis; and

 iii. the sum of all co-author contributions is equal to 100% less the candidate's stated contribution.

Name of Co-Author	William Robertson		
Contribution to the Paper	Participated in developing the ideas and concepts, assisted in analysing and interpreting the obtained results, and provided revision of manuscript. Provided expertise and advice on the magnetic concepts and code employed in the development of this manuscript.		
Signature		Date	15/02/2021

Name of Co-Author	Benjamin Cazzolato		
Contribution to the Paper	Participated in developing the ideas and concepts, assisted in analysing and interpreting the obtained results, and provided revision of manuscript. Provided critical understanding of signal processing techniques employed in the development of this manuscript.		
Signature		Date	15/02/2021

Name of Co-Author	Mergen Ghayesh		
Contribution to the Paper	Participated in developing the ideas and concepts, assisted in analysing and interpreting the obtained results, and provided revision of manuscript.		
Signature		Date	18/02/2021

Name of Co-Author	Nataliia Sergiienko		
Contribution to the Paper	Participated in developing the ideas and concepts, assisted in analysing and interpreting the obtained results, and provided revision of manuscript. Provided a code template related to using the linear hydrodynamics tool NEMOH.		
Signature		Date	15/02/2021

Please cut and paste additional co-author panels here as required.

Performance enhancement of submerged wave energy device using bistability

B. W. Schubert, W. S. P. Robertson, B. S. Cazzolato, M. H. Ghayesh, N. Y. Sergiienko

Abstract

The performance of a submerged cylindrical point absorbing wave energy converter was explored under the addition of different nonlinear stiffness (bistable) conditions. The limitations of previous studies were addressed by incorporating higher-fidelity modelling. Devices employing bistability in other energy harvesting applications, have improved the amount of power generated. For wave energy converters, most theoretical models with bistability were limited to one-degree-of-freedom, neglect nonlinearities such as viscous drag, and are excited by unrealistic sinusoidal waves. Such simplifications lead to neglecting features such as modal interactions. The presented model investigated a three-degree-of-freedom submerged point absorber with bistability subjected to regular and irregular waves. The bistable mechanism was an adjustable magnetic model such that a range of potential profiles were examined and parameterised, for generality, by features common between mechanisms. For this device, bistability may be used to obtain near optimal results and was suitably robust for changing ocean conditions. Regions of improvement were identified in terms of the changing natural frequency due to a nonlinear stiffness, and a phase matching property. In varying sea-states, a selected bistable condition demonstrated a **10–20**% improvement in power production. The consistency implies that semi-active elements may be able to adjust the bistability to enhance power production.

5.1 Introduction

Ocean wave energy generation has been the subject of over two centuries of research [1]. Typical wave energy converters (WEC) can be broadly classed as one of three types: an attenuator; a point absorber (PA); or a terminator [2]. There are other significant devices which are difficult to categorise into these classes such as oscillating water columns or overtopping devices. However, this paper focuses on a PA type WEC, which are systems in which the buoy is small relative to the wavelengths of incident waves, and, for a single PA, is subsequently relatively insensitive to wave direction. A representative diagram of the simplified CETO PA [3] used in this study is shown in Fig. 5.1. Whilst smaller than typical wavelengths, the CETO is one of the large PAs, and therefore is more accurately described as a quasi-PA. For the purposes of this paper, the CETO device will be referred

to as a PA. While the simple operation of a generic PA WEC is well known, there remains many challenges for wave energy [4]. Due to the complexity of these unique challenges in the context of wave energy, the technology as a whole remains at a low technology readiness level.
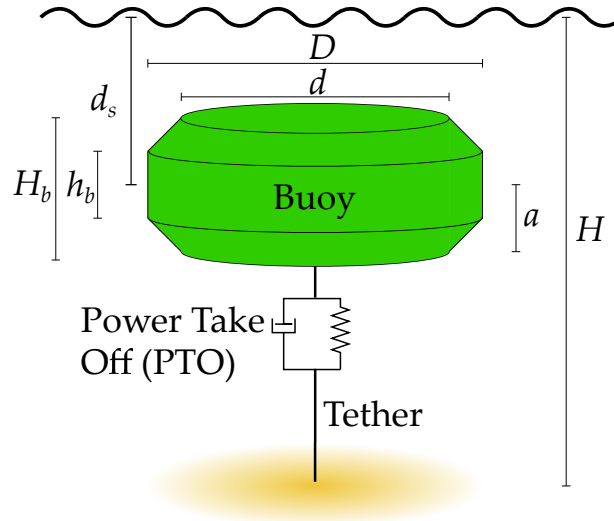

Figure 5.1: A schematic of a CETO-shaped buoy used in all simulated scenarios. A depiction of a number of geometric quantities is presented, with the definitions and values for the presented model provided in Table 5.1.

One of the areas which remains an actively studies topic is the methodology behind controlling PA devices. Hybrid control, in which passively applied dynamics supplement an active controller, may provide some advantages over active control algorithms [5]. Bistable mechanisms using nonlinear stiffness have received notable attention over the past few years. A generic bistable system is given in Fig. 5.2. For further clarity specific to wave energy, a characteristic time history of the WEC operating at low, medium, and high levels of bistability in terms of the central potential barrier is shown in Fig. 5.3, and the corresponding frequency domain displacement and generated power amplitudes are provided in Fig. 5.4. These figures simply show how increasing levels of bistability changes the resulting motion and power generation. That is, higher levels of bistability tends to force the WEC to oscillate about two different stable regions and leads to an increase in the bandwidth of power generated, while decreasing the peak performance. This finding is, in general, consistent with many bistable or nonlinear dynamics, that nonlinear systems may be very sensitive to small changes in system parameters — particularly parameters responsible for transitions between linear and nonlinear regimes.

Substantial benefits have been observed when using a bistable mechanism within the power take off unit (PTO) with simple single degree of freedom (DOF) simulation models
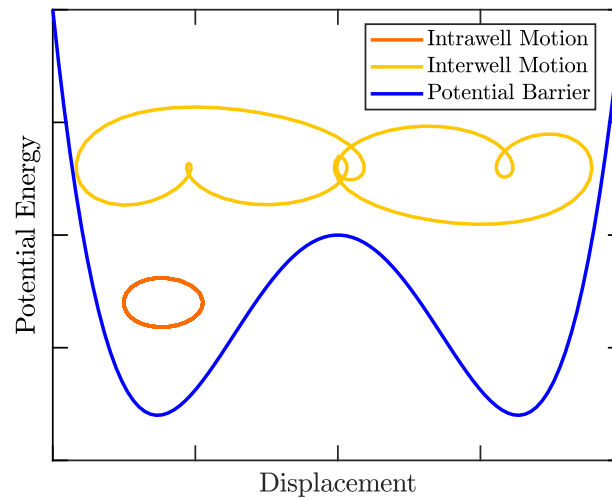
Figure 5.2: An example bistable double well potential energy barrier and motion.

[5–9]. There have been some attempts to optimise a nonlinear reactive force for power production [10], however no method of implementing this force profile was provided. Methods using an asymmetric mass distribution to emulate a nonlinear effective stiffness have also been proposed [11, 12]. A model using a bistable mechanism composed of magnets [8] found that a bistable WEC can harvest more energy than a linear WEC when the excitation frequency is less than the natural frequency of the linear system. Another magnetic design composed of coaxial cylinders concluded that bistablilty can enhance the efficiency of a floating WEC [13]. However, this study was restricted to a single DOF and used a linear stiffness only valid for small oscillations. Though the damping in the system was optimised, the linear stiffness was not. The addition of bistability in this case did show significant improvement on the suboptimised system.

Experimental investigations using different devices showed that the realistic benefit of bistability is significant and in some cases may be as much as a three times power increase due to phase matching [14, 15]. Since the geometries and general operation of WEC devices and mechanisms differ signficantly, bistability is employed in various ways to either excite super harmonics to convert low frequency oscillations into high frequency oscillations [16], or to provide passive phase matching for a floating PA WEC [15].

Conventional PAs are designed to be floating rather than submerged. Accordingly, there has been more research into floating systems than submerged systems. While both systems may seem similar, they undergo funadmentally different excitation and forces. As a result, submerged PAs typically generate lower levels of power at longer wavelengths, have reduced bandwidths, but more readily capture power from multiple DOF when compared to floating systems [17]. In particular, there is limited work in
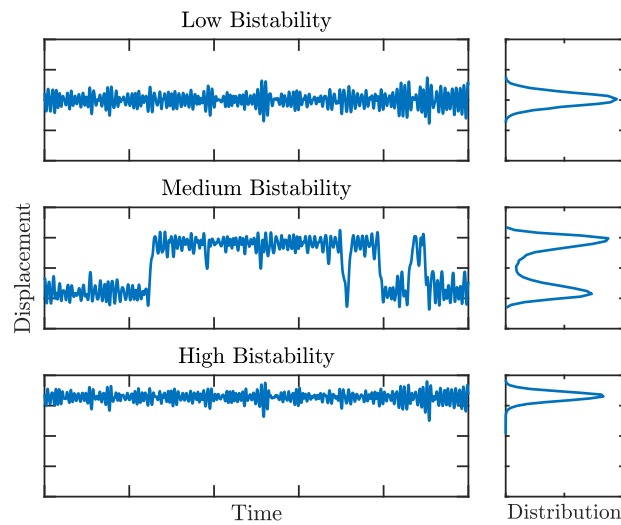
Figure 5.3: The time history of a WEC subjected to low, medium, and high central potential energy barrier bistable conditions. As the bistable levels increase, the motion indicates that the WEC is oscillating about two stable regions and occasionally "snaps through" to the other stable region by overcoming a central unstable region. The corresponding displacement distributions show the regions in which the WEC typically operates for each bistable condition. This illustrative data has been generated from the models presented in this study.

taking into account nonlinearity in stiffness in the theoretical modelling of a submerged WEC [18], and such work is related to a device that does not operate in the vertical heave direction. In addition to restricted DOFs, many of the models previously employed do not include drag. A study of a submerged WEC compares the effect of bistability in 1-DOF and 3-DOF which includes drag [19]. The study concluded that for regular waves, an improvement is only seen under certain circumstances when the device is non-optimally tuned. The study was limited to regular wave scenarios, and was primarily directed at observing if there was potential for any benefit but did not attempt to explore the cause of the benefit.

There have been numerous ideas proposed for the mechanism to provide a bistable force including mechanical springs [20], magnetic systems [8], and pneumatic systems [15]. Each of these suggestions provide unique benefits. Generally, electromagnetic reactive mechanisms in the form of direct drive systems can be expected to have smaller reactive power losses compared to alternatives such as hydraulic systems [21]. How a submerged PA WEC subject to irregular waves behaves when bistability is included, and what bistable attributes are beneficial within the context of submerged WEC, remains a gap within current literature.

In this paper, the limitation of previous studies will be addressed by incorporating
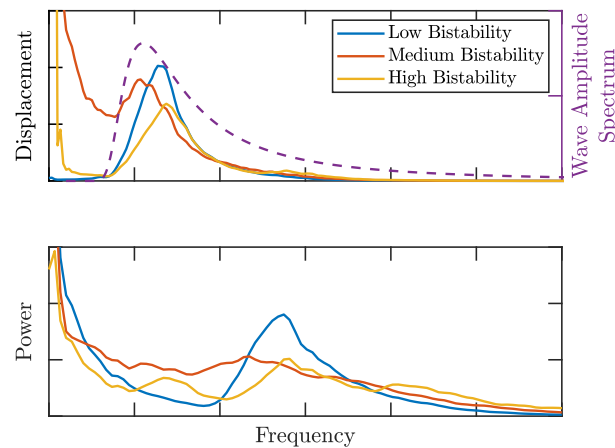
Figure 5.4: The frequency domain displacement (top) and generated power (bottom) amplitudes. The wave amplitude spectrum is also shown as a dashed line to indicate the type of excitation. These distributions show that increasing bistability often significantly alters the resulting motion spectra by reducing and shifting peaks, and broadening bandwidths. This illustrative data has been generated from the models presented in this study in order to illustrate how bistability may impact the displacement and power distributions, generally rather than quantitatively, hence no units have been included.

higher-fidelity system modelling including nonlinear coupling between the dynamic degrees of freedom. In particular, the following features differentiate the current work and contribute to the enhanced fidelity:

1. The 1-DOF model used by prior authors with relatively simple dynamics has been extended to 3 DOF to allow for coupling between DOF.

2. A drag coefficient has been included to improve the estimation of velocity dependent forces acting on the buoy and consequently preventing unrealistically large amplitudes of motion.

3. The regular wave excitation has been extended to irregular waves to better estimate the buoy performance under a more realistic broadband excitation.

4. Systems with bistability are often compared to poorly tuned monostable counterparts in the aforementioned studies. Such an assumption can lead to systems with nonlinear stiffnesses showing better performance, but could be further improved by careful selection of a linear stiffness. This study analyses both regular and irregular results with respect to the well tuned monostable counterparts to understand the real potential for improvement.

The combination of both the improved dynamic model and the broader range of simulation conditions furthers the current understanding of the applicability of bistability to submerged point absorbing WECs.

The impact of bistable control on a submerged 3-DOF PA WEC was explored to quantify how simple hydrodynamics and the passive control system interact. A 3-DOF theoretical model of the CETO device being developed by Carnegie Clean Energy [3] was constructed. The model was subjected to a set of regular waves and three different irregular waves (or sea states). A nonlinear stiffness mechanism was included and varied to understand what characteristics are important for power production capability. The mathematical models are described in Section 5.2, with the representation of the magnetic bistable mechanism given in Section 5.2.1.4, as well as a dimensionless parameter pertinent to any bistable system as a means to generalise results. The considerations and limitations of the used modelling method are outlined in Section 5.3, and the results of these simulations are presented and discussed in Section 5.4, with a summary of the findings in Section 5.5.

5.2   Mathematical models

The governing equation for both regular and irregular scenarios can be derived from the contributing forces represented in the equation

$$
\mathbf{M}\ddot{\mathbf{x}}(t) = \mathbf{F}_{\mathrm{e}}(\mathbf{x}, t) + \mathbf{F}_{\mathrm{r}}(\ddot{\mathbf{x}}, \dot{\mathbf{x}}, t) + \mathbf{F}_{\mathrm{h}} + \mathbf{F}_{\mathrm{PTO}}(\dot{\mathbf{x}}, \mathbf{x}, t)
$$
$$
+ \mathbf{F}_{\mathrm{D}}(\dot{\mathbf{x}}, \mathbf{x}, t) + \mathbf{F}_{\mathrm{bi}}(\mathbf{x}, t) \, ,
$$

(5.1)

where the inertia of each DOF of the system is represented by the matrix $\mathbf{M}$, and $\mathbf{x}$ is the position vector containing the surge (x), heave (z), and pitch (θ) coordinates. Also, $\mathbf{F}$ represents a 3-DOF force vector and the subscripts e, r, h, PTO, D, and bi indicate the excitation, radiation, hydrostatic, PTO, drag, and bistable forces, respectively. The time is represented by t, and the dependencies of each force denoted in Equation (5.1) are considered implicit in subsequent equations for succinct notation. This equation forms the basis of the governing equations for all three models presented with constituting force components either simplified or represented differently.

5.2.1   Regular waves

When subjected to a single monochromatic wave, the forces in Equation (5.1) may be quantified in the time domain through the following approaches.

5.2.1.1   Excitation force

The excitation force, $\mathbf{F}_{\mathrm{e}}$, is the superposition of the Froude-Krylov and diffraction forces and can be calculated using linear potential flow theory. This force may be considered as

the force on the buoy due to incoming waves. In the work presented here the boundary element method (BEM) solver NEMOH [22], which numerically calculates various hydrodynamic quantities using linear potential flow theory, was used to calculate the amplitude ($|\mathbf{F}_e|$) and phase ($\boldsymbol{\phi}$) of the excitation force relative to the incident wave in all 3-DOF within a range of frequencies, and can be represented in vector form as [23]

$$\mathbf{F}_e = |\mathbf{F}_e| \circ \cos(\boldsymbol{\phi} + \phi_s - \omega t) , \qquad (5.2)$$

where ω represent the excitation frequency. The Hadamard product operator, $\circ$, is used to indicate element-wise multiplication. The additional surge phase offset applied to each DOF, ϕ_s, represents the phase difference due to the horizontal position of the buoy relative to the incoming wave. This phase difference may be quantified by

$$\phi_s = kx , \qquad (5.3)$$

where k is the wavenumber, which is the solution to the dispersion relationship [24]

$$\omega^2 = gk \tanh(kH) , \qquad (5.4)$$

where the depth of the water is represented by H and the acceleration due to gravity is represented by g.

5.2.1.2 Radiation force

The radiation force may be considered as the force on the buoy due to the waves radiating when the buoy moves. This force is represented in the time domain by the Cummins equation [25],

$$\mathbf{F}_r = -\mathbf{A}_\infty \ddot{\mathbf{x}} - \int_0^t \mathbf{K}(t - t')\dot{\mathbf{x}}(t')dt' , \qquad (5.5)$$

where $\mathbf{A}_\infty$ and $\mathbf{K}$ are termed the infinite frequency added mass and the memory function, respectively. The convolution integral quantifies the influence of the previous state on the current state. In practice, this integral may be computationally expensive for active control and real time implementation, thus an alternative approach is more commonly implemented. The frequency domain representation (represented by the ˆ symbol) of the radiation force is [26]

$$\hat{\mathbf{F}}_r = -[\mathbf{B}(\omega) + i\omega\mathbf{A}(\omega)]\hat{\mathbf{x}}(i\omega), \qquad (5.6)$$

where $\mathbf{B}(\omega)$ is the frequency-dependent radiation damping and $\mathbf{A}(\omega)$ is the added mass. These hydrodynamic quantities are also able to be calculated using NEMOH and other BEM solvers. A transfer function relating the velocity to the value of the integral in Equation (5.5) may be constructed using these two hydrodynamic quantities [26]. In general, the radiation forces experienced in each DOF may be influenced by

motion in other DOFs and by geometry. Accordingly, transfer functions between all velocity components and all convolution integral components may be constructed and combined into a single state space model to account for interaction between different DOFs. Under the linear BEM theory used by NEMOH, for an axisymmetric device in a nominal horizontal position, the radiation force in the heave direction is independent of motion in the surge or pitch directions. However, the radiation forces in the surge and pitch directions are coupled. Therefore, in general the contribution of the convolution integral in each DOF, μ, which is effectively the fluid memory, may be described as

$$\dot{\mathbf{p}} = \mathbf{A}_{ss}\mathbf{p} + \mathbf{B}_{ss}\dot{\mathbf{x}} \, ,$$
$$\mu = \mathbf{C}_{ss}\mathbf{p} \, , \tag{5.7}$$

where $\mathbf{p}$ is a state vector of non-physical variables, and $\mathbf{A}_{ss}$, $\mathbf{B}_{ss}$, and $\mathbf{C}_{ss}$ are state space matrices constructed from the aforementioned transfer functions and are provided in Appendix 5.B. The memory function, or impulse response function, can be represented as [27]

$$\mathbf{K}(t) = \frac{2}{\pi} \int_0^\infty \mathbf{B}(\omega) \cos(\omega t) d\omega \, . \tag{5.8}$$

which may be split into a finite and an infinite integral which may be solved numerically and analytically, respectively [27]. Further details and reasoning may be found in the literature sources provided. Through comparison over an appropriate range of frequencies, it was found that the state space representation results with an error of less than 2%, thereby adequately representing the integral term shown in Equation (5.5). The direct evaluation is more computationally demanding than the state space representation and both methods give similar results. Therefore, the state space representation was used in this study.

5.2.1.3 Hydrostatic and PTO forces

The hydrostatic (or buoyancy) force acts only in the heave direction and is the difference between the weight of displaced water and the weight of the buoy, given by

$$F_{h,z} = \rho g V - mg \, , \tag{5.9}$$

where ρ, m, and V are the density of water, buoy mass, and buoy volume, respectively. For a fully submerged buoy, this force is constant. Accordingly, a pretension force, F_p, equal in magnitude to the hydrostatic force is included in the PTO force, in addition to a stiffness and damping term as follows

$$|\mathbf{F}_{PTO}| = -b\Delta\dot{l} - k_s\Delta l - F_p \, . \tag{5.10}$$

In Equation (5.10), b is the damping coefficient, k_s is the spring constant, and Δl is the extension of the tether. This defines the submerged nominal position to be $\Delta l = 0$. The

PTO force is quantified in terms of the tether motions and acts in the direction of the tether extension. In order to relate the tether motions to the surge, heave, and pitch coordinates, the relationship between (x, z, θ) and $(\Delta l, \alpha, \phi)$, with both sets of coordinates represented in Fig. 5.5, is

$$\Delta l = \sqrt{(x - a\sin\theta)^2 + (z + l + a - a\cos\theta)^2} - l \,,$$

$$\alpha = \arctan\left(\frac{x - a\sin\theta}{z + l + a - a\cos\theta}\right) \,, \qquad (5.11)$$

$$\phi = \theta - \alpha \,,$$

where a and l are the distance between buoy center and tether attachment point, and the total tether length, respectively.
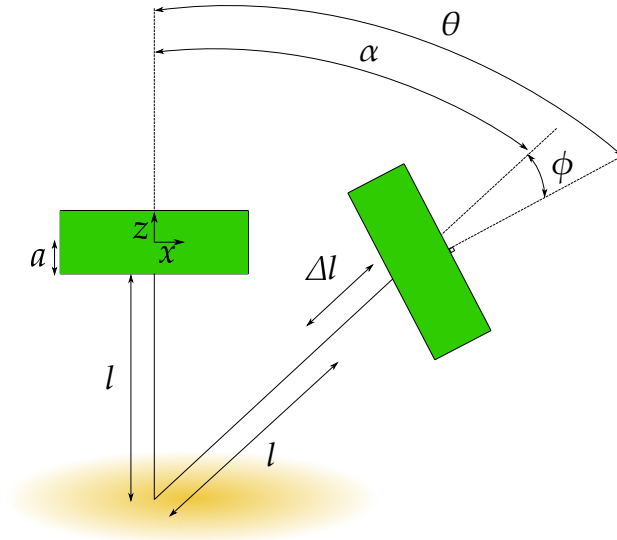
Figure 5.5: A diagram depicting the variables of two coordinate systems: $[x, z, \theta]$ and $[\Delta l, \alpha, \phi]$.

Both the damping coefficient and spring constant may be optimised for a given frequency. The optimal values may be derived [28] and for a heaving PA in a linear hydrodynamic regime are defined to be

$$b_{\text{opt}} = B_z(\omega) \,, \qquad k_{s,\text{opt}} = \omega^2(m + A_z(\omega)) \,, \qquad (5.12)$$

where the subscript z denotes the heave component. For a 3-DOF system subjected to regular wave scenarios, the optimal PTO stiffness may be found approximately by using Equation (5.12) as an initial estimate, and adjusting k_s until the time-averaged power is at a local maximum. The PTO damping was found using the same method as the

optimal stiffness, using Matlab's constrained nonlinear minimisation function (fmincon) using an interior point algorithm to optimise for power. In the 3-DOF scenarios for single tether WECs, heave is often considered the most influential DOF related to power production. The instantaneous power generated by the WEC is approximated by

$$P_{\text{inst}}(t) = b\Delta\dot{l}^2(t) \, . \tag{5.13}$$

The power performance of the device may therefore be represented by the time-averaged power, given by

$$\overline{P}_{\text{avg}} = \frac{1}{T} \sum_{j=t_i}^{j=t_f} P_{\text{inst},j}\Delta t_j \, , \tag{5.14}$$

where t_i, t_f, Δt_j, and T are the initial time, final time, the jth time step, and the total time interval, respectively. These initial and final times are chosen to discard any transient effects. This metric may be used to quantify the impact of bistable additions on the overall power production.

5.2.1.4 Force inducing bistability

A force which can lead to a bistable scenario, such as a magnetic force, may induce a two well potential energy barrier, as depicted on Fig. 5.2. Such systems exhibit unique dynamic features not seen in systems with only a single potential well. These features include two single period steady state responses for a given excitation frequency due to the bifurcation of responses, a large dependence on initial conditions and excitation amplitudes, stochastic resonances (resonating using a combination of low amplitude inputs), and the excitation of input frequency harmonics [29]. In this context, some form of stochastic resonance is expected if the bistable parameters are selected appropriately. This is primarily a result of real ocean waves been stochastic in nature. However, for this system, it is uncertain whether the phenomenon of stochastic resonance will actually provide a benefit. The inclusion of all these features may lead to broader resonance bandwidths particularly at lower frequencies, frequency up-conversion which turns low frequency oscillations into higher frequency oscillations, and performance improvement in stochastic excitation contexts. The main benefit of bistability is thought to occur during *inter*well motion rather than *intra*well due to the snap-through property [9]. In this case, this snap-through mechanism forms an avenue for low amplitude oscillations to change into large amplitude oscillations if the excitation is sufficient to overcome the dividing potential barrier [29]. The escape from a potential well can broaden the frequency range of a generator [30]. While each of these characteristic features may be exploited for different applications, bistable wave energy systems may be well suited given the low frequency and stochastic nature of ocean waves.

For the purposes of this study, a magnetic dipole model was used to create a bistable system. A depiction of the WEC PTO model with bistability is given in Fig. 5.6. The
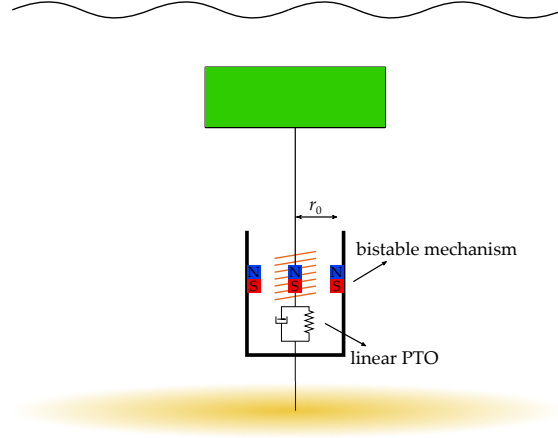

Figure 5.6: An example WEC with a magnetic bistable mechanism within the PTO. The blue and red symbolise the poles of a magnetic spring.

potential energy between two magnetic dipoles, in this case between the stationary outer dipole and the dipole within the translator, may be derived from [31]

$$U_{\text{bi}} = -\mathbf{m}_{\text{d},1} \cdot \mathbf{B}_{\text{d},2} = -\mathbf{m}_{\text{d},2} \cdot \mathbf{B}_{\text{d},1} \,, \tag{5.15}$$

where $\mathbf{m}_{\text{d},1}$ is the dipole moment of the first dipole, $\mathbf{B}_{\text{d},2}$ is the magnetic field of the second dipole at the location of the first dipole, and $\cdot$ represents the dot product. The same potential energy exists if deriving the potential energy of the other dipole. The force between the two magnets may then be defined as [31]

$$\mathbf{F}_{\text{bi}} = -\nabla U_{\text{bi}} = \nabla (\mathbf{m}_{\text{d},1} \cdot \mathbf{B}_{\text{d},2}) \,. \tag{5.16}$$

Assuming magnetisation in the vertical direction at nominal position, the dipole moments are given by

$$\mathbf{m}_{\text{d}} = (0, 0, V_{\text{m}} M) \,, \tag{5.17}$$

where V_{m} is the volume of the magnet, and M is the magnetisation field per unit volume. The magnetic field for a dipole is given by

$$\mathbf{B}_{\text{d},2} = -\frac{\mu_0}{4\pi} \nabla \frac{\mathbf{m}_{\text{d},1} \cdot \mathbf{r}}{r^3} \,, \tag{5.18}$$

where $\mathbf{r}$ and r are the displacement and distance between the dipoles, respectively, and μ_0 is the permeability of free space [32]. Using Equations (5.16) and (5.18), the force between the two dipoles may be derived as

$$\mathbf{F}_{\text{bi}} = \frac{\mu_0 M_1 V_1 M_2 V_2}{4\pi} \left(\frac{9\Delta l}{(r_0^2 + \Delta l^2)^{\frac{5}{2}}} - \frac{15\Delta l^3}{(r_0^2 + \Delta l^2)^{\frac{7}{2}}} \right) \hat{\mathbf{l}} \,, \tag{5.19}$$

where r_0 is the horizontal distance between dipoles (as shown in Fig. 5.6) and $\hat{\mathbf{I}}$ is the unit vector in the direction of the tether extension. The subscripts $_1$ and $_2$ refer to the two magnetic poles. Similarly, the potential energy of this force can be derived as

$$U_{\text{bi}} = -\frac{\mu_0 M_1 V_1 M_2 V_2}{4\pi} \left(\frac{-1}{(r_0^2 + \Delta l^2)^{\frac{3}{2}}} + \frac{3\Delta l^2}{(r_0^2 + \Delta l^2)^{\frac{5}{2}}} \right) . \qquad (5.20)$$

The potential energy of the dipole representation superimposed with the potential energy from a linear stiffness, provides the intended bistable profile. Additional theoretical dipoles may be added by superposition to scale the central peak in potential energy. For the purposes of quantifying the magnetic potential energy and force, and to generalise the degree of bistability between any mechanism, the dimensionless parameter $\overline{\gamma}$ is proposed, which is the ratio of the average potential energy surface density from the incoming wave field, U_{wave}, and the potential energy of the bistable system at the nominal position, $U_{\text{bi},z=0}$, that is

$$\overline{\gamma} = \frac{U_{\text{bi},z=0}}{U_{\text{wave}}} . \qquad (5.21)$$

For a regular wave, the time-averaged potential energy per unit area, $\hat{U}_{\text{wave}}$, may be expressed as [33]

$$\hat{U}_{\text{wave}} = \frac{1}{4}\rho g A^2 , \qquad (5.22)$$

where A is the amplitude of the incoming wave. The parameter $\overline{\gamma}$ may be varied to define the height of the central potential peak in the potential well, represented in Fig. 5.7a. In addition, the location of the stable regions can also be varied, in this case by the changing the horizontal distance between dipole r_0 while keeping $\overline{\gamma}$ constant. The impact of changing r_0 on the potential wells is given in Fig. 5.7b. Varying these parameters gave a large range of possible force and potential profiles which were used to build an understanding around which bistable conditions are favourable for the ocean wave energy context. It was found that trends were more clearly visualised when $\overline{\gamma}$ is scaled by r_0^2, therefore the scaled dimensionless parameter γ is defined as

$$\gamma = \frac{\overline{\gamma}}{r_0^2} , \qquad (5.23)$$

which represents the potential energy of the buoy normalised by the potential energy of the upstream wave over an equivalent projected area.

5.2.1.5 Drag force

The viscous drag force is a nonlinear force often neglected in simple models given by

$$\mathbf{F}_{\text{D}} = -\frac{1}{2}\rho \mathbf{C}_{\text{D}} \circ \mathbf{A}_{\text{D}} \circ \text{sign}(\dot{\mathbf{x}}_{\text{r}}) \circ \dot{\mathbf{x}}_{\text{r}} \circ \dot{\mathbf{x}}_{\text{r}} , \qquad (5.24)$$
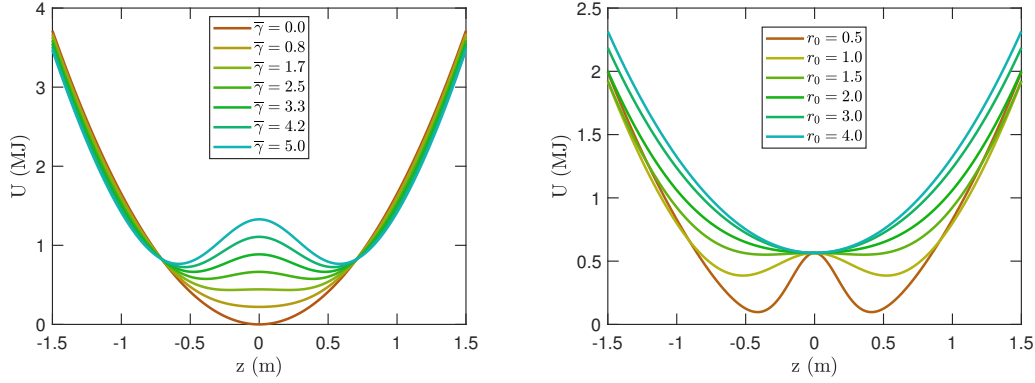
(a) The impact of $\overline{\gamma}$ variations for $r_0 = 1$m.

(b) The impact of r_0 variations for $\overline{\gamma} = 4$.

Figure 5.7: Examples of how varying the bistable parameters may change the potential energy profile of the system.

where $\mathbf{C}_D$, $\mathbf{A}_D$, and $\dot{\mathbf{x}}_r$ are the 3-DOF coefficients of drag, characteristic area, and relative velocity of the buoy with respect to the surrounding fluid, respectively. As an approximation, the instantaneous fluid velocity at the geometric center of the buoy was used. This assumption is made with the understanding that PAs are typically small compared to the wavelength of the incident wave. By assuming a linear wave, the fluid velocity in the heave and surge directions may be estimated as

$$
\begin{aligned}
\dot{x}_f &= A\omega \frac{\cosh(k(H + z - d_s))}{\sinh(kH)} \cos(kx - \omega t) \\
\dot{z}_f &= A\omega \frac{\sinh(k(H + z - d_s))}{\sinh(kH)} \sin(kx - \omega t) \,,
\end{aligned}
\tag{5.25}
$$

where d_s is the submergence depth of the geometric center of the buoy.

Combining these descriptions of forces into Equation (5.1) gives the model of a 3-DOF submerged PA WEC. Further descriptions and model specifics may be found in Section 5.3.

5.2.2 Irregular waves

As an extension to the 3-DOF model, irregular waves, which are more representative of real ocean waves, may be used. Irregular waves may be considered the superposition of many regular waves of different frequencies and are categorised by a spectrum. Various methods of calculating wave spectra exist such as the JONSWAP or Pierson-Moskowitz spectra. For the purpose of this study, and for simplicity, the method used is the JONSWAP wave spectrum, $S(\omega)$, given by [33]

$$
S(\omega) = \frac{\alpha_s g^2}{\omega^5} \exp\left(-\frac{5}{4}\left(\frac{\omega_p}{\omega}\right)^4 \right) \Gamma^R \,,
\tag{5.26}
$$

103

where α_s and ω_p are the slope parameter and peak frequency, respectively. The R term is given by

$$R = \exp\left(-\frac{1}{2\sigma^2}\left(\frac{\omega}{\omega_p} - 1\right)^2\right), \tag{5.27}$$

where σ is a measure of peak width and is 0.07 when $\omega < \omega_p$ and 0.09 when $\omega < \omega_p$. Two important parameters which may be used to describe an irregular wave are the significant wave height, H_s, and the average zero-crossing wave period, T_z. The slope parameter may be approximated by

$$\alpha = \frac{\pi^3 Hs^2}{g^2 Tz^4}, \tag{5.28}$$

and the peak-enhancement factor, Γ, can be approximated by

$$\Gamma = 7(1 - 2.18 \times 10^{-5})\frac{g^2 T_z}{H_s^2}. \tag{5.29}$$

Once the spectrum is known, a time series of the wave elevation may be produced. This time series is the superposition of individual frequency waves, with amplitudes related to the specified wave spectrum. Regular wave elevation, η_{reg}, is represented as

$$\eta_{\text{reg}}(t) = A\cos(-\omega t), \tag{5.30}$$

whereas the irregular wave elevation, η_{irr}, is given by

$$\eta_{\text{irr}}(t) = \sum_{j=1}^{N} \sqrt{2S(\omega_j)\Delta\omega_j}\cos(-\omega_j t + \epsilon_j), \tag{5.31}$$

where ϵ_i is a randomly generated phase offset for each discrete frequency in the spectrum and N is the number of discrete frequencies [34].

5.2.2.1 Excitation force

The excitation force for irregular waves can be calculated [35] using Equation (5.31) and extending Equation (5.2) giving

$$\mathbf{F}_e(t) = \sum_{j=1}^{N} \sqrt{2S(\omega_j)\Delta\omega_j}|\mathbf{F}_{e,j}| \circ \cos(\boldsymbol{\phi} - \omega_j t + \phi_s + \epsilon_j). \tag{5.32}$$

5.2.2.2 PTO force

As an irregular wave has many frequencies, the frequency for which the PTO is tuned using Equation (5.12) is the energy frequency which may be calculated using the following equations [36]

$$f_e = \frac{1}{T_e}, \tag{5.33}$$

where T_e is the energy period, calculated by

$$T_e = 2\pi \frac{m_{-1}}{m_0} \, , \tag{5.34}$$

where m_n is the spectral moment defined as

$$m_n = \int_0^\infty S(\omega)\omega^n d\omega \, . \tag{5.35}$$

5.2.2.3 Drag force

The drag force for the irregular scenario has the same form as Equation (5.24), however the relative fluid velocities are calculated slightly differently. For linear wave theory, superposition may be used to give

$$
\begin{aligned}
\dot{x}_f &= \sum_{j=1}^{N} A_j \omega_j \frac{\cosh(k_j(H + z - d_s))}{\sinh(k_j H)} \cos(k_j x - \omega_j t + \epsilon_j) \\
\dot{z}_f &= \sum_{j=1}^{N} A_j \omega_j \frac{\sinh(k_j(H + z - d_s))}{\sinh(k_j H)} \sin(k_j x - \omega_j t + \epsilon_j) \, ,
\end{aligned}
\tag{5.36}
$$

which provides a method to estimate the fluid velocity at the center of the buoy to be used in the calculation of the drag force.

5.2.2.4 Potential energy

The time-averaged potential energy of the wave, U_{wave}, is a metric used in Equation (5.21) to classify the degree of bistability. For an irregular wave, the time-averaged potential energy per unit area may be expressed as [33]

$$\hat{U}_{\text{wave}} = \frac{1}{4}\rho g \sum_{j=1}^{N} A_j{}^2 = \frac{1}{2}\rho g \sum_{j=1}^{N} S(\omega_j)\Delta\omega \, . \tag{5.37}$$

To calculate the time-averaged potential energy for a given buoy, $\hat{U}_{\text{wave}}$ may be multiplied by the horizontal cross-sectional area of the buoy.

5.3 Simulation considerations

For each simulation, there were an number of considerations and parameters specific to each scenario. These considerations and parameters will be provided in this section. In the regular wave simulations, the WEC system was excited by a series of monochromatic

waves and the resulting dynamic behaviour was analysed for each frequency to quantify motion and power performance. For each frequency, the optimal stiffness found through a local optimisation search was used in initial regular wave simulations. To test the impact of bistability on poorly tuned conditions, the optimal stiffness for a single frequency was used in an additional set of regular wave simulations. Each individual regular wave simulation was relatively fast — taking approximately 10 seconds.

For the irregular scenario, the WEC was excited by an irregular wave with locally optimised PTO settings. The bistable parameters γ and r_0 were varied to explore the impact on power production. The same simulations were run using the sub-optimal PTO settings found from Equations (5.12) and (5.33) to explore the sensitivity to tuning. The mechanisms of any improvements seen were explored through the phase relationship between the excitation force and tether velocity, as well as the stiffness potential energy profiles. The robustness of the bistable control system was tested by subjecting the WEC with a sub-optimal PTO setting to a different irregular wave. Then to establish if any trends were present, two more irregular wave spectra were simulated using the corresponding sub-optimal PTO settings for each respective wave. The irregular wave scenarios were more challenging to simulate due to the long simulation times required to get reliable time averaged results, and the multitude of frequencies involved. Depending on the case, an individual simulation could take approximately 10-15 minutes. The model dimensions and scenario conditions are outlined below.

5.3.1   Model dimensions

The geometry of the buoy was selected to be similar to the CETO design developed by Carnegie Clean Energy [3]. The diagram in Fig. 5.1 details various relevant physical quantities. These physical quantities as well as some general quantities used in the simulations are listed in Table 5.1. The drag properties for a buoy of this shape were sourced from literature [37] and are given in Table 5.2.

5.3.2   Scenario conditions

The parameters pertinent to the regular and irregular scenarios are detailed in Tables 5.3 and 5.4, respectively. The optimal PTO conditions for the irregular waves are only provided for scenario 1, because scenarios 2 and 3 are to specifically test non-optimal PTO conditions with bistability to check the robustness of bistability. The mathematical model presented in the previous section was built and simulated in MATLAB and Simulink (MathWorks Inc., Natick MA, USA). A variable step solver was selected to run the simulation, with Simulink automatically selecting either ode45 or ode15s, depending on the stiffness of the simulation. This measure of numerical stiffness may change

Table 5.1: Simulation parameters

Parameter	Value	Units
Water depth, H	40	m
Submersion depth (buoy center), d_s	7	m
Inner diameter, d	17	m
Outer diameter, D	20	m
Inner height, h_b	3	m
Outer height, H_b	6	m
Attachment arm, a	3	m
Water density, ρ	1025	kg/m^3
Buoy density, ρ_{buoy}	0.7ρ	kg/m^3
Pitch moment of inertia, I_θ	3.29×10^7	kg m^2
Acceleration due to gravity, g	9.81	m/s^2

Table 5.2: Drag properties

	x	z	θ
Coefficient of drag, C_D	0.7	1.28	0.22
Characteristic area, A_D	DH_b	$\pi\left(\frac{D}{2}\right)^2$	$D^4 D$

depending on the degree of nonlinearity, hence the automatic solver selection was employed to ensure a suitable solver was selected for each simulation. Three different irregular wave scenarios were used to determine the robustness of the bistable control algorithm. The magnetic coefficients given in Equation 5.19 were determined by the specified parameter γ.

Table 5.3: Simulation parameters for the regular wave scenarios

Parameter	Value	Units
Wave amplitude, A	0.5	m
Excitation frequency, ω	0.1–2	rad/s
Horizontal dipole spacing, r_0	1.5	m
Scaled normalised potential, γ	0–10	m^{-2}
Simulation time, T	2000	s

Table 5.4: Simulation parameters for the irregular scenarios

Parameter	Scenario		
	1	2	3
Wave height, H_s (m)	1.5	1	1
Wave period, T_z (s)	8	8	12
PTO stiffness, k_s (MN/m)	3.10	3.11	1.18
Optimal PTO stiffness, $k_{s,\text{opt}}$ (MN/m)	2.40	N/A	N/A
PTO damping, b (MNs/m)	0.892	0.896	0.051
Optimal PTO damping, b_{opt} (MNs/m)	1.15	N/A	N/A
Simulation time, T (s)	3000	3000	3000

5.4 Results and discussion

The results for the simulation scenarios described in Section 5.3 are presented and discussed in the following sections.
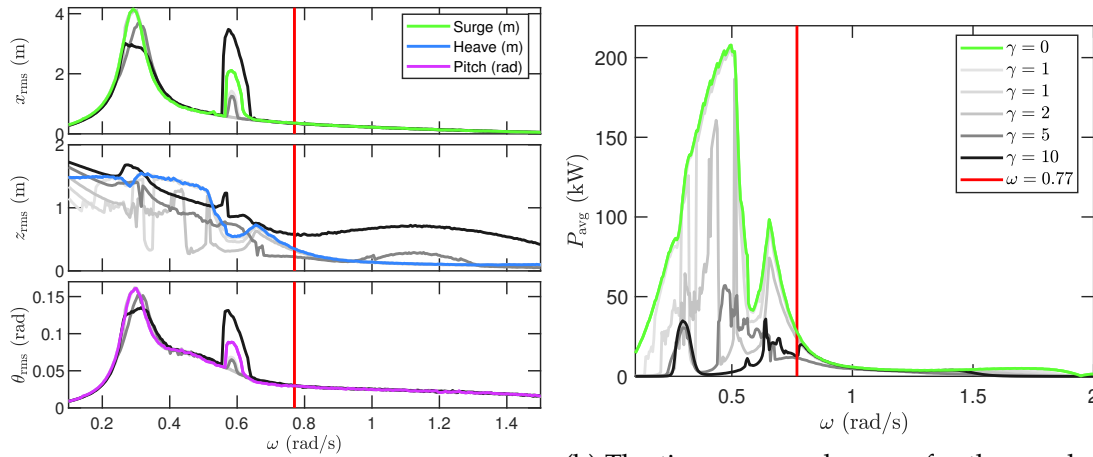
5.4.1 Regular waves

The regular wave scenarios were simulated with locally optimised and then suboptimal PTO conditions. The resulting motion RMS and time-averaged power for the optimal condition with varying γ are shown in Figs 5.8a and 5.8b, respectively. The motion RMS is calculated by

$$\mathbf{x}(t) = \sqrt{\frac{1}{N_t} \sum_{j=1}^{N_t} \mathbf{x}(t_j)^2} \,, \tag{5.38}$$

where N_t is the number of time steps and the summation and square operations are performed across each DOF. The results for the suboptimal conditions (tuned to frequency $\omega = 0.77$ rad/s) are given in Figs 5.9a and 5.9b, respectively. The frequency $\omega = 0.77$ rad/s was selected as it represents an off-peak response with a reasonable response amplitude.

As seen in Fig. 5.8b, the addition of bistability for an optimally tuned system subjected to regular waves is detrimental to the power generation performance. Such a result is expected as additional stiffness will only lead to suboptimal tuning. However, for a suboptimally tuned system subjected to regular waves, shown in Fig. 5.9b, there are bistable conditions under which substantial improvements are seen, particularly at lower frequencies. The main benefit is seen when the scaled dimensionless potential $\gamma < 2$; beyond this level the motion performance is reduced. However, higher levels
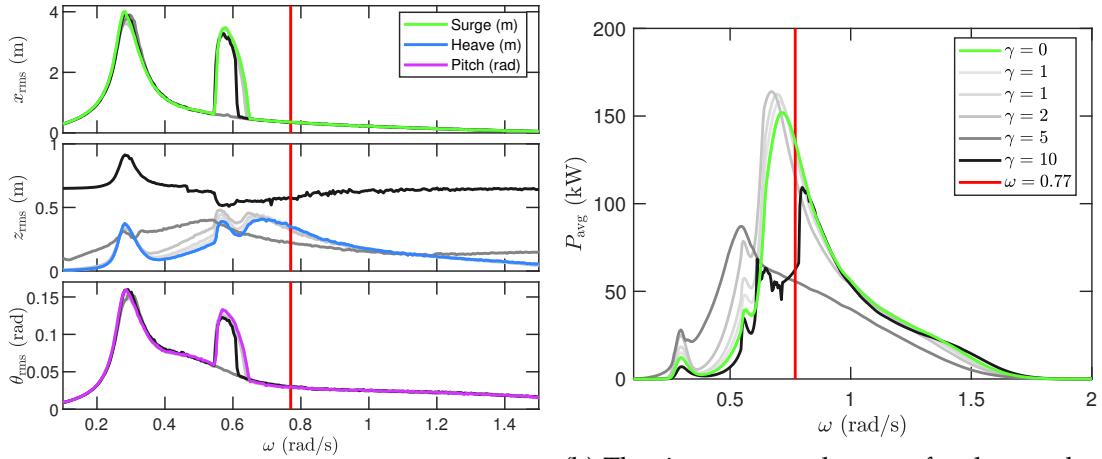
(a) The RMS of the motion for the regular wave scenarios.

(b) The time-averaged power for the regular wave scenarios.

Figure 5.8: The results for the regular wave scenarios varying γ (indicated by varying shade) where the PTO conditions are locally optimised for each frequency. These optimised values were found using the method described in Section 5.2.1.3. The frequency step between each regular wave scenario was around 0.0048 rad/s, with 400 cases sampled for each different γ. In this case, the PTO is tuned and the maximum power is obtained with zero bistability.

of bistability seem to provide a slight benefit to higher frequencies. This agrees with conventional findings as higher frequencies tend to be lower amplitude and are hence, the motions are constrained to one side of the potential well. When restricted to one side of a potential well, a higher stiffness is seen, making such regions suitably tuned for higher frequencies. Similarly, at lower levels of bistability, lower stiffnesses are seen and in general would be more suited to lower frequency excitation throughout most operating conditions. Though the resultant power is still less than the optimally tuned scenarios, bistability has acted to improve the power production potential for a system tuned to a single frequency, thereby making this passive control system more robust for regular wave conditions.

The motion RMS shown in Figs 5.8a and 5.9a show varying results as the level of bistability changes. The impact is most evident in the heave results. In the optimally tuned condition, the heave results are inconsistently altered by the inclusion of bistability, with many large amplitude responses at low frequencies reduced to small amplitude oscillations. This indicates the sensitivity of the optimal conditions at lower frequencies. However, for the detuned results, the heave RMS increases for lower levels of bistability, and decreases for higher levels, similar to the corresponding time averaged power results. The surge and pitch motions generally tended to reduce for both optimal and non-optimal conditions.

(a) The RMS of the motion for the regular wave scenarios.

(b) The time-averaged power for the regular wave scenarios.

Figure 5.9: The results for the regular scenarios and varying γ (indicated by varying shade) where the PTO conditions are tuned for $\omega = 0.77$ rad/s. The optimised values for $\omega = 0.77$ rad/s were found using the method described in Section 5.2.1.3. The PTO had a stiffness of 3.79 MN/m and a damping of 1.89 MNs/m. The frequency step between each regular wave scenario was around 0.0048 rad/s, with 400 cases sampled for each different γ. These results show the impact of bistability for regular scenarios that are not optimally tuned, whereas Fig. 5.8b presents the impact of bistability for regular scenarios that are optimally tuned.

To understand the origins of the peaks seen in the motion RMS, the sub-optimal frequency domain responses (ignoring geometric and drag nonlinearities) for surge, $\hat{x}$, heave, $\hat{z}$, pitch, $\hat{\theta}$ along with the transfer function between excitation force and wave amplitude are provided in Fig. 5.10. These results demonstrate that the driving factor behind the widest peak shown in Fig. 5.9a is the force amplitude at different frequencies combined with the system dynamics. Consequently, the predominant peak in power in Fig. 5.9b is due to the heave motion, primarily governed by the force amplitude at each frequency. The additional peaks seen are due to large motions in the surge and pitch DOF. It can also been seen that the surge and pitch DOFs are coupled through hydrodynamics, but heave is not coupled in the frequency domain. The absence of coupling stems from the linearisation about a nominal position. In this nominal position, the radiation force in heave is not coupled to either surge or pitch, and the geometric nonlinearity from the tether is not present. These assumptions provide clarity as to why they may be insufficient to fully capture indicative dynamics intrinsic to the system. The time domain results demonstrate that all DOFs interact to some degree. One of the key differences between the frequency domain and time domain simulations is the addition of drag, which reduces the amplitude of motion observed in surge and pitch to much
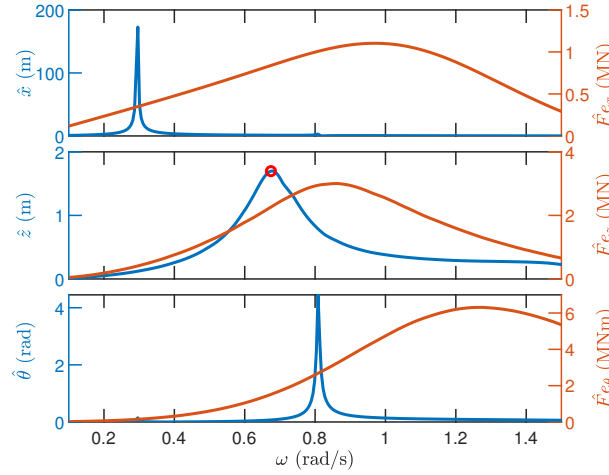
Figure 5.10: The frequency domain results for surge, heave, and pitch when geometric nonlinearities from the tether and drag forces are excluded and the sub-optimal tuning is used. The circle marker indicates the peak response which approximately matches with time domain RMS results. The excitation force amplitude at each frequency is also provided to illustrate the driving mechanism behind the major peak seen in the motion results. These frequency domain results are effectively how the linearised system would respond if excited by a regular wave at each frequency.

more realistic levels. The pitch resonance is no longer noticeable in the time domain results, likely due to a combination of geometric and drag nonlinearities.

The lower two peaks seen in the heave RMS results for the non-optimised system are not present in the frequency domain responses, and therefore are likely the result of coupling with another DOF. Each excitation frequency results in different hydrodynamic characteristics, which causes the natural frequency of the system to change. The natural frequencies in surge, $\omega_{n,x}$, heave, $\omega_{n,z}$, and pitch, $\omega_{n,\theta}$, for the submerged PA were derived as

$$\omega_{n,x} = \sqrt{\frac{g(\rho V - m)}{(l + a)(m + A_x(\omega))}} \, , \tag{5.39}$$

$$\omega_{n,z} = \sqrt{\frac{k_s}{m + A_z(\omega)}} \, , \tag{5.40}$$

$$\omega_{n,\theta} = \sqrt{\frac{a(a + l)F_{\mathrm{p}}}{l(I_\theta + A_\theta(\omega))}} \, , \tag{5.41}$$

where $A_x(\omega)$, $A_z(\omega)$, and $A_\theta(\omega)$ are the surge, heave, and pitch frequency dependent added mass, respectively. The natural frequencies $\omega_{n,x}$ and $\omega_{n,z}$ have been derived previously [11], and the derivation for $\omega_{n,\theta}$ is given in Appendix 5.A. The natural frequencies for both the optimised system and the suboptimal system are provided on

Fig. 5.11. Unsurprisingly, the natural frequency in the heave DOF for the optimal system closely follows the excitation frequency, with only a small deviation around the second peak in surge (i.e. when surge and pitch motions become significant). Therefore, the general best practice for such systems is to tune the PTO to enforce the heave natural frequency to equal the frequency of excitation.
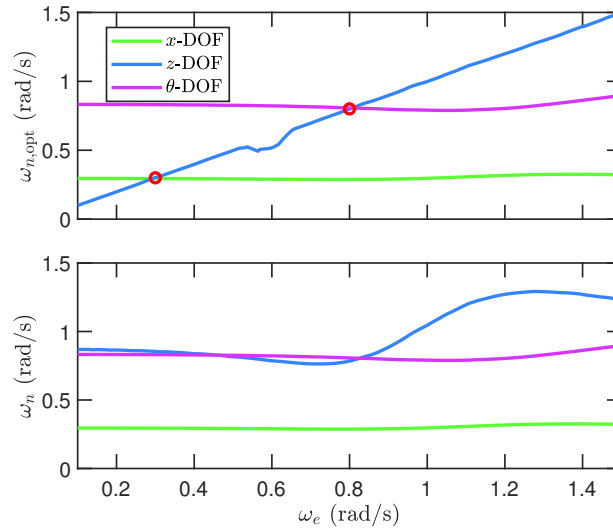

Figure 5.11: The natural frequencies (ω_n) in surge, heave, and pitch as the excitation frequency (ω_e) changes. The natural frequencies for the optimised system ($\omega_{n,\text{opt}}$) is shown on the top as well as red circles indicating the point at which the heave and surge, and heave and pitch natural frequencies coincide, respectively. The natural frequencies for the sub-optimal system are provided on the lower graph.

Another interesting quality occurs when the heave and surge natural frequencies coincide. The surge natural frequency (0.3 rad/s) does not change significantly with frequency, and is evident on the motion results as a large peak in the surge RMS. At the first harmonic of this frequency (0.6 rad/s) another peak occurs. Even in the sub-optimal results in Figs 5.9a and 5.9b these peaks are seen to influence the performance of the device. The pitch natural frequency results in a peak in the frequency domain but does not appear in the time domain results, even when the heave and pitch natural frequencies coincide. The frequency domain responses combined with the respective natural frequencies exemplify why drag, additional DOFs, and geometric nonlinearities should not be ignored. Ignoring these factors can lead to overestimation of motion, slight shifts in frequency peaks, and the absence of significant peaks altogether.

5.4.2 Irregular waves with optimal and non-optimal tuning

The irregular wave Scenario 1 (Table 5.4) with an optimised PTO linear stiffness was simulated and the time-averaged power for varying γ and r_0 is given in Fig. 5.12a. The same scenarios were simulated with the non-optimal linear stiffness and the corresponding results are given in Fig. 5.12b.
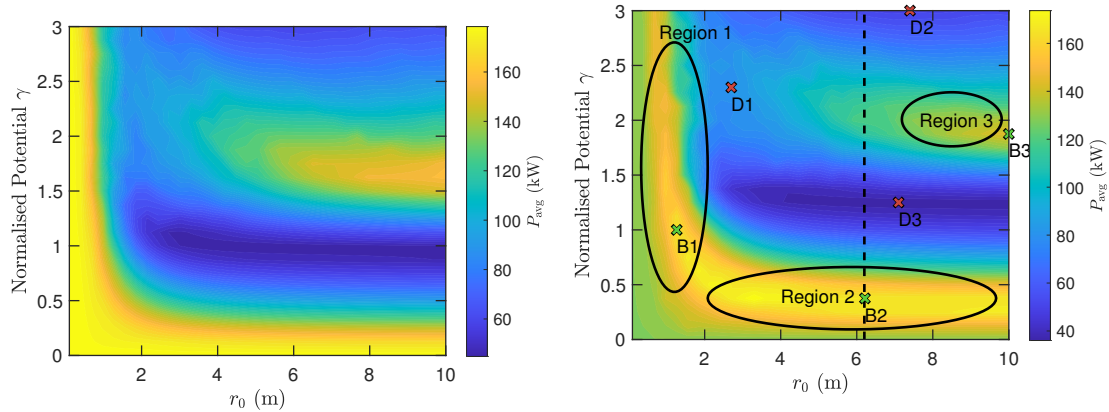
(a) The time-averaged power when the optimal linear PTO stiffness from Table 5.4 is used.

(b) The time-averaged power when non-optimal linear PTO stiffness from Table 5.4 is used.

Figure 5.12: The time-averaged power for the irregular wave Scenario 1 and varying γ and r_0 parameters. Green (B1, B2, and B3) and red crosses (D1, D2, and D3) indicates beneficial and detrimental points of interest, respectively. The dashed vertical line indicates the r_0 values over which a time lag analysis was conducted. Particular regions of interest are labelled.

Comparing the optimal with non-optimal, the resulting peak power performance seen in Figs 5.12a and 5.12b are the same, however the peak occurs at different bistable conditions. This demonstrates that a bistable system is capable of achieving the same optimal results as an optimal passively tuned controller. Therefore, the same conclusion may be inferred as for regular waves; for an optimally tuned system, bistability does not increase the amount of power extracted. However, the results from the non-optimal condition showed clear regions of beneficial and detrimental impacts. The main benefit is seen when $\gamma < 1$ which indicates that the bistability (or the potential energy profile) is beneficially exploited when the overall system is monostable. There are three principal regions of benefit observed in the power generation results for the non-optimal PTO irregular wave Scenario 1:

1. Region 1: $r_0 < 2$m and $\gamma < 3$,

2. Region 2: $r_0 > 5$ and $\gamma = 1.5$–2.5, and

113

3. Region 3: $r_0 > 2m$ and $\gamma < 1$,

which are marked in Fig. 5.12b. The mechanisms behind the benefit seen in each of these
regions provide insight for optimal bistable conditions and is explored in the following
section.

5.4.3 Irregular waves – phase and natural frequency

To further investigate these beneficial regions indicated in Fig. 5.12b, the time-averaged
power and time lag, t_{lag}, between the excitation force and tether velocity for varying γ
and a constant r_0 for irregular wave Scenario 1 are given in Fig. 5.13. The simulations
sampled are shown by the line on Fig. 5.12b which passes through Region 2 and the
edge of Region 3. A time lag was used as a proxy for phase lag as the phase difference
for an irregular wave is not clearly defined. The time lag was calculated using Matlab's
cross correlation function (xcorr), which measures the similarity between two signals
as one signal is offset in time. The time offset at which the maximum cross correlation
occurs has been taken to be the time lag. The phase relationship shows that this system
experiences strong phase matching, which is beneficial for power as the power maxima
correlate with minimising lag for some levels of bistability. There also exists a region
between $\gamma = 0.75$ and $\gamma = 1.75$ where the power reduces to a minimum, indicating that
for some levels of bistability, very poor tuning exists, so a finer understanding of how
bistability impacts the tuning parameters in each bistable scenario is required. It should
be noted that a negative time lag here represents the scenario when the excitation force is
leading the tether extension velocity. The significant drop and increase in lag at low and
high γ respectively, may be a result of the system oscillating near resonance conditions
in each region. The zero crossing period is 8 seconds, which corresponds to the jumps
in the time lag, indicating the presence of a sudden phase shift. These results suggest
that the effective stiffness experienced by the system when power is maximised (due
to change in bistable circumstance) causes the system to be well tuned for the incident
irregular wave conditions. The jumps in time lag at $\gamma = 0.4$ and 2.5 in monochromatic
systems would typically indicate the presence of a resonant condition. For this irregular
excitation spectrum, a similar effective resonant condition feature may be the cause
behind these sharp jumps.

The results in Fig. 5.12b demonstrate that any beneficial or detrimental effect due to
the nonlinear stiffness is highly dependent on both γ and r_0. To emphasise the substantial
difference between the bistable circumstances over each region, the stiffness potential en-
ergy profile, U_{stiff}, around the peak power response as well as the normalised histogram
showing the distribution of tether extension, $\overline{\Delta l}$, are shown in Fig. 5.14a, respectively.
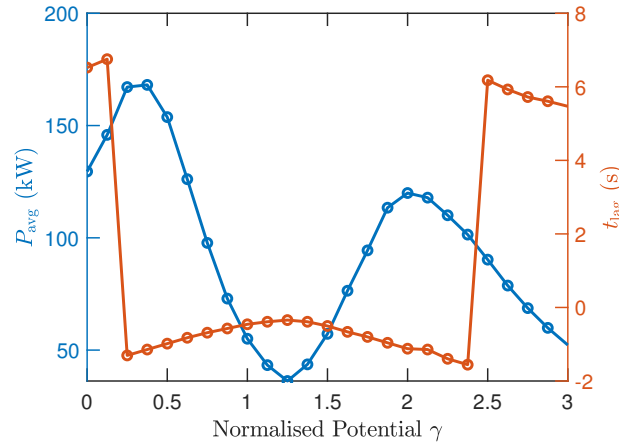Additionally, a number of potential profiles which demonstrated detrimental responses

Figure 5.13: The time-averaged power and time lag between the excitation force and tether velocity for irregular wave Scenario 1 and varying γ, and a value of $r_0 = 6.2$ (corresponding to the dashed line from Fig. 5.12b. The discretisation of the time lag is due to the finite sampling frequency.

are shown in Fig. 5.14b. The normalised distribution of tether extension is overlaid on these graphs to indicate the change in resulting system dynamics. Due to the nonlinear stiffness of the system, the effective natural frequency, ω_n, of the system in heave also changes during operation. This property may be calculated as

$$\omega_n = \sqrt{\frac{k_s + \frac{\partial \mathbf{F}_{\text{bi}}}{\partial l}}{m + A_{z,\infty}}} \, , \tag{5.42}$$

where $\frac{\partial \mathbf{F}_{\text{bi}}}{\partial l}$ represents the contribution to the stiffness due to the bistable force and $A_{z,\infty}$ represents the infinite frequency added mass in the heave direction. The effective natural frequencies for the beneficial and detrimental cases are given in Fig. 5.15a and Fig. 5.15b, respectively.

There are several known mechanisms through which bistability can improve performance of systems [29]. The snap-through mechanism in which the central peak in the potential well is frequently overcome seems to not provide much benefit here, and is overall detrimental, as depicted in the results presented in Fig. 5.14b for case $r_0 = 2.7$ and $\gamma = 2.3$. The regions that showed some benefit may be explained by different mechanisms. In Region 1, the natural frequency of the system (see Fig. 5.15a, B1) dips below the optimal linear natural frequency. The location of the oscillations in these scenarios imply that the system is operating in a physical regime which is exposed to near-optimal natural frequencies. This property would improve the power performance as the device would be effectively tuned for a large portion of the operating range, due to the large range of natural frequencies in standard operation. Such a system should be robust for varying sea conditions. By extension, the best results, seen in Region 2, are

115
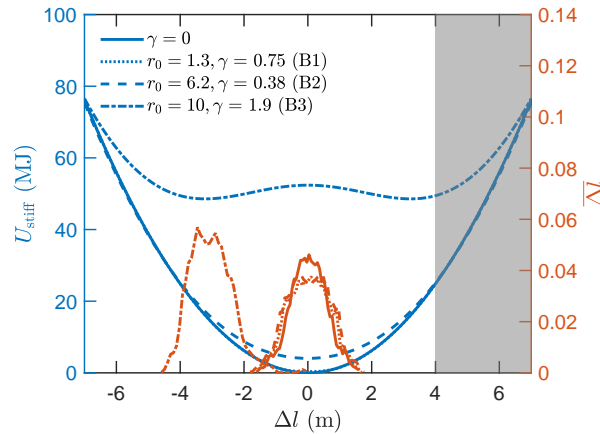
(a) Beneficial bistable potential energy profiles.
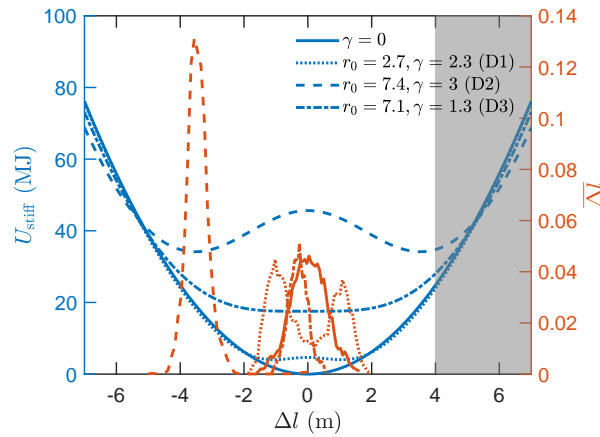
(b) Detrimental bistable potential energy profiles.

Figure 5.14: The stiffness potential energy (U_{stiff}) profiles around the bistable conditions
which (a) provide a benefit or (b) are detrimental to power production capability. The
corresponding normalised distribution of tether extension ($\overline{\Delta l}$) is shown to indicate the
change in resulting system dynamics. The shaded region indicates tether extensions for
which the buoy may breach the surface.

when the natural frequencies of the system are at, or close to, the optimal linear natural
frequency. As Region 2 just touches the optimal frequency, such systems are not exposed
to the large range of natural frequencies seen in Region 1, but are well tuned for a given
operational condition. Consequently, it is expected that for changing sea conditions,
such passive control systems would detune. In Region 3, the effective stiffness about
the nominal position is negative, creating a new equilibrium area. The effective natural
frequency at the new equilibrium position coincides with the optimal linear natural
frequency. This is the same fundamental finding as Regions 1 and 2, but about a new
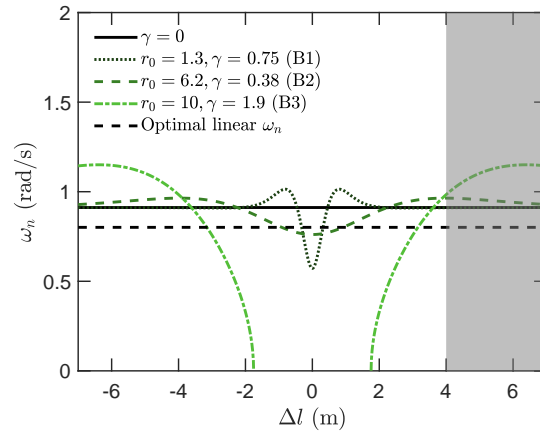
(a) Beneficial effective natural frequency profiles.
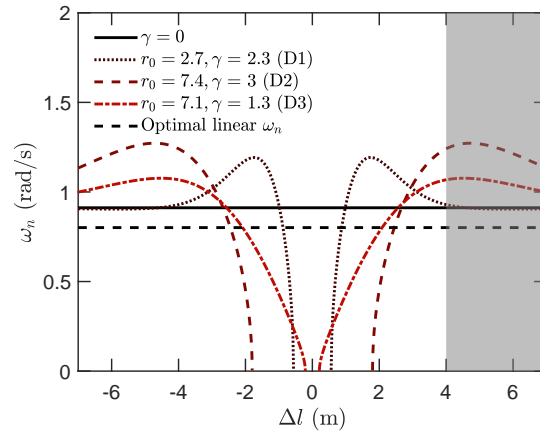
(b) Detrimental effective natural frequency profiles.

Figure 5.15: The effective natural frequency profiles around the bistable conditions which (a) provide a benefit or (b) are detrimental to power production capability. The optimal linear frequency is also shown for reference. Ranges of Δl with $\omega_n = 0$ indicate regions of negative stiffness in which the effective natural frequency is not real, hence this range has not been included on this graph. The shaded region indicates tether extensions for which the buoy may breach the surface.

operating condition. This shows that the best performance is when the operating natural frequency roughly matches the optimal linear natural frequency and when the heave component of the excitation force and tether velocity are in phase. In contrast, in the regions of significant detrimental contributions (see Fig. 5.15b) the operating natural frequency has been shifted further away from the optimal natural frequency, or rather, the natural frequency around the equilibrium point does not coincide with the optimal linear natural frequency. In these cases, bistability has acted to inhibit motion as if the

system was poorly tuned.

5.4.4 Irregular waves – changing sea states

To test the robustness of the bistable systems, the PTO conditions from the detuned irregular wave Scenario 2 were used for irregular wave Scenario 1 excitation. The resulting time-averaged power is shown in Fig. 5.16a. Furthermore, maps for non-optimal PTO configurations for irregular wave Scenarios 2 and 3 are given in Figs 5.16b and 5.16c, respectively. These additional plots demonstrate the applicability of such systems to a variety of sea states.

Results from regular waves demonstrated that a bistable system can exhibit improved responses when the system is suboptimal, thereby improving the robustness of the passive control system. Similarly, if a system is tuned for one irregular wave, the performance when subjected to an alternative sea state is an indication of the robustness of the passive system. The results presented in Fig. 5.16a demonstrate how the system responds to irregular wave Scenario 2 when non-optimally tuned for irregular wave Scenario 1. The trend of results resemble the findings of Fig. 5.12b, with local maxima around similar regions. This finding indicates that a bistable system may be found which is well suited to both sea states. Furthermore, such a passive system would be suitably robust to deal with the changing sea states observed in real ocean conditions.

The results from the simulations of irregular wave Scenarios 2 and 3 depict similar trends. Compared to irregular wave Scenario 1, irregular wave Scenario 2 has a lower significant wave height, and irregular wave Scenario 3 has a lower significant wave height and a higher zero-crossing wave period as shown in Table 5.4. The regions of optimal performance (Region 2) and good phase matching (Region 3) did shift a small amount for different wave conditions, but the regions which are exposed to a larger range of natural frequencies (Region 1) was reasonably consistent, as expected. For example, if a control system with $\gamma = 0.625$, and $r_0 = 3$ was selected (as marked in each graph in Fig. 5.16), all systems would experience a 10–20% improvement to power production compared to the initial passive control system without bistability when tuned for the energy frequency of the specific irregular wave. The variety of waves presented show that there are common trends seen in the benefit of bistability for different conditions and imply that if a sea state can be characterised, a suitable bistable potential energy profile could be determined. Therefore, in addition to a robust passive control system, it may be beneficial to provide an active or semi-active component to make fine adjustments to the bistable force as required.

The findings presented in this work imply that bistability or nonlinear stiffness can provide some passive benefit for a specific system and a given sea state, and that this benefit will be relatively robust in applying to changing sea conditions without the need for sophisticated control systems. To further extend this work, the impact of nonlinear

(a) The resultant time-averaged power when tuned for the irregular wave Scenario 2 and excited by the irregular wave Scenario 1.

(b) The resultant time-averaged power when tuned for and excited by the irregular wave Scenario 2.

(c) The resultant time-averaged power when tuned for and excited by the irregular wave Scenario 3.
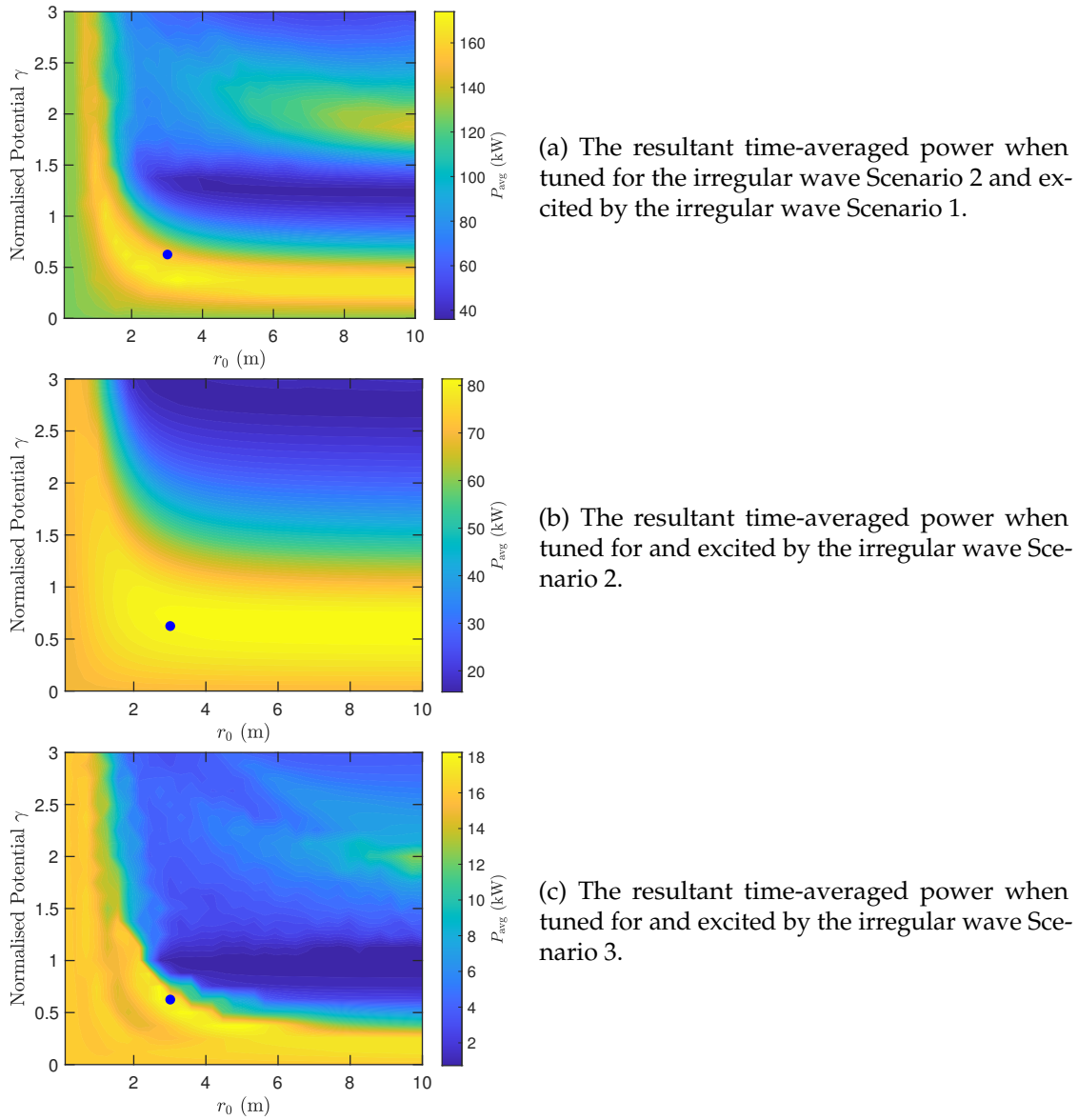
Figure 5.16: The resultant time-averaged power of scenarios using the non-optimal linear PTO stiffness for different irregular wave scenarios for varying γ and r_0. A common point is identified on each for comparison purposes. Subfigure (a) represents a system tuned for one irregular wave, but excited by another, while subfigures (b) and (c) represent a system tuned for respective irregular waves. These results show that the bistable system is reasonably robust for varying sea states.

hydrodynamics on bistable mechanics should be explored either by including a nonlinear representation of Froude-Krylov forces, or by simulating using computational fluid dynamics. The practical implementation of these should also be further investigated as the presented approach effectively constructs a particular potential profile from fictitious magnetic dipoles. In principle, if an optimal nonlinear stiffness is identified, a passive system can be constructed by springs or magnets to realise the benefit. Additionally, an active component to adjust the nonlinear stiffness subsystem based on a changing sea state could be included to further improve the system. Furthermore, while an understanding of how bistability impacts a single PA in a passive control context is useful, in reality such WECs will more likely be deployed in arrays. The array context should therefore also be further explored with bistability to understand the impact of nonlinear stiffness on coupling dynamics between submerged PA WECs.

5.5 Conclusion

The impact of a nonlinear stiffness or a bistable force acting on a submerged point absorbing wave energy converter was investigated. A model of a 3-DOF CETO-shaped device was constructed and subjected to regular waves. The degree of bistability was varied. The resultant motion and time averaged power showed that for an optimally tuned system, bistability provided no benefit, whereas for a non-optimally tuned system, certain levels of bistability were able to improve the performance for different frequency ranges. Lower levels of bistability seem to benefit lower frequencies, while higher levels benefit higher frequencies. The same model was then subjected to an irregular wave to better reflect real operating conditions. Again for an optimally tuned system, nonlinear stiffness tended to reduce performance, but for sub-optimally tuned conditions, bistability was able to obtain near optimal performance. By varying the bistable potential profile three regions of benefit were observed. The primary mechanism of improvement was due to the nonlinear stiffness exposing the operating system to a range of apparent natural frequencies, specifically in close proximity to the optimal linear natural frequency, which resulted in improved performance for a range of operating conditions. This mechanism seems to be robust over varying sea states with a consistent 10–20% improvement to power production in the systems simulated. Another linked mechanism is a passive phase matching property which appears to be associated with the natural frequency of the system but was demonstrated to be strongly connected with the power generation capability. The addition of a bistable force has been shown to provide a robust passive control system with common performance trends between different ocean conditions, which invites the possibility of an active bistable system to adjust the nonlinear stiffness force appropriately for different sea conditions.

Acknowledgment

Appendix 5.A Pitching natural frequency

Consider the device shown in Fig. 5.17 for small oscillations in the θ direction. The
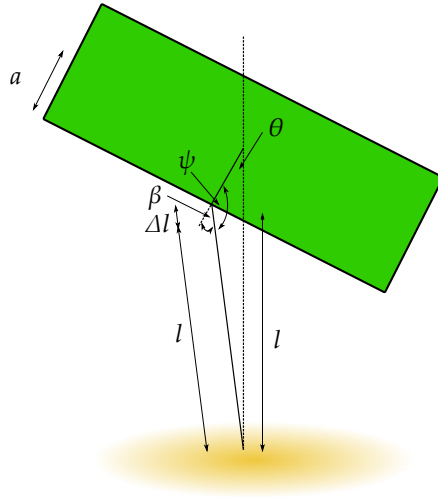

Figure 5.17: A submerged WEC PA oscillating about the nominal position. Various geometric definitions are shown to aid the derivation.

governing equation is

$$I_\theta \ddot{\theta} = -A_\theta(\omega) - B_\theta(\omega) - T_{\text{PTO}} \, , \tag{5.43}$$

where T_{PTO} is the moment due to the applied PTO force, and $B_\theta(\omega)$ is the frequency dependent radiative damping in pitch. The PTO moment can be described as

$$T_{\text{PTO}} = a F_{\text{PTO}} \sin(\beta) \, , \tag{5.44}$$

where β is defined according to Fig. 5.17. Noting that

$$\beta = 180 - \psi \, , \tag{5.45}$$

where β is defined according to Fig. 5.17, and the trigonometric identity

$$\sin(\theta) = \sin(180 - \theta) \, , \tag{5.46}$$

substituting into Equation (5.44) yields

$$T_{\text{PTO}} = a F_{\text{PTO}} \sin(\psi) \, . \tag{5.47}$$

121

Now, using the sine rule

$$\sin(\psi) = \frac{(a+l)\sin(\theta)}{l+\Delta l} \; . \tag{5.48}$$

To find Δl, note the geometric relationship

$$(l + \Delta l)^2 = (l + a(1 - \cos(\theta))^2 + (a\sin(\theta))^2 \; , \tag{5.49}$$

which simplifies to

$$\Delta l = \sqrt{l^2 + 2a(a+l)(1 - \cos(\theta))} \; . \tag{5.50}$$

Differentiating with respect to time gives

$$\Delta \dot{l} = \frac{a(a+l)\sin(\theta)\dot{\theta}}{\sqrt{l^2 + 2a(a+l)(1 - \cos(\theta))}} \; . \tag{5.51}$$

Nothing that the force from the PTO acting in the tether is

$$F_{\text{PTO}} = b\Delta \dot{l} + k_s \Delta l + F_{\text{P}} \; , \tag{5.52}$$

which, upon substitution of Equations (5.50) and (5.51) in Equation (5.43), rearranging, and using the small angle approximation, gives

$$(I_\theta + A_\theta(\omega))\ddot{w} = -B_\theta(\omega)\dot{\theta} - \frac{a(a+l)F_{\text{P}}}{l} \; . \tag{5.53}$$

Assuming simple harmonic motion

$$\theta = C \exp^{i\omega_{n,\theta}t} \tag{5.54}$$

where C is an arbitrary coefficient. Using this assumption, differentiating and substituting into Equation (5.53) and then equating real components yields

$$-\omega_{n,\theta}^2 (I_\theta + A_\theta(\omega)) = -\frac{a(a+l)F_{\text{P}}}{l} \; , \tag{5.55}$$

which reduces to

$$\omega_{n,\theta} = \sqrt{\frac{a(a+l)F_{\text{P}}}{l(I_\theta + A_\theta(\omega))}} \; , \tag{5.56}$$

which is the natural frequency in the pitching direction for a submerged single tether buoy.

Appendix 5.B   Radiation force statespace representation

The state space representation of the convolution integral term in the radiation force is given by the following augmented matrices with the state equation

$$\dot{\mathbf{p}} = \mathbf{A}_{ss}\mathbf{p} + \mathbf{B}_{ss}\dot{\mathbf{x}} ,$$
$$\mu = \mathbf{C}_{ss}\mathbf{p} .$$

(5.57)

$\mathbf{A}_{SS}$ is a block diagonal matrix of the form

$$\mathrm{diag}(\mathbf{A}_1, \mathbf{A}_2, \ldots \mathbf{A}_5) ,$$

where $\mathbf{A}_i$ are of the form

$$\mathbf{A}_i = \begin{bmatrix} a_1 & a_2 & \ldots & a_n \\ \ddots & & & 0 \\ & \mathbf{I}_{n-1} & & \vdots \\ & & \ddots & 0 \end{bmatrix}$$

where $\mathbf{I}_{n-1}$ is a $(n-1)$ identity matrix. The coefficients of the $\mathbf{A}_{ss}$ are given below.

Table 5.5: State matrix coefficients

Matrix	a_1	a_2	a_3	a_4	a_5	a_6	a_7	a_8
$\mathbf{A_1}$	-2.36	-11.55	-18.38	-40.82	-40.64	-49.47	-24.64	-15.33
$\mathbf{A_2}$	-2.49	-25.23	-45.64	-157.8	-178.3	-309.0	-170.2	-152.6
$\mathbf{A_3}$	-1.99	-8.04	-9.87	-15.71	-8.80	-6.45	-0.60	
$\mathbf{A_4}$	-2.24	-10.37	-14.77	-32.5	-28.43	-36.95	-16.22	-12.48
$\mathbf{A_5}$	-2.02	-8.76	-10.32	-20.04	-11.22	-11.30		

The $\mathbf{B}_{ss}$ is

$$\mathbf{B}_{ss} = \begin{pmatrix} 1 & 0 & 0 \\ & \mathbf{0}_{7\times 3} & \\ 0 & 0 & 1 \\ & \mathbf{0}_{7\times 3} & \\ 0 & 1 & 0 \\ & \mathbf{0}_{6\times 3} & \\ 1 & 0 & 0 \\ & \mathbf{0}_{7\times 3} & \\ 0 & 0 & 1 \\ & \mathbf{0}_{5\times 3} & \end{pmatrix} ,$$

(5.58)

123

the $\mathbf{C}_{ss}$ is

$$\mathbf{C}_{ss} = 1 \times 10^8 \times \begin{bmatrix} \mathbf{C}_1 & \mathbf{C}_2 & \mathbf{C}_3 \end{bmatrix}^T$$

$$
\mathbf{C}_1 = \begin{bmatrix} 0.0014 \\ 0.0032 \\ 0.0139 \\ 0.0210 \\ 0.0367 \\ 0.0302 \\ 0.0197 \\ 0 \\ -0.0074 \\ -0.0152 \\ -0.1651 \\ -0.3337 \\ -0.8734 \\ -1.0858 \\ -0.9568 \\ \mathbf{0}_{22\times 1} \end{bmatrix}, \quad
\mathbf{C}_2 = \begin{bmatrix} \mathbf{0}_{16\times 1} \\ 0.0120 \\ 0.0278 \\ 0.0780 \\ 0.1084 \\ 0.0827 \\ 0.0079 \\ \mathbf{0}_{15\times 1} \end{bmatrix}, \quad
\mathbf{C}_3 = \begin{bmatrix} \mathbf{0}_{23\times 1} \\ -0.0084 \\ -0.0185 \\ -0.0732 \\ -0.1007 \\ -0.1553 \\ -0.1046 \\ -0.0780 \\ 0 \\ 0.1142 \\ 0.2339 \\ 0.7428 \\ 0.6863 \\ 0.6644 \\ 0 \end{bmatrix}
$$

References

[1] J. Cruz. *Ocean Wave Energy*. 1st ed. Springer-Verlag Berlin Heidelberg, 2008. DOI: 10.1007/978-3-540-74895-3.

[2] B. Drew, A. R. Plummer, and M. N. Sahinkaya. "A review of wave energy converter technology". In: *Proceedings of the Institution of Mechanical Engineers, Part A: Journal of Power and Energy* 223.8 (2009), pp. 887–902. DOI: 10.1243/09576509JPE782. eprint: http://dx.doi.org/10.1243/09576509JPE782.

[3] *WHAT IS CETO*. Accessed: January 2018. URL: https://www.carnegiece.com/wave/what-is-ceto/.

[4] D. Greaves and G. Iglesias. *Wave and Tidal Energy*. John Wiley & Sons, 2018.

[5] Z. Wu, C. Levi, and S. F. Estefen. "Wave energy harvesting using nonlinear stiffness system". In: *Applied Ocean Research* 74 (May 2018), pp. 102–116. DOI: 10.1016/j.apor.2018.02.009.

[6] X.-T. Zhang, J.-M. Yang, and L.-F. Xiao. "An oscillating wave energy converter with nonlinear snap-through Power-Take-Off systems in regular waves". In: *China Ocean Engineering* 30.4 (July 2016), pp. 565–580. DOI: 10.1007/s13344-016-0035-5.

[7]   D. Younesian and M.-R. Alam. "Multi-stable mechanisms for high-efficiency and broadband ocean wave energy harvesting". In: *Applied Energy* 197 (2017), pp. 292–302. DOI: http://dx.doi.org/10.1016/j.apenergy.2017.04.019.

[8]   X. Xiao, L. Xiao, and T. Peng. "Comparative study on power capture performance of oscillating-body wave energy converters with three novel power take-off systems". In: *Renewable Energy* 103 (Apr. 2017), pp. 94–105. DOI: 10.1016/j.renene.2016.11.030.

[9]   X. Zhang et al. "Application of an adaptive bistable power capture mechanism to a point absorber wave energy converter". In: *Applied Energy* 228 (Oct. 2018), pp. 450–467. DOI: 10.1016/j.apenergy.2018.06.100.

[10]   O. Abdelkhalik and S. Darani. "Optimization of nonlinear wave energy converters". In: *Ocean Engineering* 162 (Aug. 2018), pp. 187–195. DOI: 10.1016/j.oceaneng.2018.05.023.

[11]   F. Meng et al. "Modal analysis of a submerged spherical point absorber with asymmetric mass distribution". In: *Renewable Energy* 130 (2019), pp. 223–237. DOI: https://doi.org/10.1016/j.renene.2018.06.014.

[12]   F. Meng et al. "A sensitivity study on the effect of mass distribution of a single-tether spherical point absorber". In: *Renewable Energy* 141 (2019), pp. 583–595. DOI: 10.1016/j.renene.2019.03.149.

[13]   H. Zhang et al. "Efficiency enhancement of a point wave energy converter with a magnetic bistable mechanism". In: *Energy* 181 (Aug. 2019), pp. 1152–1165. DOI: 10.1016/j.energy.2019.06.008.

[14]   A. Têtu et al. "Physical and Mathematical Modeling of a Wave Energy Converter Equipped with a Negative Spring Mechanism for Phase Control". In: *Energies* 11.9 (2018), p. 2362.

[15]   J. H. Todalshaug et al. "Tank testing of an inherently phase-controlled wave energy converter". In: *International Journal of Marine Energy* 15 (Sept. 2016), pp. 68–84. DOI: 10.1016/j.ijome.2016.04.007.

[16]   R. L. Harne and K. W. Wang. "A review of the recent research on vibration energy harvesting via bistable systems". In: *Smart Materials and Structures* 22.2 (Jan. 2013), p. 023001. DOI: 10.1088/0964-1726/22/2/023001.

[17]   N. Y. Sergiienko et al. "Performance comparison of the floating and fully submerged quasi-point absorber wave energy converters". In: *Renewable Energy* 108 (Aug. 2017), pp. 425–437. DOI: 10.1016/j.renene.2017.03.002.

[18]   L. Wang, H. Tang, and Y. Wu. "On a submerged wave energy converter with snap-through power take-off". In: *Applied Ocean Research* 80 (Nov. 2018), pp. 24–36. DOI: 10.1016/j.apor.2018.08.005.

[19]   B. W. Schubert et al. "Enhancement of a 3-DOF submerged wave energy device using bistability". In: *International Marine Energy Journal* (May 2020). In print.

[20]   X. Zhang et al. "Mechanism and sensitivity for broadband energy harvesting of an adaptive bistable point absorber wave energy converter". In: *Energy* 188 (Dec. 2019), p. 115984. DOI: 10.1016/j.energy.2019.115984.

[21]   A. Pecher and J. P. Kofoed. *Handbook of ocean wave energy*. Springer London, 2017.

[22]   A. Babarit. *NEMOH user manual*. Ecole Centrale de Nantes. Jan. 2014.

[23]   J. Falnes. "A review of wave-energy extraction". In: *Marine Structures* 20.4 (Oct. 2007), pp. 185–201. DOI: 10.1016/j.marstruc.2007.09.001.

[24]   S.-C. Jiang et al. "Analytical Solution of a Wave Diffraction Problem on a Submerged Cylinder". In: *Journal of Engineering Mechanics* 140.1 (Jan. 2014), pp. 225–232. DOI: 10.1061/(asce)em.1943-7889.0000637.

[25]   W. Cummins. *The impulse response function and ship motions*. Tech. rep. David Taylor Model Basin, Washington DC, 1962.

[26]   T. Perez and T. I. Fossen. "A Matlab toolbox for parametric identification of radiation-force models of ships and offshore structures". In: *Modeling, Identification and Control: A Norwegian Research Bulletin* 30.1 (2009), pp. 1–15. DOI: 10.4173/mic.2009.1.1.

[27]   J. A. Armesto et al. "Comparative analysis of the methods to compute the radiation term in Cummins' equation". In: *Journal of Ocean Engineering and Marine Energy* 1.4 (2015), pp. 377–393.

[28]   J. Falnes. *Ocean waves and oscillating systems: Linear interactions including wave-energy extraction*. Cambridge University Press, 2002.

[29]   R. L. Harne and K.-W. Wang. *Harnessing bistable structural dynamics: For vibration control, energy harvesting and sensing*. John Wiley & Sons, 2017.

[30]   B. Mann and B. Owens. "Investigations of a nonlinear energy harvester with a bistable potential well". In: *Journal of Sound and Vibration* 329.9 (2010), pp. 1215–1226. DOI: https://doi.org/10.1016/j.jsv.2009.11.034.

[31]   D. Griffiths. *Introduction to Electrodynamics*. Pearson Education, 2014.

[32]   K. W. Yung, P. B. Landecker, and D. D. Villani. "An analytic solution for the force between two magnetic dipoles". In: *Physical Separation in Science and Engineering* 9.1 (1998), pp. 39–52.

[33]   S. Gran. "A Course in Ocean Engineering (Developments in Marine Technology)". In: Elsevier Science Ltd, 1992. Chap. 2, pp. 187–199.

[34]   O. Faltinsen. "Sea loads on ships and offshore structures". In: vol. 1. Cambridge University Press, 1993. Chap. 2, pp. 22–29.

[35] J. Hals. "Modelling and phase control of wave-energy converters". PhD thesis. Norwegian University of Science and Technology, 2010.

[36] S. Sheng et al. "Model research and open sea tests of 100 kW wave energy convertor Sharp Eagle Wanshan". In: *Renewable Energy* 113 (2017), pp. 587–595. DOI: https://doi.org/10.1016/j.renene.2017.06.019.

[37] A. Rafiee and J. Fiévez. "Numerical prediction of extreme loads on the CETO wave energy converter". In: *Proceedings of the 11th European Wave and Tidal Energy Conference, Nantes, France*. 2015.

Chapter 6

Linear and nonlinear hydrodynamic models for dynamics of a submerged point absorber wave energy converter

As identified in the previous chapter, the nonlinear stiffness mechanism can offer some advantage in either the floating or submerged scenario. However, this finding was based on simulations that use linear potential flow hydrodynamic representations. Therefore, the influence of nonlinear fluid-structure interactions should be quantified and understood in order to clarify if the previous findings are reflective of more realistic conditions.

The chapter consists of one published journal article which compares four different methods of representing the hydrodynamic fluid-structure interactions. The different methods are incremental steps to introduce pose-dependence on hydrodynamic parameters beginning with the assumption that the hydrodynamic parameters do not change during simulation, and end with a fully nonlinear CFD model for a range of different frequencies. The purpose of this chapter is to answer the following research question: *What impact do the nonlinear hydrodynamic effects have on a submerged quasi-PA WEC, and is the linear potential flow hydrodynamic representations suitable for representative simulations?*

Further analysis comparing the different hydrodynamic models for spherical and cylindrical shaped submerged WECs may be found in Appendix B. This analysis in this appendix modelled the differently shaped WECs using linear, pseudo-nonlinear, and fully nonlinear hydrodynamics. The pseudo-nonlinear representation includes pose-dependence by using the linear hydrodynamic representation to estimate the hydrodynamic properties at different poses. The pseudo-nonlinear model demonstrated some basic nonlinear behaviours, however, it did not match the fully nonlinear model. This discrepancy implied that the excitation force is not the main hydrodynamic non-

linearity for the modelled systems and justified further investigation of the different
hydrodynamic influences, leading to the published journal article presented in this
chapter.

This section consists of the published journal article:

**Schubert, B.W., Robertson, W.S., Cazzolato, B.S. and Ghayesh, M.H., 2020. Linear and
nonlinear hydrodynamic models for dynamics of a submerged point absorber wave
energy converter.** *Ocean Engineering,* **197, p.106828.**

The article in its published format is available at `https://doi.org/10.1016/j.
oceaneng.2019.106828`.

Statement of Authorship

Title of Paper	Linear and nonlinear hydrodynamic models for dynamics of a submerged point absorber wave energy converter
Publication Status	☑ Published ☐ Accepted for Publication ☐ Submitted for Publication ☐ Unpublished and Unsubmitted work written in manuscript style
Publication Details	Schubert, B.W., Robertson, W.S., Cazzolato, B.S. and Ghayesh, M.H., 2020. Linear and nonlinear hydrodynamic models for dynamics of a submerged point absorber wave energy converter. Ocean Engineering, 197, p.106828.

Principal Author

Name of Principal Author (Candidate)	Benjamin Schubert
Contribution to the Paper	Developed ideas and concepts • Conducted a comprehensive literature review • Outlined the concepts of the paper to address the gaps in literature based on knowledge of the field Performed the modelling • Developed a structured mesh of a CETO-shaped buoy in the CFD software OpenFOAM • Varied different mesh and dynamic parameters and methods of calculation to find suitable CFD simulation • Validated the CFD model using data found in literature • Developed a model of the CETO-shaped buoy to estimate the hydrodynamic parameters using the potential flow solver NEMOH at different submergence levels and excitation frequencies • Coneptualised, developed the pseudo-nonlinear modelling method by determining the hydrodynamic parameters at different poses of the CETO-shaped buoy using the potential flow solve NEMOH • Implemented the pseudo-nonlinear modelling technique in Simulink through gain scheduling techniques • Developed a simulation in Simulink to predict the dynamic behaviour of the CETO-shaped wave energy converter at different regular wave elevations and submergence depths • Performed convergence studies between different modelling techniques in highly linear conditions Interpreted results • Collected and stored data from simulation results • Post processed the data using Matlab and ParaView • Analysed and collated time domain data into respective performance metrics and compared the results of different modelling approaches at different freuqencies • Interpreted results between different scenarios Writing • Solely developed the first full draft of the manuscript • Applied comments provided by all co-authors • Responsible for revising the manuscript after review • Acted as corresponding author
Overall percentage (%)	80%
Certification:	This paper reports on original research I conducted during the period of my Higher Degree by Research candidature and is not subject to any obligations or contractual agreements with a third party that would constrain its inclusion in this thesis. I am the primary author of this paper.

Signature		Date	2/2/2021

Co-Author Contributions

By signing the Statement of Authorship, each author certifies that:

    i.   the candidate's stated contribution to the publication is accurate (as detailed above);

    ii.   permission is granted for the candidate in include the publication in the thesis; and

    iii.   the sum of all co-author contributions is equal to 100% less the candidate's stated contribution.

Name of Co-Author	William Robertson		
Contribution to the Paper	Participated in developing the ideas and concepts, assisted in analysing and interpreting the obtained results, and provided revision of manuscript. Provided insight of signal processing techniques employed in the development of this manuscript.		
Signature		Date	15/02/2021

Name of Co-Author	Benjamin Cazzolato		
Contribution to the Paper	Participated in developing the ideas and concepts, assisted in analysing and interpreting the obtained results, and provided revision of manuscript. Provided insight of signal processing techniques employed in the development of this manuscript.		
Signature		Date	15/02/2021

Name of Co-Author	Mergen Ghayesh		
Contribution to the Paper	Participated in developing the ideas and concepts, assisted in analysing and interpreting the obtained results, and provided revision of manuscript.		
Signature		Date	18/02/2021

Please cut and paste additional co-author panels here as required.

Linear and nonlinear hydrodynamic models for dynamics of a submerged point absorber wave energy converter

B. W. Schubert, W. S. P. Robertson, B. S. Cazzolato, M. H. Ghayesh

Abstract

This study compares the response of a submerged CETO-shaped point absorber wave energy converter using linear, partially-nonlinear, pseudo-nonlinear, and fully-nonlinear methods to model hydrodynamic effects. Linear potential flow models calculate hydrodynamic parameters to represent the fluid-structure interaction; typical dynamic models apply these parameters without pose-dependence. The partially-nonlinear method evaluates excitation forces at different poses to introduce a pose-dependent excitation force; in addition to the excitation force, the pseudo-nonlinear method calculates hydrodynamic coefficients using linear potential flow methods and includes pose-dependence through interpolating pre-calculated parameters to represent the radiation force. The fully-nonlinear CFD model is a numerical wave tank validated against published data. The applicability of linear-based methods has been explored by comparing the motion, force, and power of the system under various operating conditions against the fully-nonlinear results. It was expected that for low amplitude waves results tend towards the linear results; however, for both low amplitude waves and increased submergence depth, linear methods provided poor representations of the nonlinear CFD results. Geometric nonlinearities were insufficient to capture all the nonlinear behaviour. A frequency-dependent nonlinearity was identified in the water above the buoy resonating. For such submerged point absorbers, linear methods do not adequate represent the influential nonlinear effects.

6.1   Introduction

The concept of harvesting ocean wave energy has been in development for over two centuries [1]. As demand for power moves towards renewable sources of energy, a world-wide interest has been building since the 1970s. A variety of different devices and operation principles have been proposed in literature and in practice [2]. These devices are primarily in the research and prototype stage [3], and require further development to achieve economic viability for large scale energy production [4]. Specifically, high fidelity modelling is an essential part of the design stage. Faster modelling techniques would benefit both research and commercial efforts.

A point absorber (PA) is a common wave energy converter (WEC), is small relative to an incident wave [1], and can be either floating or submerged, as shown schematically in Figure 6.1. For designing such devices, efficient and accurate computational models of the system dynamics are essential. These modelling methods can be used to estimate device performance, implement and test control systems, and are more cost effective than constructing a prototype. The device modelled and analysed in this study is based on a CETO-like device previously studied [5] and is a cylindrically shaped device that is nominally submerged, as shown in Figure 6.2. To model WEC systems, typical methods include using linear boundary element method (BEM) solvers such as ANSYS Aqwa (ANSYS, Inc., Canonsburg PA, USA), WAMIT (WAMIT, Inc., Chestnut Hill MA, USA), and NEMOH (L'École Centrale De Nantes, Nantes, France), to find various hydrodynamic parameters. Simulations of the model dynamics can use these parameters to quantify various hydrodynamic forces acting on the buoy. An alternative approach, which is fully nonlinear, is the computationally intensive numerical wave tank (NWT) CFD approach. NWT are becoming increasingly common within research communities and industry [6].

The BEM (used for wave energy applications) and CFD approaches are considered linear and nonlinear in principle, respectively. The benefits of BEM techniques include fast solutions suited to studies requiring many iterations such as optimisation. As the BEM is linear, they do not account of nonlinearities seen in the fluid-structure interaction such as overtopping, slamming, flow separation, or viscosity. Additionally, BEM techniques provide the hydrodynamic parameters about a nominal pose and ignore geometric nonlinearities associated with a change of position and orientation. It has been shown that results from linear BEM solvers rapidly lose accuracy as the buoy deviates from the nominal position and nonlinearities become more influential [7].

Fully nonlinear CFD approachs use numerical solvers based on the Navier Stokes equation [8]. These models should be validated experimentally to ensure high fidelity reliable results [6]. Typical CFD methods are computationally intensive and are often not validated against experimental results. While computational resources are becoming more readily available, alternative techniques to capture nonlinear effects using faster approaches would provide valuable improvements to current modelling techniques.

The most relevant nonlinearity for small heaving PA WEC systems is considered to be within the excitation force [8] as it may capture parametrically excited motions not found in simple linear representations. Furthermore, for small heaving PA WEC system, diffraction and radiation effects are typically small compared to the Froude-Krylov force, one component of the excitation force [9]. Accordingly, previous attempts to capture nonlinear effects have focussed on the hydrodynamic excitation force. Such attempts include: extending the linear potential flow model to a fully nonlinear potential flow model [10]; recalculating the hydrodynamic forces at each time step with the linear solver [11, 12];

partially extending the hydrodynamic force to a second order approximation [12]; using a gain scheduling method to include the impact of orientation on hydrodynamic parameters [13]. Extending the hydrodynamic forces found from BEM solvers by considering the instantaneous pose dependence is often termed partially nonlinear within literature [8]. These methods demonstrate some improvement compared to the linear model but are often only suited to particular circumstances. Most of these methods [11–13] are applied to *floating* buoys for which the hydrodynamic parameters are heavily dependent on wetted area. Submerged buoys, however, have a significantly different depth dependence, independent of wetted area. The fully nonlinear potential flow model [10] pertains to a submerged cylindrical PA which has small dimensions and is subject to low amplitude waves. Such conditions predispose linear models to give acceptable results. While such nonlinear potential flow models appear promising, it is commonly accepted that such techniques for calculating hydrodynamic properties require further research [8]. Another alternative is the weak-scatterer approach where the free surface conditions on the instantaneous wave elevation is linearised, and the fluid-structure interactions are calculated for exact positions. This model has been applied to a submerged buoy, and has been shown to agree with linear models for linear conditions and demonstrate significant deviations from linear theory for nonlinear conditions [14]. The importance of including nonlinear effects for control systems for wave energy systems has been demonstrated through the introduction of two nonlinear measures for wave-to-wire models [15]. One measurement was related to the hydrodynamic interaction and the other refers to the nonlinear effects in the power take-off (PTO).

Recently, some effort have been made to assess the pressure field accuracy for representing the Froude-Krylov force [16]. It was found that for a heaving PA, Wheeler's stretching method of Airy's linear wave theory was suitable to capture nonlinearity assuming small radiation and diffraction forces. This method was applied to a six degree of freedom (DOF) model [17] and showed how such nonlinearities impact power generation. However, no CFD or fully nonlinear model was presented for validation purposes, and the device modelled was floating and far smaller than the CETO shaped device presented in this study. A reconfigurable oscillating surge wave energy converter has also been modelled using multiple linear hydrodynamic gains with some success [18]. Additionally, for this type of oscillating surge device, an enhanced nonlinear time domain numerical model in which pitch angle dependence was introduced in the excitation torque and a nonlinear representation of the radiation torque, was shown to improve the estimated torques when compared to experimental results [19].

Models of WEC systems are often restricted to one or two degrees of freedom, depending on the mode of operation of the buoy. However, for submerged multi-DOF PA WECs, the change of hydrodynamic parameters which couple DOF for varying poses (particularly orientations) may be significant in capturing coupling between DOF

and other oscillatory modes. This change of hydrodynamic parameters due to pose is fundamental to the operation of such systems. Overall, it is generally expected that linear models overestimate WEC performance [5], as many hydrodynamic nonlinearities are neglected. For the context of submerged buoys, comparisons between linear and nonlinear modelling techniques remains an area of ongoing research.

Previous work on a pseudo-nonlinear modelling technique incorporates pose dependence in the hydrodynamic parameters [20]. Previously, two buoys were analysed: a cylindrical buoy, for which the hydrodynamic parameters are dependent on position and orientation, and a spherical buoy, for which the hydrodynamic parameters depend only on position due to symmetry. Linear, pseudo-nonlinear, and fully nonlinear hydrodynamic modelling techniques were compared and it was shown that the pseudo-nonlinear method followed the trend of the nonlinear results, but significantly overestimated the performance of the devices. Pseudo-nonlinear results for the spherical buoy were a better approximation of the CFD results than for the cylindrical buoy. The buoys differed in size, were close to the surface, and were subject to regular waves of 1m height. These findings indicate a significant dependence on operating conditions such as submergence depth and wave amplitude.

This paper extends previous work to explore the impact of the submergence depth and wave height on the validity of the including pose dependent hydrodynamic nonlinearity when looking at the dynamic performance of a submerged PA WEC. A comparison between a linear, partially nonlinear, pseudo-nonlinear, and fully nonlinear models will be presented for varying wave heights and submergence depths. The 3DOF models are subject to regular waves and include surge, heave, and pitch hydrodynamic dependence. The linear model uses hydrodynamic parameters about a nominal position, which are found using the BEM solver NEMOH. For the context of wave energy devices, a comparison between NEMOH and WAMIT was conducted [21]. This comparison concluded that for submerged point absorbers, such as the WEC considered in the present study, the difference between open source solver NEMOH and the commercially available solver WAMIT is minimal.

The linear model ignores any spatial nonlinearities in the hydrodynamic forces, but includes the geometric nonlinearities associated with the direction of the PTO force inherent in 3DOF modelling. The partially nonlinear model uses linear hydrodynamic forces, and introduces pose dependence through gain-scheduling the excitation force. The pseudo-nonlinear method uses the same BEM solver to provide the hydrodynamic parameters at a series of locations over the motion amplitude. Linearly interpolating these values at a given position for each time step provides pose-dependent hydrodynamic parameters to represent radiation forces as well as pose-dependent excitation forces. A NWT in OpenFOAM has been constructed and validated against experimental data available in literature [5]. This validated fully nonlinear model is used to infer the

accuracy of the linear and pseudo-nonlinear models. One case was analysed in depth and demonstrated significant nonlinear behaviour not represented in any of the three linear based models. A summary of the differences between the modelling approaches is given in Table 6.1.

The mathematical formulation of the WEC model is provided in Section 6.2 in the form of equations of motion and a discussion of each relevant force for each modelling technique. Validation of the fully nonlinear CFD model is given in Section 6.3. The simulation process and parameters of each proposed test scenario is provided in Section 6.4 with results display in Section 6.5. The interpretation and implications of these findings are presented in Section 6.6, with a summary of the process and findings in Section 6.7.

6.2 Mathematical model of WEC

In this study, a cylindrical buoy is modelled in three DOF, with pose represented as

$$\mathbf{x} = \begin{pmatrix} \text{Surge} \\ \text{Heave} \\ \text{Pitch} \end{pmatrix} = \begin{pmatrix} x \\ z \\ \theta \end{pmatrix}. \tag{6.1}$$

In the time domain, the motion of this system can be described using the modified Cummins equation [5], expressed as

$$\mathbf{M}\ddot{\mathbf{x}} = \mathbf{F}_e + \mathbf{F}_{rad} + \mathbf{F}_h + \mathbf{F}_{PTO} + \mathbf{F}_d \tag{6.2}$$

where $\mathbf{M}$ is a matrix which contains the inertial terms for each DOF, and $\mathbf{F}_e$, $\mathbf{F}_{rad}$, $\mathbf{F}_h$, $\mathbf{F}_{PTO}$, and $\mathbf{F}_d$ represent the excitation, radiation, hydrostatic, PTO, and drag force respectively. The methods used to calculate some of these terms vary between the linear, pseudo-nonlinear, and fully nonlinear approaches. Specific descriptions of each term and calculation method is discussed throughout the remainder of this section.

6.2.1 Excitation force

The excitation force, $\mathbf{F}_e$, is the superposition of the diffraction and Froude-Krylov forces [12]. Within the linear model, $\mathbf{F}_e$ is described as

$$\mathbf{F}_e = \mathbf{F}_{e,amp} \circ \cos(\sigma + \sigma_s - \omega t), \tag{6.3}$$

where $\mathbf{F}_{e,amp}$ and σ are the amplitude and phase vectors of the excitation force in 3DOF respectively, t denotes time, and ω is the wave frequency. The Hadamard product operator, $\circ$, is used to indicate element-wise multiplication. The linear model proposes that $\mathbf{F}_{e,amp}$ and σ are functions only of ω, whereas the pseudo-nonlinear model includes

137

pose dependence, causing the $\mathbf{F}_{\text{e,amp}}$ and σ hydrodynamic parameters to be dependent on $\mathbf{x}$. The heave and pitch directly impact these parameters, while surge changes the location of the buoy relative to the incident wave. Therefore, the impact of the surge position on the phase of the excitation force, σ_{s}, is quantified by

$$\sigma_{\text{s}} = kx \, , \tag{6.4}$$

where k is the wavenumber, which is the solution to [22]

$$\omega^2 = gk \tanh(kh) \, , \tag{6.5}$$

where h is the water depth, and g is the acceleration due to gravity. The partially nonlinear and pseudo-nonlinear excitation force may be expressed as

$$\mathbf{F}_{\text{e}}(z, \theta, \omega) = \mathbf{F}_{\text{e,amp}}(z, \theta, \omega) \circ \cos(\sigma(z, \theta, \omega) + \sigma_{\text{s}} - \omega t) \, . \tag{6.6}$$

The partially nonlinear and pseudo-nonlinear representation of the excitation force was accomplished using a discrete gain scheduling method. For each DOF, the operating range was discretised into 13 steps, which necessitates prior knowledge of the approximate bounds of motion. The bounds of the linear model may be considered an appropriate first guess. During simulation, the instantaneous heave and pitch were used to interpolate between the excitation force amplitude and phase for each DOF. A similar interpolation technique has been applied previously for 1DOF floating body [13], and is fundamentally a computationally cheap alternative to recalculating the excitation force at each time step applied in other studies [11].

6.2.2 Radiation force

As a buoy oscillates in the fluid, waves are radiated outward. The effective force on the buoy due to this effect is known as the radiation force, $\mathbf{F}_{\text{r}}$, and can be calculated in the time using the Cummins equation [23],

$$\mathbf{F}_{\text{r}} = -\mathbf{A}_\infty \ddot{\mathbf{x}} - \int_0^t \mathbf{K}(t - t') \dot{\mathbf{x}}(t') dt' \, , \tag{6.7}$$

where $\mathbf{A}_\infty$ and $\mathbf{K}$ represent the infinite frequency added mass and memory function, respectively. This memory function and integral quantifies the impact of the past state of the fluid on the current state. The radiation force in the frequency domain may be represented as

$$\hat{\mathbf{F}}_{\text{r}} = -[\mathbf{B}(\omega) + i\omega \mathbf{A}(\omega)]\hat{\mathbf{x}}(i\omega) \, , \tag{6.8}$$

where $\mathbf{B}(\omega)$ is the radiation damping and $\mathbf{A}(\omega)$ is the added mass, both of which are frequency-dependent. A well established method in WEC modelling uses the hydrodynamic parameters $\mathbf{B}(\omega)$ and $\mathbf{A}(\omega)$ to construct a transfer function to identify the

relationship between the velocity and the integral in Equation (6.7) [24]. Fifth order transfer functions were used in the construction of this system representation as these were found to approximately fit the numerical data provided from NEMOH. The linear and partially nonlinear models assume that the hydrodynamic parameters $\mathbf{B}(\omega)$ and $\mathbf{A}(\omega)$ are only frequency dependent, whereas the pseudo-nonlinear method introduces position dependence by representing the system as a series of state space models which depend on the coordinates z and θ. This method was implemented in a Simulink simulation through the use of a linear parameter varying (LPV) block to represent the radiation force using position and velocity as inputs. This LPV technique is a method to represent a model with dynamics that vary as a function of time-varying parameters. In this case, the time-varying parameters are heave and pitch, and the previously calculated grid of state-space representations are used to interpolate for the radiation force. Further information on LPV systems may be found within Matlab documentation [25].

6.2.3 Hydrostatic and PTO forces

The hydrostatic force is common in all models and acts only the z direction, represented by

$$F_{h,z} = \rho g V - mg \, , \tag{6.9}$$

where ρ is the density of water, V is the volume of the buoy, and m is the mass of the buoy. This force is constant for submerged buoys and is compensated by a constant force from the PTO. The variable PTO force is modelled as a spring-damper arrangement such that,

$$\mathbf{F}_{\text{PTO}} = \mathbf{T}(-b_{\text{PTO}}\Delta\dot{l} - k_{\text{PTO}}\Delta l - |\mathbf{F}_{h,z}|) \, , \tag{6.10}$$

with b_{PTO} and k_{PTO} being the damping coefficients and spring constants respectively, and Δl being the tether extension of the WEC. By extending the model to 3DOF, this introduces nonlinear relationship between terms through the PTO force [26], as seen in Equation (6.10) in the form of a transformation $\mathbf{T}$. The transformation of coordinates $(x, z, \alpha + \phi) \rightarrow (\Delta l, \alpha, \phi)$, shown in Figure 6.1, can be described by the set of following equations:

$$\Delta l = \sqrt{(x - a\sin(\alpha + \phi))^2 + (z + l + a - a\cos(\alpha + \phi))^2} - l \, , \tag{6.11}$$

$$\alpha = \arctan\left(\frac{x - a\sin(\alpha + \phi)}{z + l + a - a\cos(\alpha + \phi)}\right) , \tag{6.12}$$

$$\phi = (\phi + \alpha) - \alpha \, , \tag{6.13}$$

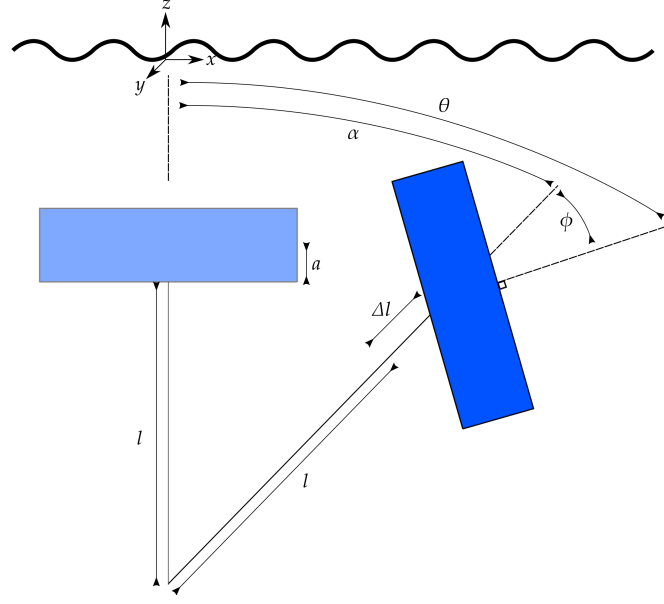where a and l are the distance between buoy centre and tether attachment point, and

Figure 6.1: A cylindrical WEC showing two different coordinate systems (surge, heave, pitch) = $(x, z, \theta) \rightarrow (\Delta l, \alpha, \phi)$.

the tether length, respectively. It should be noted that $(\phi + \alpha)$ is another representation of pitch, θ, decomposed into two parts, ϕ, the angle of the buoy relative to the tether, and α, the angle of the tether. The rate of change of tether extension, $\Delta \dot{l}$, can be derived by taking the first time derivative of Equation (6.11), and is given by

$$\Delta \dot{l} = \frac{(x - a\sin(\alpha + \phi))(\dot{x} - a\cos(\alpha + \phi)(\dot{\alpha} + \dot{\phi}))}{\sqrt{(x - a\sin(\alpha + \phi))^2 + (z + l + a - a\cos(\alpha + \phi))^2}}$$
$$+ \frac{(z + l + a - a\cos(\alpha + \phi))(\dot{z} + a\sin(\alpha + \phi)(\dot{\alpha} + \dot{\phi}))}{\sqrt{(x - a\sin(\alpha + \phi))^2 + (z + l + a - a\cos(\alpha + \phi))^2}} . \quad (6.14)$$

The forces and moment from the PTO may then be calculated and applied to the buoy in the initial coordinate system of surge, heave, and pitch, by using simple trigonometric relationships. In the above equations, it is assumed that the tether is fixed at the bottom of an axisymmetric buoy.

The damping and stiffness parameters may be optimised for a given frequency using linear hydrodynamics for a single DOF [27]. By assuming tether extension is primarily associated with vertical motion, optimal conditions are:

$$b_{\text{PTO, opt}}(\omega) = B_z(\omega) , \qquad k_{\text{PTO, opt}}(\omega) = \omega^2 (m + A_z(\omega)) . \quad (6.15)$$

These equations are valid only for linear hydrodynamics and when the PA is restricted to oscillate in heave, but for the purposes of this study are referred to as optimal conditions.

140

Optimal conditions result in relatively large amplitudes of buoy oscillation, which, for small submergence depths, may result with the buoy breaching the water surface. To prevent breaching, the optimal stiffness was used, and a sufficiently large damping coefficient common to all scenarios was selected to reduce oscillation amplitude. The values used for stiffness and damping are common to the linear, partially nonlinear, pseudo-nonlinear, and fully nonlinear simulations for the sake of comparison and consistency. The instantaneous power generated, P, may be approximated in all simulations as,

$$P = b_{\text{PTO}} \Delta \dot{l}^2 \,. \tag{6.16}$$

6.2.4 Drag force

In fully nonlinear simulations, the drag force, $\mathbf{F}_{\text{D}}$, may be calculated directly at each time step. However, in the linear, partially nonlinear, and pseudo-nonlinear methods, the drag force is approximated using a constant drag coefficient, $\mathbf{C}_{\text{D}}$. The drag force in this case is approximated by

$$\mathbf{F}_{\text{D}} = -\frac{1}{2} \mathbf{C}_{\text{D}} \rho \mathbf{A}_{\text{D}} \dot{\mathbf{x}}_{\text{r}} |\dot{\mathbf{x}}_{\text{r}}| \,, \tag{6.17}$$

where $\dot{\mathbf{x}}_{\text{r}}$ and $\mathbf{A}_{\text{D}}$ are the velocity of the buoy relative to the surrounding fluid and the characteristic area, respectively. For pitch, the characteristic area is taken to be D^5, where D represents the outer diameter of the buoy, and the velocity is taken to be $\dot{\theta}$ [28].

6.2.5 BEM hydrodynamics calculation

The BEM typically uses potential theory to calculate the excitation and radiation forces at a given frequency for a described buoy [11]. Using Bernoulli's equation, the total pressure can be linearised and expressed as the superposition of four pressure components,

$$p = p_{\text{s}} + p_{\text{d}} + p_{\text{Di}} + p_{\text{r}} \,, \tag{6.18}$$

where p_{s} and p_{d} represent the static and dynamic pressures respectively, and, p_{Di} and p_{r} represent the pressures associated with the diffraction and radiation forces. The excitation force is the superposition of Froude-Krylov (FK), $\mathbf{F}_{\text{FK}}$, and diffraction forces, $\mathbf{F}_{\text{Di}}$, which are calculated by integrating the respective pressures over the surface of the buoy,

$$\mathbf{F}_{\text{FK}} = -\oiint_S p_{\text{d}} \hat{\mathbf{n}} \, dS \,, \qquad \mathbf{F}_{\text{Di}} = -\oiint_S p_{\text{Di}} \hat{\mathbf{n}} \, dS \,, \tag{6.19}$$

where S and $\hat{\mathbf{n}}$ represent the surface and the normal to the surface, respectively. The pressures are derived from analytical formulas for the flow potential. Similarly the

radiation force, $\mathbf{F_r}$, can be calculated as

$$\mathbf{F_r} = - \oiint_S p_r \hat{\mathbf{n}} \, dS \tag{6.20}$$

and is subdivided to inertial and damping terms for the $\mathbf{A}$ and $\mathbf{B}$ values from Equation (6.8). This method has the advantage of being faster than fully nonlinear methods but is linearised and ignores all second order diffraction and radiation terms [11]. For the purpose of this study, the BEM solver NEMOH was used for the linear, partially nonlinear, and pseudo-nonlinear models.

6.2.6 Model differences summary

The differences between the nonlinearities represented in the four proposed models is summarised in Table 6.1.

Table 6.1: Model hydrodynamic nonlinearity summary

Model	Nonlinear Excitation	Nonlinear Radiation	Fully Nonlinear
Linear			
Partially nonlinear	✓		
Pseudo-nonlinear	✓	✓	
CFD	✓	✓	✓

6.2.7 Fully nonlinear calculation

The fully nonlinear CFD calculations are governed by the Navier-Stokes equations which are a series of fundamental equation capturing the mass continuity, momentum conservation, and energy conservation of the fluid, given by Equations (6.21), (6.22), and (6.23), respectively [8]:

$$\frac{\partial \rho}{\partial t} + \nabla (\rho \mathbf{u}) = 0 \,, \tag{6.21}$$

$$\frac{\partial u}{\partial t} + (\mathbf{u}\nabla)\mathbf{u} = -\frac{1}{\rho}\nabla \mathbf{p} + \mathbf{F_{ext}} + \frac{\mu}{\rho}\nabla^2 \mathbf{u} \,, \tag{6.22}$$

$$\rho(\frac{\partial \epsilon}{\partial t} + \mathbf{u}\nabla \epsilon) - \nabla(K_H \nabla T) + \rho \nabla \mathbf{u} = 0 \,, \tag{6.23}$$

where $\mathbf{u}$ and μ are the fluid velocity and viscosity, respectively. The pressure field and external force is represented by $\mathbf{p}$ and $\mathbf{F_{ext}}$. Additionally, ϵ, K_H, and T represent the internal energy, heat conduction coefficient, and temperature.

These equations have the advantage of fully describing the nonlinear behaviour of the fluid. The ensuing fluid-buoy interaction subject to the given fluid conditions may then be solved. As there is no analytical solution, due to complexity, the equations must be solved numerically. Such processes have large computational cost but have been used to simulate WEC systems for decades [6]. For a CFD model to provide meaningful results, it should be validated. The most trusted method of validation is a comparison against experimental data [6].

6.3 Model validation

A high fidelity fully nonlinear model was constructed and validated to provide confident comparison between linear, partially nonlinear, pseudo-nonlinear and fully nonlinear simulation scenarios. For the purposes of validation, the geometries of an existing buoy with experimental results [5] were used within all simulations. A schematic of the buoy is given in Figure 6.2, and the corresponding values are provided in Table 6.2.
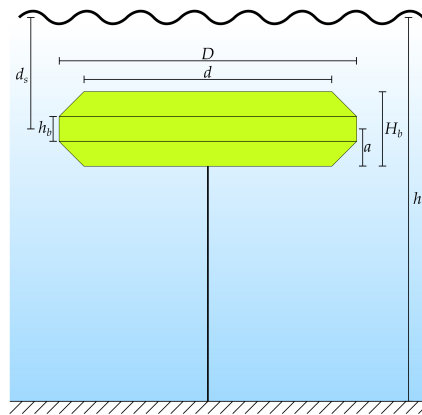

Figure 6.2: A schematic of the modelled submerged symmetrical CETO-like buoy.

The numerical wave tank used in this investigation was constructed in OpenFOAM with dimensions (x, y, z) of $(330, 200, 50)$ metres. The large y dimension reduces boundary effects along the walls. The solver application used was *olaDyMFlow*, which has the advantage of active wave absorption, reducing the necessary relaxation and absorption zones. Though the experimental validation study [5] did not provide PTO stiffness and damping parameters, time series data was provided, which enabled estimation of the PTO properties through multivariable regression.

The NWT was first subject to waves without the buoy present and the resolution was increased until convergence in wave height occurred. The buoy was then included but held fixed and the force around the static buoy was checked for convergence and compared to BEM methods. The buoy was then permitted to move in the aforementioned

143

Table 6.2: CETO-like buoy geometry

Parameter	Value	Units
Volume, V	1.7475×10^3	m^3
Buoy density, ρ_{buoy}	0.7ρ	$\mathrm{kg\,m}^{-3}$
Inner diameter, d	17	m
Outer diameter, D	20	m
Inner height, h_b	3	m
Outer height, H_b	6	m
Attachment arm, a	3	m

DOF. The whole model was then compared to existing experimental data [5]. The wave
theory used was based on established criteria of wave properties and physical set up
[29]. The NWT and WEC specific parameters used in all these simulations are given in
Table 6.3.

Table 6.3: Validation simulation parameters

Parameter	Value	Units
Acceleration of gravity, g	9.81	$\mathrm{m\,s}^{-2}$
Water density, ρ	1025	$\mathrm{kg\,m}^{-3}$
Kinematic viscosity of water, ν	1.004×10^{-6}	$\mathrm{m}^2\,\mathrm{s}^{-1}$
Water depth, h	40	m
Submersion depth, d_{s}	5	m
Tether length, Δl	32	m
PTO damping, b_{PTO}	0.628	$\mathrm{MN\,s\,m}^{-1}$
PTO stiffness, k_{PTO}	3.91	$\mathrm{MN\,m}^{-1}$
Mesh convergence period, T_v	16	s
Mesh convergence wave height, η_v	5	m
Mesh convergence wave theory	Stokes V	—
Force convergence period, T_v	16	s
Force convergence wave height, η_v	3	m
Force convergence wave theory	Stokes II	—

6.3.1 Wave height convergence

Convergence of the fluid mesh within the NWT is vital to ensure appropriate representa-
tion of wave propagation. This process can be divided into two parts: convergence in
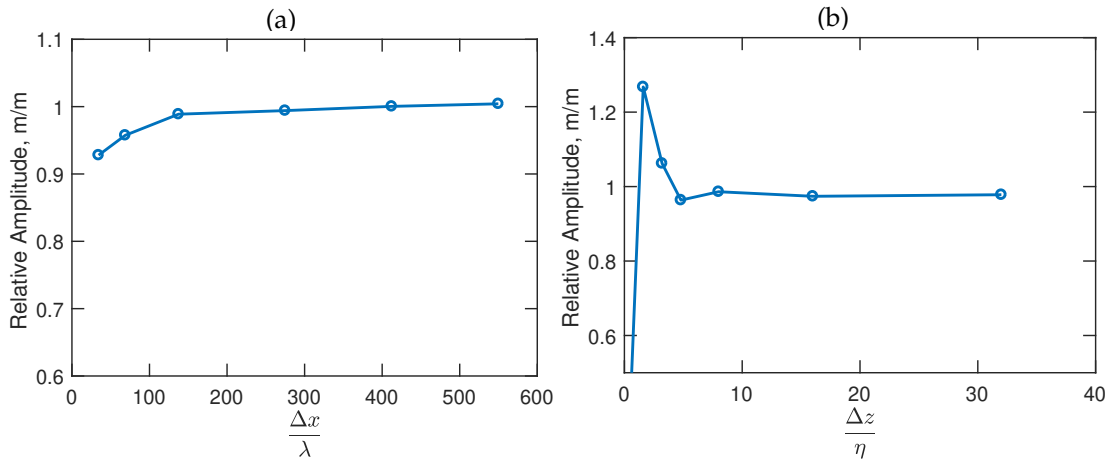
Figure 6.3: The wave height response when a given number of cells in the x (a) direction per wavelength and z (b) direction per wave height was used.

the x-direction, and convergence in the z-direction. The y-direction is assumed to be not as important due to the wave direction being in the x-direction.

In these simulations, the parameters in Table 6.3 were employed. The parameter, $\Delta x / \lambda$ is the number of cells per wavelength and is the parameter held constant in future simulations to ensure appropriate resolution. An initial guess of 4 cells per wave height in the z direction and 80 cells in the y direction were used. The measured wave height relative to the desired wave height as x resolution increases is given in Figure 6.3a. This set of simulations shows that after approximately 140 cells per wavelength, the wave height converges. The wave height ratio converges to around 1, and the z resolution was also checked for convergence. The number of cells per wave height, $\Delta z / \eta$, and the corresponding wave height relative to the desired wave height is shown in Figure 6.3b.

Mesh convergence is achieved at around 10 cells per wave height. The measured wave height is within 3% of the desired wave height, which indicates adequate resolution in the y direction.

6.3.2 Excitation force convergence

To improve the validity of the CFD model, the pressure force around the stationary buoy was measured and compared to BEM solutions. The resolution of a certain volume around the buoy was doubled, and the surface of the buoy had cells that were doubled again. The variable parameter used in these simulations to check for convergence was the distance d_m around the buoy in which the cell resolution was doubled. This distance d_m was varied and the resulting force on the buoy over time is given in Figure 6.4.

The results show that the force converged when d_m reaches around 3m. However, results did not converge to the linear approximation (a sinusoid). Given the proximity
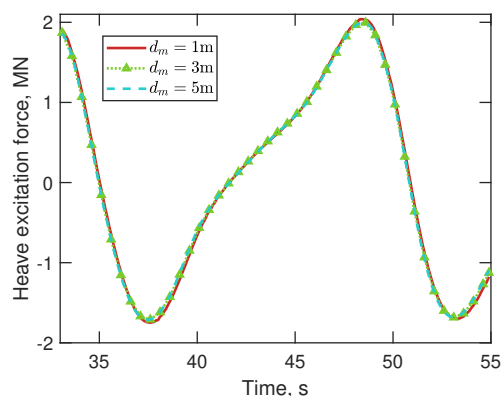
Figure 6.4: The time domain response of the force for various distances d_m around the mesh in which the mesh resolution was doubled.

of the buoy to the surface, it is expected to see a highly nonlinear result. It is therefore acceptable for the force convergence step that the linear and nonlinear forces do not match. The resulting mesh is shown in Figure 6.5.
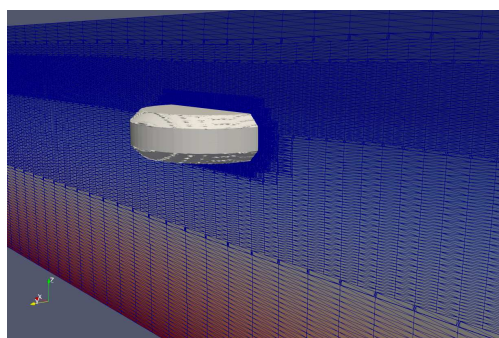

Figure 6.5: The NWT with the CETO-like buoy.

6.3.3 Experimental comparison

To validate the CFD model, a comparison between simulation results and experimental data adopted from literature [5] was performed. The surge, heave, and pitch motion, along with the tether extension, tether velocity, and PTO force are provided in Figure 6.6. An arbitrary time offset (common for all plots) was applied for comparison purposes to ensure results are in phase.

The results show that the CFD results and the experimental data follow much the same trend. Specifically, the tether extension, tether velocity, and PTO force give a strong match. The study providing the experimental data did not provide an estimation of experimental error, so an assumed 10% error is used based on common experimental setups [6]. The Pearson correlation coefficients are a measure of linear dependence be-
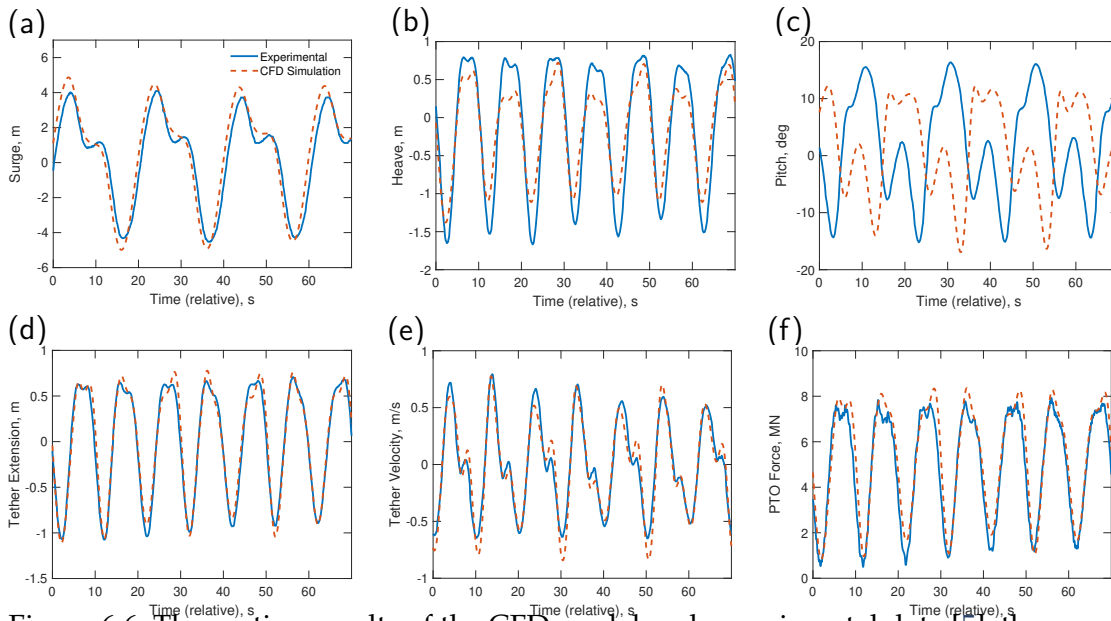
Figure 6.6: The motion results of the CFD model and experimental data [5]; the wave height was 3m, and the wave period was 10s.

tween two signals and may be used to quantify the difference between the experimental and numerical results. The correlation of these signals were calculated using the Matlab function *corrcoef*, and the signals were within 6% difference, excluding surge and pitch. The surge and pitch CFD results correlate to experimental values with 15% and -138% difference, respectively.

It is not uncommon for pitch CFD results to incorrectly replicate experimental results [5], possibly due to the assumption of uniform density in the CFD model. As surge and pitch motions are linked, this same error could also account for the slight discrepancy in the surge result as this is a secondary force and moment due to coupling of motion rather than a direct pressure effect. The established level of difference in heave motion and tether characteristics validates this CFD model, justifying the use of this model as a high fidelity comparison tool.

6.4 Simulation procedure

The validated CFD model provides a method to qualify and quantify the accuracy of the linear, partially nonlinear, and pseudo-nonlinear techniques. Three scenarios are proposed to determine the conditions influencing the fidelity of the pose dependent models.

The models constructed using linear, partially nonlinear, pseudo-nonlinear, and fully nonlinear methods were excited by regular waves over a range of frequencies. Due

to computational resources, only a subset of frequencies were sampled for the CFD simulations. The parameters g, ρ, v, h, and b_{PTO} were common in all simulations and scenarios. These parameters were used to calculate the linear hydrodynamic parameters in NEMOH. For each excitation frequency, a constant value of PTO damping was used, and the optimal PTO stiffness was calculated according to Equation (6.15).

The linear and pseudo-nonlinear methods assume constant drag coefficients. These drag coefficients are found in a previous study [5] which constructs and validates a CFD model. This study determines the drag coefficients by prescribing the motion of the body to oscillation in each DOF within the still numerical wave tank. The pressure force on experienced by the buoy, $\mathbf{F}_P$ was quantified and curve fitting tools were then used to match the coefficients in the Morison equation given by

$$\mathbf{F}_P = \mathbf{C}_I\ddot{\mathbf{x}} + \frac{1}{2}\rho\mathbf{C}_D\mathbf{A}_D\dot{\mathbf{x}}|\dot{\mathbf{x}}| \,, \tag{6.24}$$

where $\mathbf{C}_I$ represents an inertial coefficient. The calculated drag coefficients are provided in Table 6.4.

Table 6.4: Drag coefficients.

|	x	z	θ
Coefficient of drag, C_D	0.7	1.28	0.22

The scenarios are outlined in Table 6.5 and were constructed to determine the performance of the pseudo-nonlinear method for low amplitude oscillations and increased submergence depths. The range of values for the pseudo-nonlinear BEM hydrodynamics gain scheduling method was selected to suit the expected motion range.

Table 6.5: The scenario specific parameters.

Parameter	Scenario 1	Scenario 2	Scenario 3
Submergence depth, d_s	7 m	7 m	11 m
Wave height, η	1 m	0.2 m	1 m
Wave theory	Stokes II	Stokes I	Stokes II
BEM range, z (m)	−1 to 1	−0.1 to 0.1	−1 to 1
BEM range, θ (deg)	−15 to 15	−15 to 15	−15 to 15

The lookup table required for the pseudo-nonlinear method has a resolution of 13 sampled points linearly spaced between the BEM range specified for heave and pitch. A total of 169 points were contained within the constructed lookup table. The variation due to surge ultimately manifests as the surge phase offset, σ_s, represented in Equation
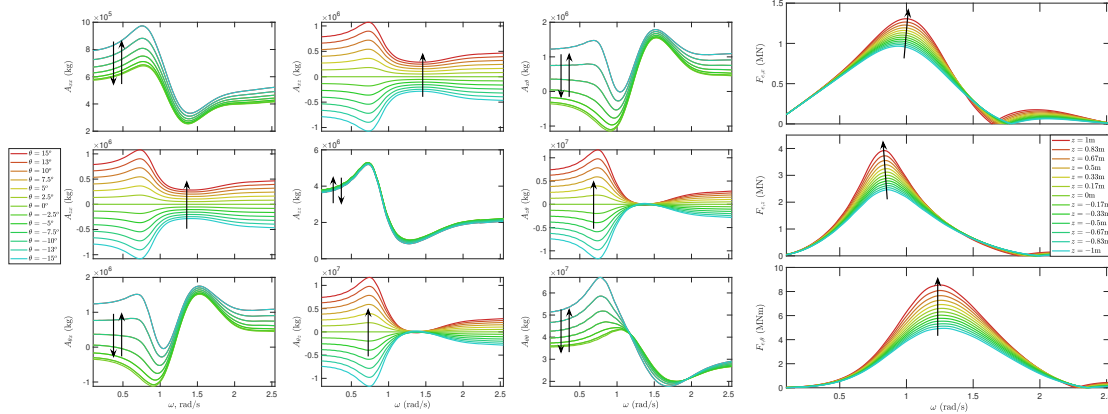
(a) Hydrodynamic added mass varying pitch orientations for $z = 0$.

(b) Excitation force varying heave for $\theta = 0$.

Figure 6.7: Example hydrodynamic added mass and excitation force for varying DOFs. The arrows indicate the direction of change of hydrodynamic added mass and excitation force as the respective DOFs are varied.

6.6. The CFD simulations use the resolution found in Section 6.3. The periods and PTO stiffnesses for each scenario (denoted by subscripts 1, 2, and 3) used in the CFD simulations are provided in Table 6.6.

Table 6.6: Simulation conditions.

Period (s)	6	7	8	9	10	12	14
$k_{\text{PTO, opt 1}}$ (MN m^{-1})	3.33	3.32	3.48	3.18	2.51	1.62	1.12
$k_{\text{PTO, opt 2}}$ (MN m^{-1})	3.33	3.32	3.48	3.18	2.51	1.62	1.12
$k_{\text{PTO, opt 3}}$ (MN m^{-1})	4.38	3.48	2.89	2.39	1.94	1.32	0.95

6.5 Results

6.5.1 Hydrodynamic results from NEMOH

When the pose of the buoy changes, the corresponding hydrodynamics vary substantially. To characterise this change, the excitation forces for varying pitch positions and the added mass for varying heave positions are provided in Figures 6.7a and 6.7b, respectively.

149

The excitation force is known to have a much larger amplitude as the buoy approaches the surface. For a change in pitch angle, the change is less intuitive, leading to the formation of different peak force frequencies. As heave location increases, the magnitude of added mass increases. Similar trends are seen in the radiative damping. These features in the hydrodynamic parameters emphasise the limitation of standard linear modelling, that the nonlinearities in these hydrodynamic parameters are not included.

6.5.2 Linear conditions convergence

To initially check that all models converge to similar motions in linear conditions, the models with scenario 1 conditions were subject to a long period, low amplitude wave, with a stiffness such that operation was off-resonance. The parameters for this check for convergence for linear conditions are contained in Table 6.7 and the time domain results of the tether extensions are shown in Figure 6.8.

Table 6.7: Parameters for model convergence under linear conditions.

Parameter	Value	Units
Water depth, h	40	m
Submersion depth, d_s	7	m
Tether length, Δl	30	m
Wave height, η	0.4	m
Wave Period, T_w	29	m
PTO damping, b_PTO	0.628	$\mathrm{MN\,s\,m^{-1}}$
PTO stiffness, k_PTO	1.12	$\mathrm{MN\,m^{-1}}$

The CFD results for this convergence test show some evidence of transient effects. However, all the results converge to similar motion amplitudes, particularly the linear, partially nonlinear, and pseudo-nonlinear models. This provides some confidence in each model in producing consistent results for linear conditions.

6.5.3 Model dynamics

To benchmark the linear based systems, the first scenario consist of a shallow submersion depth and a relatively large amplitude wave (Table 6.5). Monochromatic waves were used to excite the WEC. The resulting motion for each monochromatic wave was analysed by finding the root mean square (RMS) of the oscillation. The RMS was used to incorporate the impact of multiple modes of oscillation present. Other important parameters to explore the performance of a WEC include the maximum PTO force, and
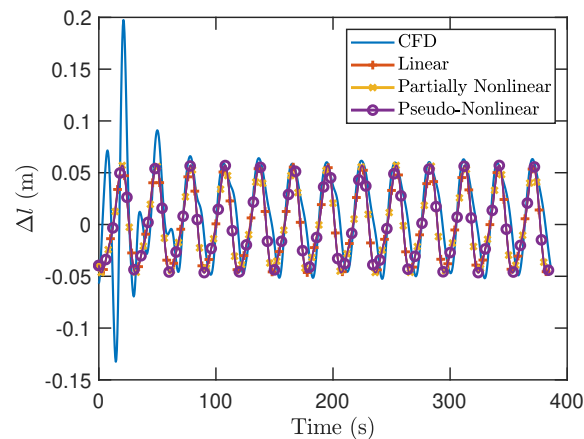
Figure 6.8: The time domain response of the tether extension when the buoy is excited a long period and low amplitude wave.

the RMS of the instantaneous power generated. Transient effects for each simulation were discarded where practically possible to ensure the steady state operation of WEC was considered. Scenario 2 required the longest calculation time, some taking upwards of 47 days to complete. The simulation time of each scenario was selected to be 200s for each scenario, the most intensive mesh had 5319938 cells, and the simulation was parallelised over 32 CPU cores on a single node with Skylake Intel CPU architecture with 9665 MB of memory per CPU. For simulations with a wave period 14, only 14.2 periods were simulated and may have slight transient influences. Simulations with other wave periods were observed to have settled into a steady state. The motion RMS, maximum PTO force, and the power RMS for each scenario are shown in Figures 6.9a, 6.9b, 6.9c, 6.10a, 6.10b, 6.10c, 6.11a, 6.11b, and 6.11c, respectively.

Given the significant discrepancy between the linear based models and the CFD model, the combined hydrodynamic forces (excitation and radiation) from the linear models were compared with the pressure forces experienced by the buoy in the CFD model. The respective forces for Scenario 1, with a period of 10s were found and presented in Figure 6.12a. Furthermore, the forces for the same scenario when the linear models were subject to the CFD motion are given in Figure 6.12b. To further visualise the motion, images of the NWT during the motion are provided in Figure 6.13.

The linear simulations were conducted on a standard desktop computer, whereas the CFD simulations were conducted on the super computer Phoenix, hosted by The University of Adelaide. Each simulation was parallelised over 32 processors. Each scenario and period for the CFD simulations demonstrated different computational requirements, whereas the linear, partially nonlinear, and pseudo-nonlinear showed similar computation time. Scenario 1 with a period of 10s was selected as representative of typical computation requirements and a comparison of the typical computational
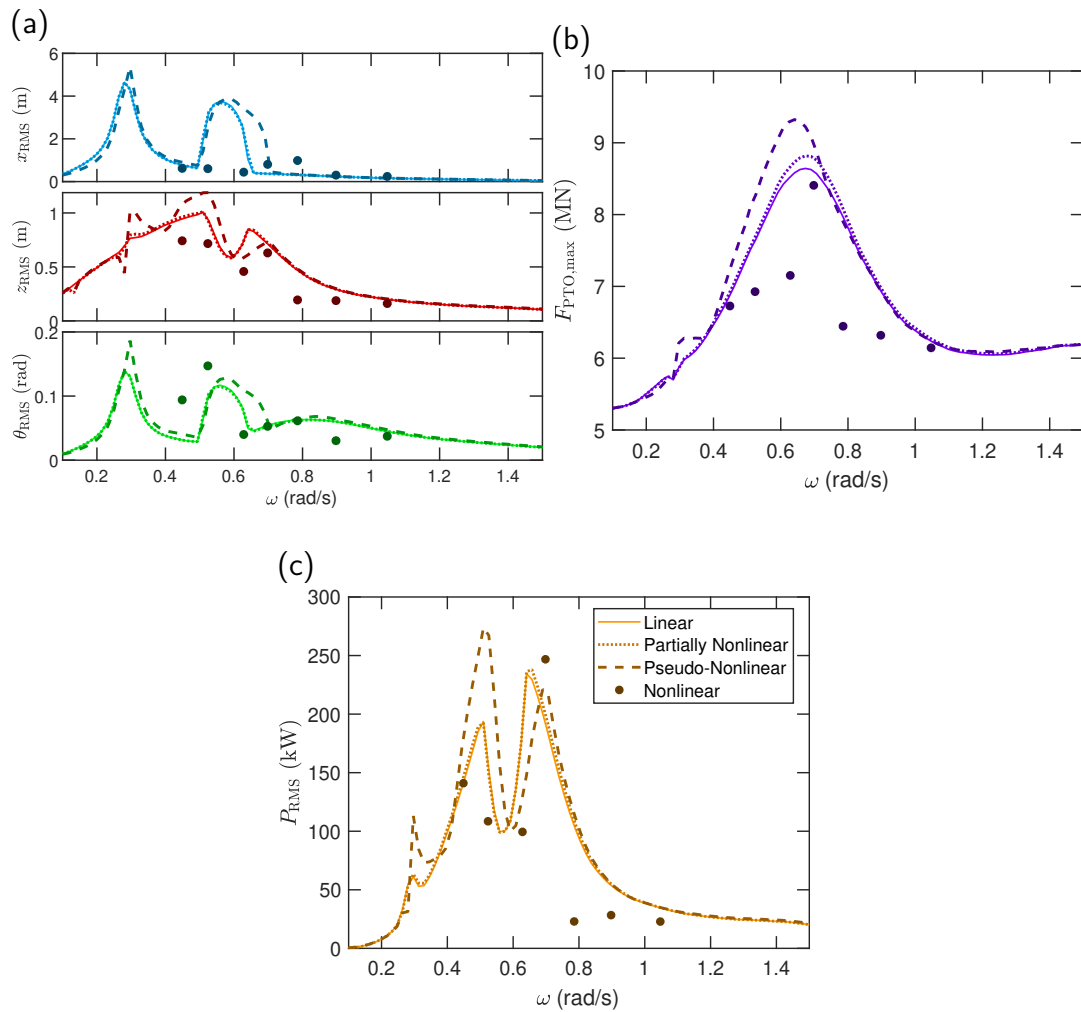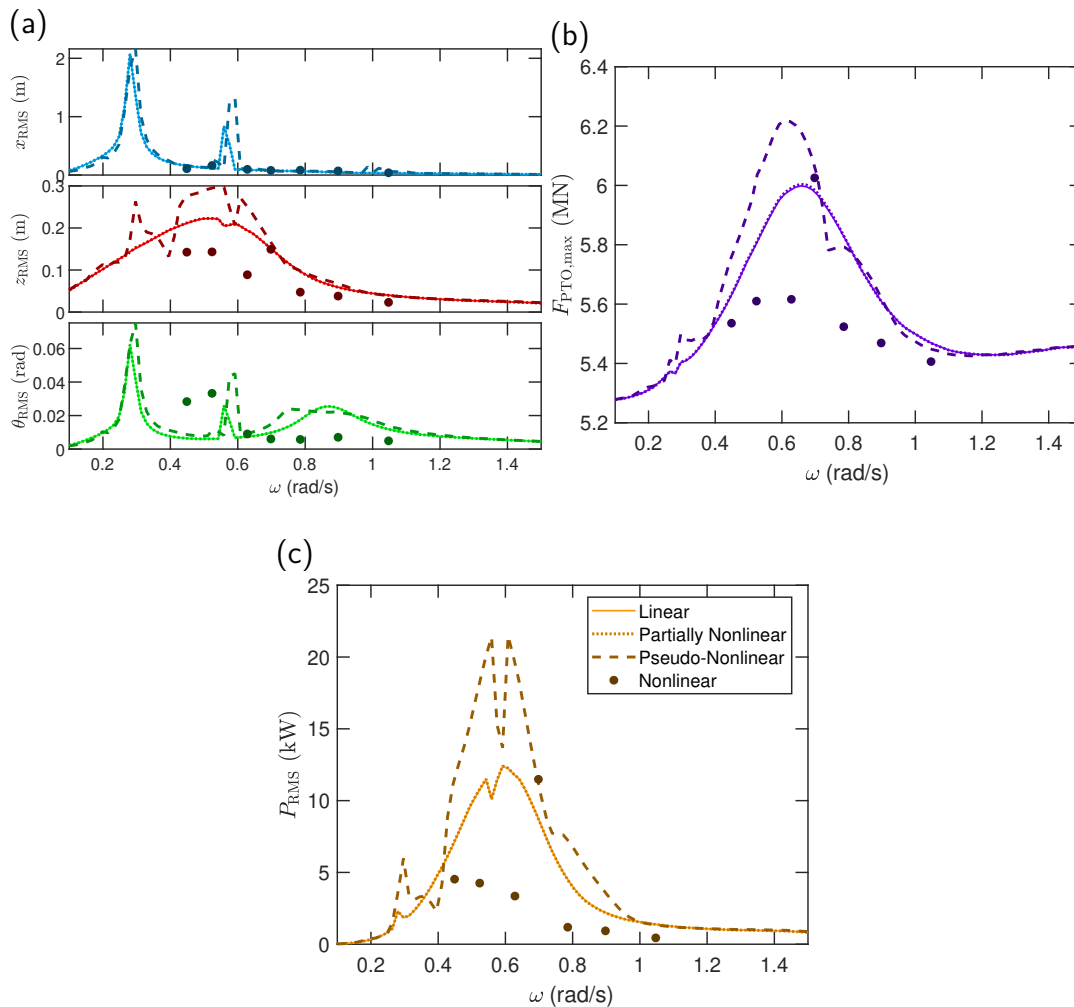
Figure 6.9: The performance characteristics of the WEC at varying excitation frequencies under Scenario 1 conditions for the linear (–), partially nonlinear ($\cdots$), pseudo-nonlinear (- - -), and fully nonlinear (CFD) (●) methods: (a) the RMS of the CETO-like buoy motions, (b) the maximum PTO force of the CETO-like buoy, (c) the power RMS of the CETO-like buoy.

time for each model is given below in Table 6.8.

6.6 Discussion

In all three scenarios, the linear and partially nonlinear kinematics were almost identical. The most significant difference was seen in Scenario 1, specifically in the maximum PTO force where the partially nonlinear results approach the trend seen in the pseudo-nonlinear results (see Figure 6.9b). The pseudo-nonlinear results generally indicate

Figure 6.10: The performance characteristics of the WEC at varying excitation frequencies under Scenario 2 conditions for the linear (–), partially nonlinear (· · ·), pseudo-nonlinear (- - -), and fully nonlinear (CFD) (•) methods: (a) the RMS of the CETO-like buoy motions, (b) the maximum PTO force of the CETO-like buoy, (c) the power RMS of the CETO-like buoy.

a slightly larger amplitude motion response compared to all other models. The CFD results were found to generally have a lower motion RMS, maximum force, and power RMS with the exception of one frequency (see Figure 6.9a). The significant differences between the linear based methods and the CFD indicate that for submerged WEC, the pose-dependent representations of the excitation and radiation forces are insufficient to describe the fluid-structure interaction even for linear wave conditions.

In Scenario 1, the peak in the surge motion is widened in the pseudo-nonlinear model, whereas the linear and partially nonlinear are almost indistinguishable. This
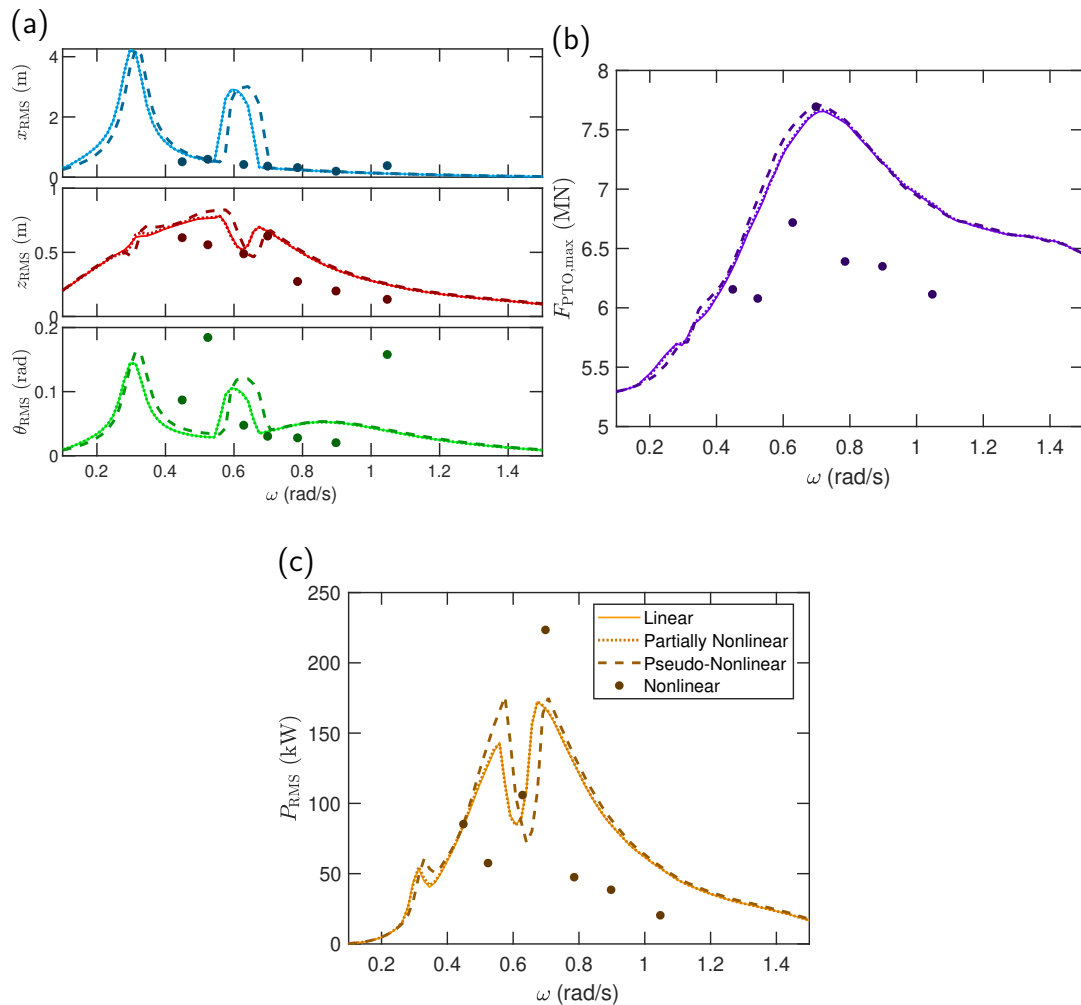
Figure 6.11: The performance characteristics of the WEC at varying excitation frequencies under Scenario 3 conditions for the linear (–), partially nonlinear (· · ·), pseudo-nonlinear (- - -), and fully nonlinear (CFD) (●) methods: (a) the RMS of the CETO-like buoy motions, (b) the maximum PTO force of the CETO-like buoy, (c) the power RMS of the CETO-like buoy.

indicates that the most influential change in the modelling methods was the pose-dependent radiation force representation. Additionally, the heave motion RMS of the pseudo-nonlinear method in some cases shifts towards the CFD results, while in others, shifts away, with no strong trend seen overall.

The most favourable condition in the CFD results is seen at the 9 s wave period, where the power RMS is largest in all models (see Figures 6.9c, 6.10c, and 6.11c). This may be due to strong interaction between heave and surge modes as both seem to be experiencing increased oscillations, as seen in Figure 6.9a. A peak in this frequency region
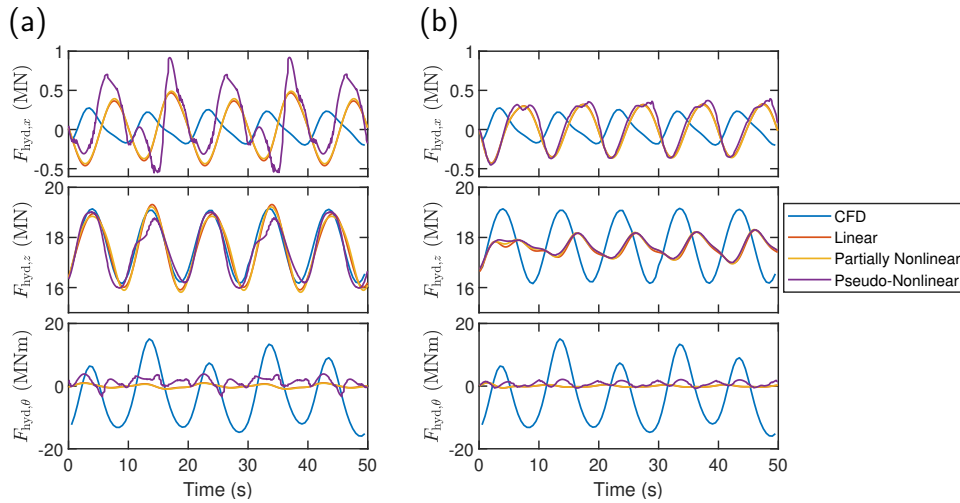
Figure 6.12: The combined hydrodynamic pressure forces of the linear, partially nonlinear, pseudo-nonlinear, and fully nonlinear models when subject to Scenario 1 conditions with a period of 10s: (a) resultant hydrodynamic forces during simulation of each model when the buoy trajectory is not constrained, and (b) resultant hydrodynamic forces during simulation of each model when the buoy trajectory is constrained to follow positions from CFD model.

Table 6.8: Comparison of computation time.

Model	Computation time (s)
Linear	2.3
Partially nonlinear	3.8
Pseudo-nonlinear	30.0
CFD	388221 (4.5 days)

is not predicted in the linear models, and therefore may arise from some inherently nonlinear phenomenon. The motion from the CFD model at this wave period is shown in Figure 6.13. These series of images depict how the body of water above the buoy oscillates up and down resulting in fluid rushing from all sides into the center creating a jet of water. In the situation shown, this occurrence is roughly in phase with the wave. Due to the phase relationship, this effect may be acting to improve oscillation amplitude, whereas for other frequencies, this occurrence would not be in phase with excitation and therefore would destructively interfere with oscillations. This peak in performance is also seen in scenarios 2 and 3, indicating this effect is frequency dependent rather than amplitude or submergence depth dependent.

Similar shifts in motion RMS are seen in Scenario 2, where the heave motions are also changed, and the surge peaks have shifted slightly to higher frequencies. Under

(a) $t = 50$ s.

(b) $t = 51$ s.

(c) $t = 52$ s.

(d) $t = 53$ s.

(e) $t = 54$ s.

(f) $t = 55$ s.

(g) $t = 56$ s.

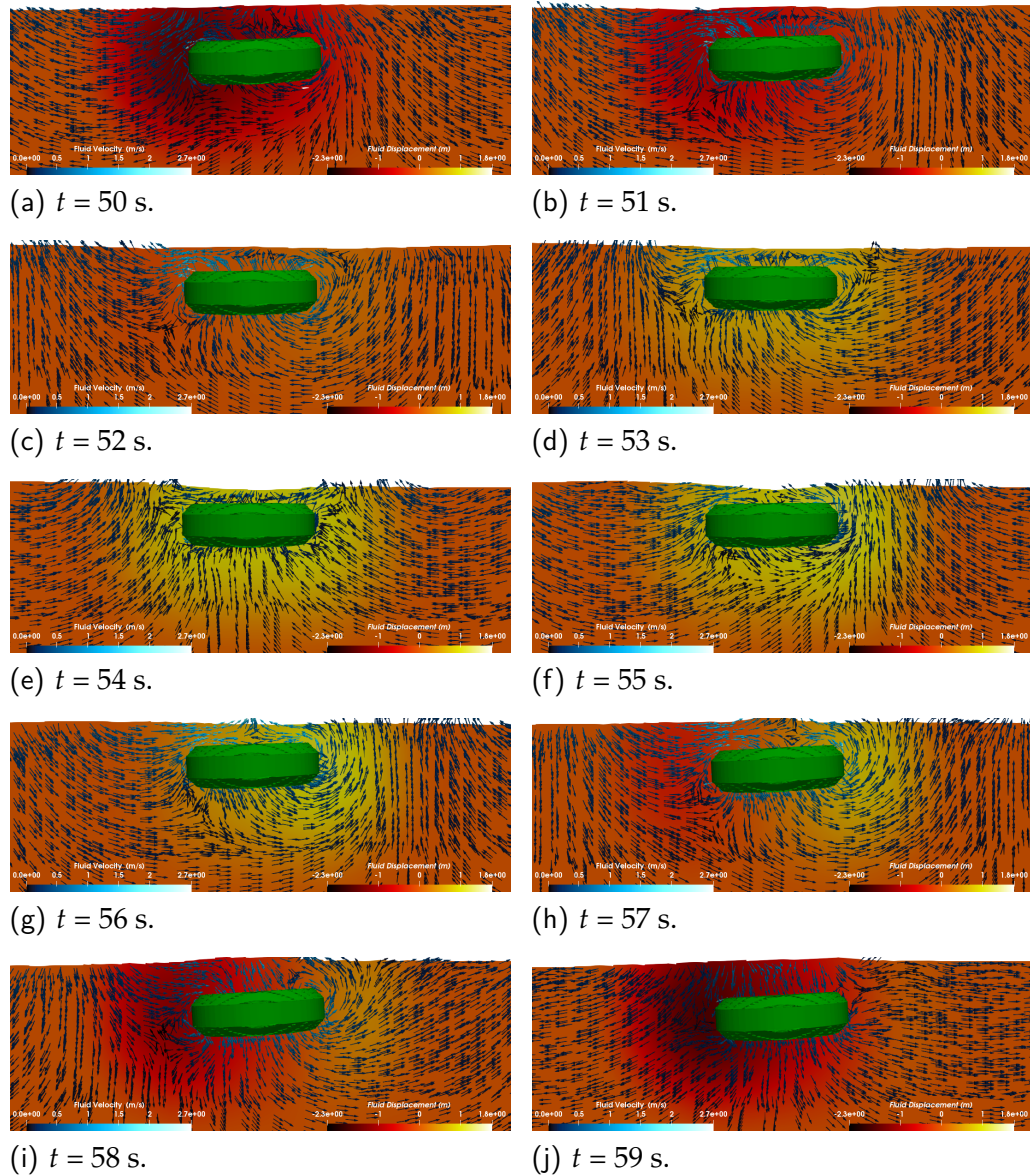(h) $t = 57$ s.

(i) $t = 58$ s.

(j) $t = 59$ s.

Figure 6.13: The buoy in the NWT during operation. The fluid velocity and position are
shown for Scenario 1 conditions with a 9 s period wave.

this lower amplitude excitation, the heave motion RMS in the pseudo-nonlinear method
forms multiple peaks and shows a stronger coupling to surge and pitch motions. The
trends of the PTO force in Scenario 2 are similar to the results from Scenario 1 in that the
pseudo-nonlinear method predicts larger forces for low frequency waves and converges
to the forces found in CFD simulations at higher frequency waves. The pseudo-nonlinear
method shows more prominent peaks for the power generation performance but are

generally poorer estimates of the CFD results than the other linear models.

When the submergence depth was increased in Scenario 3, the differences between the linear, partially nonlinear, and pseudo-nonlinear reduce. This aligns with the understanding that more hydrodynamic nonlinearity occurs closer to the surface. However, the trends of the linear results still do not typically follow the fully nonlinear results, indicating that the linear models do not account for important fluid interactions. The hydrodynamic pressure forces from CFD Scenario 1 with wave period of 9 s were compared with the combined excitation and radiation force simulated in the three linear models in Figure 6.12a to further understand what modelling deficiencies are present. These results show reasonably good matching between the heave hydrodynamic forces but a poor phase and amplitude match in the surge and pitch hydrodynamic forces. For these hydrodynamic forces, different trajectories were followed due to the different modelling methods. To eliminate this modelling discrepency, the linear models were subject to the motion seen in the CFD simulations and the resulting forces are given in Figure 6.12b. A large difference between all forces is seen, with the most inconsistent being the pseudo-nonlinear hydrodynamic force. The significant difference in pitch is thought to be due to transient effects and the result of the oscillating water above the buoy. Drag forces from the CFD simulations were found to be negligible compared to the other hydrodynamic forces in this case. These results again show that linear methods are not capable of quantifying significant nonlinearities for a WEC of this shape and type.

The disparity between validated nonlinear CFD model and the pseudo-nonlinear and linear models demonstrate that the nonlinearity of the hydrodynamic excitation and radiation force is not the major nonlinearity in the system. The CFD model depicted in Figure 6.13 demonstrates that the fluid around the buoy is subject to some nonlinear flow characteristic as the body of fluid above the buoy seems to oscillate with the buoy rather than with the wave. The large diameter of the CETO buoy relative to the submergence depth may be the reason for this significant impact the fluid structure interaction leading to perturbation of the body of water above the oscillating buoy. This situation is not accounted for within the presented linear models and may be the source of the large discrepancy. For such systems, these linear models evidently lack the fidelity to appropriately replicate experimental results.

In practice, the full 6DOF system should be considered. For the purposes of this study, the axisymmetric submerged PA was restricted to 3DOF to further explore the use of linear potential flow models in representing the relevant hydrodynamics. It should be noted that this restriction prevents the model from predicting parametric excitation of roll, sway, and yaw modes of oscillation. These features could be implemented by extending the model to 3DOF, which is conceptually no more challenging but requires more computation.

The findings show that the excitation forces are not always the major nonlinearity for PA WEC, which disagrees with current understandings of PA considerations [8]. Specifically, the pseudo-nonlinear method which includes the nonlinearity due to pose in the excitation and radiation forces is seen in this work to be inadequate for replicating the nonlinear results. For large flat submerged buoys, there seems to be a dominant nonlinearity in the coupling between the buoy and the body of water above the buoy. One recommendation arising from this work is to use the hydrodynamic forces from the CFD model and linear models to quantify the impact of the nonlinearity and construct an additional term to implement within the linear model. Some possible approaches include regression techniques to parameterise parts of the nonlinear hydrodynamic interaction. This approach may approximate some nonlinear aspects seen in fully nonlinear systems and improve the fidelity and simulation speed of the overall model. Such models are important for design and optimisation purposes.

6.7   Conclusion

This study compared four models of a submerged PA WEC; specifically, linear, partially nonlinear, pseudo-nonlinear, and fully nonlinear models were presented. The linear uses hydrodynamic parameters calculated using linear BEM tools about a single nominal position, the partially nonlinear model uses the same linear tools to implement gain scheduling to introduce pose dependence in the excitation forces. The pseudo-nonlinear uses hydrodynamic parameters calculated for a range of orientations and positions to incorporate the nonlinear pose-dependence for excitation and radiation forces. The constructed fully nonlinear CFD model was validated against experimental data from literature. The comparison between models showed that in all cases, the linear based models were insufficient to quantify the nonlinear fluid-structure interactions. Specifically, a frequency dependent nonlinearity was identified as the body of water above the buoy oscillating. This oscillation caused significant disruption and the breakdown of linear wave approximations. The nonlinearity in the excitation force was small compared to the nonlinearity in the radiation force, but both excitation and radiation nonlinearities diminished with increased submergence depth. Introducing pose dependent hydrodynamic forces as presented in this paper tends to overestimate the motion. However, at higher frequencies the linear and nonlinear models converged to give similar results. Overall the identified difference in hydrodynamic forces is significant but seemed frequency dependent and periodic. If this nonlinearity can be quantified, it may be possible to implement into the linear models to improve the fidelity and speed leading to more suitable models for optimisation.

Acknowledgement

References

[1] J. Cruz. *Ocean Wave Energy*. 1st ed. Springer-Verlag Berlin Heidelberg, 2008. DOI: 10.1007/978-3-540-74895-3.

[2] B. Drew, A. R. Plummer, and M. N. Sahinkaya. "A review of wave energy converter technology". In: *Proceedings of the Institution of Mechanical Engineers, Part A: Journal of Power and Energy* 223.8 (2009), pp. 887–902. DOI: 10.1243/09576509JPE782. eprint: http://dx.doi.org/10.1243/09576509JPE782.

[3] P. Hardy et al. "A maximum capture width tracking controller for ocean wave energy converters in irregular waves". In: *Ocean Engineering* 121 (2016), pp. 516–529. DOI: http://dx.doi.org/10.1016/j.oceaneng.2016.05.045.

[4] J. Chozas. *INTERNATIONAL LEVELISED COST OF ENERGY FOR OCEAN ENERGY TECHNOLOGIES An analysis of the development pathway and Levelised Cost Of Energy trajectories of wave, tidal and OTEC technologies*. Tech. rep. Ocean Energy Systems, May 2015.

[5] A. Rafiee and J. Fiévez. "Numerical prediction of extreme loads on the CETO wave energy converter". In: *Proceedings of the 11th European Wave and Tidal Energy Conference, Nantes, France*. 2015.

[6] C. Windt, J. Davidson, and J. V. Ringwood. "High-fidelity numerical modelling of ocean wave energy systems: A review of computational fluid dynamics-based numerical wave tanks". In: *Renewable and Sustainable Energy Reviews* 93 (Oct. 2018), pp. 610–630. DOI: 10.1016/j.rser.2018.05.020.

[7] J. Davidson, S. Giorgi, and J. V. Ringwood. "Linear parametric hydrodynamic models for ocean wave energy converters identified from numerical wave tank experiments". In: *Ocean Engineering* 103 (2015), pp. 31–39. DOI: http://dx.doi.org/10.1016/j.oceaneng.2015.04.056.

[8] M. Penalba, G. Giorgi, and J. V. Ringwood. "Mathematical modelling of wave energy converters: A review of nonlinear approaches". In: *Renewable and Sustainable Energy Reviews* 78 (Oct. 2017), pp. 1188–1207. DOI: 10.1016/j.rser.2016.11.137.

[9]   G. Giorgi and J. V. Ringwood. "Comparing nonlinear hydrodynamic forces in heaving point absorbers and oscillating wave surge converters". In: *Journal of Ocean Engineering and Marine Energy* 4.1 (Aug. 2017), pp. 25–35. DOI: 10.1007/s40722-017-0098-2.

[10] E. Guerber et al. "A fully nonlinear implicit model for wave interactions with submerged structures in forced or free motion". In: *Engineering Analysis with Boundary Elements* 36.7 (July 2012), pp. 1151–1163. DOI: 10.1016/j.enganabound.2012.02.005.

[11] M. Penalba et al. "Influence of nonlinear Froude–Krylov forces on the performance of two wave energy points absorbers". In: *Journal of Ocean Engineering and Marine Energy* 3.3 (June 2017), pp. 209–220. DOI: 10.1007/s40722-017-0082-x.

[12] A. Merigaud, J.-C. Gilloteaux, and J. V. Ringwood. "A nonlinear extension for linear boundary element methods in wave energy device modelling". In: *Volume 4: Offshore Geotechnics; Ronald W. Yeung Honoring Symposium on Offshore and Ship Hydrodynamics*. ASME, July 2012. DOI: 10.1115/omae2012-83581.

[13] A. McCabe, G. A. Aggidis, and T. Stallard. "A time-varying parameter model of a body oscillating in pitch". In: *Applied Ocean Research* 28.6 (2006), pp. 359–370.

[14] L. Letournel et al. "Weakly nonlinear modeling of submerged wave energy converters". In: *Applied Ocean Research* 75 (June 2018), pp. 201–222. DOI: 10.1016/j.apor.2018.03.014.

[15] M. Penalba and J. V. Ringwood. "Linearisation-based nonlinearity measures for wave-to-wire models in wave energy". In: *Ocean Engineering* 171 (Jan. 2019), pp. 496–504. DOI: 10.1016/j.oceaneng.2018.11.033.

[16] G. Giorgi and J. V. Ringwood. "Relevance of pressure field accuracy for nonlinear Froude–Krylov force calculations for wave energy devices". In: *Journal of Ocean Engineering and Marine Energy* 4.1 (Dec. 2017), pp. 57–71. DOI: 10.1007/s40722-017-0107-5.

[17] G. Giorgi and J. V. Ringwood. "A compact 6-DoF nonlinear wave energy device model for power assessment and control investigations". In: *IEEE Transactions on Sustainable Energy* 10.1 (Jan. 2019), pp. 119–126. DOI: 10.1109/tste.2018.2826578.

[18] L. Papillon et al. "Parametric modelling of a reconfigurable wave energy device". In: *Ocean Engineering* 186 (Aug. 2019), p. 106105. DOI: 10.1016/j.oceaneng.2019.06.010.

[19] D. J. Crooks. "Nonlinear hydrodynamic modelling of an oscillating wave surge converter". PhD thesis. Queen's University Belfast, 2017.

[20] B. W. Schubert et al. "Pseudo-Nonlinear Hydrodynamic Coefficients for Modelling Point Absorber Wave Energy Converters". In: *The 4th Asian Wave and Tidal Energy Conference, Taipei*. 2018.

[21] M. Penalba, T. Kelly, and J. V. Ringwood. "Using NEMOH for modelling wave energy converters: a comparative study with WAMIT". In: *Centre for Ocean Energy Research (COER), Maynooth University, Co. Kildare, Ireland* (2017).

[22] S.-C. Jiang et al. "Analytical Solution of a Wave Diffraction Problem on a Submerged Cylinder". In: *Journal of Engineering Mechanics* 140.1 (Jan. 2014), pp. 225–232. DOI: 10.1061/(asce)em.1943-7889.0000637.

[23] W. Cummins. *The impulse response function and ship motions*. Tech. rep. David Taylor Model Basin, Washington DC, 1962.

[24] T. Perez and T. I. Fossen. "A Matlab toolbox for parametric identification of radiation-force models of ships and offshore structures". In: *Modeling, Identification and Control: A Norwegian Research Bulletin* 30.1 (2009), pp. 1–15. DOI: 10.4173/mic.2009.1.1.

[25] MathWorks. *MATLAB Control System Toolbox: LPV System*. The MathWorks, Natick, MA, USA. 2019.

[26] J. Orszaghova et al. "Transverse motion instability of a submerged moored buoy". In: *Proceedings of the Royal Society A: Mathematical, Physical and Engineering Sciences* 475.2221 (Jan. 2019), p. 20180459. DOI: 10.1098/rspa.2018.0459.

[27] J. Falnes. *Ocean waves and oscillating systems: Linear interactions including wave-energy extraction*. Cambridge University Press, 2002.

[28] N. Sergiienko et al. "Feasibility study of the three-tether axisymmetric wave energy converter". In: *Ocean Engineering* 150 (Feb. 2018), pp. 221–233. DOI: 10.1016/j.oceaneng.2017.12.055.

[29] B. Le Méhauté. *An introduction to hydrodynamics and water waves*. Springer Science & Business Media, 2013.

Chapter 7

Nonlinear stiffness enhancement of submerged wave energy device in high fidelity model

The previous chapters identify the benefit of a nonlinear stiffness mechanism, showed that the impact of a fully nonlinear hydrodynamic representation of fluid-structure interaction is significant, and identified linear potential flow models are insufficient to capture some of the significant hydrodynamic influences. Therefore, the nonlinear stiffness models should be extended to a high fidelity scenario to attain a more representative estimate of device performance.

This chapter combines a nonlinear stiffness representation into a validated CFD scenario for both regular and irregular waves. This chapter is designed to answer the following research question: *How does a nonlinear stiffness mechanism affect the system performance of a submerged WEC under high fidelity hydrodynamic fluid-structure interactions in three degrees of freedom?*

This section consists of the submitted journal article:

Schubert, B.W., Robertson, W.S., Cazzolato, B.S., Ghayesh, M.H. and Sergiienko, N.Y., 2020. Nonlinear stiffness enhancement of submerged wave energy device in high fidelity model. Submitted to *Renewable Energy.*

Statement of Authorship

Title of Paper	Nonlinear stiffness enhancement of submerged wave energy device in high fidelity model
Publication Status	☐ Published ☐ Accepted for Publication ☑ Submitted for Publication ☐ Unpublished and Unsubmitted work written in manuscript style
Publication Details	Schubert, B.W., Robertson, W.S., Cazzolato, B.S., Ghayesh, M.H. and Sergiienko, N.Y., 2020. Nonlinear stiffness enhancement of submerged wave energy device in high fidelity model. Submitted to Renewable Energy.

Principal Author

Name of Principal Author (Candidate)	Benjamin Schubert
Contribution to the Paper	Developed ideas and concepts • Conducted a comprehensive literature review • Outlined the concepts of the paper to address the gaps in literature based on knowledge of the field Performed the modelling • Developed a structured mesh of a CETO-shaped buoy in the CFD software OpenFOAM • Varied different mesh and dynamic parameters and methods of calculation to find suitable CFD simulation • Validated the CFD model using data found in literature • Performed convergence studies for regular waves of different frequencies, irregular waves, and the nonlinear stiffness control system in CFD model. • Developed a model of the CETO-shaped buoy to estimate the hydrodynamic parameters using the potential flow solver NEMOH • Developed a simulation in Simulink to predict the dynamic behaviour of the CETO-shaped wave energy converter • Varied the control system of the dynamic simulations emphasise different performances • Optimised control parameters for the regular and irregular wave contexts • Parameterised nonlinear stiffness force and implemented into dynamic model in both CFD and Simulink models Interpreted results • Collected and stored data from simulation results • Post processed the data using Matlab and ParaView • Performed spectral analysis of time domain results • Interpreted results between different scenarios Writing • Solely developed the first full draft of the manuscript • Applied comments provided by all co-authors • Acting as corresponding author.
Overall percentage (%)	80%
Certification:	This paper reports on original research I conducted during the period of my Higher Degree by Research candidature and is not subject to any obligations or contractual agreements with a third party that would constrain its inclusion in this thesis. I am the primary author of this paper.

Signature		Date	2/2/2021

Co-Author Contributions

By signing the Statement of Authorship, each author certifies that:

i.   the candidate's stated contribution to the publication is accurate (as detailed above);

ii. permission is granted for the candidate in include the publication in the thesis; and

iii. the sum of all co-author contributions is equal to 100% less the candidate's stated contribution.

Name of Co-Author	William Robertson		
Contribution to the Paper	Participated in developing the ideas and concepts, assisted in analysing and interpreting the obtained results, and provided revision of manuscript. Provided critical understanding of signal processing techniques employed. Provided expertise and advice on the magnetic concepts and code employed in the development of this paper.		
Signature		Date	15/02/2021

Name of Co-Author	Benjamin Cazzolato		
Contribution to the Paper	Participated in developing the ideas and concepts, assisted in analysing and interpreting the obtained results, and provided revision of manuscript. Provided critical understanding of signal processing techniques employed.		
Signature		Date	15/02/2021

Name of Co-Author	Mergen Ghayesh		
Contribution to the Paper	Participated in developing the ideas and concepts, assisted in analysing and interpreting the obtained results, and provided revision of manuscript.		
Signature		Date	18/02/2021

Name of Co-Author	Nataliia Sergiienko		
Contribution to the Paper	Participated in developing the ideas and concepts, assisted in analysing and interpreting the obtained results, and provided revision of manuscript. Provided a code template related to using the linear hydrodynamics tool NEMOH.		
Signature		Date	15/02/2021

Please cut and paste additional co-author panels here as required.

Nonlinear stiffness enhancement of a submerged wave energy device in a high fidelity model

B. W. Schubert, W. S. P. Robertson, B. S. Cazzolato, N. Y. Sergiienko, M. H. Ghayesh

Abstract

A three degree of freedom submerged wave energy converter with a nonlinear stiffness mechanism was modelled using both linear and nonlinear hydrodynamics. The linear hydrodynamics scenario used linear potential flow methods to predict the fluid-structure interaction, while the nonlinear hydrodynamic scenario use computational fluid dynamics (OpenFOAM). The potential energy of the nonlinear stiffness mechanism was varied relative to the potential energy of the incident wave. The wave energy converter was excited using regular and irregular waves. The nonlinear stiffness scenarios were compared to scenarios with optimised linear control parameters. When compared to optimal conditions, models using linear hydrodynamics to emulate both regular and irregular waves showed no improvement in power generation. In the regular wave nonlinear hydrodynamic scenarios, the nonlinear stiffness showed inconsistent improvements to power production and significant detuning at different levels of nonlinearity. The irregular wave scenario using nonlinear hydrodynamic methods demonstrated a small improvement compared to optimised linear control parameters when the nonlinear stiffness potential energy peak was less than half the potential energy of the incident wave. The nonlinear stiffness improved the robustness of the wave energy converter, and was an effective method for detuning the system, depending on the degree of nonlinearity.

7.1 Introduction

Ocean wave energy is part of the emerging marine renewable energy sector. To improve the viability of ocean wave energy, the performance of potential wave energy devices must be enhanced. This paper explores the application of a novel nonlinear stiffness mechanism to a submerged wave energy device within a high fidelity CFD model, in order to improve the power generating potential.

Renewable energy currently accounts for a quarter of total energy production. By 2050, the share of renewable energy in the total energy supply may rise to 63% [1]. The largest contributors will be solar photovoltaic and wind. While these forms of energy production have a competitive levelised cost of energy compared to conventional energy generation [2], the daily fluctuation creates large variation in the instantaneous power demand, which may not be sufficiently addressed with conventional base load coal (or
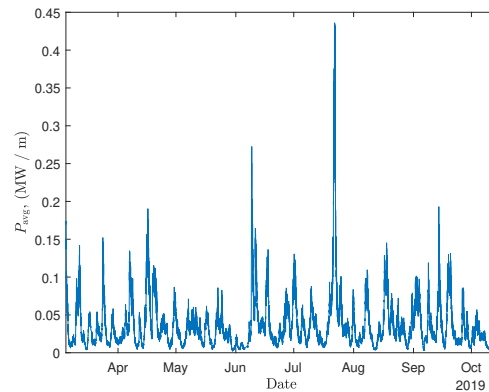
Figure 7.1: The measured power (per metre of wave crest length) in ocean waves off the coast of Torbay, Western Australia between the 5th of March 2019 and 14th of October 2019. The power is calculated from the wave spectra measured every half hour by assuming deep water waves [3]. The water depth and wavelength of waves observed at Torbay are not sufficient to classify the waves as deep water waves. Therefore, the values of power provided in this figure are not truly represented, but are sufficient to demonstrate the substantial seasonality of such wave climates.

gas) generation due to the cycle down and up times. A less variable renewable energy source to provide a base load, such as ocean wave energy, may offer a solution to the fluctuations of conventional renewable energy in some scenarios. As an example, the wave power off the coast of Torbay, Western Australia between the 5th of March 2019 and 14th of October 2019 is given in Fig. 7.1 (data available from the University of Western Australia at https://wawaves.org/). As seen, the observed daily fluctuations seen in ocean waves are relatively small and change over the course of days rather than hours. This demonstrates the potential of wave energy as a source of base load renewable energy. For wave energy to become economically feasible, a control strategy to enhance the power generated for local and variable wave conditions should be constructed. Due to the immense set-up costs, it is impractical to test these control strategies in situ. Therefore, sophisticated and reliable models must be constructed to optimise, develop, and test control systems of wave energy devices.

There have been many different WECs proposed over several decades, with many fundamentally different modes of operation [4]. A common subset of WECs known as PA typically have an axisymmetric geometry which is small relative to incident wavelengths [5]. One of the benefits of a PA is the insensitivity to wave direction, rendering PAs versatile for changing ocean conditions. There are both floating and submerged variations of PA such as the WEC by CorPower Ocean [6] and the CETO device by Carnegie Clean Energy [7], respectively. This research will focus on submerged buoys. Such buoys are typically pretensioned to counteract the buoyancy force and
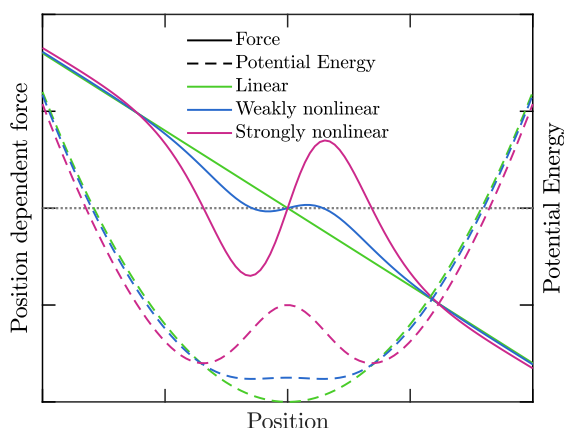
Figure 7.2: A heuristic example of how the additional nonlinear stiffness term may impact the position-dependent force and potential energy profile. A linear, weakly nonlinear, and strongly nonlinear stiffness is presented to provide an intuitive comprehension of such additions. The grey dotted line indicates zero force.

consequently require some form of reactive control to tune for particular wave conditions. There have been many active and passive control strategies proposed to improve the performance of WECs. Some examples of active strategies include latching, declutching, and reactive loading control [8]. However, for optimal control, knowledge of the future wave is required [9]. There has been a recent attempt at wave force predictions which used a Kalman filter as an estimator of the wave force, and then an autoregressive model to predict the future force for a required time horizon [10]. However, further work is required to improve the applicability of such methods. Passive control strategies may be an attractive solution to the difficulty of active control strategies which rely on estimating complex fluid-structure interactions [11]. One type of passive control is the introduction of a nonlinear stiffness element (using conventional springs, or via magnetic/pneumatic means) which can lead to stronger coupling between modes of motion such as converting lower frequency oscillations into higher frequency oscillation, broadening the bandwidth of the device, or promoting less periodic dynamics [12]. This feature has the potential to be beneficially exploited for power generation. Additionally, if the nonlinearity of the stiffness is extended, it may create regions of negative stiffness and form a situation where two or more stable regions exist; if two stable regions exist the system is said to be bistable. An example of the nonlinear stiffness, position-dependent force, and potential energy trends of the position-dependent force are provided in Fig. 7.2. There exists a number of demonstrated benefits of such nonlinear mechanisms for the context of energy harvesting [12]. In particular, stochastic resonance [12] may be used to effectively shift the low amplitude oscillations of broadband signals to larger amplitude oscillations, which may shift the vibrations into a more favourable range for power

generation. Research focussed on using magnetic forces (or similar) for vibration energy harvesting [13–17] provide a good framework to build upon the application of wave energy.

Current research involving similar nonlinear stiffness mechanisms focused on WECs have been directed towards floating devices. In many cases the validity of the findings may have been undermined by: particular limitations in the form of model assumptions; comparisons to suboptimal conditions; and, low fidelity representations of hydrodynamics. A range of nonlinear augmentations and limitations will be discussed in the following sections as well as how these limitations will be addressed in this study.

7.1.1 Model assumptions of nonlinear stiffness in literature

It is necessary to make assumptions to simplify a model as a means to understand the underlying dynamics in preliminary studies. For the context of WECs augmented with nonlinear mechanisms, such simplifications include:

- a reduction of degrees of freedom (DOFs) modelled [11, 18–25],;

- neglecting viscous drag [11, 19–24, 26];

- not accounting for some hydrodynamic effects [13]; or,

- restricting the excitation of the model to unrealistic simple sinusoidal waves [11, 20, 22, 23].

The reduced DOF models may result in significant nonlinear behaviour not being captured [27]. While single DOF models may capture the basic system behaviour and are an appropriate starting point for linear systems, the introduction of nonlinearities requires the use of higher fidelity simulations to give better approximation of hydrodynamic forces for more reliable conclusions. For a floating PA, previous work has concluded that viscous drag contributes a relatively small nonlinearity [28] and so may reasonably be neglected for some devices. However, this may not be true when introducing a nonlinear stiffness or bistable mechanism. Including all hydrodynamic effects is a critical step in understanding how such wave energy systems will perform. Cases in which models are only excited by regular sinusoidal waves can give indicative results for how a device will perform under narrowband excitation. However, nonlinearities often involve cross couplings between different modes of oscillation. It is therefore difficult to classify the performance of a device with nonlinear stiffness under stochastic excitation (real ocean conditions) purely from simple monochromatic excitation.

This study addresses these modelling limitations by presenting a submerged quasi-PA model to a 3 DOF (surge, heave, and pitch) system to simulate additional modes of motion. Viscous drag coefficients based on literature values [29] are included within

linear hydrodynamic simulations. These linear hydrodynamic simulations are compared to a fully nonlinear hydrodynamic CFD model, which has been validated and demonstrates convergence for the nonlinear stiffness addition. In order to form a stronger understanding of real world application, both regular and irregular excitation scenarios are simulated, and are compared to optimised conditions found under linear hydrodynamic conditions.

7.1.2 Suboptimal comparisons

Previous research has attempted to identify and quantify the improvement that nonlinear stiffness can provide theoretically. However, the major shortcoming of most pertinent research is the comparison of the nonlinear stiffness scenario with a suboptimal linear case [19, 24, 30]. Some studies optimised the power take off (PTO) damping [24, 26], and found that a nonlinear stiffness or bistable mechanism can greatly improve the efficiency of a floating buoy WEC. However, the models did not include a linear stiffness force, so could be considered sub-optimally tuned initially. Additionally, some of the proposed models were restricted to a single DOF [19, 24, 26], and only examined regular wave cases [24]. Another study presents a floating PA with a linear, cubic, and quintic stiffness to create monostable, bistable, and tristable scenarios, respectively [21]. This study optimised the PTO damping but did not optimise the linear stiffness, was restricted to 1 DOF, and examined both regular and irregular waves. The findings of this study showed that nonlinear stiffness may be used to enhance the robustness of the WEC to irregular wave excitation. There have been experimental studies which show remarkable improvement in the efficiency of the device [30, 31] but only when compared against suboptimal conditions. These studies emphasise how such nonlinear devices can improve the robustness of systems by partially tuning WECs for various conditions when compared to untuned or poorly tuned conditions.

The present research optimises the linear PTO stiffness and damping for both regular and irregular conditions, and use these as the basis of comparison for the improvement seen arising from the nonlinear stiffness component.

7.1.3 Linear and nonlinear hydrodynamics

For a submerged body, the hydrodynamic interaction between the structure and the surrounding fluid can be modelled via a variety of methods. These methods range between using linear diffraction-radiation boundary element methods potential flow solvers such as NEMOH (L'École Centrale De Nantes, Nantes, France) or WAMIT (WAMIT, Inc., Chestnut Hill MA, USA) to fully nonlinear validated CFD models, as well as many intermediate methods. Linear potential flow based models calculate hydrodynamic coefficients to quantify the hydrodynamic added mass and radiation damping to quantify

the excitation force acting on the buoy due to the wave, and the force due to the buoy radiating waves. These linear models do not account for nonlinearities due to variation in buoy pose, and assumes that the waves and fluid behave completely linearly. Such linear models are typically only accurate for conditions such as small motions, low amplitude waves, or near equilibrium conditions [32]. For the context of a submerged quasi-PA, both NEMOH and WAMIT provide almost identical results [33]. In contrast to linear hydrodynamic models, are the fully nonlinear CFD models, in which a numerical wave tank (NWT) is constructed and the Navier Stokes equations are numerically solved by discretising spatially and temporally. Such CFD models are more computationally expensive [34], but if validated, can be excellent tools in accurately quantifying various nonlinear hydrodynamic effects.

Other methods to quantify fluid-structure interaction, with varying degrees of fidelity, have been detailed extensively [28]. One indicative example is the pseudo-nonlinear hydrodynamics model [27, 35], proposed by the same authors of this paper, in which a linear potential flow solver is used to pre-calculate the various hydrodynamic properties over a range of poses. The hydrodynamic forces are then found during simulation through gain scheduling methods. This method did exhibit similar trends over a range of frequencies as seen in a CFD model for linear conditions, but failed to characterise influential nonlinearities, demonstrating that models based on linear potential flow theory are not sufficient to satisfactorily characterise fluid-structure interaction for submerged quasi-PA WECs for general wave conditions. One reason for this is the assumptions of linear theory that the wave height is small compared to the wavelength and the water depth. The fluid flow in the shallow region above the buoy does not satisfy these linear theory assumptions for typical incident waves. Furthermore, the waves above such a structure become very steep and often break, significantly deviating from the sinusoidal variation presumed by linear theory [36]. This influences the resultant hydrodynamic forces and the resultant device motion responses.

The inclusion of high fidelity hydrodynamics within models employing a nonlinear stiffness mechanism is a current gap within the literature. One of our previous studies analysed a 3 DOF submerged quasi-PA for both optimal and suboptimised PTO stiffness, for regular and irregular wave conditions [37]. This study showed that the addition of nonlinear stiffness did not, in general, improve the power production capability of the WEC, but did make it more robust to changing sea conditions and could provide a passive control mechanism if the parameters were selected appropriately for a given location. That study only used linear hydrodynamic coefficients found from potential flow models. To address this limitation, this paper presents a model with linear hydrodynamics and a nonlinear stiffness mechanism and are compared to counterpart simulations using nonlinear hydrodynamics.

The contributions of this study to the wider research field can be summarised as:

- quantifying the real potential benefit of a nonlinear stiffness mechanism to submerged WECs by comparing against optimised linear passive control systems;

- improving the fidelity of performance estimates by extending the model to 3 DOF, incorporating additional hydrodynamic effects, and exciting the system by more representative ocean conditions; and,

- implementing the nonlinear stiffness mechanism in a validated fully nonlinear hydrodynamic CFD model to further explore the potential of the adapted passive control system.

The linear and nonlinear models employed in this study will be detailed in Section 7.2. The optimisation and control considerations are presented in Section 7.3 and the specific simulation parameters given in Section 7.4. The resultant findings will be presented and discussed in Section 7.5, with the conclusions outlined in Section 7.6.

7.2 Mathematical models

While there are many different WEC designs [4], this paper uses the CETO-shaped submerged quasi-PA as shown in Fig. 7.3 as a representative device which provides three independent degrees of freedom (assuming x-z plane of symmetry). The geometric parameters of the model are given in Table 7.1.
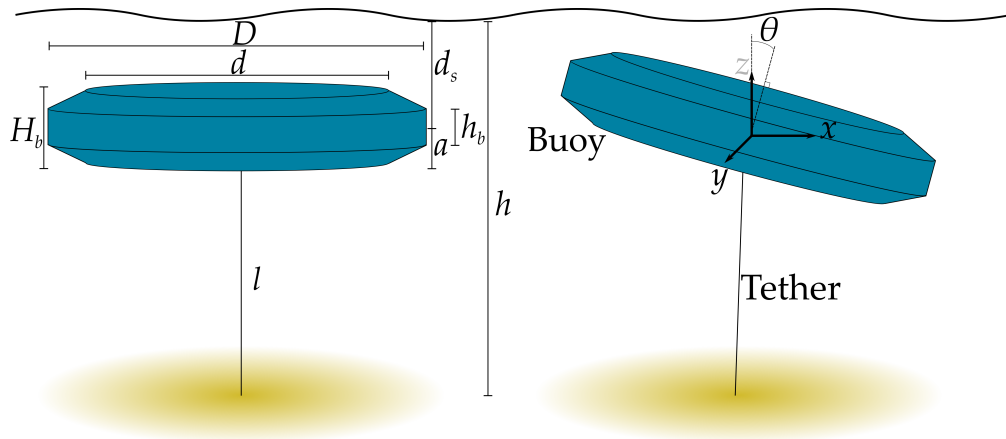

Figure 7.3: A schematic of the CETO-shaped submerged buoy used in this study with various geometric features (defined in Table 7.1) and a coordinate system annotated. The origin of the coordinate system is at the nominal position and directions of the surge (x), heave (z), and pitch (θ) positions of the buoy are provided.

To simulate this quasi-PA, two distinct hydrodynamic models were employed. The fundamental difference between them were the methods to quantify the fluid-structure

Table 7.1: Geometric parameters. All dimensions are in metres.

Parameter	Value
Depth of water, h	40
Attachment arm, a	3
Original tether length, l	30
Outer diameter, D	20
Inner diameter, d	17
Outer height, H_b	6
Inner height, h_b	3
Submersion depth (buoy center), d_s	7

interaction. The first model primarily employed a linear potential flow solver (NEMOH) to estimate hydrodynamic parameters, which were combined within a Simulink simulation to calculate the response of the WEC system to a both regular and irregular wave excitations. This model did include some nonlinearities such as geometric variation of tether forces, position dependence of excitation forces, and viscous drag. However, for the purposes of nomenclature, this model will be referred to as the linear model. The second model uses an OpenFOAM CFD NWT to simulate the motion of the submerged buoy. This numerical solver calculates the hydrodynamic pressure and viscous forces acting on the buoy. The individual forces and considerations of each model is discussed in the following subsections.

7.2.1   Linear model

The dynamics of the system is governed by the equation

$$\mathbf{M\ddot{x}} = \mathbf{F}_e + \mathbf{F}_r + \mathbf{F}_s + \mathbf{F}_{PTO} + \mathbf{F}_D + \mathbf{F}_g \, , \qquad (7.1)$$

where $\mathbf{M}$ and $\mathbf{x}$ are the inertial mass matrix and position vector, respectively. The relevant forces given by $\mathbf{F}_e$, $\mathbf{F}_r$, $\mathbf{F}_b$, $\mathbf{F}_{PTO}$, $\mathbf{F}_D$, and $\mathbf{F}_g$ represent the excitation force, radiation force, hydrostatic force, PTO force, drag force, gravitational force respectively. The position of the 3 DOF buoy is parametrised by surge (x), heave (z), and pitch (θ) represented as

$$\mathbf{x} = \begin{bmatrix} x \\ z \\ \theta \end{bmatrix} \, . \qquad (7.2)$$

The pitch is the rotation about the y axis shown in Figure 7.3 For clarity, the WEC and the corresponding coordinate directions are schematically represented in Fig. 7.3. The

inertial mass matrix is given by

$$\mathbf{M} = \begin{bmatrix} m & 0 & 0 \\ 0 & m & 0 \\ 0 & 0 & I_\theta \end{bmatrix}, \tag{7.3}$$

where m and I_θ are the mass and pitch moment of inertia at the center of gravity and about the y axis which passes horizontally through the centre of gravity, respectively. The inertial quantities of the WEC, as well as other relevant parameters are provided in Section 7.4.

The excitation, radiation, hydrostatic, and drag force are products of the fluid-structure interactions. To quantify the excitation and radiation forces within the linear model, the potential flow boundary element method (BEM) solver, NEMOH, was used. To aid in a conceptual understanding of the forces; the excitation force describes the non-viscous hydrodynamic forces acting on the buoy due to the incident and scattered wave; and, the radiation force can be thought of as the force due to waves radiated as the buoy moves.

7.2.1.1 Excitation force

Individual regular waves have a wave elevation, η, described by

$$\eta = A_w \cos(\omega_e t), \tag{7.4}$$

where A_w is the amplitude of the incident wave and ω_e is the excitation frequency. The corresponding excitation force of such a wave is represented as

$$\mathbf{F}_e = \mathbf{F}_{e,\text{amp}} \circ A_w \cos(\sigma - \omega_e t + \sigma_s), \tag{7.5}$$

where $\circ$ represents the Hadamard product (element-wise) operator, and σ represents the phase of the excitation force relative to the incident wave. Both the amplitude, $\mathbf{F}_{e,\text{amp}}$, and phase, σ, of the excitation force were calculated using the BEM solver NEMOH for a range of frequencies. The phase offset due to the surge position, σ_s, is

$$\sigma_s = kx, \tag{7.6}$$

where k is the wavenumber, found as the solution which satisfies the dispersion relationship [38]

$$\omega_e^2 = gk \tanh(kh), \tag{7.7}$$

where h is the depth of water and g is the gravitational acceleration.

7.2.1.2 Radiation force

The radiation force can be described mathematically as [39]

$$\mathbf{F}_r = -\mathbf{A}_\infty \ddot{\mathbf{x}} - \int_0^t \mathbf{K}_r(t - t')\dot{\mathbf{x}}dt' \,, \tag{7.8}$$

where $\mathbf{A}_\infty$ represents the infinite frequency added mass, and $\mathbf{K}_r$ is the matrix of impulse responses. The first and second time derivatives of the position are represented by $\dot{\mathbf{x}}$ and $\ddot{\mathbf{x}}$, respectively. The additional inertia term can be considered a result of the surrounding fluid acting on the buoy and is readily quantifiable through NEMOH. The convolution integral is often thought to represent the fluid memory effects and a result of the radiated wave due to the motion of the buoy [40]. This integral can be computationally intensive to integrate into time domain simulations. An alternative method has been proposed which uses finite frequency domain data to construct a state space representation of the integral in the time domain [41]. Firstly, the radiation force in the frequency domain takes the form

$$\mathbf{F}_r(\omega) = \omega^2 \mathbf{A}(\omega)\mathbf{x}(\omega) - i\omega \mathbf{B}(\omega)\hat{\mathbf{x}}(\omega) \,, \tag{7.9}$$

where $\mathbf{A}(\omega)$ and $\mathbf{B}(\omega)$ are the frequency dependent hydrodynamic added mass and radiation damping, respectively, and the frequency domain representation of the acceleration and velocity are represented by $\hat{\ddot{\mathbf{x}}}$ and $\hat{\mathbf{x}}$, respectively. Both of the hydrodynamic quantities are readily calculated through NEMOH. A time domain representation can be constructed using the Marine Systems Simulator toolbox [41]. It is important to note that for the linear model, the excitation and radiation forces are calculated under the assumption of very small oscillations, that is, the position of the buoy does not deviate much from a nominal position, about which the hydrodynamic coefficients are calculated.

7.2.1.3 Hydrostatic and PTO forces

The buoyancy/ hydrostatic force is constant for a submerged buoy but is partially counteracted by the force of gravity, which is

$$\mathbf{F}_g = m\mathbf{g} \,, \tag{7.10}$$

where $\mathbf{g}$ represents the acceleration of gravity applied in the heave direction. The hydrostatic force is given by

$$\mathbf{F}_s = -\mathbf{g}\rho V \,, \tag{7.11}$$

where V and ρ represent the volume of the buoy and the density of water, respectively. The hydrostatic force acts in the z direction. These two forces result in a net hydrostatic force

$$\mathbf{F}_{s,\text{net}} = -\mathbf{g}(\rho V - m) \,, \tag{7.12}$$

. To counteract this net force and ensure the buoy remains submerged, the tether may
be pre-tensioned. For the purposes of this study, in addition to the pre-tension force a
passive control system with a linear spring and damper is augmented with an additional
nonlinear spring. The force due to the nonlinear element, F_{nl} will be discussed in Section
7.2.2. The force in the PTO acts in the direction of the tether, $\hat{\mathbf{l}}$, and has a combined force
of

$$\mathbf{F}_{\text{PTO}} = (-k_{\text{PTO}}\Delta l - b_{\text{PTO}}\Delta \dot{l} - |\mathbf{F}_{s,\text{net}}| - F_{\text{nl}})\hat{\mathbf{l}} , \tag{7.13}$$

where k_{PTO}, b_{PTO}, Δl, and $\Delta \dot{l}$ are the linear stiffness, damping coefficient, tether exten-
sion, and rate of tether extension, respectively. As the model is 3 DOF, a coordinate
transformation is required to relate the Cartesian position of the buoy to the tether ex-
tension. The coordinate transform $(x, z, \theta) \rightarrow (\Delta l, \alpha, \phi)$ is represented diagrammatically
in Fig. 7.4. The following set of nonlinear geometric relationships were used to find the
tether extension and rate of tether extension from the buoy pose and vice versa [27]

$$\Delta l = \sqrt{(x - a\sin\theta)^2 + (z + l + a - a\cos\theta)^2} - l , \tag{7.14}$$

$$\alpha = \arctan\left(\frac{x - a\sin\theta}{z + l + a - a\cos\theta}\right) , \tag{7.15}$$

$$\phi = \theta - \alpha , \tag{7.16}$$

$$\Delta \dot{l} = \frac{(x - a\sin(\alpha + \phi))(\dot{x} - a\cos(\alpha + \phi)(\dot{\alpha} + \dot{\phi}))}{\sqrt{(x - a\sin(\alpha + \phi))^2 + (z + l + a - a\cos(\alpha + \phi))^2}}$$
$$+ \frac{(z + l + a - a\cos(\alpha + \phi))(\dot{z} + a\sin(\alpha + \phi)(\dot{\alpha} + \dot{\phi}))}{\sqrt{(x - a\sin(\alpha + \phi))^2 + (z + l + a - a\cos(\alpha + \phi))^2}} , \tag{7.17}$$

where a and l represent the distances between the tether attachment lever arm and the
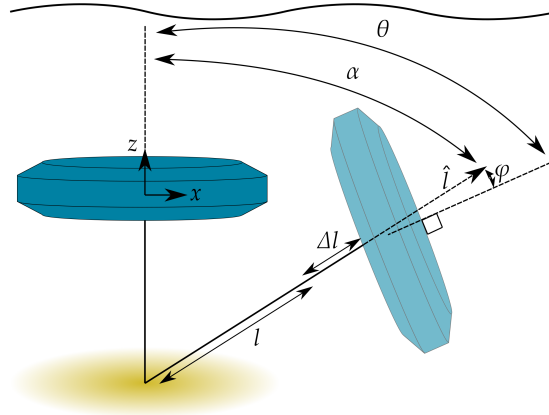

Figure 7.4: A graphical representation of the coordinate transform which maps $(x, z, \theta) \rightarrow (\Delta l, \alpha, \phi)$.

equilibrium tether length, respectively, and are defined in Fig. 7.3. The PTO force may then be related back to the original Cartesian coordinate system by the relationship

$$\mathbf{F}_{\mathrm{PTO}}(x, z, \theta) = |\mathbf{F}_{\mathrm{PTO}}(\Delta l, \alpha, \phi)| \begin{bmatrix} \sin(\alpha) \\ \cos(\alpha) \\ a\sin(\phi) \end{bmatrix} . \tag{7.18}$$

This equation expresses the contributions of the absolute value of the PTO force in the surge, heave, and pitch directions.

7.2.1.4 Drag force

The drag force, $\mathbf{F}_{\mathrm{D}}$, may be approximated by a quadratic term using Morison drag formulation and represented in 3 DOF as [42]

$$\mathbf{F}_{\mathrm{D}} = \begin{bmatrix} -\frac{1}{2}\rho C_{d,x}|\dot{x} - \dot{x}_{\mathrm{f}}|(\dot{x} - \dot{x}_{\mathrm{f}}) \\ -\frac{1}{2}\rho C_{d,z}|\dot{z} - \dot{z}_{\mathrm{f}}|(\dot{z} - \dot{z}_{\mathrm{f}}) \\ -\frac{1}{2}\rho C_{d,\theta}D^5|\dot{\theta}|\dot{\theta} \end{bmatrix} , \tag{7.19}$$

where $\dot{x}$, $\dot{z}$, $\dot{\theta}$ represent the buoy velocities in the surge, heave, and pitch directions, respectively. The coefficients $C_{d,x}$, $C_{d,z}$, and $C_{d,\theta}$ are the drag coefficients in the x, z, and θ directions and are available in literature for this shaped buoy [29]. The fluid velocities in the x and z directions, $\dot{x}_{\mathrm{f}}$ and $\dot{z}_{\mathrm{f}}$, respectively, are approximated by the undisturbed velocity of the fluid at the centre of the buoy and may be calculated using linear wave theory using [43]

$$\dot{x}_{\mathrm{f}} = A_{\mathrm{w}}\omega_{\mathrm{e}}\frac{\cosh(k(h + z - d_s))}{\sinh(kh)}\cos(kx - \omega_{\mathrm{e}}t) , \tag{7.20}$$

$$\dot{z}_{\mathrm{f}} = A_{\mathrm{w}}\omega_{\mathrm{e}}\frac{\sinh(k(h + z - d_s))}{\sinh(kh)}\sin(kx - \omega_{\mathrm{e}}t) , \tag{7.21}$$

where h is the depth of the water channel and d_s is the submergence depth of the buoy.

7.2.1.5 Irregular waves

The previous description of the hydrodynamic forces are for regular, or monochromatic, waves. Such waves are not present in real ocean conditions. Instead, an irregular wave, which may be defined by a spectrum, is a more indicative scenario for quantifying performance under realistic conditions. Under linear assumptions, the principle of superposition may be used to describe and implement waves scenarios with multiple frequencies. Under such scenarios, the irregular wave elevation, η_{irr}, of a spectrum, S, may be described by

$$\eta_{\mathrm{irr}} = \sum_{j=1}^{N} A_{\mathrm{w,j}}\cos(\omega_{\mathrm{e,j}}t + \epsilon_j) , \tag{7.22}$$

177

where N is the number of frequencies within the spectrum and ϵ represents a random phase offset applied at each frequency uniformly distributed over $[0, 2\pi]$ [44]. The amplitude of each regular wave component may be found from the chosen spectrum and resolution and is represented by

$$A_{\text{w,j}} = \sqrt{2S(\omega_{\text{e},j})\Delta\omega_{\text{e},j}} \,, \tag{7.23}$$

where $\Delta\omega_{\text{e}}$ represents the width of the frequency band. The excitation force from such a wave may be similarly represented as

$$\mathbf{F}_{\text{e,irr}} = \sum_{j=1}^{N} A_{\text{w,j}} \, \mathbf{F}_{\text{e,amp},j} \circ \cos(\sigma_j - \omega_{\text{e},j}t + \sigma_s + \epsilon_j) \,. \tag{7.24}$$

The radiation force representation remains consistent with the regular wave case, but the fluid velocity for the x and z direction used in the drag force representation becomes

$$\dot{x}_{\text{f,irr}} = \sum_{j=1}^{N} A_{\text{w,j}}\omega_{\text{e},j} \frac{\cosh(k_j(h + z - d_s))}{\sinh(k_j h)} \cos(k_j x - \omega_{\text{e},j}t + \epsilon_j) \,, \tag{7.25}$$

$$\dot{z}_{\text{f,irr}} = \sum_{j=1}^{N} A_{\text{w,j}}\omega_{\text{e},j} \frac{\sinh(k_j(h + z - d_s))}{\sinh(k_j h)} \sin(k_j x - \omega_{\text{e},j}t + \epsilon_j) \,. \tag{7.26}$$

The specific spectrum used to excite the buoy is consistent between the linear and nonlinear models and will be taken from available data to emulate real conditions.

7.2.2 Nonlinear stiffness force

A force generated by a nonlinear stiffness mechanism may arise from a number of different sources included oblique spring systems [23], asymmetric mass distributions [45], nonuniform cross-sectional areas for floating buoys, magnets [37], or multiple coupled linear systems [20]. To generalise the nonlinear force regardless of origin, in this study, a simple magnetic dipole model is used to characterise a particular force profile, but will be varied using one parameter related to the potential energy of the incident wave. This approach allows significant variation of such force profiles and, as the variable parameter is related to the potential energy of the incident wave, could be considered a reasonably general representation of how many nonlinear stiffness systems with bistable properties would act under a given excitation. Furthermore, employing a magnetic representation allows for more sophisticated modelling techniques which construct a wide range of actuator designs with nonlinear force profiles [46] in future work and makes a simple magnetic model an intuitive solution to build upon. The nonlinear stiffness force between two dipoles acting in the tether can be represented

(using previous notations) by [47]

$$F_{\text{nl}} = C \left(\frac{9\Delta l}{(r_0^2 + \Delta l^2)^{\frac{5}{2}}} - \frac{15\Delta l^3}{(r_0^2 + \Delta l^2)^{\frac{7}{2}}} \right), \tag{7.27}$$

where C is a set of material properties and constants, and r_0 is the horizontal distance between dipoles. Since the dipole model is only used to construct the trend of the force, for the purposes of this study the parameters C and r_0 may be considered non-physical numbers to vary to determine beneficial nonlinear stiffness force profiles. Prior research indicates that a nonlinear stiffness force may provide a beneficial phase-matching property by exposing the system to a range of different stiffnesses and therefore natural frequencies which allow for near resonance oscillations over a range of conditions [37].

7.2.2.1 Potential energy

The parameter C effectively dictates the magnitude of the nonlinear stiffness force but is not an intuitive quantity. Instead, the potential energy of the nonlinear stiffness component, U_{nl}, can be quantified relative to the time-averaged potential energy of the incident wave over the horizontal area of the buoy, U_{wave}. This non-dimensional potential energy ratio, γ is defined to be

$$\gamma = \frac{U_{\text{nl}}}{U_{\text{wave}}}, \tag{7.28}$$

where U_{nl} is

$$U_{\text{nl}} = C \left(\frac{-1}{(r_0^2 + \Delta l^2)^{\frac{3}{2}}} + \frac{3\Delta l^2}{(r_0^2 + \Delta l^2)^{\frac{5}{2}}} \right). \tag{7.29}$$

For regular waves, the average potential energy per horizontal unit area, $\hat{U}_{\text{wave}}$, can be described as [48]

$$\hat{U}_{\text{wave}} = \frac{1}{4}\rho g A_{\text{w}}^2. \tag{7.30}$$

By multiplying by the horizontal area of the buoy, the total time averaged potential energy from the wave is

$$U_{\text{wave}} = \frac{1}{4}\rho g A_{\text{w}}^2 \pi \left(\frac{D}{2} \right)^2. \tag{7.31}$$

For irregular waves, the same principle of superposition applies, giving the average potential energy of the wave

$$U_{\text{wave,irr}} = \sum_{j=1}^{N} \frac{1}{4}\rho g A_{\text{w,j}}^2 \pi \left(\frac{D}{2} \right)^2. \tag{7.32}$$

The benefit of determining C based on a specified γ is that this non-dimensional parameter indicates if the central barrier, exemplified in Fig. 7.2, may be overcome. That is, for γ values greater than 1, the energy from the wave would likely be insufficient to induce coupled motion between possible stable regions, leading to simple monostable behaviour in a potential well. The total potential energy of the PTO stiffness, $U_{\text{stiffness}}$, is given by

$$U_{\text{stiffness}} = \frac{1}{2} k_{\text{PTO}} \Delta l^2 + U_{\text{nl}} . \tag{7.33}$$

To illustrate the effect the nonlinear stiffness on the potential energy profile of the total PTO stiffness, the potential energy profiles for a range of γ and r_0 values are shown in Fig. 7.5. This representation of a nonlinear stiffness force has been used in both the linear
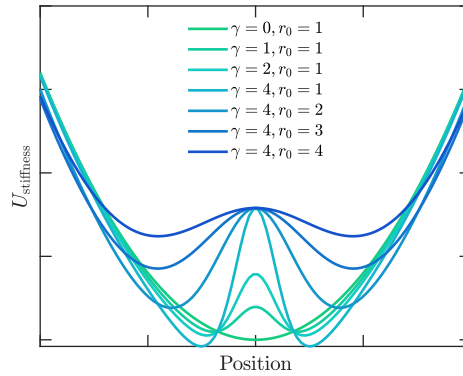
Figure 7.5: A graphical representation of potential energy profiles resulting from a range of γ and r_0 values. Increasing the normalised potential energy ratio, γ, increases the central peak in the potential energy profile, while increasing r_0 tends to widen the location of the stable regions and provide less dramatic gradients.

and nonlinear hydrodynamics models.

7.2.3 CFD model

The representation of hydrodynamic forces in the linear model is limited as it is based upon assumptions to simplify the calculations. A higher fidelity estimation method, if validated, is a CFD simulation [34]. The model used in this study is similar to a CFD model that has been previously validated [27]. To demonstrate the validity of this model, the wave amplitudes for two different wave periods are considered, as well as a comparison to experimental data from previous work [29]. Previous models did not include a nonlinear stiffness mechanism or irregular waves. Therefore, to provide some confidence in the solutions for including these two additional factors, care was taken to ensure results from CFD simulations converged.

7.2.3.1 Model description

In this study the NWT was constructed using OpenFOAM with a domain size of $(200, 50, 50)$ m in the $(x_{CFD}, y_{CFD}, z_{CFD})$ directions, respectively. The water depth is 40 m, and the buoy is located at $x_{CFD} = 100$ m, $y_{CFD} = 0$ m, and $z_{CFD} = -7$ m. A previous study by the same authors [27], using a similar configuration, suggested resolution limitations in the x and z directions for accurate simulation of waves. A number of CFD settings used in this model have been adjusted, which allowed for a reduction of the resolution requirements found in the previous study. A meshed domain of the same number of cells was used for all regular wave scenarios. Due to the varied wave frequencies the resolution metric for the x direction (cells per wavelength $(\Delta x / \lambda)$) effectively changed between these scenarios, with a maximum of 883.1 and a minimum of 76.5. The resolution in the z direction for the regular wave scenarios was 3.0. The domain was initially constructed with a cell count of $(98, 10, 38)$ in the (x, y, z) directions. To better capture the surface effects, the cell size was halved in each direction (effectively splitting each cell into 8) within $-10 \leq z \leq 7$, defined as Region 1. The cell size was halved again within $-5 \leq z \leq 5$, defined as Region 2 (see Fig. 7.6). To establish the validity of using the mesh to emulate water waves, the minimum and maximum periods of the regular wave scenarios were simulated without the buoy. Regular waves of periods 5 s and 22 s with wave heights of 1 m were simulated. The NWT produced waves with wave heights of 0.98 m and 1.02 m at an x position of 100 m, for 5 s and 22 22, respectively. This small 2% difference between the desired and observed wave heights demonstrates that the proposed NWT successfully produced the necessary waves over the required range of wave periods.

The buoy was included into the computational domain at the required location with a surface cell size of half of the cell size in Region 2. To manage the transition between different mesh resolution levels, a minimum number of three cells between each resolution level was enforced during the mesh construction process. The rectangular cells were snapped to the surface of the buoy while satisfying a range of mesh quality criteria. The mesh within 20 m of the buoy was allowed to deform during the simulation and the buoy was constrained to move only in surge, heave, and pitch directions. An indicative diagram of the NWT setup is shown in Fig. 7.6.

An identically shaped buoy in a similar scenario was used in a previous study [29]. This work presented experimental results which have been used in this study as a means to validate the proposed CFD scenario. The buoy was excited by a regular wave of period 10 s and wave height 3 m. The buoy was located at a submergence depth of $z = -5$ with a PTO stiffness of 4.0 MN/m and PTO damping of 0.63 MNs/m. These settings were used for validation purposes. All other geometric and physical parameters remain the same and are given in Section 7.4. The proposed CFD model was adjusted to match the hypothetical full scale parameters, which were scaled down in the experiment
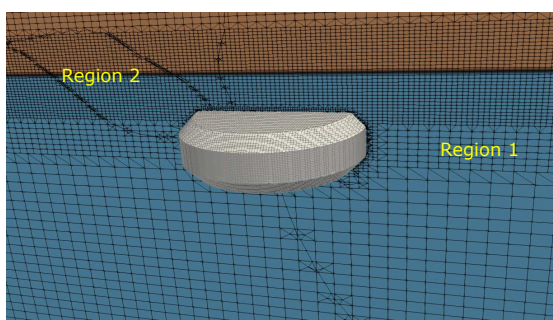
Figure 7.6: A schematic of the CETO-shaped submerged buoy in a NWT showing the quality of meshing around the buoy. The mesh of the water was conformed to the surface of the buoy using snappyHexMesh within OpenFOAM. The stray mesh lines are a result of the image rendering process and do not represent the mesh structure.

and a comparison between the scaled resultant motions is given in Fig. 7.7. These results show that the CFD scenario produced results reasonably similar to experimental work. The similarity was quantified using the Pearson correlation coefficients [49], which are a measure of linear dependence between two signals. The Matlab function *corrcoef* calculated the Pearson correlation coefficients, p, for each set of results shown in Fig. 7.7. The pitch results are reasonably different, however, it is not uncommon for pitch results in CFD to inadequately represent experimentally determined values in some scenarios [29]. The experimental work presented may not have been restricted to 3DOF as the CFD scenarios were, which could lead to some discrepencies. The remaining values, which are more influential for bistability (particularly heave and the tether extension) within the recommended 90% for a model to be considered validated [34]. This validation scenario uses a 3 m wave height, while the remaining CFD scenarios in this study use 1 m wave height. This implies that the mesh resolution parameters, cells per wave height and wavelength, are greater than for the some of the 1 m scenarios. However, the forces and motion are more significant in the validation scenario. While not presented in this paper, other important mesh metrics were identified through the development of the validation scenario including the aspect ratio of the cells and the number of cells along each direction of the buoy. For consistency between the scenarios and stability of the CFD simulations, it was considered more important to maintain these factors than reduce the cells per wave height.

The solver used in OpenFOAM to generate the waves was olaDyMFlow [50] and the waves were produced using the required fluid regime specific for the wave case [51]. A custom library was constructed to implement the nonlinear mechanism as presented in Sections 7.2.1.3 and 7.2.2. The convergence for the nonlinear stiffness addition and irregular wave extensions are presented in 7.A and 7.A, respectively.
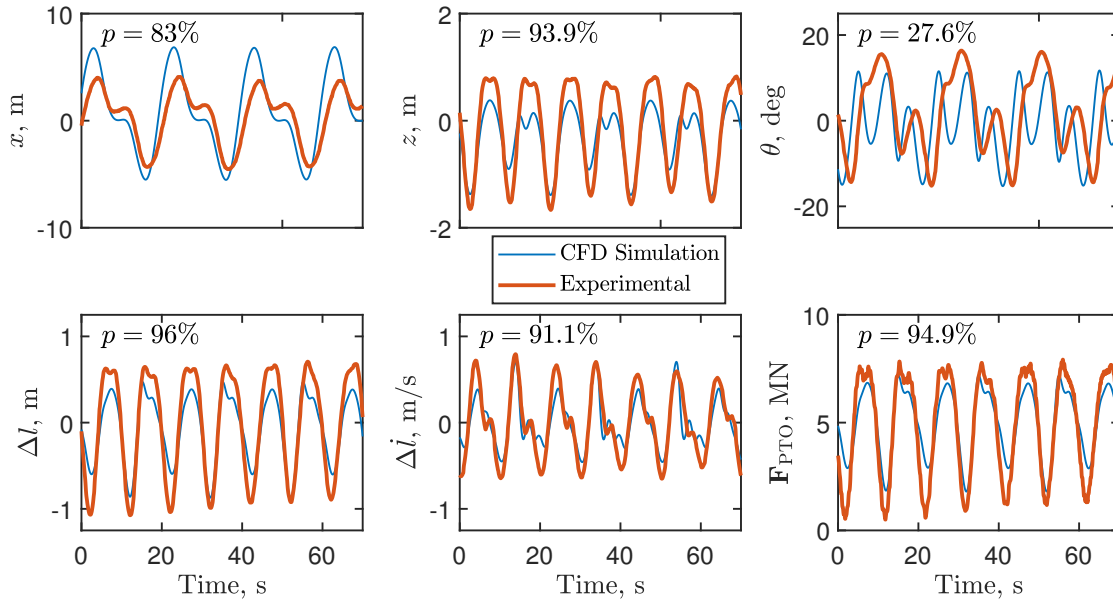
Figure 7.7: A comparison between the experimental data presented in a previous study [29] and NWT generated data using the proposed CFD model. The Pearson correlation coefficients, shown above each plot, indicate a strong agreement between most degrees of freedom and calculated values. The heave motion is well captured by CFD ($p > 90\%$) and since this motion primarily influences Δl, $dot\Delta l$, and $\mathbf{F}_{PTO}$, these variables also agree well. Therefore, the model is therefore considered validated for use in this study.

7.3 Optimisation and control

In order to evaluate the true benefit of nonlinear stiffness for a WEC, it is important to compare against optimal conventional linear scenarios. Most literature to date optimises either stiffness or damping (see Section 7.1.2). For the case of floating buoys, nonlinear stiffness is considered intrinsic to the system as a non-uniform cross section area of the buoy results in a nonlinear hydrostatic stiffness, and additional nonlinear stiffness aims to counteract this intrinsic nonlinearity. However, for this study on submerged buoys, the nonlinear stiffness mechanism is considered an additional component and cases with varying degrees of nonlinearity were compared against the case with both stiffness and damping optimally tuned. The optimal parameter that was maximised was the time average power, P_{avg}, given by

$$P_{avg} = \frac{1}{T} \sum_{j=1}^{n_t} P_{inst,j} \Delta t_j \,, \tag{7.34}$$

where T represents the total time period, Δt; represents the time step, n_t; represents the number of time steps, and $P_{inst,j}$; represents the instantaneous power at each time, j,

183

given by

$$P_{\text{inst},j} = b_{\text{PTO}} \Delta \dot{l}_j^2 \, . \tag{7.35}$$

The time averaged power is the metric by which the performance of the WEC model
and control system is quantified. Other factors such as conversion efficiency, tether force
limits, or grid connection should be included to provide a better metric for estimating
real performance. However, for the purposes of quantifying the impact of nonlinear
stiffness in the context of nonlinear hydrodynamics, the time averaged power is the
primary baseline indicative measure.

7.3.1 Control PTO settings

For linear hydrodynamics and a single DOF, the optimal stiffness and damping of the
control force acting through the PTO is well known [52]. The ideal control parameters
for a simplistic situation (assuming linear conditions and no viscous damping) are

$$k_{\text{PTO,ideal}} = \omega_e^2 (m + A_z) \, , \tag{7.36}$$

$$b_{\text{PTO,ideal}} = B_z \, , \tag{7.37}$$

where A_z and B_z are the hydrodynamic added mass and damping in the heave direction,
respectively. While these are overly simplistic, they are a useful starting point for small
motions as the tether extension is mostly associated with heave. The k_{PTO} and b_{PTO}
parameters were optimised in the model using linear hydrodynamic parameters through
the Matlab function *fmincon* using Equations (7.36) and (7.37) as the initial points. The
optimal stiffness often resulted in the natural frequency in heave coinciding with the
excitation frequency. However, there were particular frequencies in which surge and
pitch were significant contributors to power performance. To understand why, the
natural frequencies in each DOF should be considered. These natural frequencies may
be derived as [37, 53]

$$\omega_{n,x}(\omega_e) = \sqrt{\frac{g(m - \rho V)}{(l + a)(m + A_x(\omega_e))}} \, , \tag{7.38}$$

$$\omega_{n,z}(\omega_e) = \sqrt{\frac{k_{\text{PTO}}}{m + A_z(\omega_e)}} \, , \tag{7.39}$$

$$\omega_{n,\theta}(\omega_e) = \sqrt{\frac{a(a + l)F_s}{l(I_\theta + A_\theta(\omega_e))}} \, . \tag{7.40}$$

The natural frequency for each DOF at each excitation frequency after local optimisation
is shown in Fig. 7.8. The surge natural frequency does not vary much over the frequency
range, implying that a significant peak in the surge response is expected around 0.29

rad/s, which happens to coincide with the heave natural frequency at one excitation frequency. Therefore, some interaction between those two DOF at that frequency is expected. Also, generally the heave natural frequency of the optimal system tends to follow the excitation frequency which makes some intuitive sense. However, at the second harmonic of surge (around 0.58 rad/s) the heave natural frequency of the optimal system deviates, implying that the interaction between heave and surge may be important for those frequencies. This is likely related to Mathieu instability [54], which is triggered when the excitation is close to twice the surge natural frequency. Similar to the surge-heave intersection point, the pitch-heave intersection point occurs at 0.8 rad/s which might indicate magnified motion. However, this frequency is reasonably high for waves, so this interaction may be less significant. Further results are presented and discussed in relation to these natural frequencies in Section 7.5.
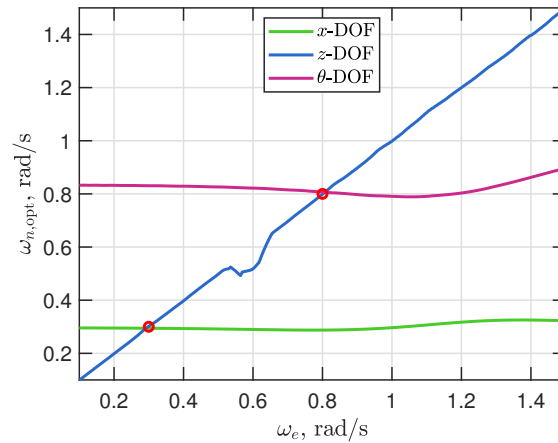
Figure 7.8: The natural frequency of the optimally tuned system $\omega_{n,\text{opt}}$ in each DOF for different monochromatic excitation frequencies, ω_{e}. The circles represent points of where the natural frequencies of different DOF coincide. Magnified motion in each DOF are anticipated at this locations.

The PTO optimal parameters were found for both regular and irregular wave conditions under linear hydrodynamic conditions and were used consistently between corresponding linear and nonlinear hydrodynamic simulations.

7.4 Simulation configuration

The geometric parameters between the regular and irregular wave simulations for both the linear and nonlinear hydrodynamics were consistent between corresponding simulations and are outlined in this section, as well as the simulation test conditions. Convergence studies have been undertaken in order to justify the use of the validated CFD model for the nonlinear stiffness and irregular wave extension.

7.4.1 Parameters and Test conditions

The simulation parameters are presented in Table 7.2. The test conditions for the regular and irregular wave scenarios are provided in Tables 7.3 and 7.4. Conditions which are specifically relevant to either linear hydrodynamics or nonlinear hydrodynamics are labelled LH or NLH, respectively.

Table 7.2: Physical and geomtric simulation constants

Parameter	Value
Water density, ρ, kg/m^3	1025
Acceleration due to gravity, g, m/s^2	9.81
Mass, M, kg	1.25×10^6
Pitch moment of inertia, I_θ, kg m^2	3.3×10^7
Drag Coefficient (Surge), $C_{d,x}$	0.7
Drag Coefficient (Heave), $C_{d,z}$	1.28
Drag Coefficient (Pitch), $C_{d,\theta}$	0.22
Nonlinear geometric feature, r_0, m	1.5

Table 7.3: Regular wave test conditions. Where variables associated with linear and nonlinear hydrodynamics are indicated with LH and NLH, respectively.

Parameter	Value
Wave amplitude, A_w, m	0.5
Frequency range (LH), rad/s	$0.1 - 2$
Period range (NLH), s	$5, 6, 7, 8, 9, 10, 11, 12, 14, 18, 22$
Time length (LH), $T_\mathrm{reg,\,lin}$, s	2000
Time length (NLH), $T_\mathrm{reg,\,nl}$, s	600
Dimensionless potential, γ_reg	$0 - 20$

For the nonlinear hydrodynamic simulations, transient effects present in the beginnings of simulations occupied a larger portion of the simulation. Therefore, in order to preserve the consistency of the comparison, the final five periods of data were used for analysis of regular waves. The solver, olaDyMFlow, uses active wave absorption to prevent or minimise reflected waves [50, 55]. During wave height convergence tests across all the simulated wave periods, only a single regular wave was observed in the NWT and a small difference (2%) between the desired and observed wave heights. From these factors, wave reflections are not expected to significantly impact the CFD results. In the linear hydrodynamic simulations, the second half was used as this typically gave very consistent and stable oscillations for monochromatic excitation. For irregular waves, spectral analysis techniques were used to minimise the impact of transient features on

the resulting dynamics.

The irregular wave spectrum used in both linear and nonlinear hydrodynamic simulations was selected based on the typical wave climate observed at the Torbay site between the 5th of March 2019 and 14th of October 2019 (data available from the University of Western Australia at https://wawaves.org/). The significant wave height, H_s, and the energy period, T_e, were calculated for the energy density spectra data between these two dates using [3]

$$T_e = 2\pi \frac{m_{-1}}{m_0} , \quad H_s = 4\sqrt{m_0} , \tag{7.41}$$

where the nth spectral moment is defined as

$$m_n = \int_0^\infty S(\omega)\omega^n d\omega , \tag{7.42}$$

where ω represents the frequencies which compose the irregular wave in rad/s. A colour map indicating the probability of finding a sea state is presented in Fig. 7.9.
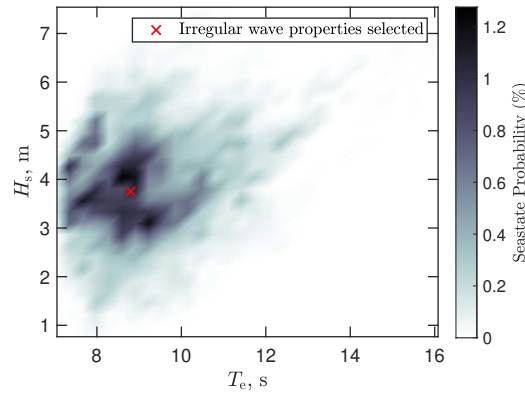
Figure 7.9: The wave climate at the Torbay site depicted as a probability of finding a sea state with a particular H_s and T_e. The red marker indicates the irregular wave properties selected for modelling in this study.

The sea state selected to be used in the irregular wave simulations was parametrised by $H_s = 3.75$ m and $T_e = 8.8$ s. As the data provided was non-uniformly spaced in the frequency domain, a representative spectrum was generated using the H_s and T_e parameters and approximating the sea state as a Pierson-Moskowitz spectrum represented by [56]

$$S(f) = \frac{A_{PM}}{f^5} \exp(-\frac{B_{PM}}{f^4}) , \tag{7.43}$$

where f represents the frequencies that compose the irregular wave in Hz, and A_{PM} and B_{PM} are

$$A_{PM} = \frac{5H_s^2 f_P^4}{16} , \quad B_{PM} = \frac{5f_P^4}{4} , \tag{7.44}$$

respectively. The peak frequency in the spectrum, f_P, can be approximated from the
energy period as [56]

$$f_P = \frac{0.858}{T_e} . \tag{7.45}$$

The measured data covers the winter half of a year, which would mean the seasonal
variability in the Albany wave climate would skew the most probable sea state to more
severe conditions than if long term data was used. While the generated spectrum may
differ from the measured spectrum or the true spectrum due to seasonal variability,
it does provide a basis for modelling the WEC in a semi-realistic wave climate and
provides a sufficient test case for this study.

Table 7.4: Irregular wave test conditions

Parameter	Value
Significant Wave Height, H_s, m	3.75
Energy Period, T_e, s	8.80
Number of discrete frequencies	150
Simulation time (LH), $T_{irr, linear}$, s	1000
Simulation time (NLH), $T_{irr, nl}$, s	1000
Dimensionless potential, γ_{irr}	$0 - 20$
Optimal PTO stiffness, $k_{opt,pto}$, MN/m	1.98
Optimal PTO damping, $b_{opt,pto}$, MNs/m	1.81

A comparison between the desired Pierson-Moskowitz power spectral density and
the experimentally measured power spectral density is shown in Fig. 7.10 and was
decomposed into 150 equispaced frequencies between 0.2rad/s and 2π rad/s. While
there are some differences between the spectra, numerically integrating each spectra
with respect to frequency gave a 1.1% difference in the mean square value between the
Pierson-Moskowitz model compared to the measured data. The Pierson-Moskowitz
representation was therefore deemed an good representation of the selected irregular
wave and indicative of the measured wave climate. A random phase offset was then
applied according to the methodology previously outlined (see Section 7.2.1.5. The
same spectra was implemented in the linear and nonlinear hydrodynamic scenarios.
Verifications in the NWT using irregular waves and nonlinear stiffness are presented
in Appendix 7.A and Appendix 7.B, respectively. The frequency resolution used to
model the irregular wave was limited by the computational resources. The number of
frequencies selected was 150. While this does not ensure non-repeating waves over the
time period simulated, the same parameters were used in both the linear and nonlinear
hydrodynamic scenarios to ensure consistency of comparison. Since the spectrum is
an approximation of a measured spectrum, the changes between the simulations due
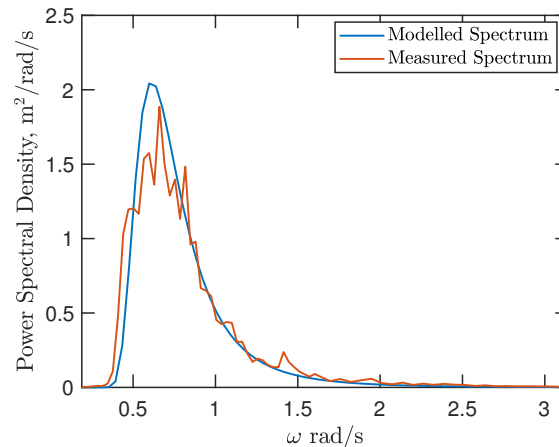
Figure 7.10: The measured and modelled Pierson-Moskowitz power spectral density of the irregular wave selected for simulations.

to the additional nonlinear stiffness is the investigated result rather than the absolute performance of the WEC in this hypothetical irregular wave.

The simulation time for the linear and nonlinear hydrodynamic irregular wave scenarios was also limited by the computational resources required by the CFD simulations. Given the limited number of discrete frequencies and the potential for repeated signals, it was considered important to keep the linear and nonlinear hydrodynamic irregular wave simulations consistent for the sake of comparison.

7.5 Results and discussion

To understand how the nonlinear stiffness impacts the capability of the WEC to capture power from waves, the regular wave scenario was first analysed using only linear hydrodynamics. When excited by regular waves, the motion of the device typically oscillates at the excitation frequency, the natural frequencies (in any DOF), or harmonics of either. Whereas when a nonlinear stiffness is present and significant, the system is exposed to a range of stiffnesses and natural frequencies. Therefore, the system may oscillate at a range of frequencies. Whether this is beneficial or detrimental is explored below.

Including the nonlinear hydrodynamics to model the fluid-structure interaction further complicates the model as secondary fluid effects such as potential surface breaching, complex drag forces, and the fluid above the WEC oscillating as a separate subsystem. These effects may alter the system response and therefore change the optimal conditions of the buoy. The linear and nonlinear hydrodynamic models are compared below for both the regular and irregular wave conditions.

7.5.1 Regular waves with linear hydrodynamics

The inclusion of the nonlinear stiffness in regular wave scenarios can lead to excitation of multiple frequencies. Some indicative results for the regular wave with a period of 10 seconds with varying γ are shown in Fig. 7.11. The frequency representation of the heave displacement amplitude was constructed by applying a hamming window to the heave time series and using the Matlab function *pwelch* to obtain a power spectral density. The power spectral density was then converted and scaled to give the amplitude spectrum. This example shows that with no nonlinear stiffness, simple single frequency motion in heave is observed.
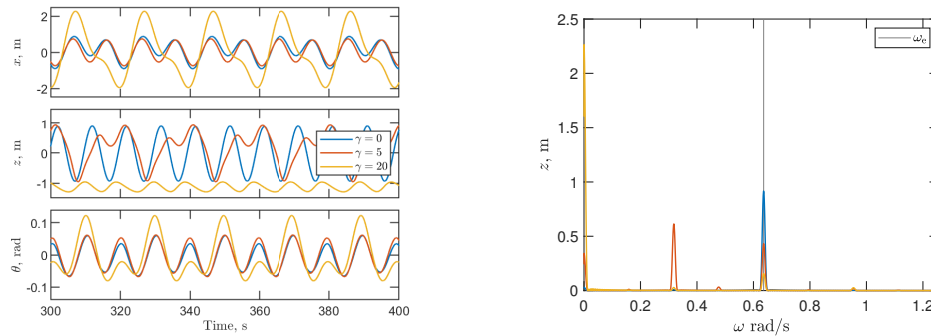
(a) Time domain displacements of each DOF.

(b) Frequency domain representation of the heave displacement.

Figure 7.11: The surge, heave, and pitch motions for the wave excitation period of 10 seconds. The results of linear hydrodynamic simulations with three different nonlinear stiffnesses are given. This example demonstrates a typical change in behaviour observed in the regular wave results as γ is increased, the heave motion moves from single frequency to multi-frequency and then becomes restricted to one side. The $\gamma = 5$ nonlinear stiffness scenario resulted in the excitation of a sub-harmonic as well as a number of other small frequency components.

While the excitation of multiple frequencies is observed and reasonably common in such systems, the time averaged power given in Fig. 7.12 shows that for optimally tuned systems under a linear hydrodynamic regime the inclusion of stiffness nonlinearity reduces the amount of power absorbed. The system was simulated with many varying γ, but for graphical clarity, only a subset of the results are shown.

A broader depiction of how the performance changes for both excitation frequency ω_e and nonlinear stiffness potential energy γ can be seen in the map of the time averaged power, presented in Fig. 7.14. To demonstrate how the nonlinear stiffness introduces additional complexity in the resultant motion, the map presented in Fig. 7.13 shows the regions of γ and ω_e where a higher number of frequencies are observed in the ensuing motion. Each point on this map represents the number of significant peaks seen in
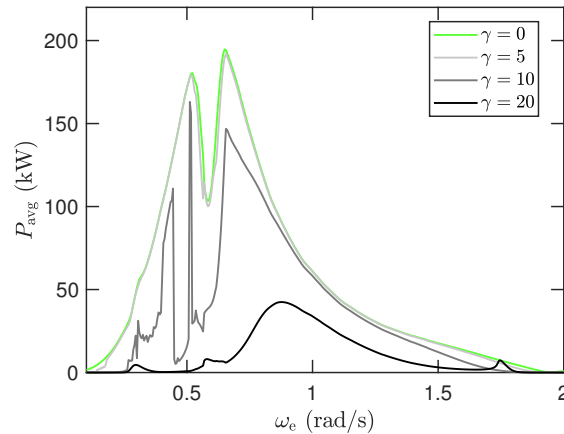
Figure 7.12: The time averaged power of optimally tuned regular wave scenarios in the linear hydrodynamics model for various levels of nonlinear stiffness parametrised by γ. Increasing γ reduces the time averaged power.

the power density spectrum of each simulation. Other measures of complexity such as the Crest Factor and Kurtosis were also analysed and showed the same trend. This graph shows the frequencies and γ values for which the nonlinear stiffness creates more complex behaviour and should be understood in conjunction with the map of the time averaged power. In the regions for which the nonlinearity in the stiffness has the largest impact, the power absorbed is greatly reduced from optimal conditions. This means that the system is effectively detuned at those frequencies.

These conclusions are found using results for simulations with linear hydrodynamics and regular wave excitation, which may not be representative of realistic conditions. Another limitation of these results is that the regular wave scenarios were optimised to determine the best linear stiffness and damping for each frequency. Therefore, the additional nonlinear stiffness expectedly provides no tangible benefit for such cases.

7.5.2 Regular waves with nonlinear hydrodynamics

Using linear hydrodynamics, such as in Section 7.5.1, can produce indicative results under some conditions. However, such models cannot capture all hydrodynamic effects observed in real conditions. Therefore, the impact of nonlinear stiffness was also explored under nonlinear hydrodynamic conditions (CFD) and compared to linear hydrodynamic conditions. In many cases, the observed dynamics and the general trend over the frequency range was consistent between the simulations using linear and nonlinear hydrodynamics. However, the nonlinear hydrodynamic model did shift the observed peaks in the motion, and these nonlinear hydrodynamic coupled with the nonlinear stiffness to induce larger motions and provide a slight benefit at some frequencies. The resultant motion for each DOF at each frequency of excitation for both linear and
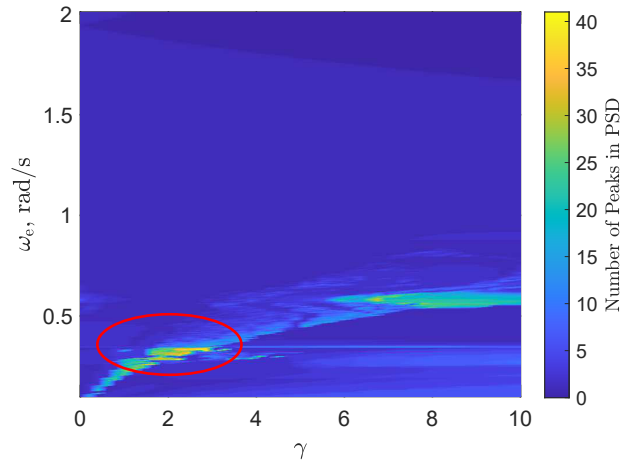
Figure 7.13: A map showing the number of peaks present in the power spectral density of the heave motion for the simulation excited by individual regular waves with varying nonlinear stiffnesses. This graph shows that the most complex behaviour is seen around $\gamma = 2$ and $\omega_e = 0.25$ (circled in red) and region of complexity tends to follow a curved path but does not extend into higher frequencies for the nonlinearities tested.

nonlinear hydrodynamics is given in Fig. 7.15 in terms of the root-mean-square of the time domain signal about the stable equilibrium point (to compensate for an offset due to bistability for comparative purposes).

These results show that nonlinear stiffness does result in shifting the effective natural frequencies but generally tends to reduce the heave motion for most cases. The results from the CFD scenarios show some differences at peaks or slight offsets from linear hydrodynamic counterparts, but generally match the trends well in heave. Given the sharp jumps observed as the nonlinear stiffness changes, it is understandable that the system may be sensitive to small differences between the models. Additionally, nonlinear stiffnesses can give rise to chaotic motions, although further investigations would be required before concluding if such behaviour was present in this case. Interestingly, the surge and pitch results also indicate a general trend correspondence at some frequencies with some additional or shifted frequency peaks. However, the second peak seen in the surge results (which is the second harmonic of the surge natural frequency from Fig. 7.8) seems to have shifted to the right, that is, from around 0.6 rad/s to 0.8 rad/s. This demonstrates that the linear system does not fully capture the extent of the hydrodynamic complexity present in the fluid-structure interactions.

While it is clear that the nonlinear stiffness impacted the motion, it is difficult to determine if this is beneficial or detrimental to the power production from the motion alone. The time averaged power for the full range of regular waves is presented in Fig. 7.16. These results again indicate that there is a difference in the peaks observed the time averaged power between the linear and nonlinear hydrodynamic regimes.
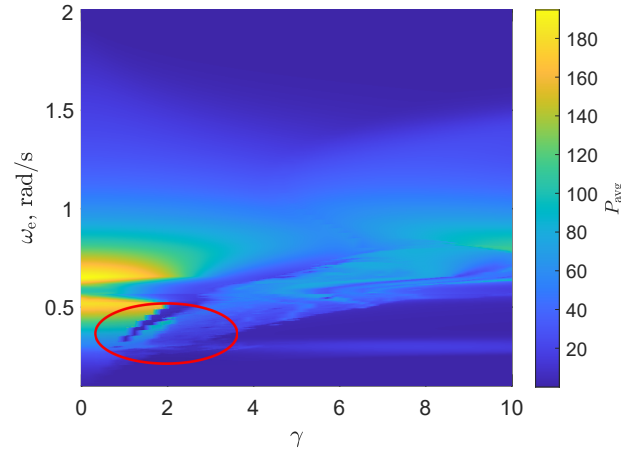
Figure 7.14: A map showing the time averaged power absorbed by the PTO for the simulation excited by individual regular waves with varying nonlinear stiffnesses. Compared to the graph seen in Fig. 7.13, it can be seen that regions which experience the largest impact from nonlinear stiffness sustain a reduction in time averaged power (circled in red), indicating that the nonlinear stiffness is reducing the performance of the system.

Furthermore, there are some frequencies at which a small amount of nonlinearity in the stiffness does provide some small improvement. It is challenging, however, to form a general conclusion on the basis of these findings given the inconsistent impact nonlinear stiffness has at different frequencies. However, like many other nonlinear dynamical systems, lower frequencies are more likely to see a potential benefit from lower levels of nonlinearity, while the higher frequencies are more likely to see a potential benefit from higher levels of nonlinearity. It should also be noted that as the optimisation was conducted using linear hydrodynamics, the switch to nonlinear hydrodynamics may have resulted in the PTO settings becoming sub-optimal, and therefore the additional nonlinear stiffness offered some improvement at those particular frequency ranges.

As an alternative representation of the overall performance, the time-averaged power of the linear and nonlinear hydrodynamic scenarios may be integrated over frequency to provide an indicative estimate on overall power performance at different levels on nonlinear stiffness. This weighted integrated value may be approximated as

$$P_{\text{avg,int}} = \frac{\sum\limits_{j=1}^{n_\omega} P_{\text{avg},j} \Delta\omega_{\text{e},j}}{\sum\limits_{j=1}^{n_\omega} \Delta\omega_{\text{e},j}} \, , \tag{7.46}$$

where n_ω is the number of excitation frequencies and $\Delta\omega_{\text{e},j}$ is the bin width of the jth excitation frequency step.
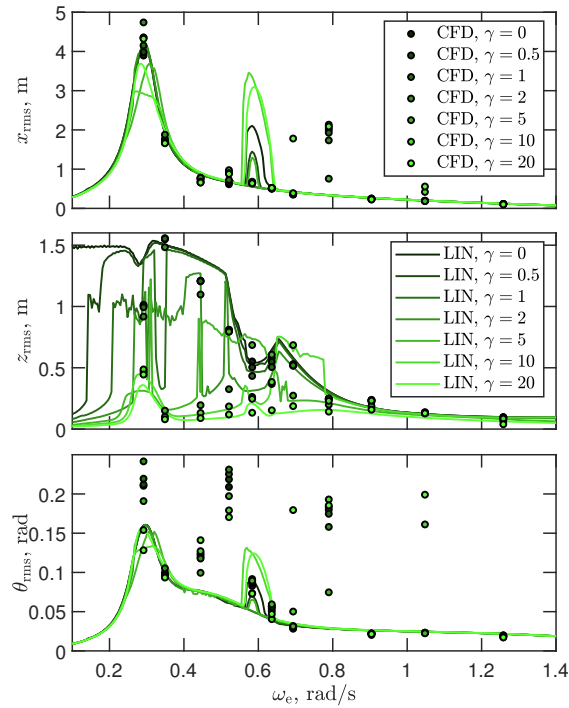
Figure 7.15: The root-mean-square of the motion in each DOF about the stable equilibrium point. The motion observed using the linear and nonlinear hydrodynamic regimes is presented for various degree of nonlinear stiffness potential parametrised by γ. In the surge DOF, the nonlinear hydrodynamic scenarios show that one peak has been shifted to the right. In the heave DOF, the general trend of the motion rms between the linear and CFD models as the nonlinear stiffness increase does match, with few exceptions. This supports the conclusion that the nonlinear stiffness acts to detune the optimised system.

These integrated values are presented in Table 7.5. These values are a proxy to describe the change in performance for different nonlinear stiffnesses. Therefore, the absolute values do not provide an indication of the performance of the system, but the trend for each hydrodynamic scenario indicates broadly how the overall performance may be influenced by the nonlinear stiffness. The trend show that as the nonlinear stiffness is introduced into the optimised system, the expected time average power generally reduces for regular waves even though some frequencies experience an increase in time average power.

A trajectory plot of one scenario which displays an improvement, $\omega_e = 1.05$ rad/s, is given in Fig. 7.17. This plot shows the resultant surge and heave motion of the system with linear and nonlinear hydrodynamics for the scenario $\gamma = 0$ and the scenario where $\gamma = 10$. This figure shows the last two periods of motion. The linear hydrodynamics scenarios take one period of excitation wave to complete one cycle, while the nonlinear
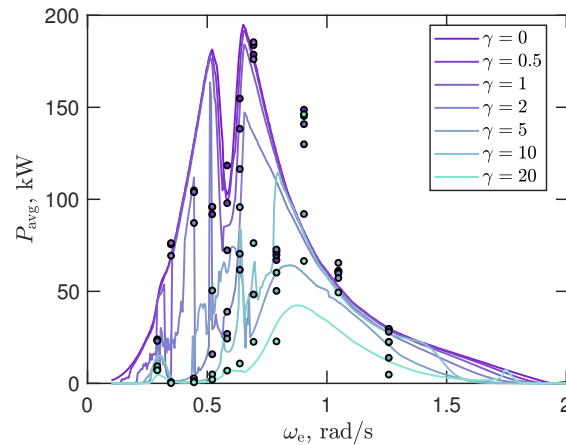
Figure 7.16: The time averaged power of the linear and nonlinear hydrodynamic scenarios for various excitation frequencies and levels of nonlinear stiffnesses parameterised by γ.

Table 7.5: The time-averaged power weighted by frequency integrated with respect to excitation frequency

γ	Linear $P_{\mathrm{avg,int}}$ kW	CFD $P_{\mathrm{avg,int}}$ kW
0	57	83
0.5	55	81
1	51	78
2	35	64
5	22	39
10	24	48
20	10	21

hydrodynamics scenario take one when the PTO stiffness is linear, and two periods when the PTO stiffness is nonlinear. When the nonlinear stiffness is added, the linear hydrodynamic scenario show a small reduction in heave which could explain why the linear scenario shows a reduction in power generation. Whereas, in the nonlinear scenario, the motion changes from one period to two period and experiences increased surge and increased heave amplitudes.

This fundamental change in the type of motion is induced by the nonlinear stiffness. This two period motion is observed at other frequencies even without any nonlinear stiffness but does not guarantee high levels of time-averaged power. Such behaviour is possibly a Mathieu-type period-doubling instability [54] in surge/sway as this corresponds to the critical condition with the frequency of the parametric excitation being close to twice the surge natural frequency. To demonstrate how the nonlinear stiffness might change the motion detrimentally, the CFD motion trajectories of the regular wave

with frequency $\omega_e = 0.70$ rad/s with various levels of γ is given in Fig. 7.18. These trajectories clearly show that as the motion becomes less periodic, the time average power dramatically reduces. The breakdown in periodic motion occurs for large gamma values, this motion is perhaps chaotic, though this would require further study. Since the system is heavily damped, it is unlikely to observe exponential growth in higher order motion leading to instability or chaotic trajectories. Understandably, this breakdown results in an inconsistent phase between the excitation force and the tether extension velocity, so increasing γ could be an effective method of detuning the system during extreme conditions.
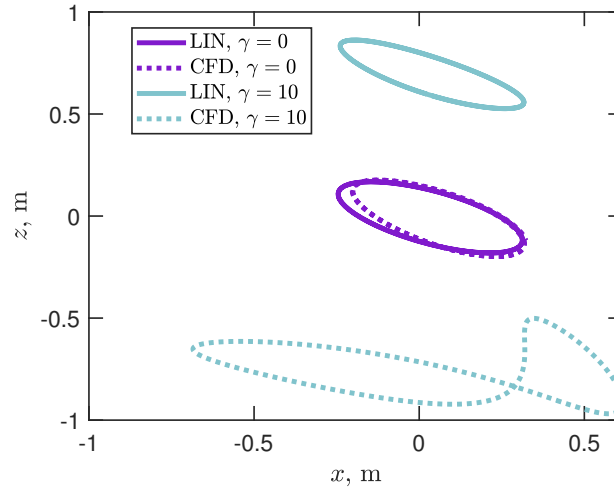
Figure 7.17: The heave and surge trajectory of the buoy when the system is excited by a regular wave of frequency $\omega_e = 1.05$ rad/s. The scenarios with no nonlinear stiffness and large nonlinear stiffness is presented. The final two periods of the excitation wave is presented. The addition of the nonlinear stiffness in the CFD simulation has excited two period motion, which in this case has had an observed benefit to time-averaged power.

Within both the linear and nonlinear hydrodynamic simulations a drop in the time average power occurs around 0.58 rad/s. The trajectory of the WEC in the linear hydrodynamic scenarios for various levels of nonlinear stiffness is given in Fig. 7.19. This shows two period motion is present even for a purely linear stiffness. This is characteristic of a Mathieu-type period doubling instability. The addition of nonlinear stiffness changes the shape of the trajectory, and in the case of $\gamma = 2$ and $\gamma = 5$, one period and six period motion are observed, respectively. In particular, in the case of the six period motion, $\gamma = 5$, an increase in power from $\gamma = 2$ is noted. This suggests that the nonlinear stiffness is promoting more complex multi-periodic dynamic behaviour. Overall, the comparison between linear and nonlinear hydrodynamics highlights the potential difference in optimally tuned conditions and emphasises the sensitivity to PTO parameters. For regular waves under both linear and nonlinear hydrodynamic consider-
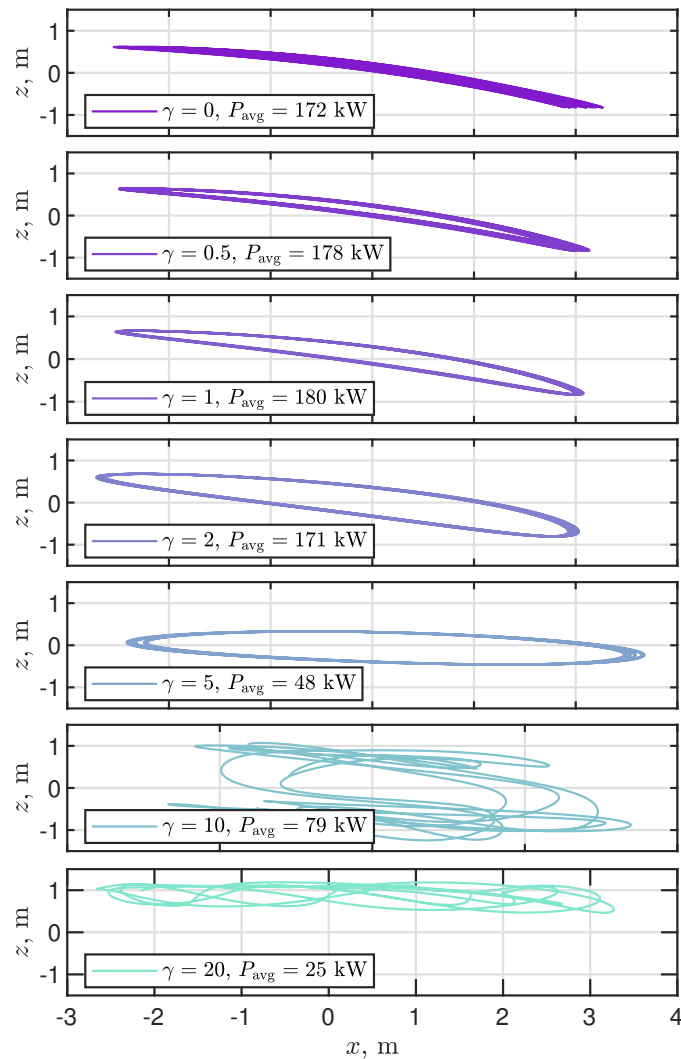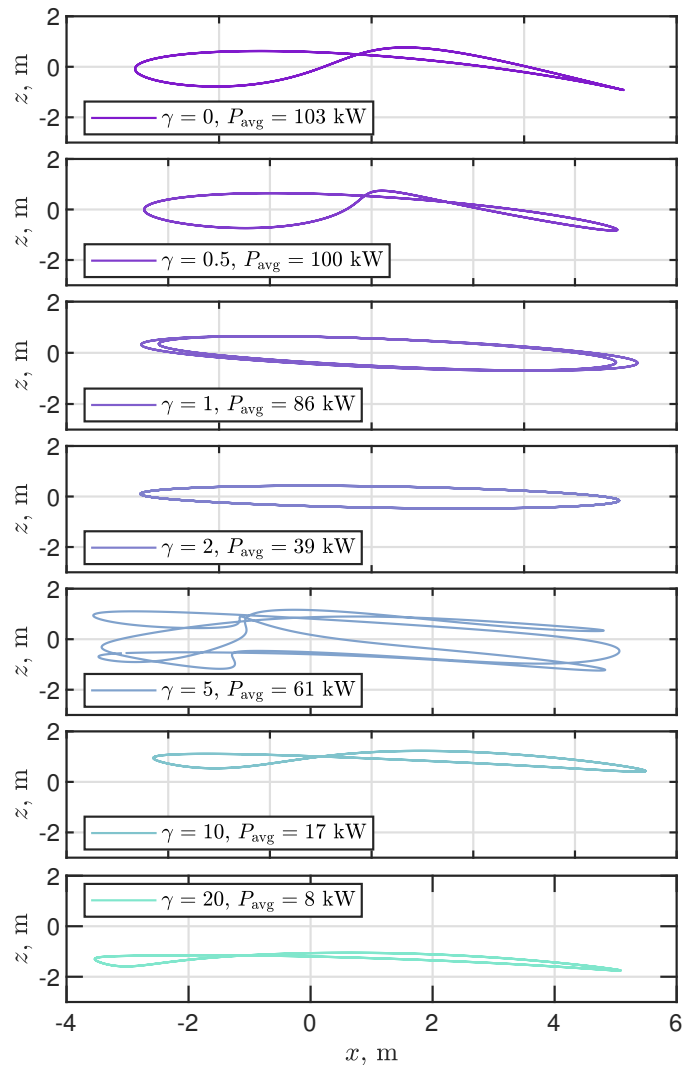
Figure 7.18: The heave and surge trajectory of the buoy when the system is excited by a regular wave of frequency $\omega_e = 0.70 \, \text{rad/s}$ in the CFD model. Results from simulations with various levels of nonlinear stiffness parameterised by γ are present and show that in this case a small amount of nonlinearity in the stiffness ($\gamma = 1$) improved the power performance, while too much caused the motion to become nonperiodic which reduced the time-averaged power significantly.

ations, the proposed nonlinear stiffness does not improve upon an already optimised system. The optimised PTO parameters found using linear hydrodynamics provided generally good power performance for the nonlinear hydrodynamic simulations, but were not optimal. Nonlinear stiffness has also been shown to excite multiple period motion as well as non-periodic motion. When the motion induced is multi-period, this can provide an increase in time-averaged power. Whereas if the motion induced is

197

Figure 7.19: The heave and surge trajectory of the buoy when the system is excited by a regular wave of frequency $\omega_e = 0.57$ rad/s in the Linear model. Results from simulations with various levels of nonlinear stiffness parameterised by γ are present.

non-periodic the time-averaged power deteriorates quickly. The CFD simulations did show that the peaks in the resultant motion and time-averaged power changed between the linear and nonlinear hydrodynamic simulations. However, regular waves may not be representative of real sea conditions. Therefore irregular wave scenarios were analysed to assess any potential benefit of nonlinear stiffness systems in the context of submerged PA WECs.

7.5.3 Irregular waves

Irregular wave excitation of submerged quasi-PA was simulated using both linear and nonlinear hydrodynamic methods. The response of the tether extension for various degrees of nonlinear stiffness is given in Fig. 7.20. As γ increases, the tether extension changes from oscillating about the nominal position, to being restricted to one side of a bistable system. Around $\gamma = 0.5$, the system is rarely constrained to one side, while for $\gamma = 1$, the system rarely crosses the central barrier. The linear hydrodynamics model seems to permit oscillation between the stable points more readily.
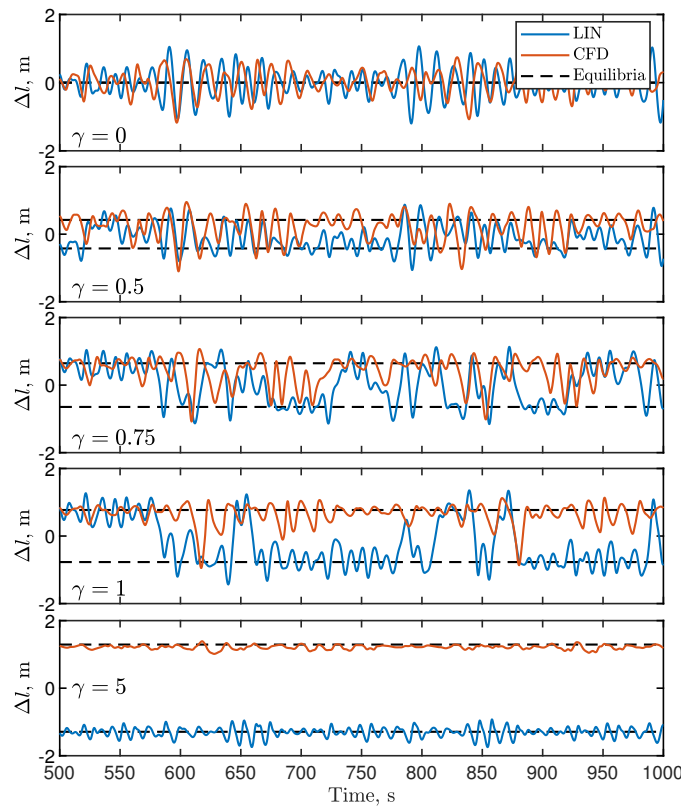
Figure 7.20: The tether extension of the device when excited by irregular waves. The linear and nonlinear hydrodynamic models are presented for varying degrees of nonlinear stiffness parameterised by γ. As γ increases, the equilibria shifts and the motion is more constrained to one side. The linear hydrodynamics model seems to permit oscillations between the stable points more readily than the CFD model.

To understand how the spectra of the motion is impacted as a result of the nonlinear stiffness, the amplitude spectra of the surge, heave, and pitch modes is given in Fig. 7.21. These amplitude spectra were found using the Matlab function *pwelch* by dividing the total time series into 10 equal samples with 70% overlap, applying a Hamming

window, and converting the resulting power spectral density to an amplitude spectrum. These results show that γ can broaden the frequency response in heave, but tends to reduce the peaks. If γ becomes too large, the overall motion can be greatly reduced leading to effective detuning of the device. The general trend between the linear and nonlinear hydrodynamic models is similar, however, the CFD model predicts larger surge motions, while the linear model predicts larger heave motions, particularly around lower frequencies as γ increases. Pitch motion is also noticeably increased in the CFD model and shows significant coupling with surge as the peaks occur at similar locations.
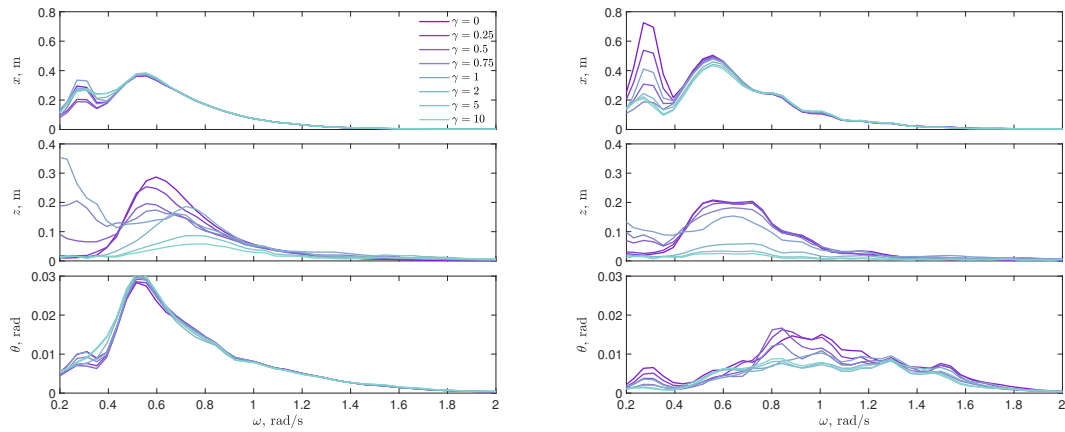
(a) Motions in each DOF using linear hydrodynamics.

(b) Motions in each DOF using nonlinear hydrodynamics.

Figure 7.21: The spectra of the surge, heave, and pitch motions in the linear and nonlinear hydrodynamic regimes when the system is excited by irregular waves for different nonlinear stiffnesses parameterised by γ.

The motion shows a frequency broadening feature trend in which as γ increase, the peak is reduced but spread over a wider frequency range. The resulting absorbed power should be analysed to understand whether this feature is beneficial or detrimental. To check for convergence, the time-averaged power calculated at each time step, $P_{\mathrm{avg,i}}$ (which may be considered the cumulative energy divided by the duration up until each time step) for a nonlinear stiffness characterised by $\gamma = 0.5$ is presented in Fig. 7.22. This metric is calculated using Equation (7.34), where, instead of using total duration of the simulation, only the duration up until each time step in the simulation is considered. This measure should asymptote towards a final value. It can be observed that in both the linear and nonlinear hydrodynamic irregular wave simulations, there is a rough convergence in the time-averaged power. Results from other levels of nonlinear stiffness were also analysed and showed the same behaviour. While there is still a small amount of variation in the final value, each simulation finished at the same time and the first 300 s were discarded to remove transient effects. Therefore, it is reasonable to use the

final time-averaged power as a comparative metric. However, longer simulations would provide more confidence in the absolute value of the time-averaged power.
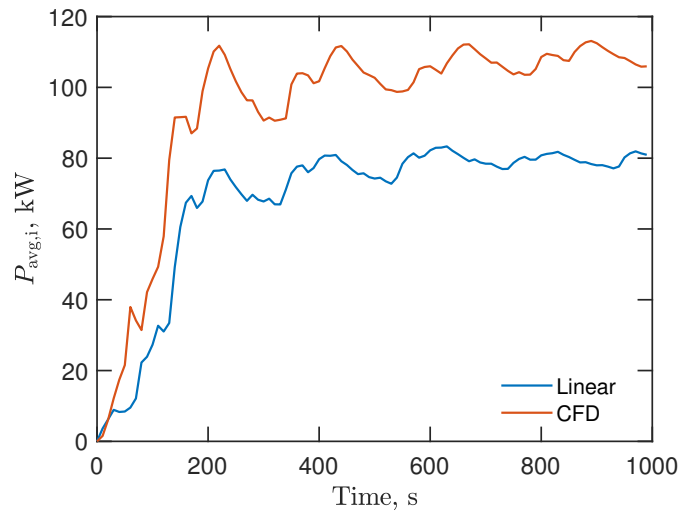

Figure 7.22: The time-averaged power in the linear and nonlinear hydrodynamic irregular wave models calculated at each time step for $\gamma = 0.5$. This plot demonstrates there is a rough convergence in the time-averaged power for both linear and CFD simulations.

The time-averaged power of the PTO for various γ is presented in Fig. 7.23. These results show that the linear model predicts no benefit due to the nonlinear stiffness, whereas the nonlinear model does predict some benefit for lower levels of γ. The improvement shown is around 5.5% and occurs around $\gamma = 0.25$, but the power still less than what is predicted in the linear hydrodynamic optimal scenario. The improvements are observed for $\gamma \leq 0.5$, demonstrating that the potential energy contribution of the nonlinear stiffness should be less than half the potential energy of the incident irregular wave. The reason for this could be the change in optimal conditions for the nonlinear system. While a 5.5% improvement is relatively small, these findings demonstrate that the nonlinear stiffness can effectively improve the robustness of such systems if the true optimal PTO conditions are unknown, which will commonly be the case for a constantly changing sea state in real ocean conditions. These results are for one random seed, due to computational difficulties of extensive CFD simulations, and further investigation is needed to strengthen the generality of this finding. However, it has been shown in Chapter 4, that the standard deviation between time-averaged power of different irregular wave realisations with similar parameters is around 1%, therefore the 5.5% is a notable improvement.

The nonlinear stiffness mechanism effectively changes the natural frequency of the system. Therefore the nonlinearity is exposing the system to a range of natural frequencies during operation rather than a single tuned frequency. This feature, particularly in

irregular waves, means that the system is less sensitive to the initial linear PTO parameters and that a small amount of nonlinearity can assist the system to better generate power from real ocean conditions.
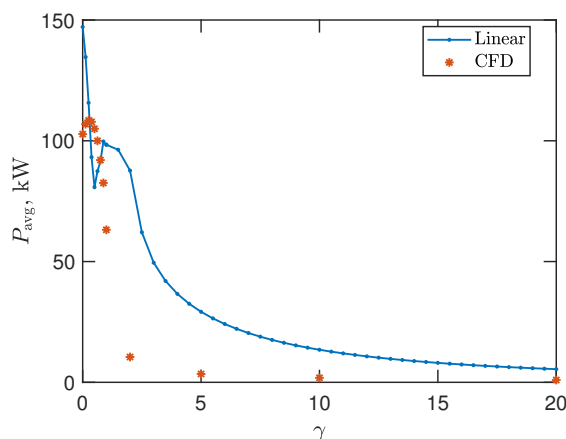

Figure 7.23: The time-averaged power in the linear and nonlinear hydrodynamic irregular wave models for various levels of nonlinear stiffness parameterised by γ.

7.5.4 Nonlinear stiffness performance impact

These findings show that the nonlinear stiffness in regular waves shows no improvement in power generation compared to optimal PTO conditions in the linear hydrodynamics settings and shows inconsistent improvement across different frequencies in the nonlinear hydrodynamics scenarios. This finding is in contrast to current literature conclusions (with only linear hydrodynamics), which indicate that a nonlinear stiffness can lead to significant improvements. The literature findings however, do not benchmark against an optimised linear system, and therefore do not accurately assess the true potential benefit of nonlinear stiffness mechanism. Furthermore, this work demonstrates that including nonlinear hydrodynamics and extending to multi-DOF, the natural frequency and optimal parameters are impacted. Consequentially, it is important to employ high fidelity simulations to obtain indicative performance estimates. For irregular waves, the nonlinear stiffness can assist in broadening the frequency band of the motion response as it exposes the system to a range of natural frequencies due to the nonlinear effective stiffness. The time-averaged power for irregular waves was improved in the nonlinear hydrodynamics compared to the optimised PTO settings. However, the optimisation was undertaken for the linear system, which may not hold for the nonlinear hydrodynamics regime. The 5.5% improvement suggests that a small degree of nonlinearity in the stiffness can improve the robustness of submerged WEC system for sea states as it may not be possible to determine optimal parameters as the spectrum changes over time

in real ocean conditions. Additionally, there are regions where the nonlinear stiffness greatly diminishes the dynamic response, which could be an effective method to detune the system during extreme conditions.

7.6   Conclusion

This work explored the potential improvement of a passive control system for a submerged PA WEC. The passive control system proposed consisted of a nonlinear stiffness mechanism in addition to a conventional linear stiffness and damping system. Such WECs are often modelled in simplified scenarios with limited DOF, hydrodynamic assumptions, or wave conditions. This work addressed these limitations by extending the system to 3 DOF and simulated the devices using both linear hydrodynamics (using a linear potential flow BEM solver) and nonlinear hydrodynamics (using CFD). The CFD model was validated against a known scenario. In addition, the system was simulated in regular and irregular waves to understand how the system dynamics changed with the nonlinear stiffness in high fidelity scenarios. The true effectiveness of the nonlinear stiffness mechanism was determined by comparing against scenarios with optimised linear stiffness and damping parameters. These parameters were optimised using only linear hydrodynamics.

The results showed that under regular conditions and linear hydrodynamics, there was no improvement to the power generation. Similarly, the regular conditions with nonlinear hydrodynamics showed inconsistent improvement over a range of frequencies. The extension to irregular waves with linear hydrodynamics again showed no improvement compared to the irregular wave scenario with optimal linear control parameters. However, the nonlinear hydrodynamic simulations of irregular waves showed an improvement when the potential energy of the nonlinear stiffness (at the nominal position) was less than half of the potential energy of the incident irregular wave with the best performance observed at 25% of the irregular wave potential energy.

The improvements were likely a result of the change in optimal conditions between linear and nonlinear control parameters, but demonstrated that the nonlinear stiffness mechanism may be used to broaden the frequency response and improve the robustness of the system for the simulated irregular wave. The limitations such as a short time series, a specific random realisation of the phases of irregular wave components, and the small number of frequency components suggests that further investigations would be needed to explore the generality of these results. Additionally, the results showed scenarios in which the nonlinear stiffness significantly reduces the motion and time-averaged power, which indicates such a mechanism could also be used to effectively detune the system during extreme wave conditions in which the device may be at risk.

Acknowledgment

Appendix 7.A CFD convergence - Irregular wave

To check for convergence within the irregular wave, the NWT generated the prescribed
wave, and the surface elevation was recorded every 0.5 s of simulation time for 1000
seconds. The wave elevation at the point (100,0,0) m was calculated at each time step
and recorded to construct an elevation time series. Convergence of the irregular wave
was considered by varying the number of initial cells in different directions prior to
the cell size halving, represented by (n_x, n_y, n_z), and by observing how the elevation
compares to the desired wave elevation in the modelled spectrum. A diagram of this
wave elevation time series is given in Fig. 7.24. The resultant power spectral density of
this time series were calculated using the Matlab function *pwelch* by dividing the total
time series into 25 equal samples with 70% overlap and applying a Hamming window.
The power spectral densities of the various different meshed scenarios were compared
and are given in Fig. 7.25. The time series data shows an approximate agreement
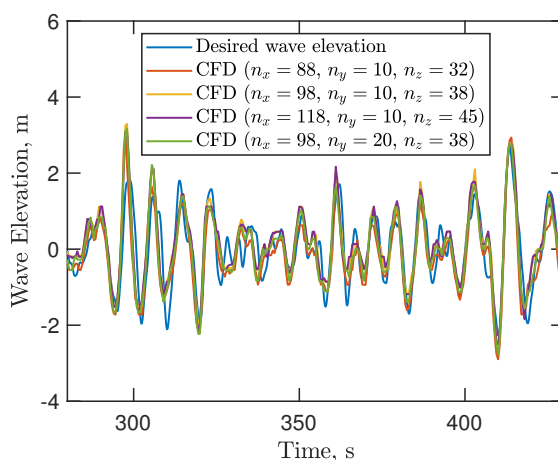
Figure 7.24: The wave elevation time series of the selected irregular wave generated in
the CFD simulations. The number of cells in each direction was varied to check that an
approximate convergence had been achieved.

between wave elevations. Given the stochastic nature of these waves and the minimal
change seen as the number of cells is increased and decreased, this signal was deemed
sufficient for the purpose of emulating real wave conditions. The resulting spectra
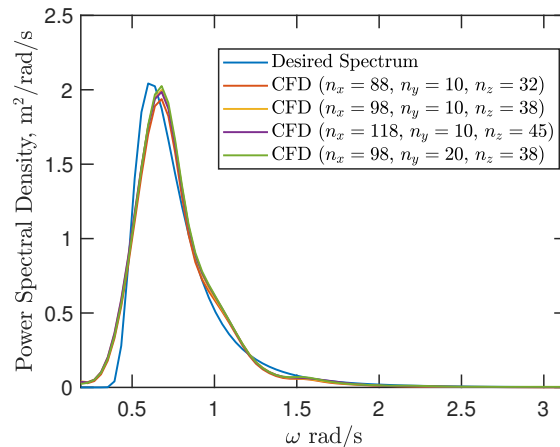indicate that the mesh settings used gave reasonably converged results. Numerically

Figure 7.25: The power spectral density of the generated irregular wave elevation time series in the CFD simulations compared to the desired modelled Pierson-Moskowitz spectrum. The number of cells in each direction was varied to check that an approximate convergence had been achieved.

integrating the power spectral density resulted with a difference of around 5 to 6.5% in the mean square value compared to the desired spectrum and therefore the spectrum with $(n_x, n_y, n_z) = (98, 10, 38)$ was selected to adequately represent the desired wave spectrum. It should be noted that with further time series data and an increased sampling rate, a more reliable convergence could be obtained, but due to the computational intensity of CFD, the strong agreement between simulated data, and the stochastic nature of real waves, additional data for perfect spectrum representation was considered unnecessary.

Appendix 7.B CFD convergence - Nonlinear stiffness

The nonlinear stiffness is another additional component to the validated CFD model that needed to be checked for convergence in order to maintain reliable results in lieu of experimental data. Accordingly, the scenario with the largest γ was subject to a range of different meshes. The resultant tether extension of the buoy subject to a regular wave of period 22 s with a γ of 20 for various meshes is provided in Fig. 7.26.

These results indicate that the cell count in each direction of the mesh of $(n_x, n_y, n_z) = (98, 10, 38)$ was able to capture the effect of nonlinear stiffness in the largest γ scenario. This limited check could further be validated if experimental data of such a scenario was available. The case selected has the most extreme nonlinear stiffness, to the degree that the system is bistable, hence the tether motion is restricted to one side (positive in this case) and the energy from the wave is insufficient to overcome the central barrier.
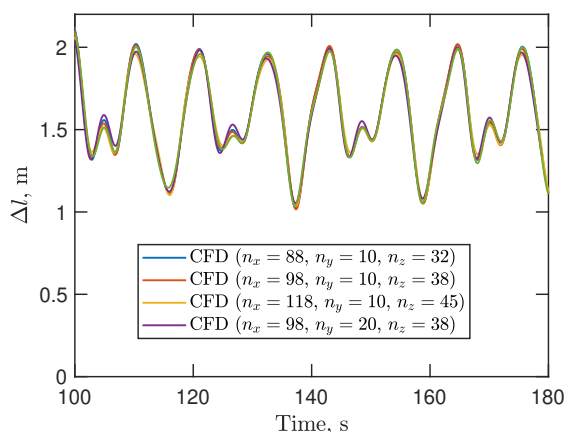
Figure 7.26: The resulting tether extension of the buoy subject to regular wave scenario
with period of 22 s and $\gamma = 20$ with a range of different meshing scenarios. The results
are very similar and the addition of the nonlinear stiffness within the CFD simulations
for the mesh parameters given is therefore acceptable.

This physical understanding is consistent with expected behaviour, which supports the
validity of using this implementation of nonlinear stiffness in CFD scenarios.

Based on the validation scenario presented in Section 7.2.3, the convergence of the
irregular wave, and the convergence of the bistability, the proposed NWT is sufficient
to adequately simulate the submerged WEC under both regular and irregular wave
conditions with a nonlinear stiffness mechanism.

References

[1]   D. Gielen et al. "The role of renewable energy in the global energy transforma-
       tion". In: *Energy Strategy Reviews* 24 (Apr. 2019), pp. 38–50. DOI: 10.1016/j.esr.
       2019.01.006.

[2]   C. Clauser and M. Ewert. "The renewables cost challenge: Levelized cost of
       geothermal electric energy compared to other sources of primary energy – Review
       and case study". In: *Renewable and Sustainable Energy Reviews* 82 (Feb. 2018),
       pp. 3683–3693. DOI: 10.1016/j.rser.2017.10.095.

[3]   W. Sheng and H. Li. "A method for energy and resource assessment of waves
       in finite water depths". In: *Energies* 10.4 (Apr. 2017), p. 460. DOI: 10.3390/
       en10040460.

[4]   A. F. de O. Falcão. "Wave energy utilization: A review of the technologies".
       In: *Renewable and Sustainable Energy Reviews* 14.3 (Apr. 2010), pp. 899–918. DOI:
       10.1016/j.rser.2009.11.003.

[5]   J. Cruz. *Ocean Wave Energy*. 1st ed. Springer-Verlag Berlin Heidelberg, 2008. DOI: `10.1007/978-3-540-74895-3`.

[6]   *CorPower's Wave Energy Concept*. Accessed: December 2020. URL: `https://www.corpowerocean.com/technology/`.

[7]   *CETO Next Generation*. Accessed: December 2020. URL: `https://www.carnegiece.com/portfolio/ceto-next-generation/`.

[8]   B. Drew, A. R. Plummer, and M. N. Sahinkaya. "A review of wave energy converter technology". In: *Proceedings of the Institution of Mechanical Engineers, Part A: Journal of Power and Energy* 223.8 (2009), pp. 887–902. DOI: `10.1243/09576509JPE782`. eprint: `http://dx.doi.org/10.1243/09576509JPE782`.

[9]   J. Falnes. "On non-causal impulse response functions related to propagating water waves". In: *Applied Ocean Research* 17.6 (Dec. 1995), pp. 379–389. DOI: `10.1016/S0141-1187(96)00007-7`.

[10]   Z. Shahroozi. "Force Prediction and Estimation for Point Absorber Wave Energy Converter". MA thesis. Uppsala University, 2019.

[11]   Z. Wu, C. Levi, and S. F. Estefen. "Wave energy harvesting using nonlinear stiffness system". In: *Applied Ocean Research* 74 (May 2018), pp. 102–116. DOI: `10.1016/j.apor.2018.02.009`.

[12]   R. L. Harne and K.-W. Wang. *Harnessing bistable structural dynamics: For vibration control, energy harvesting and sensing*. John Wiley & Sons, 2017.

[13]   M. Masoumi and Y. Wang. "Repulsive magnetic levitation-based ocean wave energy harvester with variable resonance: Modeling, simulation and experiment". In: *Journal of Sound and Vibration* 381 (Oct. 2016), pp. 192–205. DOI: `http://dx.doi.org/10.1016/j.jsv.2016.06.024`.

[14]   S. Palagummi and F. Yuan. "A bi-stable horizontal diamagnetic levitation based low frequency vibration energy harvester". In: *Sensors and Actuators A: Physical* 279 (Aug. 2018), pp. 743–752. DOI: `10.1016/j.sna.2018.07.001`.

[15]   N. Stephen. "On energy harvesting from ambient vibration". In: *Journal of Sound and Vibration* 293.1–2 (2006), pp. 409–425. DOI: `http://dx.doi.org/10.1016/j.jsv.2005.10.003`.

[16]   R. L. Harne and K. W. Wang. "A review of the recent research on vibration energy harvesting via bistable systems". In: *Smart Materials and Structures* 22.2 (Jan. 2013), p. 023001. DOI: `10.1088/0964-1726/22/2/023001`.

[17]   B. Mann and B. Owens. "Investigations of a nonlinear energy harvester with a bistable potential well". In: *Journal of Sound and Vibration* 329.9 (2010), pp. 1215–1226. DOI: `https://doi.org/10.1016/j.jsv.2009.11.034`.

[18] O. Abdelkhalik and S. Darani. "Optimization of nonlinear wave energy converters". In: *Ocean Engineering* 162 (Aug. 2018), pp. 187–195. DOI: 10.1016/j.oceaneng.2018.05.023.

[19] L. Wang, H. Tang, and Y. Wu. "On a submerged wave energy converter with snap-through power take-off". In: *Applied Ocean Research* 80 (Nov. 2018), pp. 24–36. DOI: 10.1016/j.apor.2018.08.005.

[20] X. Xiao, L. Xiao, and T. Peng. "Comparative study on power capture performance of oscillating-body wave energy converters with three novel power take-off systems". In: *Renewable Energy* 103 (Apr. 2017), pp. 94–105. DOI: 10.1016/j.renene.2016.11.030.

[21] D. Younesian and M.-R. Alam. "Multi-stable mechanisms for high-efficiency and broadband ocean wave energy harvesting". In: *Applied Energy* 197 (2017), pp. 292–302. DOI: http://dx.doi.org/10.1016/j.apenergy.2017.04.019.

[22] X.-T. Zhang, J.-M. Yang, and L.-F. Xiao. "An oscillating wave energy converter with nonlinear snap-through Power-Take-Off systems in regular waves". In: *China Ocean Engineering* 30.4 (July 2016), pp. 565–580. DOI: 10.1007/s13344-016-0035-5.

[23] H. Zhang et al. "Efficiency enhancement of a point wave energy converter with a magnetic bistable mechanism". In: *Energy* 181 (Aug. 2019), pp. 1152–1165. DOI: 10.1016/j.energy.2019.06.008.

[24] X. Zhang et al. "Mechanism and sensitivity for broadband energy harvesting of an adaptive bistable point absorber wave energy converter". In: *Energy* 188 (Dec. 2019), p. 115984. DOI: 10.1016/j.energy.2019.115984.

[25] L. Silva et al. "Stochastic analysis of nonlinear wave energy converters via statistical linearization". In: *Applied Ocean Research* 95 (Feb. 2020), p. 102023. DOI: 10.1016/j.apor.2019.102023.

[26] Z. Wu, C. Levi, and S. F. Estefen. "Practical considerations on nonlinear stiffness system for wave energy converter". In: *Applied Ocean Research* 92 (Nov. 2019), p. 101935. DOI: 10.1016/j.apor.2019.101935.

[27] B. W. Schubert et al. "Linear and nonlinear hydrodynamic models for dynamics of a submerged point absorber wave energy converter". In: *Ocean Engineering* 197 (Feb. 2020), p. 106828. DOI: 10.1016/j.oceaneng.2019.106828.

[28] M. Penalba, G. Giorgi, and J. V. Ringwood. "Mathematical modelling of wave energy converters: A review of nonlinear approaches". In: *Renewable and Sustainable Energy Reviews* 78 (Oct. 2017), pp. 1188–1207. DOI: 10.1016/j.rser.2016.11.137.

[29]   A. Rafiee and J. Fiévez. "Numerical prediction of extreme loads on the CETO wave energy converter". In: *Proceedings of the 11th European Wave and Tidal Energy Conference, Nantes, France*. 2015.

[30]   J. H. Todalshaug et al. "Tank testing of an inherently phase-controlled wave energy converter". In: *International Journal of Marine Energy* 15 (Sept. 2016), pp. 68–84. DOI: 10.1016/j.ijome.2016.04.007.

[31]   A. Têtu et al. "Physical and Mathematical Modeling of a Wave Energy Converter Equipped with a Negative Spring Mechanism for Phase Control". In: *Energies* 11.9 (2018), p. 2362.

[32]   E. Guerber et al. "A fully nonlinear implicit model for wave interactions with submerged structures in forced or free motion". In: *Engineering Analysis with Boundary Elements* 36.7 (July 2012), pp. 1151–1163. DOI: 10.1016/j.enganabound.2012.02.005.

[33]   M. Penalba, T. Kelly, and J. V. Ringwood. "Using NEMOH for modelling wave energy converters: a comparative study with WAMIT". In: *Centre for Ocean Energy Research (COER), Maynooth University, Co. Kildare, Ireland* (2017).

[34]   C. Windt, J. Davidson, and J. V. Ringwood. "High-fidelity numerical modelling of ocean wave energy systems: A review of computational fluid dynamics-based numerical wave tanks". In: *Renewable and Sustainable Energy Reviews* 93 (Oct. 2018), pp. 610–630. DOI: 10.1016/j.rser.2018.05.020.

[35]   J. Davidson and R. Costello. "Efficient Nonlinear Hydrodynamic Models for Wave Energy Converter Design—A Scoping Study". In: *Journal of Marine Science and Engineering* 8.1 (Jan. 2020), p. 35. DOI: 10.3390/jmse8010035.

[36]   G. McCauleya et al. "Non-linear hybrid model for forced heave of a shallowly submerged cylinder." In: *35th International Workshop on Water Waves and Floating Bodies*. International Workshop on Water Waves and Floating Bodies. 2020.

[37]   B. W. Schubert et al. "Performance enhancement of submerged wave energy device using bistability". In: *Ocean Engineering* 213 (Oct. 2020), p. 107816. DOI: 10.1016/j.oceaneng.2020.107816.

[38]   J. N. Newman. *Marine hydrodynamics*. The MIT press, 2018.

[39]   W. Cummins. *The impulse response function and ship motions*. Tech. rep. David Taylor Model Basin, Washington DC, 1962.

[40]   T. Perez and T. I. Fossen. "Joint identification of infinite-frequency added mass and fluid-memory models of marine structures". In: *Modeling, Identification and Control* 29.3 (2008), pp. 93–102. DOI: 10.4173/mic.2008.3.2.

[41] T. Perez and T. I. Fossen. "A Matlab toolbox for parametric identification of radiation-force models of ships and offshore structures". In: *Modeling, Identification and Control: A Norwegian Research Bulletin* 30.1 (2009), pp. 1–15. DOI: 10.4173/mic.2009.1.1.

[42] N. Sergiienko et al. "Feasibility study of the three-tether axisymmetric wave energy converter". In: *Ocean Engineering* 150 (Feb. 2018), pp. 221–233. DOI: 10.1016/j.oceaneng.2017.12.055.

[43] R. Salmon. "Introduction to ocean waves". In: *Scripps Institution of Oceanography, University of California, San Diego* (2008).

[44] O. Faltinsen. "Sea loads on ships and offshore structures". In: vol. 1. Cambridge University Press, 1993. Chap. 2, pp. 22–29.

[45] F. Meng et al. "A sensitivity study on the effect of mass distribution of a single-tether spherical point absorber". In: *Renewable Energy* 141 (2019), pp. 583–595. DOI: 10.1016/j.renene.2019.03.149.

[46] W. Robertson, B. Cazzolato, and A. Zander. "Axial force between a thick coil and a cylindrical permanent magnet: optimizing the geometry of an electromagnetic actuator". In: *IEEE Transactions on Magnetics* 48.9 (2012), pp. 2479–2487. DOI: 10.1109/TMAG.2012.2194789.

[47] B. W. Schubert et al. "Enhancement of a 3-DOF submerged wave energy device using bistability". In: *Proceedings of the 13th European Wave and Tidal Energy Conference*. 2019.

[48] S. Gran. "A Course in Ocean Engineering (Developments in Marine Technology)". In: Elsevier Science Ltd, 1992. Chap. 2, pp. 187–199.

[49] D. Freedman, R. Pisani, and R. Purves. "Statistics (international student edition)". In: *Pisani, R. Purves, 4th edn. WW Norton & Company, New York* (2007).

[50] P. Higuera, I. J. Losada, and J. L. Lara. "Three-dimensional numerical wave generation with moving boundaries". In: *Coastal Engineering* 101 (July 2015), pp. 35–47. DOI: 10.1016/j.coastaleng.2015.04.003.

[51] B. Le Méhauté. *An introduction to hydrodynamics and water waves*. Springer Science & Business Media, 2013.

[52] J. Falnes. *Ocean waves and oscillating systems: Linear interactions including wave-energy extraction*. Cambridge University Press, 2002.

[53] F. Meng et al. "Modal analysis of a submerged spherical point absorber with asymmetric mass distribution". In: *Renewable Energy* 130 (2019), pp. 223–237. DOI: https://doi.org/10.1016/j.renene.2018.06.014.

[54] J. Orszaghova et al. "Transverse motion instability of a submerged moored buoy". In: *Proceedings of the Royal Society A: Mathematical, Physical and Engineering Sciences* 475.2221 (Jan. 2019), p. 20180459. DOI: 10.1098/rspa.2018.0459.

[55] P. Higuera. *olaFOAM Reference Manual*. Feb. 2016.

[56] C. Stansberg et al. "The specialist committee on waves final report and recommendations to the 23rd ITTC". In: *Proceedings of the 23rd ITTC* 2 (2002), pp. 505–551.

Chapter 8

Conclusion

8.1 Overall conclusions

The research presented in this thesis is focussed on the application of a nonlinear stiffness mechanism to a submerged PA WEC. The primary purpose of the nonlinear stiffness mechanism is to enhance the ability for the device to extract power from an incident ocean wave. The fidelity of the modelled WEC was systematically increased by extending the model from 1 DOF to 3 DOF, including geometric nonlinearities, position dependent nonlinear hydrodynamic influences, and combining the nonlinear stiffness into a holistic high fidelity CFD scenario to assess the device performance under regular and irregular excitation.

An initial simplified 1 DOF model was constructed to identify the intrinsic differences in the application of nonlinear stiffness in floating and submerged WEC scenarios. It was found that floating systems that have suboptimal linear control stiffness benefit significantly from an effective negative stiffness produced from a nonlinear stiffness. The functional reason is that the negative stiffness counteracts the significant buoyancy force acting on the floating buoy. If a negative linear control force was introduced, the buoy system may be optimally tuned, and any additional nonlinearity only acts to reduce the performance of the WEC. For the submerged context, a position dependent force is required for submergence and the effective stiffness from buoyancy is zero. Therefore, the optimal stiffness was found to be positive and any additional nonlinear stiffness degrades the performance. However, if the optimised systems are excited by irregular waves, which slowly vary over time and are stochastic in nature, the nonlinear stiffness can provide a benefit to the system for different phase relationship between different wave components, thereby enhancing the robustness of the system. However, the improvement and the variation observed in different irregular wave realisations are comparable in magnitude. Alternatively, if the nonlinear stiffness was intentionally selected poorly, this presents an opportunity to effectively detune the system during

extreme conditions to protect the device.

The model was then extended to 3 DOF to allow for cross coupling between different modes of motion and geometric nonlinear forces acting through the tether direction. The system was subjected to both regular and irregular waves. It was shown that if the system was suboptimally tuned, the nonlinear stiffness can provide a direct benefit to the power captured. The primary mechanism driving the improvement was that the nonlinear stiffness exposes the system to a range of effective natural frequencies. If the excitation frequency falls into the range of effective natural frequencies over the operating region of the device, the system showed good performance. Compared to an optimised control system, the nonlinear augmentation did not improve upon the power captured, but was able to achieve approximately the same maximum power. The nonlinear mechanism was also able to enhance the robustness to other irregular waves, and for certain conditions a consistent 10–20% improvement was observed.

Improving the fidelity of simulation by modelling the 3 DOF dynamics was an important step to determine whether the behaviour was consistent. However, limiting the fluid-structure interaction to simplified linear hydrodynamic models undermines the fidelity and reliability of the results. Therefore, the hydrodynamic forces were examined by modelling the system using four different approaches; linear, partially nonlinear, pseudo-nonlinear, and fully nonlinear CFD. The linear assumed the hydrodynamic properties did not change during operation, so is only representative for small motions. The partially nonlinear and pseudo-nonlinear attempt to capture the position dependence of the system by using the results from the linear potential flow method to apply gain scheduling the excitation force, and the excitation and radiation forces, respectively. The fully nonlinear model calculates the fluid forces at each time step and was validated against experimental data. It was shown the models founded on the linear potential flow method do not suitably represent all the influential hydrodynamic forces acting on the buoy. In particular, a frequency dependence influence was identified as the body of water above the buoy resonates, acting to either impede or assist the vertical motion of the buoy. Therefore, it was concluded that fully nonlinear hydrodynamic representations are required to provide more indicative results.

The final component of this research was the introduction of the nonlinear stiffness force to the high fidelity hydrodynamic model. The system was again excited using regular and irregular waves for varying degrees of nonlinear stiffness. It was observed that for low levels of nonlinear stiffness, the absorbed power may be increased compared to optimised conditions. This finding is a result of the nonlinear hydrodynamics shifting the effective natural frequency, and as the nonlinear stiffness exposes the system to a range of natural frequencies, the system experiences a benefit in irregular waves for low levels of nonlinear stiffness. In regular waves, an inconsistent result is observed across different frequencies with the nonlinear stiffness. However, the irregular waves are

more representative of real ocean conditions. Therefore, a mechanism which provides a small amount of nonlinear stiffness relative to the average potential energy of the incident wave may provide a benefit in terms of increased robustness to changing ocean conditions, resulting with an increase in the amount of power harnessed from waves. This finding shows that passive control systems may be an attractive option to reduce the reliance on active components for tuning of WECs.

8.2 Original contributions

The author considers the following contributions to be substantial additions to the field of wave energy:

1. extending the linear hydrodynamic model to incorporate position dependence in the excitation and radiation force for submerged WECs;

2. modelling the result of an additional nonlinear stiffness mechanism to an optimised, multiple DOF system;

3. expanding the modelling of bistable systems in the wave energy field by applying a nonlinear stiffness within a high fidelity validated CFD scenario, demonstrating the real potential for such devices;

4. quantifying and standardising the degree of nonlinear stiffness or bistability relative to the potential energy of the wave and providing recommendations as to what features of a bistable system would likely be beneficial;

5. investigating the mechanisms behind how nonlinear stiffness and bistability provide enhanced features in submerged WECs;

6. identifying the true potential of nonlinear stiffness compared to optimised conditions as a tool of enhance robustness for changing sea conditions.

8.3 Future work

This research presented the application of nonlinear stiffness within validated high fidelity simulations. Throughout the development of this research, it was necessary to restrict the scope in some areas. Accordingly, there remains a number of potential areas which could be further explored to improve upon the understanding and applicability of nonlinear stiffness in the wave energy context.

1. To further elaborate on the potential of the nonlinear stiffness, experimental work would be needed to practically demonstrate the potential benefit. Scaled experiments in a wave flume would assist the validation of the nonlinear augmentation

and may identify additional beneficial or detrimental features due to higher order hydrodynamic influences not seen in simulations.

2. The addition of a passive nonlinear stiffness mechanism could be applied in conjunction with an active control system. The fundamental purpose of such a combination would be to reduce the dependence on active components to reduce cost and improve the power efficiency by relying upon passive means to provide the essential reactive control. Alternatively, an adaptive control system which would vary the nonlinear stiffness profile based on ocean conditions may offer some tangible benefit.

3. A further extension should be an economic analysis based on experimental results, component costs and efficiencies, different power take off arrangements, and alternative control strategies in conjunction with the nonlinear stiffness.

4. This work was also primarily restricted to a submerged PA WEC of a specified geometry. Adjusting the geometry, especially for floating systems may see a more pronounced performance improvement due to nonlinear stiffness. Specifically, if the nonlinear trend was selected to counteract the nonlinear hydrostatic stiffness (which is dependent on buoy geometry), a net linear stiffness may be formed to provide a well tuned passive device.

5. The nonlinear stiffnesses in this work were formed using magnetic representations. Higher fidelity representations of the nonlinear stiffness contained with alternative power take off, either through magnetic or other means, would further assist in identifying suitable and cost effective passive systems.

Appendix A

Enhancement of a 3-DOF submerged wave energy device using bistability

This paper is the outcome of a preliminary investigation into using bistability to enhance a submerged wave energy device. It explores the impact of nonlinear stiffness on time averaged power for systems that are optimal and suboptimal in both 1 DOF and 3 DOF contexts. This study may be considered an extension to Chapter 4 and a preliminary study to Chapter 5. This paper was presented at the 13th European Wave and Tidal Energy Conference, in Naples Italy. It was subsequently selected as being among the best submitted to the conference and was included in a special issue of the International Marine Energy Journal.

The conceptual development of this study may be attributed, in part, to all authors. All code, simulations, processing of results and most interpretation was conducted by B. Schubert. Other interpretation and technical oversight was provided by the remaining coauthors.

Enhancement of a 3-DOF submerged wave energy device using bistability

Benjamin W. Schubert, William S. P. Robertson, Benjamin S. Cazzolato, and Mergen H. Ghayesh

Abstract—The dynamic response of a submerged CETO shaped quasi-point absorbing wave energy converter coupled to a bistable power take off is presented in this study. Whilst the impact of bistability has been shown in a limited number of situations to improve the amount of power generated, many models have been restricted to a single degree of freedom and often ignore drag effects. To overcome these model limitations, a submerged single tether point absorber with a bistable power take off was modelled using both 1 and 3 degrees of freedom. The device was subjected to regular waves and included a simple model of viscous drag. The bistable mechanism was provided by a magnetic dipole model quantified by a dimensionless parameter applicable to any bistable system. The performance of the device was is assessed by the theoretical power generated. Over each model, the previously observed benefit of bistability was not consistently obtained. Simulations of regular waves demonstrated an increase in generated power for suboptimal conditions for some frequencies, while a reduction in generated power was observed in optimal conditions. The performance increase showed strong correlation to the phase relationship between the motion and exciting forces as a result of bistability.

Index Terms—bistable, passive control, performance enhancement, submerged point absorber

I. INTRODUCTION

OCEAN wave energy has been the subject of over two centuries of research according to [1]. Over this time many individual designs have been proposed with differing modes of operation. A number of typical wave energy converters (WEC) are discussed in [2] and can be broadly classed as one of three types: an attenuator, a point absorber (PA), or a terminator. This paper focuses on a PA type WEC, which are systems in which the buoy is small relative to the wavelengths of the incident waves, and are subsequently relatively insensitive to wave direction. A representative diagram of a point absorber with a generic buoy is shown in Fig. 1. While the simple operation of a generic PA WEC is well known, there remains many challenges for wave energy, as identified in [3]. Areas in which further work is required before commercialisation are: materials and manufacture; fluid dynamics and hydrodynamics; survivability and reliability; environmental resources; devices and arrays; power conversion and control; infrastructure and grid connection; marine operations
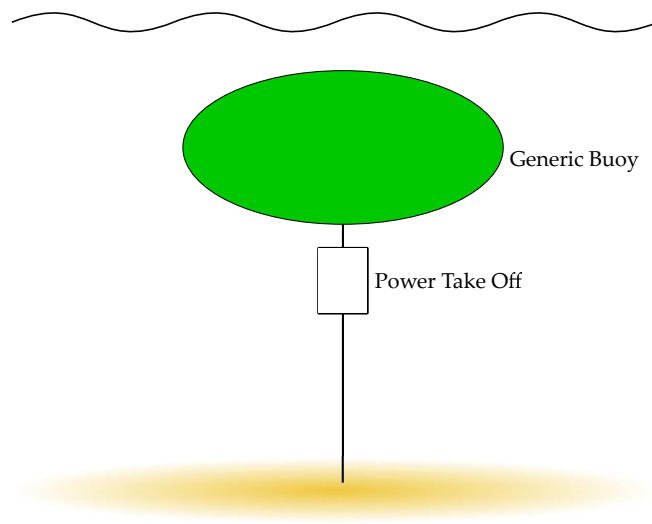
Fig. 1. A single tether submerged generic PA WEC.

and maritime safety; socio-economic implications; and environmental impact. Due to the complexity of these unique challenges in the context of wave energy, the technology as a whole remains at a low technology readiness level, a measure used to quantify progress to commercialisation.

Within the area of power conversion and control, hybrid control, in which passively applied dynamics supplements the active controller, may provide some advantages in complexity over active control algorithms. References [4]–[7] propose different bistable mechanisms within the power take off unit (PTO) and show for simple single degree of freedom (DOF) models that a substantial benefit is seen. Methods to create a nonlinear stiffness without bistability have been preposed such as in [8] in which an assymetric mass distribution is used to change the effective stiffness. A bistable mechanism using magnets is given in [6] which, being an electromagnetic system, has the advantage of having relatively small reactive power losses compared to other reactive mechanisms, such as hydraulic systems. Furthermore, a multi-DOF device and the potential for bistability to improve the efficiency of WEC devices was investigated in [9]. Experimental work within [10] and [11] demonstrated on different devices that the realistic benefit of bistability applied to is significant and in some cases may be as much as a three times power increase. A method to optimize a nonlinear stiffness has been presented in [12]. Each device and mechanism is different and bistability is employed in various ways to either excite super harmonics to convert low frequency oscillations

into high frequency oscillations, such as in [13], or to passively phase match floating buoys, such as in [11]. Of the work presented, only [9] is related to submerged WECs and does not operate in the vertical heave direction. In addition to the restricted DOF, many of the proposed models do not include even simplistic drag; how these model deficiencies impact the benefit of bistability, as well as the mechanism behind the benefit within the context of submerged WECs, remains a gap within current literature.

To advance the technology, a whole system approach is suggested in [14], where an understanding of all parts of the complex system are considered and an understanding of interaction between components is developed. With this guiding principle, the impact of bistable control on a submerged 3-DOF PA WEC was explored in the present study to quantify how simple hydrodynamics and the passive control system inter-act. Four models were constructed: an optimal 1-DOF model, a suboptimal 1-DOF model, an optimal 3-DOF model, and a suboptimal 3-DOF model, all subjected to a set of regular waves. The mathematical models are described in Section II, with the representation of the magnetic bistable mechanism given in Section II-A4, as well as a dimensionless parameter relevant to any bistable system as a means to generalize results. The considerations and limitations of the used modelling method are outlined in Section III, and the results of these simulations are presented in Section IV. These results are discussed in detail in Section V, with a summary of the findings in Section VI.

II. MATHEMATICAL MODELS

The governing equations for the 1-DOF and 3-DOF systems can be derived from the contributing forces represented by:

$$\mathbf{M}\ddot{\mathbf{x}} = \mathbf{F}_\mathrm{e} + \mathbf{F}_\mathrm{r} + \mathbf{F}_\mathrm{h} + \mathbf{F}_\mathrm{PTO} + \mathbf{F}_\mathrm{D} + \mathbf{F}_\mathrm{bi} \;, \qquad (1)$$

where $\mathbf{F}$ represents a force and the subscripts e, r, h, PTO, D, and bi indicate the excitation, radiation, hydrostatic, PTO, drag, and bistable forces, respectively. The inertial mass of each DOF of the system in represented by the matrix $\mathbf{M}$, and $\mathbf{x}$ is the position vector containing the surge (x), heave (z), and pitch (θ) coordinates. This equation forms the basis for the governing equations for all three models presented with constituting force components either simplified or represented differently.

A. Single DOF

By simplifying (1) to 1-DOF and ignoring the viscous drag force, the following governing equation can be constructed to represent a simple WEC model:

$$M_z \ddot{z} = F_{\mathrm{e},z} + F_{\mathrm{r},z} + F_{\mathrm{h},z} + F_{\mathrm{PTO},z} + F_{\mathrm{bi},z} \;, \qquad (2)$$

where the subscript z represents only the heave component. A time domain representation of each force is provided in the following sections.

1) Excitation force

The excitation force for the 1-DOF system, $F_{\mathrm{e},z}$, can be calculated using linear potential flow theory and is the superposition of the Froude-Krylov and diffraction forces. This force may be considered as the force on the buoy due to incoming waves. In the work presented here the boundary element method (BEM) solver NEMOH, described in [15], was used to calculate the amplitude ($\hat{\mathbf{F}}_\mathrm{e}$) and phase ($\phi$) of the excitation force (in all 3-DOF) and can be represented as

$$F_{\mathrm{e},z} = \hat{F}_{\mathrm{e},z} \cos(\phi_z - \omega t) \;, \qquad (3)$$

where ω and t represent the excitation frequency and time, respectively.

2) Radiation force

The radiation force can be considered as the force on the buoy due to the waves radiated as the buoy moves in calm water. This force is represented in the time domain by the Cummins equation as [16],

$$\mathbf{F}_\mathrm{r} = -\mathbf{A}_\infty \ddot{\mathbf{x}} - \int_0^t \mathbf{K}(t - t') \dot{\mathbf{x}}(t') dt' \;, \qquad (4)$$

where $\mathbf{A}_\infty$ and $\mathbf{K}$ are termed the infinite frequency added mass and the memory function, respectively. The convolution integral addresses the influence of the previous state on the current state. In practice, this integral is difficult to properly quantify and an alternative approach is more commonly implemented. The frequency domain representation of the radiation force is

$$\hat{\mathbf{F}}_\mathrm{r} = -[\mathbf{B}(\omega) + i\omega\mathbf{A}(\omega)]\hat{\mathbf{x}}(i\omega), \qquad (5)$$

where $\mathbf{B}(\omega)$ is the frequency-dependent radiation damping and $\mathbf{A}(\omega)$ is the added mass. These hydrodynamic quantities are also able to be calculated using NEMOH. The method outlined in [17] uses these two hydrodynamic quantities to construct a transfer function to relate velocity to the value of the integral in (4). In the 1-DOF model, only the heave velocity contributes to the radiation force in the heave direction so a basic transfer function will suffice; whereas in 3-DOF, in general, the radiation force for any DOF may be influence by other DOFs, depending on geometry.

3) Hydrostatic and PTO forces

The hydrostatic (or buoyancy) force acts only in the heave direction and is the difference between the weight of displaced water and the weight of the buoy, given by

$$F_{\mathrm{h},z} = \rho g V - mg \;, \qquad (6)$$

where ρ, g, m, and V are the density of water, acceleration due to gravity, buoy mass, and buoy volume, respectively. For a fully submerged buoy, this force is constant. Accordingly, a pretension force equal in magnitude is included in the PTO force, in addition to a stiffness and damping term as follows:

$$F_{\mathrm{PTO},z} = -b\dot{z} - k_s z - F_{\mathrm{h},z} \;, \qquad (7)$$

where b is the damping coefficient and k_s is the spring constant. This defines the submerged nominal position to be $z = 0$.

Both the damping coefficient and spring constant may be optimized for a given frequency; the optimal values have been derived in [18] and for a heaving PA are defined to be

$$b_{\text{opt}} = B_z(\omega) \, , \qquad k_{s,\text{opt}} = \omega^2(m + A_z(\omega)) \, . \quad (8)$$

The optimal PTO stiffness condition for the 3-DOF regular wave scenarios may be found approximately by using (8) as an initial estimate, and adjusting k_s until the root mean square (RMS) of the instantaneous power is at a local maximum or until the buoy breaches the water surface. The PTO damping, b, was left unchanged in the 3-DOF model by assuming that the optimisation of the stiffness was sufficient. However, in some low frequency cases for the 1-DOF scenarios, the damping was artificially increased to ensure stability and prevent surface breaching. In the 3-DOF scenarios, heave was considered the most influential DOF, and therefore the same optimisation process may be used. These conditions were found to produce conditions in which the phsae of $F_{\text{e},z}$ and $\dot{z}$ were matched. The instantaneous power generated by the WEC is approximated by

$$P_{\text{inst}} = b\dot{\mathbf{x}}^2 \, . \quad (9)$$

4) Bistable force

A bistable force is any force that induces a two-well potential energy barrier, as depicted on Fig. 2. Such systems exhibit unique dynamic features not seen in regular linear systems. These features, explored in [19], include multiple single period steady state responses for a given excitation frequency leading to bifurcation of responses, aperiodic or chaotic behaviour, a large dependence on initial conditions and excitation amplitudes, stochastic resonances (resonating using a combination of low amplitude inputs), and the excitation of input frequency harmonics. These features can lead to broader resonance bandwidths particularly at lower frequencies, frequency up-conversion which turns low frequency oscillations into higher frequency oscillations, and performance improvement in stochastic excitation contexts. The main benefit of bistability occurs during interwell motion rather than intrawell due to the snap through property. This snap through mechanism forms a more energetic system if the excitation is sufficient to overcome the dividing potential barrier. The escape from a potential well was shown to broaden the frequency range of a generator in [20]. While each of these characteristic features may be exploited for different circumstances, wave energy as an application may be well suited given the low frequency and stochastic nature of waves.

For the purposes of this study, a magnetic dipole model was used to create a bistable system. A depiction of the WEC PTO model with bistability is given in Fig. 3.

The force between two magnetic dipoles, in this case between the stationary outer dipole and the dipole within the translator, may be derived from [21]

$$\mathbf{F}_{\text{bi}} = \nabla(\mathbf{m}_{\text{d},1} \cdot \mathbf{B}_{\text{d},2}) \, , \quad (10)$$
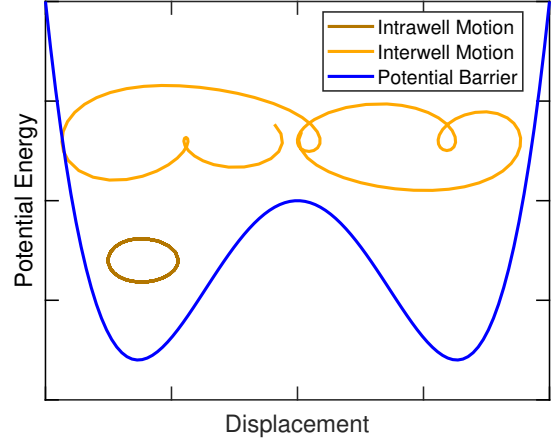

Fig. 2. An example bistable double well potential energy barrier and motion.
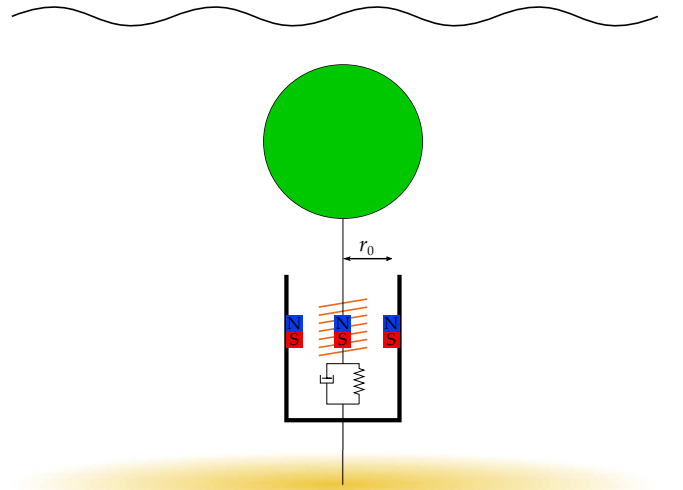

Fig. 3. An example WEC with a magnetic bistable mechanism within the PTO.

where $\mathbf{m}_{\text{d},1}$ is the dipole moment of the first dipole, and $\mathbf{B}_{\text{d},2}$ is the magnetic field of the second dipole at the location of the first dipole. Assuming magnetisation in the z direction, the dipole moments are given by

$$\mathbf{m}_{\text{d}} = (0, 0, VM) \, , \quad (11)$$

where V is the volume of the magnet, and M is the magnetisation field per unit volume. The magnetic field for a dipole is given by [22]

$$\mathbf{B}_{\text{d},2} = -\frac{\mu_0}{4\pi} \nabla \frac{\mathbf{m}_{\text{d},1} \cdot \mathbf{r}}{r^3} \, , \quad (12)$$

where $\mathbf{r}$ is the displacement between the dipoles, and μ_0 is the permeability of free space. Using (10) and (12), the vertical force between the two dipoles may be derived as

$$\mathbf{F}_{\text{bi}} = \frac{\mu_0 M_1 V_1 M_2 V_2}{4\pi} \left(\frac{9z}{(r_0^2 + z^2)^{\frac{5}{2}}} - \frac{15z^3}{(r_0^2 + z^2)^{\frac{7}{2}}} \right) \quad (13)$$

where r_0 is the horizontal distance between dipoles. Similarly, the potential energy of this force can be

derived as

$$U_{\text{bi}} = \frac{\mu_0 M_1 V_1 M_2 V_2}{4\pi} \left(\frac{-1}{(r_0^2 + z^2)^{\frac{3}{2}}} + \frac{3z^2}{(r_0^2 + z^2)^{\frac{5}{2}}} \right) \quad (14)$$

using the relationship

$$U_{\text{bi}} = -\mathbf{m}_{\text{d},1} \cdot \mathbf{B}_{\text{d},2} . \quad (15)$$

The derivation was generalized in both [22] and [23]. This force was incorrectly derived in [6] and [20], however, the end result was still a force which exhibits the intended bistable behaviour. The potential energy of the dipole representation superimposed with the potential energy from a linear stiffness, provides the intended bistable profile.

To generalize the degree of bistability between any mechanism, the dimensionless parameter γ is proposed, which is the ratio of the average potential energy of the wave over the buoy, U_{wave}, and the potential energy of the bistable system at the nominal position, $U_{\text{bi},z=0}$, that is

$$\gamma = \frac{U_{\text{bi},z=0}}{U_{\text{wave}}} . \quad (16)$$

For a regular wave, the time average potential energy per unit area, $\hat{U}_{\text{wave}}$, may be expressed as

$$\hat{U}_{\text{wave}} = \frac{1}{4}\rho g \hat{A}^2 , \quad (17)$$

where $\hat{A}$ is the amplitude of the incoming wave. The parameter γ may be varied to define the height of the central potential peak, represented in Fig. 4a. In addition, the location of the stable regions can also be varied, in this case by the changing the horizontal distance between dipole r_0 while keeping γ constant. The impact of changing r_0 on the potential wells is given in Fig. 4b. Varying these parameters gave a large range of possible force and potential profiles which were used to build an understanding around which bistable conditions are favourable for the ocean wave energy context.

The aforementioned forces were combined into (2) and the dynamic equation of a 1-DOF submerged PA WEC was formed. Further descriptions and model specifics may be found in Section III.

B. Three DOF regular waves

Expanding the model from a single degree of freedom is not trivial as the excitation, radiation, and PTO forces are significantly altered. A simple drag force is also included to improve the fidelity of the simulation. The alterations and additions are explained in the following sections.

1) Excitation force

Previously the excitation force was represented as a scalar in the z direction. However, in general, the BEM solver NEMOH can provide the excitation amplitude and phase for all 3 DOFs. In 3 DOF, the phase of the excitation force shifts as the buoy moves in the surge direction relative to the wave. The forces may be included into (1) in a similar way as in the 1-DOF model, with the inclusion of the phase offset due to surge, ϕ_s, as

$$\mathbf{F}_{\text{e}} = \hat{\mathbf{F}}_{\text{e}} \cos(\phi + \phi_s - \omega t) , \quad (18)$$

where ωt and ϕ_s are applied to each component of ϕ. The phase offset due to surge is

$$\phi_s = kx , \quad (19)$$

where k is the wavenumber, which is the solution to the dispersion relationship

$$\omega^2 = gk \tanh(kH) , \quad (20)$$

where the depth of the water is represented by H.

2) Radiation force

The radiation force for the 1-DOF model was a single transfer function between velocity and the z component of the convolution integral in (4). This may be expanded to accommodate 3-DOF by constructing a transfer function between all velocity components and all convolution integral components then representing this as a state space model. This method accounts for the interaction between DOFs, for example how the surge velocity impacts the radiation torque experience in the pitch direction. The contribution of the convolution integral, $\boldsymbol{\mu}$, may be described as

$$\dot{\mathbf{p}} = \mathbf{A}_{ss}\mathbf{p} + \mathbf{B}_{ss}\dot{\mathbf{x}} , \quad (21)$$

$$\boldsymbol{\mu} = \mathbf{C}_{ss}\mathbf{p} , \quad (22)$$

where $\mathbf{p}$ is a state vector of non-physical variables, and $\mathbf{A}_{ss}$, $\mathbf{B}_{ss}$, and $\mathbf{C}_{ss}$ are state space matrices constructed from the aforementioned transfer functions.

3) Drag force

The viscous drag force is a nonlinear force often neglected in simple models given by

$$\mathbf{F}_{\text{D}} = -\frac{1}{2}\mathbf{C}_{\text{D}}\rho\mathbf{A}_{\text{D}}|\dot{\mathbf{x}}_{\text{r}}|\dot{\mathbf{x}}_{\text{r}} , \quad (23)$$

where $\mathbf{C}_{\text{D}}$, $\mathbf{A}_{\text{D}}$, and $\dot{\mathbf{x}}_{\text{r}}$ are the coefficients of drag, characteristic area, and velocity of the buoy relative to the surrounding fluid. As an approximation, the fluid velocity at the geometric center of the buoy was used. By assuming a linear wave, the fluid velocity in the heave and surge directions may be estimated as

$$\dot{x} = \hat{A}\omega \frac{\cosh(k(H + z - d_s))}{\sinh(kH)} \cos(kx - \omega t) , \quad (24)$$

$$\dot{z} = \hat{A}\omega \frac{\sinh(k(H + z - d_s))}{\sinh(kH)} \sin(kx - \omega t) , \quad (25)$$

where d_s is the submergence depth of the geometric center of the buoy.

4) Hydrostatic and PTO forces

The 1-DOF PTO force acts only in the z direction, whereas in 3-DOF the force acts in the direction of the tether. Therefore, (7) becomes

$$\mathbf{F}_{\text{PTO}} = \mathbf{T}(-b\Delta\dot{l} - k_s\Delta l - F_{\text{h},z}) , \quad (26)$$

where the extension of the tether, Δl, is used instead of the heave coordinate z. The coordinate transform between $(x, z, \theta) \rightarrow (\Delta l, \alpha, \phi)$ is represented by $\mathbf{T}$ with
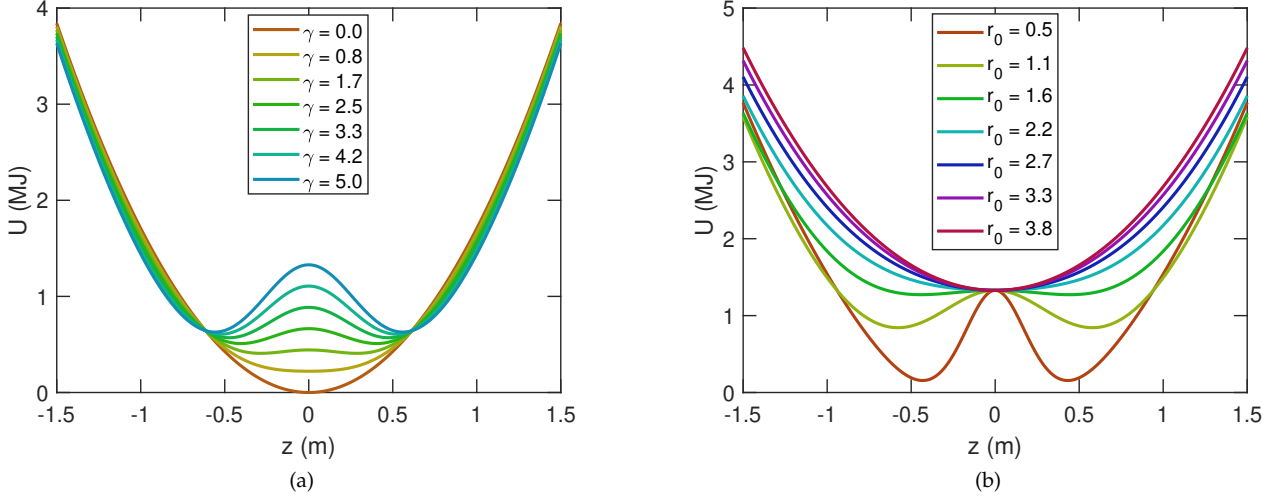
Fig. 4. Examples of how varying the bistable parameters may change the potential energy profile of the system: (4a) the impact of γ variations for $r_0 = 2$m, and (4b) the impact of r_0 variations for $\gamma = 2$.
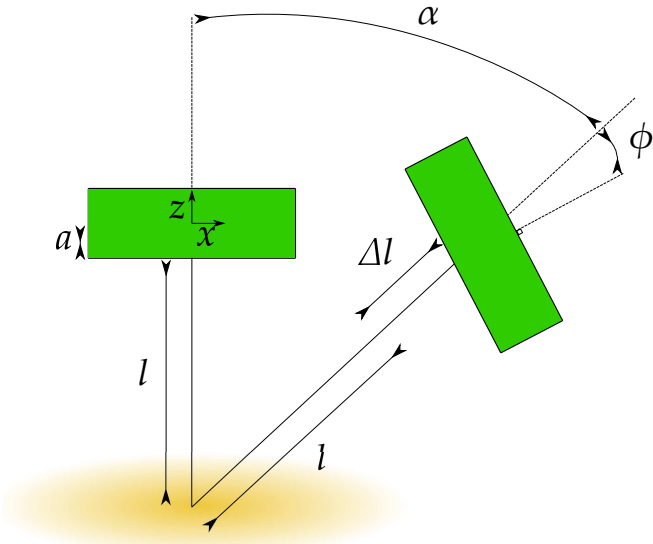

Fig. 5. A diagram depicting the variables of two coordinate systems.

coordinates defined on Fig. 5. The inverse transformation is

$$\Delta l = \sqrt{(x - a\sin\theta)^2 + (z + l + a - a\cos\theta)^2} - l \,, \quad (27)$$

$$\alpha = \arctan\left(\frac{x - a\sin\theta}{z + l + a - a\cos\theta}\right) \,, \quad (28)$$

$$\phi = \theta - \alpha \,, \quad (29)$$

where a and l are the distance between buoy center and tether attachment point, and the total tether length, respectively.

It should be noted that the proposed bistable mechanism is contained within the PTO. Therefore the bistable force undergoes the same transformation $\mathbf{T}$ to convert to (x, z, θ) coordinates. Combining these new descriptions of forces into (1) gives the model of a 3-DOF submerged PA WEC.

III. SIMULATION CONSIDERATIONS

Within each scenario, an identical WEC geometry and setup was developed. In both the 1-DOF and 3-DOF simulations, the WEC system was excited by a series of monochromatic waves and the resulting dynamic behaviour was recorded for each frequency. Within the scenarios, to show the sensitivity to tuning, the system was simulated with the PTO settings tuned to a single frequency found by (8), and then optimal conditions at each frequency. The bistable parameter γ was also varied and the resulting root mean square (RMS) motion, time-averaged power P_{avg}, and maximum steady state forces were recorded. The time-averaged power is given by

$$P_{\text{avg}} = \frac{1}{T} \sum_{j=t_i}^{j=t_f} P_{\text{inst},j} \Delta t_j \,, \quad (30)$$

where t_i, t_f, Δt_j, and T are the initial time, final time, the jth time step, and the total time interval, respectively. These are chosen to discard any transient effects. In addition to the time-averaged power metric, which is the power absorbed by the PTO, the power absorbed by the buoy from the wave can be quantified by the time-averaged excitation power, P_{e}, given by

$$P_{\text{e}} = \frac{1}{T} \sum_{j=t_i}^{j=t_f} |\mathbf{F}_{\text{e},j}||\dot{x}_j| \Delta t_j \,. \quad (31)$$

The phase between the excitation force and the tether velocity was also explored to further understand the impact of the bistable mechanism. The model dimensions and scenario conditions are outlined below.

A. Model dimensions

The geometry of the buoy was selected to be similar to the CETO design presented by [24]. The diagram in Fig. 6, details various relevant physical quantities.
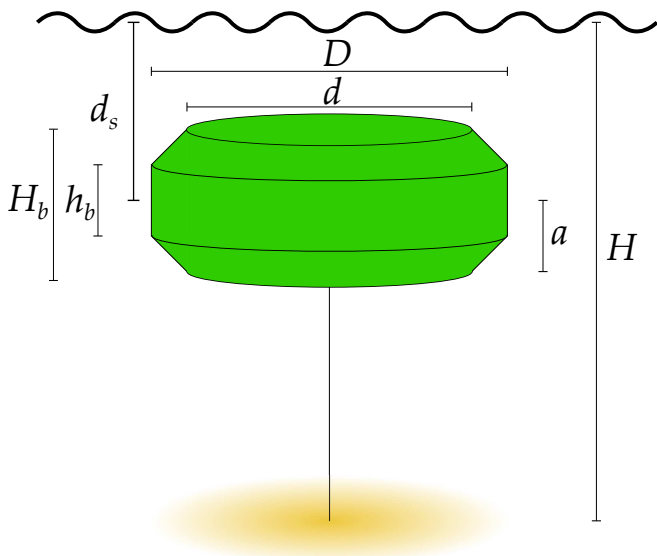
Fig. 6. A schematic of a CETO shaped buoy used in all simulated scenarios, and the definition of a number of physical quantities.

These physical quantities as well as some general quantities used in the simulations are listed below in Table I, and the drag properties based on [25] for a buoy of this shape is given in Table II.

TABLE I
SIMULATION PARAMETERS

Parameter	Value	Units
Water depth, H	40	m
Submersion depth (buoy center), d_s	7	m
Inner diameter, d	17	m
Outer diameter, D	20	m
Inner height, h_b	3	m
Outer height, H_b	6	m
Attachment arm, a	3	m
Water density, ρ	1025	$\mathrm{kg\,m^{-3}}$
Buoy density, ρ_{buoy}	0.7ρ	$\mathrm{kg\,m^{-3}}$
Acceleration due to gravity, g	9.81	$\mathrm{m\,s^{-2}}$

TABLE II
DRAG PROPERTIES

	x	z	θ
Coefficient of drag, C_{D}	0.7	1.28	0.22
Characteristic area, A_{D}	DH_b	$\pi\left(\frac{D}{2}\right)^2$	$D^4 D$

B. Scenario conditions

The parameters pertinent to the 1-DOF and 3-DOF scenarios are detailed in Table III. The model was built and simulated in MATLAB Simulink (Mathworks Inc., Natick MA, USA). A simulation time of around 2000 seconds was found to be sufficient with a ramped start-up to reduce the transient time. The second half of the simulation was used for post-processing to ensure no transient effects impacted the results.

TABLE III
SIMULATION PARAMETERS FOR THE 1-DOF AND 3-DOF SCENARIOS

Parameter	Value	Units
Wave amplitude, $\hat{A}$	0.5	m
Excitation Frequency, ω	$0.1 - 2$	rad/s
Dimensionless potential, γ	$0 - 30$	-
Dipole spacing, r_0	1.5	m

IV. RESULTS

The results for the simulation scenarios described in section III are displayed below.

A. Single DOF

The 1-DOF scenarios were simulated with the PTO configuration given by (8) at each frequency and the resulting RMS of the motion as well as the time-averaged power for varying γ are given in Figs 7a and 7b, respectively. The same results for the 1-DOF buoy simulated with PTO settings optimized for a frequency of $\omega = 0.77$ rad/s are given in Figs 8a and 8b. This frequency was chosen to avoid peaks whilst having a reasonable response.

Given the significant difference between the optimal and non-optimal scenarios, the time domain relationship between the excitation force and the velocity for the non-optimal scenario at a frequency which showed benefit ($\omega = 1$ rad/s) with varying γ is given in Fig. 9. The phase difference between the excitation force and velocity, as well as the excitation power for this case is presented in Fig. 10 and a phase plot relative to the potential energy profiles of these scenarios are given in Fig. 11.

B. Three DOF regular waves

The 3-DOF scenarios were also simulated with locally optimized and then suboptimal PTO conditions and the resulting motion RMS and time-averaged power for the optimal condition with varying γ are shown in Figs 12a and 12b, respectively. The same variables for the suboptimal conditions tuned to frequency $\omega = 0.77$ rad/s is given in Figs 13a and 13b, respectively. These results will be analysed and discussed in Section V.

V. DISCUSSION

The results for the 1-DOF simulation in the non-optimized condition show a small improvement in average power due to bistability. The motion seems to indicate that there are bands of frequencies in which there is large motion reductions. In the optimal PTO condition cases, bistability seems to greatly reduce the effectiveness of the PTO system at absorbing power. It is well known that the optimal case is when the excitation force and the velocity are in phase and any change to this caused by the bistability is detrimental. However, for the non-optimized case, bistability seems to improve the tendency of the velocity and the excitation
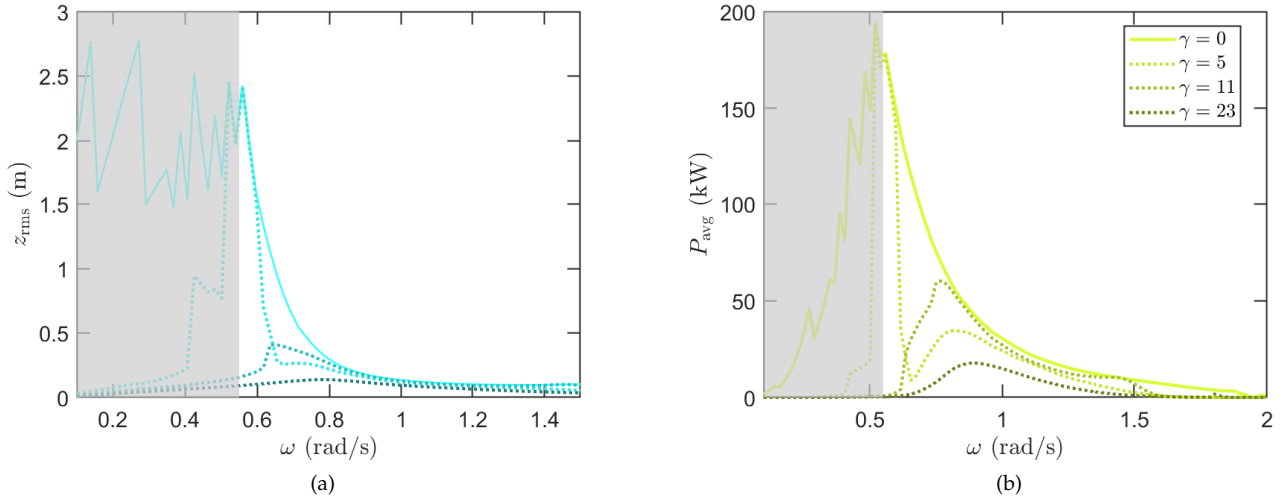
Fig. 7. The resulting peak motion (7a) and the time-averaged power (7b) for the 1-DOF scenario and varying γ, using PTO parameters found from (8). The damping of the PTO was increased for frequencies below 0.54 rad/s to prevent breaching; therefore, these results may be considered only near optimal (region shaded).
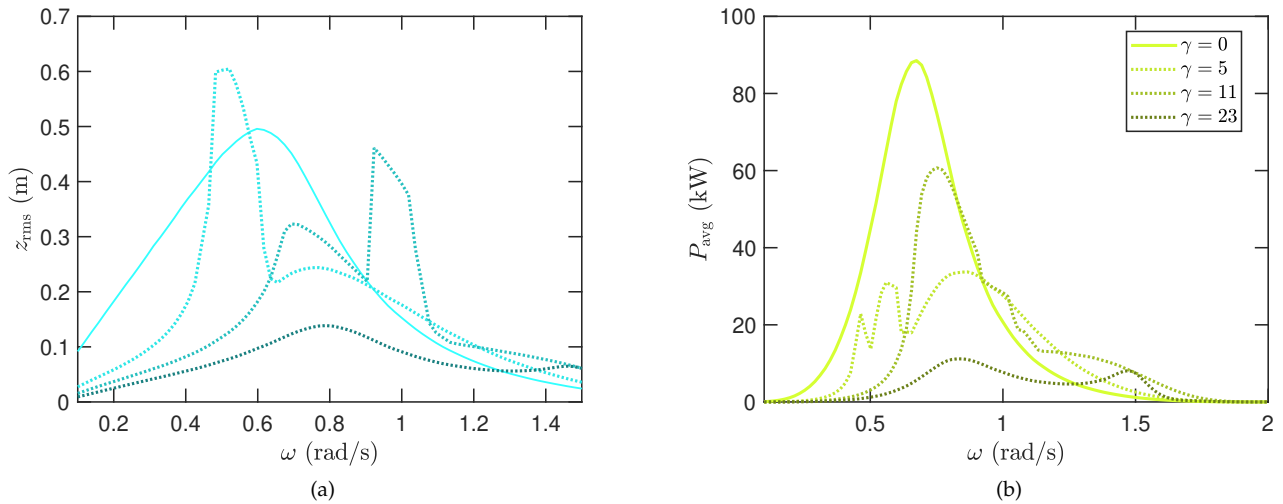

Fig. 8. The resulting peak motion (8a) and the time-averaged power (8b) for the 1-DOF scenario and varying γ, using PTO settings found from (8) at $\omega = 0.77$ rad/s.
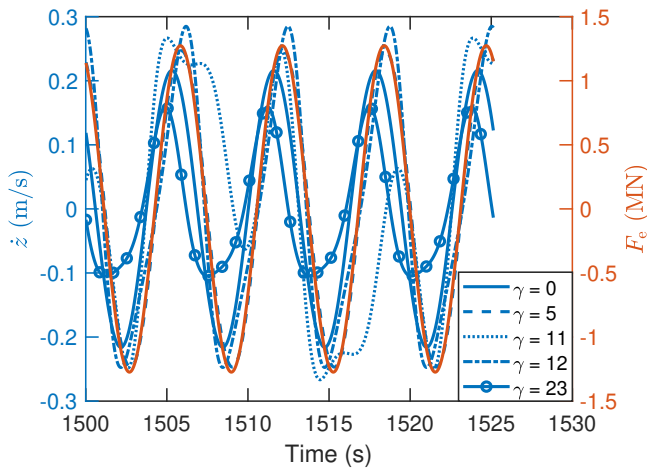
Fig. 9. The time domain relationship between the excitation force (right axis) and the velocity (left axis) for the non optimized PTO conditions and varying γ at frequency $\omega = 1$ rad/s.
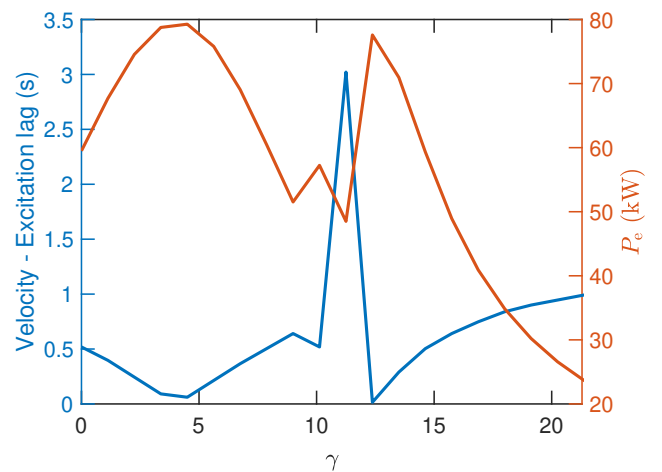
Fig. 10. The phase lag between the excitation force and velocity when excited at $\omega = 1$ rad/s for varying γ with the non-optimized PTO conditions.
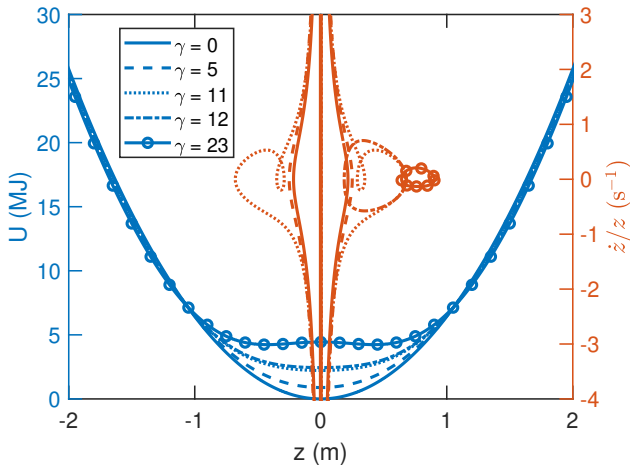
Fig. 11. The PTO potential energy profile and phase portrait of the motion when excited by $\omega = 1 \text{ rad/s}$ for varying γ with the non-optimized PTO conditions.

force to be in phase which helps in harvesting more power. The relationship between γ, velocity-excitation lag, and excitation power shows there is a strong trend indicating that the most beneficial scenario is one in which the lag time is minimized. Even when restricted to one side of the potential well, seen in Fig. 11 at $\gamma = 12$, the force due to the nonlinear stiffness seems to passively adjust the motion leading to near optimal results. The phase plots shown in Fig. 11 show the transition between an interwell motion and intrawell motion. The corresponding excitation power demonstrates that intrawell motion leads to an improvement. One explanation of this may be that the asymmetry in the potential well, when restricted to one side, allows the device to be partially tuned to a range of frequencies. This mechanism would lead to a benefit for higher frequencies at high levels of bistability due to the higher stiffnesses in those regions (seen in Fig.8b). Similarly, bistability would benefit lower frequencies at low levels of bistability due to regions of lower stiffnesses (seen in Fig. 13b). Such a property may be useful to passively partially tune a device making a system more robust. Another property of bistability seen in the $\gamma = 11$ response in Fig. 9 is the excitation of multiple frequencies. In this case, the multiple frequencies cause significant deviation from a simple sinusoid and are detrimental for energy generation. For the optimal case, in which the excitation force and velocity are already in phase, the resulting multiple harmonic motion invariably lead to a suboptimal scenario in which only part of the motion is matched. For a perfectly tuned 1-DOF submerged WEC, bistability is detrimental, otherwise, bistability seems to provide a benefit. In practice, it is difficult to find the exact PTO tuned conditions for more complex scenarios such as 3-DOF or for irregular waves. The 3-DOF simulations were all tuned using the aforementioned local optimization method. Accordingly, the inclusion of bistability also showed a decrease in average power, similar to the 1-DOF scenario. The resulting motion RMS exhibited a large reduction in heave motion and an amplification

of the surge and pitch motions at some frequencies. This is likely due to the phase altering property and the geometric nonlinear coupling between DOFs. However, overall this did not improve the time-averaged power. This finding further supports the assumption that heave is the DOF most closely associated with power production for a single tether PA WEC. For a monochromatic wave, it is feasible to run multiple simulations to determine the optimal PTO stiffness as is done in this study. In irregular waves representing real ocean waves, optimal conditions are challenging to predict and require foreknowledge of the excitation force. Therefore, exploring the characteristics of bistability in sub-optimally tuned scenarios is useful to gain insight into the performance impact to real conditions. When the 3-DOF model uses optimal conditions for frequency $\omega = 0.77 \text{ rad/s}$, a notable improvement is seen at lower frequencies, even with viscous drag forces. In some cases, over double the power is absorbed by the PTO. The highest peaks occur when $\gamma \leq 2$ indicating that the potential energy of the bistable mechanism relative to average potential energy of the wave is a contributing factor. However, for all these simulations the magnetic dipole spacing was held constant at $r_0 = 1.5 \text{ m}$. To further extend this work, the influence of the magnetic dipole spacing should be investigated to characterize favourable nonlinear potential profiles for submerged PA. Bistable mechanics within the context of irregular waves should also be considered as the passive phase matching property seen in the 1-DOF sub-optimal condition could be effective in irregular conditions. Furthermore, the impact of nonlinear hydrodynamics on bistable mechanics should quantified either by including a nonlinear representation of Froude-Krylov forces, or by simulating using computational fluid dynamics. In principle, if an optimal nonlinear stiffness potential profile is identified, a passive system can be constructed by springs or magnets to realize the benefit. One potential advantage of the nonlinear magnetic spring over conventional hydraulic or electrodynamic PTOs is that the reactive energy of such magnetic mechanisms is highly efficient, allowing the natural frequency to be altered with almost no parasitic losses.

VI. Conclusion

The impact of a bistable force acting on a submerged PA WEC was explored by simulating a CETO-like device in 1-DOF and 3-DOF regular wave scenarios, where the 3-DOF simulations included geometric nonlinearity and drag effects. The bistable force was represented as a magnetic dipole and combined with a linear stiffness to give an overall nonlinear stiffness in the system. The results showed that for a device that is not optimally tuned, bistability can provide a substantial benefit by exciting multiple frequencies and passively matching the phase of the excitation force and velocity. For optimally tuned situations, the excitation force and velocity are already in phase and the addition of nonlinear stiffness reduces the effectiveness of the device. In practice tuning a device for a given wave condition is challenging, but bistability was shown in
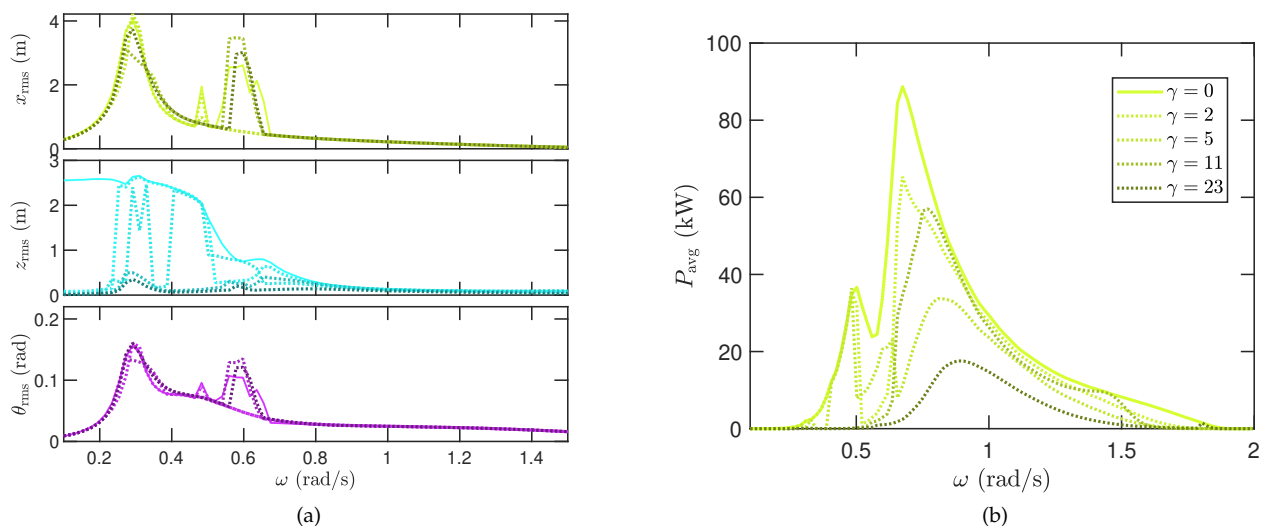
Fig. 12. The RMS of the motion (12a) and the time-averaged power (12b) for the 3-DOF scenario and varying γ (indicated by varying shade) where the PTO conditions are locally optimized for each frequency.
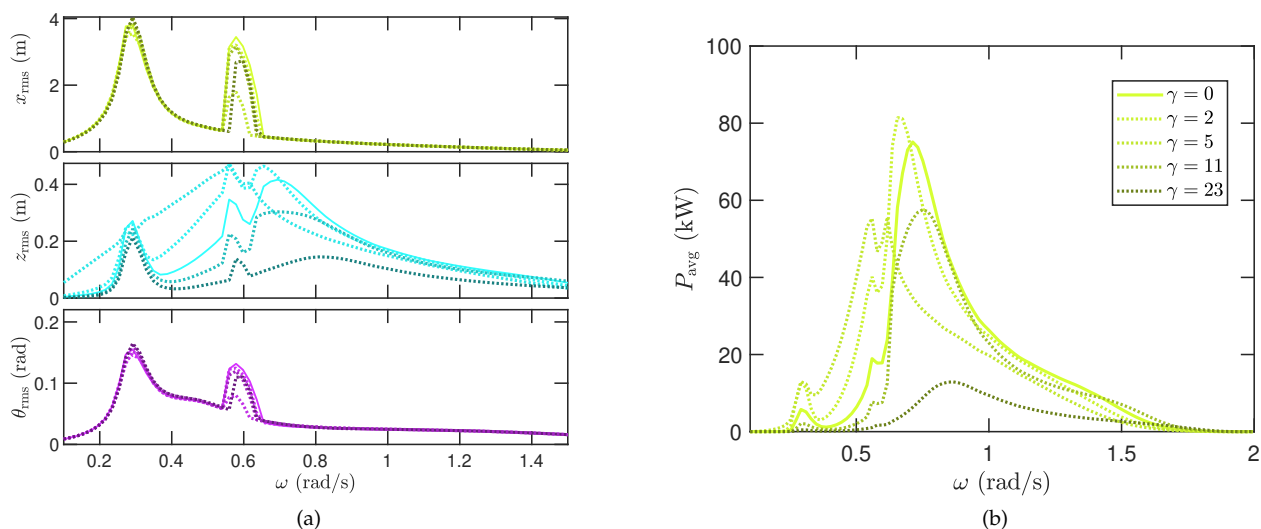

Fig. 13. The RMS of the motion (13a) and the time-averaged power (13b) for the 3-DOF scenario and varying γ (indicated by varying shade) where the PTO is tuned for $\omega = 0.77$ rad/s.

regular waves to provide a passive benefit. This work builds upon existing work in bistability by applying such a mechanism to the submerged WEC context and develops an understanding around what properties of bistable mechanics is providing the enhanced power performance.

REFERENCES

[1] J. Cruz, *Ocean Wave Energy*, 1st ed. Springer-Verlag Berlin Heidelberg, 2008.

[2] B. Drew, A. R. Plummer, and M. N. Sahinkaya, "A review of wave energy converter technology," *Proceedings of the Institution of Mechanical Engineers, Part A: Journal of Power and Energy*, vol. 223, no. 8, pp. 887–902, 2009. [Online]. Available: http://dx.doi.org/10.1243/09576509JPE782

[3] D. Greaves and G. Iglesias, *Wave and Tidal Energy*. John Wiley & Sons, 2018.

[4] X.-T. Zhang, J.-M. Yang, and L.-F. Xiao, "An oscillating wave energy converter with nonlinear snap-through power-take-off systems in regular waves," *China Ocean Engineering*, vol. 30, no. 4, pp. 565–580, Jul. 2016.

[5] D. Younesian and M.-R. Alam, "Multi-stable mechanisms for high-efficiency and broadband ocean wave energy harvesting," *Applied Energy*, vol. 197, pp. 292 – 302, 2017. [Online]. Available: http://www.sciencedirect.com/science/article/pii/S03062619173 04191

[6] X. Xiao, L. Xiao, and T. Peng, "Comparative study on power capture performance of oscillating-body wave energy converters with three novel power take-off systems," *Renewable Energy*, vol. 103, pp. 94–105, Apr. 2017.

[7] X. Zhang, X. Tian, L. Xiao, X. Li, and L. Chen, "Application of an adaptive bistable power capture mechanism to a point absorber wave energy converter," *Applied Energy*, vol. 228, pp. 450–467, Oct. 2018.

[8] F. Meng, B. Ding, B. Cazzolato, and M. Arjomandi, "Modal analysis of a submerged spherical point absorber with asymmetric mass distribution," *Renewable Energy*, vol. 130, pp. 223 – 237, 2019. [Online]. Available: http://www.sciencedirect.com/science/article/pii/S096014811830644X

[9] L. Wang, H. Tang, and Y. Wu, "On a submerged wave energy converter with snap-through power take-off," *Applied Ocean Research*, vol. 80, pp. 24–36, Nov. 2018.

[10] A. Têtu, F. Ferri, M. Kramer, and J. Todalshaug, "Physical and mathematical modeling of a wave energy converter equipped

with a negative spring mechanism for phase control," *Energies*, vol. 11, no. 9, p. 2362, 2018.

[11] J. H. Todalshaug, G. S. Ásgeirsson, E. Hjálmarsson, J. Maillet, P. Möller, P. Pires, M. Guérinel, and M. Lopes, "Tank testing of an inherently phase-controlled wave energy converter," *International Journal of Marine Energy*, vol. 15, pp. 68–84, Sep. 2016.

[12] O. Abdelkhalik and S. Darani, "Optimization of nonlinear wave energy converters," *Ocean Engineering*, vol. 162, pp. 187–195, Aug. 2018.

[13] R. L. Harne and K. W. Wang, "A review of the recent research on vibration energy harvesting via bistable systems," *Smart Materials and Structures*, vol. 22, no. 2, p. 023001, Jan. 2013.

[14] O. Danielsson, "Wave energy conversion: Linear synchronous permanent magnet generator," Ph.D. dissertation, Uppsala University, Division for Electricity and Lightning Research, 2006.

[15] A. Babarit, *NEMOH User manual*, Ecole Centrale de Nantes, Jan. 2014.

[16] W. Cummins, "The impulse response function and ship motions," David Taylor Model Basin, Washington DC, Tech. Rep., 1962.

[17] T. Perez and T. I. Fossen, "A Matlab toolbox for parametric identification of radiation-force models of ships and offshore structures," *Modeling, Identification and Control: A Norwegian Research Bulletin*, vol. 30, no. 1, pp. 1–15, 2009.

[18] J. Falnes, *Ocean waves and oscillating systems: Linear interactions including wave-energy extraction.* Cambridge University Press, 2002.

[19] R. L. Harne and K.-W. Wang, *Harnessing bistable structural dynamics: For vibration control, energy harvesting and sensing.* John Wiley & Sons, 2017.

[20] B. Mann and B. Owens, "Investigations of a nonlinear energy harvester with a bistable potential well," *Journal of Sound and Vibration*, vol. 329, no. 9, pp. 1215–1226, 2010.

[21] D. Griffiths, *Introduction to Electrodynamics.* Pearson Education, 2014. [Online]. Available: https://books.google.com.au/books?id=J9ygBwAAQBAJ

[22] K. W. Yung, P. B. Landecker, and D. D. Villani, "An analytic solution for the force between two magnetic dipoles," *Physical Separation in Science and Engineering*, vol. 9, no. 1, pp. 39–52, 1998.

[23] P. B. Landecker, D. D. Villani, and K. W. Yung, "An analytic solution for the torque between two magnetic dipoles," *Physical Separation in Science and Engineering*, vol. 10, no. 1, pp. 29–33, 1999.

[24] C. C. Energy, "What is CETO," 2018. [Online]. Available: https://www.carnegiece.com/wave/what-is-ceto/

[25] A. Rafiee and J. Fiévez, "Numerical prediction of extreme loads on the CETO wave energy converter," in *Proceedings of the 11th European Wave and Tidal Energy Conference, Nantes, France*, 2015.

Appendix B

Pseudo-nonlinear hydrodynamic coefficients for modelling point absorber wave energy converters

This paper is the outcome of an initial investigation into using different hydrodynamic modelling techniques of submerged point absorber wave energy converters which forms the foundation of Chapter 6. The study proposes a novel hydrodynamic modelling technique which uses linear potential flow to estimate hydrodynamic properties of both spherical and cylindrical buoys at different poses. The resultant simulations are compared to fully nonlinear CFD simulations. This paper was presented at the 4th Asian Wave and Tidal Energy Conference in Taipei, Taiwan, in 2018.

The conceptual development of this study may be attributed, in part, to all authors. All code, simulations, processing of results and most interpretation was conducted by B. Schubert. Other interpretation and technical oversight was provided by the remaining coauthors. Additional input around the validation of the CFD scenarios was given by A. Rafiee, but testing and interations of code development was conducted by B. Schubert.

Schubert, B. W., Meng, F., Sergiienko, N. Y., Robertson, W.S.P., Cazzolato, B. S., Ghayesh, M. H., Rafiee, A., Ding, B. and Arjomandi, M., 2018. Pseudo-nonlinear hydrodynamic coefficients for modelling point absorber wave energy converters. In: *The 4th Asian Wave and Tidal Energy Conference (AWTEC)*. Taipei, Taiwan.

Pseudo-Nonlinear Hydrodynamic Coefficients for Modelling Point Absorber Wave Energy Converters

Benjamin W. Schubert[#1], Fantai Meng[#2], Nataliia Y. Sergiienko[#3], Will Robertson[#4], Benjamin S. Cazzolato[#5], Mergen H. Ghayesh[#6], Ashkan Rafiee[*7], Boyin Ding[#8], Maziar Arjomandi[#9]

[#]*Ocean Wave Energy Research Group, School of Mechanical Engineering, The University of Adelaide*
South Australia, Australia, 5005
[1]benjamin.schubert@adelaide.edu.au
[*]*Carnegie Clean Energy limited, Perth, WA, Australia*

Abstract—**This study presents dynamic simulation results of two point absorber wave energy converters comparing between linear, pseudo-nonlinear, and CFD models. When modelling wave energy converters, linear assumptions are commonly used to simplify calculations. One such assumption is that the hydrodynamic parameters do not change with pose. This study proposes the inclusion of position and orientation dependence in force estimation, specifically the hydrodynamic terms. A comparison between linear, the proposed pseudo-nonlinear, and CFD models show the effect of the linear assumption for cylindrical and spherical submerged buoys in three degrees of freedom, subject to regular waves. For the case of strong nonlinear hydrodynamic coupling between degrees of freedom, the linear and pseudo-nonlinear models are compared with published literature trends. Accounting for pose dependence of hydrodynamic forces, drag forces, and infinite frequency inertial effects showed trends closer to CFD results but with generally higher motion amplitudes. Significant differences in results for the cylinder are due to the presence of near-surface nonlinear effects that are not captured using linear potential flow solvers. Furthermore, a second order effect was observed in the results, suggesting the proposed method may be well suited to model sufficiently submerged buoys.**

Index Terms—**Submerged point absorber, nonlinear hydrodynamics, numerical wave tank, wave energy converter, linear parameter varying**

I. Introduction

Wave energy converters (WEC), as a concept, have been developing for over two centuries [1]. As demand for power moves away from fossil-based fuels, research efforts have been intensifying since the 1970s. This enthusiasm has developed into a worldwide interest, leading to a number of technologies employing a variety of different operation principles [2]. Even with large interest globally, most devices are in the research and prototype stage [3]. For this technology to achieve economic viability for large scale energy production, a key area to develop for further study is modelling capability [4].

A common WEC design is a point absorber (PA), which is a device usually insensitive to wave direction. A typical cylindrical submerged point absorber is shown in Fig. 1. To model WECs, efficient and reliable computational methods are essential. Conventional modelling methods include linear boundary element method (BEM) solvers ANSYS AQWA [5], WAMIT [6], and NEMOH [7]. These solvers are used to calculate hydrodynamic parameters which are included in
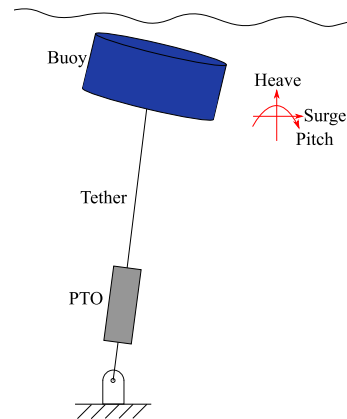

Fig. 1. A schematic of a single tether submerged cylindrical WEC displaying heave, pitch, and surge motions.

subsequent dynamic simulations. The more computationally intensive numerical wave tank (NWT) CFD approach, such as OpenFOAM or ANSYS Fluent, is becoming increasingly common in the industry. The BEM (also known as potential flow models) and NWT techniques represent linear and nonlinear approaches, respectively [1].

Linear BEM solvers provide fast solutions required for design optimisation studies. They do not account for changes in hydrodynamic coefficients as a function of geometric nonlinearities due to changes in pose, as the hydrodynamic coefficients are typically calculated around one position and orientation. Therefore, using results from linear BEM solvers cause the dynamic model to quickly lose accuracy as the motion amplitude of the buoy increases and nonlinearities become dominant [8].

Approaches to capture the nonlinear effects have been attempted previously by using extended linear solving methods, such as varying parameter model of a floating buoy with changing pitch [9]. Other models have involved recalculating the hydrodynamic parameters based on buoy wetted area at each time step for a floating spherical buoy [10] [11] and for a floating cylindrical buoy [11]. These models were constrained to move only in the heave direction. For submerged buoys,

the hydrodynamic parameters have a different dependence on depth and are independent of wetted area, which remains constant. Therefore, it is important to consider how hydrodynamic parameters change with both pitch and heave. Linear models for both floating and submerged buoys generally overestimate motion, and hence power [12], as the motion constraining effects of nonlinearities are ignored. As a whole, comparisons between linear and nonlinear modelling of submerged buoys remains largely unexplored and improvements in the current methods used may be needed to accurately model and rapidly develop these devices.

This paper explores the impact that pose has on the hydrodynamic coefficients and therefore the dynamics of two submerged point absorbers: (i) a cylinder, where coefficients are a function of position and orientation; (ii) a sphere, where coefficients are only a function of position.

Presented in this paper is a comparison between the motion characteristics of linear, pseudo-nonlinear, and fully nonlinear CFD models in three degrees of freedom (DOF) under regular (single frequency) waves. The linear model was constructed using the linear BEM solver NEMOH to find the hydrodynamic coefficients about a nominal position. The linear model does have geometric nonlinearities and drag forces but is referred to as linear in this study to reflect the method of calculating the hydrodynamic properties. The pseudo-nonlinear model used the same solver to find the hydrodynamic coefficients at a grid of points around the motion amplitude to provide linearly interpolated position-dependent hydrodynamic coefficients. Furthermore, the viscous drag force calculation incorporates velocity dependence on drag coefficients and basic orientation dependence. These coefficients and forces were used to investigate the nonlinear dynamics of the PA using MATLAB Simulink. An existing NWT in OpenFOAM was used to compare the linear and pseudo-nonlinear methods against CFD.

The mathematical model is presented in Section II. Included is the governing equation of motion and a description of each constituting term. An overview of typical linear assumptions is also provided for context. Section III discusses the implementation of the pseudo-nonlinear model and the simulation parameters. Section IV presents the results from the linear, pseudo-nonlinear, and CFD models subjected to regular waves. The results and implications on future modelling are discussed in Section V, with concluding remarks given in Section VI.

II. Mathematical Model of WEC

The schematic of the cylindrical buoy used in this study is shown in Fig. 1, with three DOF: surge, heave, and pitch, represented by

$$\mathbf{x} = \begin{pmatrix} \text{Surge} \\ \text{Heave} \\ \text{Pitch} \end{pmatrix} = \begin{pmatrix} x \\ z \\ \theta \end{pmatrix}. \tag{1}$$

Mathematically, the model can be represented by the governing equation, expressed as

$$\mathbf{M}\ddot{\mathbf{x}} = \mathbf{F}_e + \mathbf{F}_r + \mathbf{F}_h + \mathbf{F}_{pto} + \mathbf{F}_D , \tag{2}$$

where $\mathbf{M}$ is the mass matrix containing the inertial terms for each DOF, given by

$$\mathbf{M} = \begin{bmatrix} m & 0 & 0 \\ 0 & m & 0 \\ 0 & 0 & I \end{bmatrix} , \tag{3}$$

with m being the mass of the buoy and I the moment of inertia about the centre of mass in the pitch direction.

The remaining terms $\mathbf{F}_e$, $\mathbf{F}_r$, $\mathbf{F}_h$, $\mathbf{F}_{pto}$, and $\mathbf{F}_D$, are known as the excitation force, radiation force, hydrostatic or buoyancy force, power take off (PTO) force, and drag force respectively. Each of these terms, as well as how they may be estimated is discussed in the following sections, along with typical assumptions made to model them.

A. Excitation Force

The excitation force, $\mathbf{F}_e$, from waves acting on the buoy is a function of input wave frequency, wave amplitude, buoy geometry, and buoy pose.

$$\mathbf{F}_e = \mathbf{F}_{e,amp} \sin(\omega t - \boldsymbol{\phi}) , \tag{4}$$

where $\mathbf{F}_{e,amp}$ is the excitation force amplitude, and $\boldsymbol{\phi}$ is the excitation force phase vector. t represents time, and ω represents the wave frequency. The excitation force is the combination of the diffraction and Froud-Krylov forces [10].

B. Radiation Force

The radiation force, $\mathbf{F}_r$, is the force applied to the buoy as it radiates waves as a result of motion. Radiation force is commonly represented in the time domain through the Cummins equation [13], given by

$$\mathbf{F}_r = -\mathbf{A}_\infty \ddot{\mathbf{x}} - \int_0^t \mathbf{K}(t - t')\dot{\mathbf{x}}(t')dt' , \tag{5}$$

where $\mathbf{A}_\infty$ is the infinite frequency added mass and $\mathbf{K}$ is known as the memory function. This convolution integral represents the fluid memory affect in which the past state of the fluid effects the current state. In the frequency domain, the radiation force may be described as

$$\hat{\mathbf{F}}_r = -[\mathbf{B}(\omega) + i\omega\mathbf{A}(\omega)]\hat{\mathbf{x}}(i\omega), \tag{6}$$

where $\mathbf{B}(\omega)$ and $\mathbf{A}(\omega)$ is the frequency-dependent radiation damping and added mass respectively. In practice, within simulations, the radiation force is found using a well established method [14], involving constructing transfer functions from radiation damping and added mass with velocity as input and the integral in Equation (5) as the output [15]. For the purpose of these models, transfer functions of order five were found to appropriately fit the data.

C. Hydrostatic and PTO Forces

The hydrostatic force, $\mathbf{F}_h$, acts only in the heave direction and PTO force, $\mathbf{F}_{pto}$, is applied in the direction of the tether. Typically, for submerged buoys, there exists a pretension force provided by the PTO to counteract the hydrostatic force and give an equilibrium position below the surface of the

water [16]. For this study, the PTO force is considered to be a simple spring-damper arrangement,

$$\mathbf{F}_{\mathrm{pto}} = \mathbf{T}(-b\Delta\dot{l} - k\Delta l - |\mathbf{F}_{\mathrm{h}}|) \,, \qquad (7)$$

where b and k are the damping coefficients and spring constants of the PTO respectively. The extension of the tether is represented by Δl. These parameters greatly impact the dynamics, and therefore the total power generated by the device. A transform, $\mathbf{T}$, converts the PTO force to the conventional 3 DOF [16].

Both b and k can be optimised for a given frequency wave and buoy [17]. Accordingly, for the purpose of comparing between linear, pseudo-nonlinear, and fully nonlinear CFD, these values will be optimised for each frequency to compare optimal cases. Optimal values are approximately given by the following by assuming tether extension is primarily due to heave motion,

$$b_{\mathrm{opt}} = B_z(\omega) \,, \qquad k_{\mathrm{opt}} = \omega^2(m + A_z(\omega)) \,, \qquad (8)$$

where the subscript z refers to the heave direction. In the simulations, the optimal conditions gave large motion amplitudes with part of the buoy breaching the surface. To avoid this, the amplitude was reduced by increasing the damping value while using the optimal PTO stiffness to allow the range of motion to match the sampling grid.

The resonance frequencies of submerged single tether buoys for surge and heave directions are well established [18]. The two resonances approximately overlap when the following stiffness condition is met;

$$k_{\mathrm{pto,overlap}} = \frac{g(\rho V - m)(m + A_z(\omega))}{(l + a)(m + A_x(\omega))} \,, \qquad (9)$$

where l is the length of the tether, a is the distance between the tether connection point on the buoy and the center of mass, g is the acceleration of gravity, ρ is the density of water, V is the buoy volume, and A_x and A_z are the added mass in surge and heave, respectively.

When resonances coincide there will be a strong nonlinear coupling between surge and heave. This one-to-one internal resonance condition will be used in this study to demonstrate the impact of including some nonlinearities within the models. The optimal stiffness will be used for comparison with CFD cases to show the impact on weakly nonlinear operating conditions.

To calculate the power generated, PTO nonlinearities are ignored and the simplified equation for instantaneous power is

$$P_{\mathrm{inst}} = b\Delta\dot{l}^2 \,. \qquad (10)$$

D. Drag Force

The drag force, $\mathbf{F}_{\mathrm{D}}$, acting on the buoy is modelled as

$$\mathbf{F}_{\mathrm{D}} = -\frac{1}{2}\mathbf{C}_{\mathrm{D}}\rho\mathbf{A}_{\mathrm{D}}|\dot{\mathbf{x}}_{\mathrm{r}}|\dot{\mathbf{x}}_{\mathrm{r}} \,, \qquad (11)$$

where $\mathbf{C}_{\mathrm{D}}$ and $\mathbf{A}_{\mathrm{D}}$ are the coefficient of drag and characteristic area respectively, and $\dot{\mathbf{x}}_{\mathrm{r}}$ is the relative velocity of the buoy with respect to the surrounding water. The values for $\mathbf{C}_{\mathrm{D}}$ and $\mathbf{A}_{\mathrm{D}}$ are fixed in the body frame but not the global Cartesian frame and remain approximately constant for a large range of Reynolds numbers [19].

E. Typical Assumptions

The aforementioned forces are complicated to model within the time domain without a number of simplifications and assumptions. Typical assumptions include that:

- the hydrodynamic parameters are independent of buoy pose,
- the coefficients of drag are constant, independent of pitch angle and velocity, the surrounding fluid is stationary, and
- the phase of the excitation force remains constant as the buoy changes surge location.

III. Implementation of Pseudo-Nonlinear Model

In this section, the assumptions listed in Section II-E are addressed in the development of a pseudo-nonlinear dynamic model. Hydrodynamic parameters were introduced in the form of gain-scheduled methods for the excitation force and infinite frequency added mass, and an LPV (linear parameter-varying) system for the radiation force. For the cylinder, these parameters were varied as a function of heave and pitch. For the sphere, only heave was varied as the coefficients are independent of pitch. The viscous drag force was calculated by including velocity dependence in the drag coefficient in the form of Reynolds number calculations. Additionally, for the cylinder, the drag force incorporated pitch dependence by transforming the flow into vector components. For the sphere, the drag force is independent of pitch angle due to symmetry. Excitation force phase change due to motion was implemented as a function of surge, discussed in Section III-C.

A. Hydrodynamic Parameter Position Dependence

Model behaviour is highly dependent on the hydrodynamic parameters ($\mathbf{F}_e$, $\mathbf{B}(\omega)$, $\mathbf{A}(\omega)$). It is therefore critical to investigate the validity of holding these parameters constant for given frequencies as the pose of the buoy changes. Here, the calculation of these parameters was performed using NEMOH, a linear BEM solver [20]. NEMOH provides the amplitude and phase of the excitation force, the hydrodynamic damping, and added mass for a particular buoy at a range of input wave frequencies. To incorporate position dependence, the amplitude and phase of the excitation force and the infinite frequency added mass were calculated through gain-scheduled methods within Simulink. These methods linearly interpolate between a three dimensional lookup table for the cylinder (using heave and pitch), and between a two dimensional lookup table for the sphere (using heave). The radiation force was implemented with an LPV block in Simulink. This block takes an array of state-space models containing a sampling grid, enabling interpolation between models for varying heave and pitch values as required. A block diagram showing the excitation force gain-scheduled method approach is shown in Fig. 2.
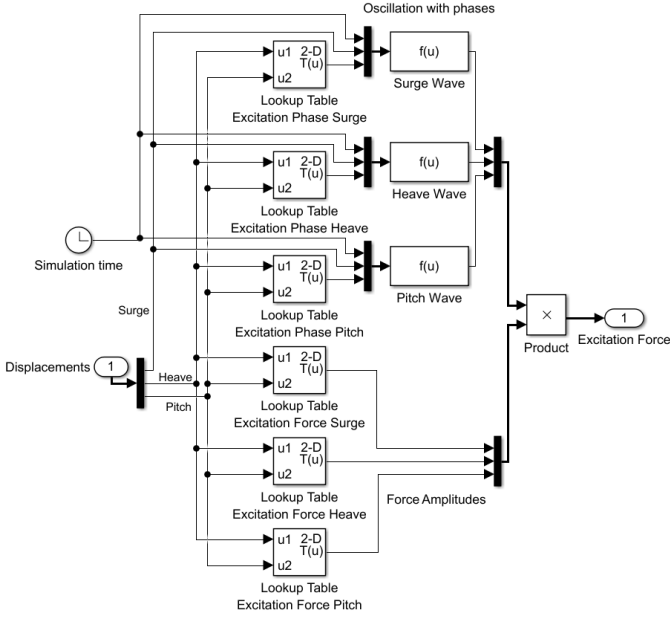
Fig. 2. Block diagram showing the excitation force gain-scheduled method approach. This details the flow of data used to find the interpolated force amplitudes for the cylinder. Force amplitudes for the spherical buoy did not use pitch values.

The range of motion for the cylinder involved varying heave position from -1.5m to 1.5m around the nominal position and pitch angle from $-10°$ to $10°$. For context, geometries of the buoys are provided on Table II. For both DOF, seven different positions and orientations were used, resulting in a sampling grid of 49 different poses. For the spherical buoy, due to symmetry, the pitch angle has no effect. Therefore, only the heave position was varied over the same range as the cylindrical buoy.

To summarise the methodology used for the proposed position-dependent hydrodynamic parameters, the following list shows the step by step procedure.

1) Specify heave and pitch positions
2) Use NEMOH to find $\mathbf{B}(\omega)$, $\mathbf{A}(\omega)$, $\mathbf{F}_{e,amp}$, and ϕ
3) Use $\mathbf{B}(\omega)$ and $\mathbf{A}(\omega)$ to create transfer functions describing how each DOF effects the radiation force in another DOF
4) Create a combined state-space for each pose
5) Combine state-space models into state-space array with sampling grid according to heave and pitch positions
6) Use the LPV block in Simulink to implement the state-space array
7) Specify $\mathbf{F}_{e,amp}$ and ϕ into respective arrays and implement in Simulink using the Lookup Table block
8) Specify each element of $\mathbf{A}_\infty$ into respective arrays and implement in Simulink using the Lookup Table block

B. Drag Force Position Dependence

The viscous drag forces acting on the Sphere and Cylinder in the surge and heave directions were approximated through a similar gain-scheduled method. Firstly, the water velocity
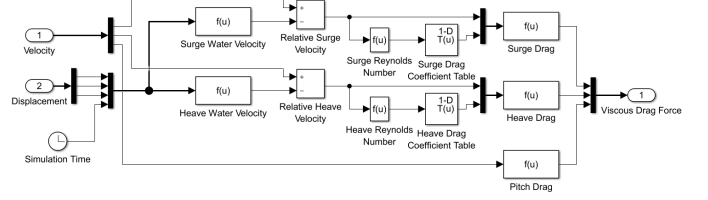

Fig. 3. Block diagram showing the viscous drag gain-scheduled method approach. This details the flow of data used to find the interpolated drag coefficients, and hence drag force amplitudes for the sphere. Force amplitudes for the cylindrical buoy change with pitch and are rotated accordingly.

around the surge and heave positions were found using established theory [17]. The velocity of the buoys relative to the fluid was then used to calculate the Reynolds number at a given time step in each direction. This number was used to find a corresponding drag coefficient based on tabulated data [19]. In the spherical case, no viscous drag torque was modelled in the pitch direction due to symmetry. For the cylindrical buoy, the drag coefficient in the pitch direction was estimated from a previous study with a similar buoy [21]. The cylindrical buoy also has viscous drag forces which are pitch dependent. For an inclined cylinder, as a step towards including position dependence in the viscous drag force, the flow is divided into components in the axial direction of the cylinder, and perpendicular to the axial direction. The forces in the respective directions are found using the previously discussed method to estimate drag coefficients in the rotated reference frame. These forces are then rotated to align with the surge and heave directions. A block diagram showing the flow of data within the pseudo-nonlinear model of the spherical buoy is given in Fig. 3. Though this does not fully capture the nonlinearity of viscous drag, it is expected that this approach is a better representation of drag effects than if the drag coefficient is assumed to be constant and the pitch rotation of the cylinder was ignored.

C. Excitation Force Phase Position Dependence

The excitation force amplitude and phase provided by NEMOH is a description of the force experienced by the buoy at a nominal surge position. Therefore, as the buoy moves in the surge direction, the force experienced by the buoy should reflect this new position. The excitation force is described in Equation (4). The phase change due to surge position (ϕ_s) can be represented in the context of the excitation force by

$$\mathbf{F}_e = \mathbf{F}_{e,amp} \sin(\omega t - \phi + \phi_s) \,, \tag{12}$$

where the phase change from surge is

$$\phi_s = kx \,, \tag{13}$$

and k is the wave number, found as the solution to [22]

$$\omega^2 = gk \tanh(kh) \,, \tag{14}$$

where h is the water depth.

D. Partially-Nonlinear Models from Literature

Previous work has included recalculating the excitation forces at each time step [11] based on the instantaneous wetted area of a floating buoy. This approach still uses a linear model for the radiation force and does not include drag forces. Additionally, the WECs were restricted to oscillate only in the heave direction. A similar study [10] calculated the excitation force at each time step based on instantaneous wetted surface, and uses a second order approximation of the diffraction and radiation force. This model also ignored viscous drag forces, was constrained to move vertically, and only simulated a single regular wave. Such techniques are common in partially-nonlinear models. Nonlinearity in the excitation force is expected to be the most influential nonlinearity within PA WEC systems [2]. Comparatively, the radiation and diffraction forces require far more computational effort and have less impact on results.

One study, closer to the presented case, uses a Fully Nonlinear Potential Flow model on a submerged cylindrical buoy [23]. The submerged cylindrical buoy is restricted to two DOF, heave and surge. This nonlinear flow model effectively simulated two dimensional NWT results for limited scenarios, involving a small buoy and small wave amplitudes (cylinder with radius of 0.05m, and wave amplitude of 1.7cm). These limitations predispose the simulation to act in a regime in which linear assumptions provide reasonable results. While nonlinear potential flow models show promising results, further research is needed to quantify overall accuracy [2]. Additionally, such models are still computationally expensive compared to linear models [24].

Nonlinearities can have differing results for a change in simulated conditions [25]. One study, on submerged spherical buoys oscillating in the heave direction, showed that a weakly nonlinear model, based on the weak scatterer approximation, predicted lower amplitudes for some frequencies and higher for others [25]. Research in this area seems to indicate that nonlinearties impact models in differing ways and cannot be summarised as a simple increase or decrease compared to the linear model.

Another study which compares linear and nonlinear hydrodynamic parameters for cylinders [26] found that for cylinders close to the surface, the added mass and radiative damping in the heave and pitch directions differ significantly between linear and nonlinear simulations, whereas the surge direction remained relatively unchanged. Also shown in this study was that vortex shedding occurs on the edge of the cylinder, though this nonlinearity is expected to have minimal impact for the case presented. A more influential result seen in this study is the formation of a chute of water as the cylinder oscillates. We expect that this phenomenon could cause significant discrepancy between linear and nonlinear models.

The proposed pseudo-nonlinear method combines the nonlinear relationships present in hydrodynamic parameters as the pose varies, with the computational speed of linear modelling, and in three DOF. For the purpose of this study, the general trend of the responses at varying frequencies will be compared to investigate the degree to which nonlinearities are captured within the proposed model. Additionally, this model applies the same pseudo-nonlinear approach towards quantifying viscous drag effects, a force ignored in previous BEM studies.

E. Simulation Parameters

To compare the performance of each model, some common parameters were selected (Table I). In addition to the simulation parameters, the properties of the buoys and PTOs must be consistent between the respective models. These properties relating to the cylindrical and spherical buoys are presented in Table II.

TABLE I
SIMULATION PARAMETERS

Parameter	Value	Units
Acceleration of gravity, g	9.81	m·s^{-2}
Water density, ρ	1025	kg·m^{-3}
Kinematic viscosity of water, ν	1.004×10^{-6}	m^2·s^{-1}
Water depth, h	50	m
Submersion depth (buoy top), ds	2.5	m
Wave amplitude, A_w	0.5	m

TABLE II
BUOY PROPERTIES

Property	Value	Units
Cylinder radius, r_c	5	m
Cylinder height, h_c	5	m
Sphere radius, r_s	5	m
Buoy density, ρ_buoys	0.7ρ	kg·m^{-3}

For the linear and pseudo-nonlinear models, the viscous drag can only be approximated from literature values. In the linear case, the drag coefficients are assumed to be constant irrespective of surge and heave position. These coefficients of drag and the corresponding characteristic areas are given in Equations (15) and (16) where $\mathbf{C}_{\mathrm{D,c}}$, $\mathbf{A}_{\mathrm{D,c}}$, $\mathbf{C}_{\mathrm{D,s}}$, and $\mathbf{A}_{\mathrm{D,s}}$ are the coefficients of drag for the cylinder, characteristic area of the cylinder, coefficients of drag for the sphere, and the characteristic area of the sphere respectively [21].

$$\mathbf{C}_{\mathrm{D,c}} = \begin{pmatrix} 1 & 0 & 0 \\ 0 & 1.1 & 0 \\ 0 & 0 & 0.2 \end{pmatrix}, \mathbf{C}_{\mathrm{D,s}} = \begin{pmatrix} 0.5 & 0 & 0 \\ 0 & 0.5 & 0 \\ 0 & 0 & 0 \end{pmatrix} \quad (15)$$

$$\mathbf{A}_{\mathrm{D,c}} = \begin{pmatrix} hr_\mathrm{c}^2 & 0 & 0 \\ 0 & \pi r_\mathrm{c}^2 & 0 \\ 0 & 0 & (2r_\mathrm{c})^5 \end{pmatrix}, \mathbf{A}_{\mathrm{D,s}} = \begin{pmatrix} \pi r_\mathrm{s}^2 & 0 & 0 \\ 0 & \pi r_\mathrm{s}^2 & 0 \\ 0 & 0 & 0 \end{pmatrix}. (16)$$

In the pseudo-nonlinear case, the drag coefficients for surge and heave are found by interpolating between tabulated results from literature [19], while the pitch drag coefficient is constant.
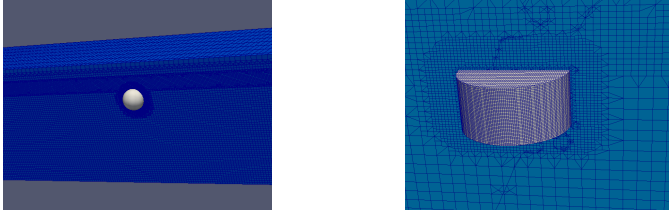
Fig. 4. A broad overview of the NWT is shown with the spherical buoy (left), and the cylindrical buoy mesh within the NWT (right).

For the fully nonlinear case, due to the computational resources required for this type of model, only five test cases were selected based on a distribution of periods. These five test cases, and the corresponding PTO parameters are given in Table III. The optimal PTO stiffness according to Equation (8) was used in these simulations. Test frequencies for the linear and pseudo-nonlinear model range from 0.1 to 2.5 rad/s.

TABLE III
CFD TEST CASES

Period (s)	6	8	10	12	14
$K_{\text{pto,cylinder}}$ (MN·m^{-1})	1.07	0.62	0.38	0.25	0.17
$K_{\text{pto,sphere}}$ (MN·m^{-1})	0.79	0.46	0.29	0.20	0.14
$B_{\text{pto,buoys}}$ (MN·s·m^{-1})	0.14	0.14	0.14	0.14	0.14

F. CFD Setup

CFD models are nonlinear models used to simulate fluid structure interaction. They are computationally expensive but can be a powerful tool to acquire accurate simulated results. The CFD model was adapted from previous studies [12], [27]. A broad view of the numerical wave tank and a detailed view of the mesh surrounding the cylindrical buoy can be seen in Fig. 4. This model has been checked for convergence and has been validated against experimental data for spherical buoys.

IV. RESULTS

A. Hydrodynamic results from NEMOH

Hydrodynamic parameters at a range of poses for the cylinder and sphere were found using NEMOH. Representative graphs of the added mass from Equation (6) for the cylindrical buoy at a heave position of 0.5m and varying pitch angles, and the added mass for the spherical buoy at varied heave positions are given in Figs 5 and 6, respectively. Radiation damping of the cylindrical and spherical buoys follow similar trends. Representative excitation forces and phases from Equation (4) are given in Figs 7 and 8 for the cylindrical and spherical buoys, respectively.

These added mass and damping coefficients were used to construct a model of the radiation force for different positions. However, for the spherical buoy, some terms fluctuate about
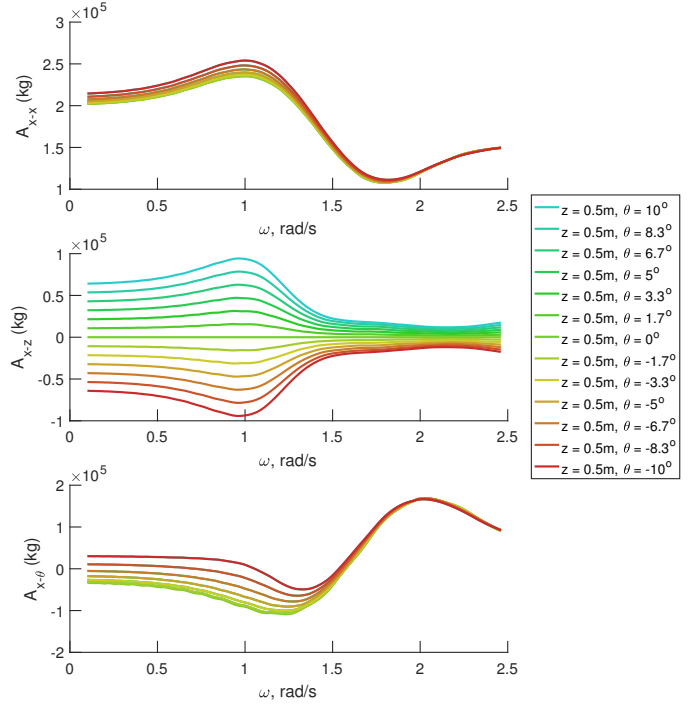

Fig. 5. Representative added mass values for the cylinder at constant surge and heave locations. Shown are the contributions to the added mass in the surge direction due to motions in all three DOF.
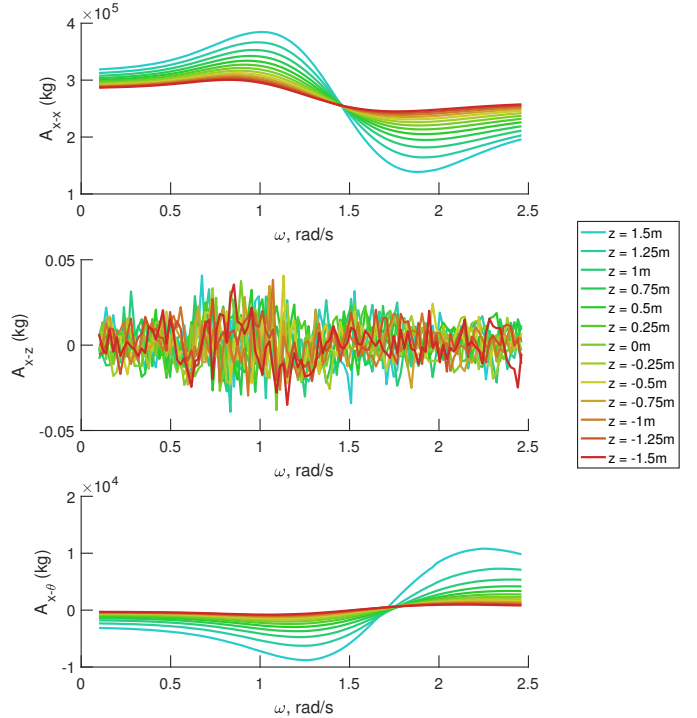

Fig. 6. Added mass values for the sphere at nominal surge location and pitch orientation. Shown are the contributions to the added mass in the surge direction due to motions in all three DOF.

zero due to numerical error or mesh imperfections. Additionally, the pitch-pitch and cross terms were expected to be zero
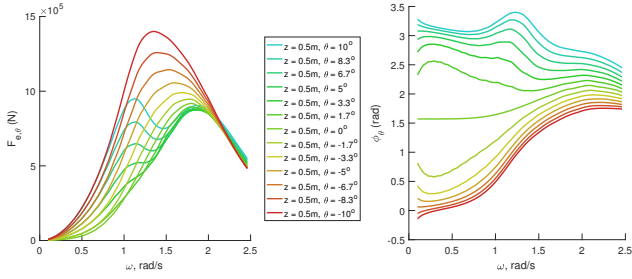
Fig. 7. Representative excitation forces (left) and phases (right) for the cylinder at nominal surge and heave locations. The excitation moment amplitude in the pitch DOF is shown.
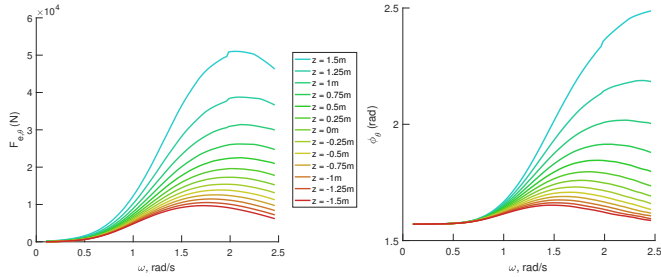

Fig. 8. Representative excitation forces (left) and phases (right) for the sphere at nominal surge location and pitch orientation. The excitation moment amplitude in the pitch DOF is shown.

but were found to be two orders of magnitude lower than surge-surge and heave-heave. These values are likely due to mesh imperfection and were also set to zero for the purpose of this study. Likewise, for the cylinder at the nominal pitch angle, the cross terms were near zero. These quantities were also set to zero in the calculation of transfer functions to prevent numerical artefacts in the radiation forces.

B. Simulation results in regular waves

In order to show the extent of the difference between the linear and pseudo-nonlinear models, the resonance frequency in heave was matched with the resonance frequency in surge using Equation (9). This provides large opportunity for strong nonlinear cross coupling effects. To isolate the effect of the hydrodynamic nonlinearity from viscous drag nonlinearity, the drag coefficient was held constant as with the linear simulations. In another set of simulations, the drag force was calculated according to the pseudo-nonlinear method with varying drag coefficient, (Fig. 9). This figure shows the oscillation amplitude for the cylinder when subjected to regular waves. A similar effect was also seen for the spherical buoy (not shown).

The linear, pseudo-nonlinear, and fully nonlinear models were subjected to simulated regular waves. Under this excitation, the steady state response of the WEC was recorded for each frequency. The mean of each DOF was found and used to center the signal for each DOF. A spectrum was obtained from this time domain signal using a Hamming window and a suitable frequency resolution. The maximum amplitude seen in each simulation was identified. The resulting peak oscillation
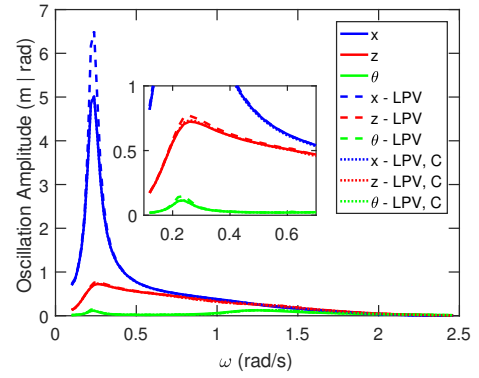

Fig. 9. The peak oscillation amplitude for the linear, pseudo-nonlinear (indicated by LPV), and pseudo-nonlinear with constant drag coefficient (indicated by LPV, C) models when the resonant frequencies in surge and heave are close. Results for the cylindrical buoy are shown.

in three DOF are presented in Figs 10 and 11 for the cylinder and sphere, respectively. The mean position of each buoy subjected to regular waves is shown in Figs 12 and 13 for the cylinder and sphere, respectively.

For practical WEC systems, another aspect to consider is the maximum PTO forces and power generated. The maximum PTO forces and the mean of the power generation were found at each frequency and displayed in Figs 14 and 15 for the cylinder and sphere, respectively.

V. DISCUSSION

The simulated results show a notable difference between the linear and pseudo-nonlinear models. For the strongly coupled case with constant drag coefficients, the linear model and the pseudo-nonlinear models are approximately equivalent with the linear model overestimating and underestimating at different frequency ranges. However, when the drag coefficient is varied as a function of velocity, larger amplitudes are seen. This indicates the constant drag coefficients lead to an overestimate of drag forces. This finding informs the interpretation of subsequent results for the linear, pseudo-nonlinear, and fully nonlinear comparison. That is, larger motion amplitudes are expected for fully nonlinear results due to an overestimate in viscous drag forces in the linear model. Optimal stiffness conditions lead to increased motion amplitudes, which were used to further compare the linear, pseudo-nonlinear, and CFD approaches.

For the optimal stiffness condition, the heave oscillation amplitude of the pseudo-nonlinear model of the cylinder shows an increase around larger amplitudes and is relatively unchanged elsewhere compared to the linear model. A noticeable difference between the results is the change in mean positions about which the buoy oscillates. In both the strongly coupled and optimal stiffness PTO conditions, the pseudo-nonlinear approach resulted in larger displacements for the cylinder than for the spherical buoy. This is expected due to spherical symmetry preventing strong coupling between DOFs. This behaviour arises due to an asymmetric force experienced by the buoy over each oscillation cycle; that is, a net drift
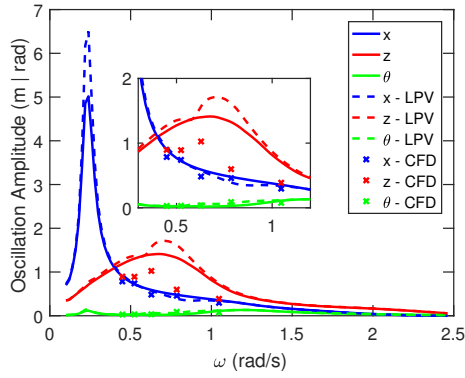
Fig. 10. The peak oscillation amplitude for the cylinder at various excitation frequencies when optimal PTO stiffness is used. The linear, pseudo-nonlinear (indicated by LPV), and fully nonlinear CFD results are shown.
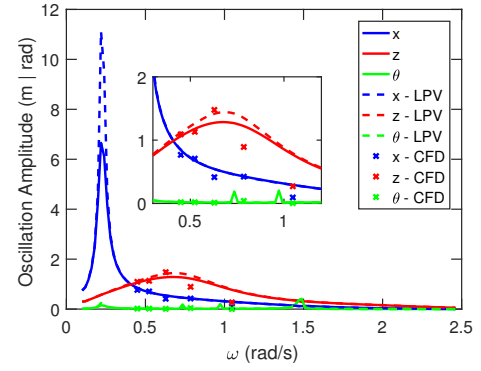

Fig. 11. The peak oscillation amplitude for the sphere at various excitation frequencies when optimal PTO stiffness is used. The linear, pseudo-nonlinear (indicated by LPV), and fully nonlinear CFD results are shown.

force. Drift forces are known to be a second order effect [28]. This behaviour is caused by a phase difference between the heave and surge excitation forces. This phase difference, coupled with the changing position of the buoy, creates a net movement in one direction until the stiffness force of the PTO is large enough to balance this drifting effect. The CFD results show the same bias trend though different peak locations and magnitudes for the spherical buoy. However, the mean position of the cylindrical buoy was clearly over-estimated in the pseudo-nonlinear method. One speculated result of this surge bias is that the tether extension is more coupled with rotation, allowing pitch to have more influence over power generation.

The difference between linear and pseudo-nonlinear oscillation amplitudes may, in part, be due to coupling between the three modelled DOF. This coupling can be seen in the hydrodynamic parameters in Fig. 5 for non-zero pitch angles. For the cylinder, pitch has a large effect on the effective added mass between surge and heave and pitch and heave motions. In the linear system, these cross terms are typically neglected as the pitch angle position is assumed to be zero. Conversely, the amplitude of oscillation of the spherical buoy is relatively unchanged for all DOF. Due to symmetry, the cross terms are zero and a changing heave location does not lead to strong hydrodynamic coupling. Consequently, less change between linear and nonlinear models is expected for spherical buoys.

The CFD results (Fig. 11) demonstrate that the linear model loses accuracy as the motion amplitude increases, agreeing with literature expectation. Results for the pseudo-nonlinear method do not clearly match CFD results but show a closer trend than the linear case, indicating that the LPV method captures some, but not all, nonlinearity in the hydrodynamics acting on the buoy. The trend for the sphere seems to be the peak thinning and a higher peak amplitude. The pseudo-nonlinear model results begin to show the same increase in peak amplitude. The pseudo-nonlinear model of the cylindrical buoy showed two distinct peaks, a large deviation from the linear model. Increased heave amplitudes occurred around the same frequencies as decreased surge amplitudes, indicating

some degree of coupling between heave and surge. The CFD results for the cylinder again show that the pseudo-nonlinear results capture trends better than linear counter-parts, though with greatly decreased amplitudes. The pseudo-nonlinear method gives larger amplitudes due to asymmetry in excitation forces in heave direction. That is, the exponential trend in excitation force indicates a greater increase for excitation force amplitude above the nominal position than decrease for below (Fig. 8). Therefore, nonlinearity in the excitation force is being captured. However, the motion amplitude is far less in the fully nonlinear CFD model (Fig. 10), indicating there is significant nonlinearity missing which the linear BEM hydrodynamic coefficients do not capture.

Other nonlinear forces acting on the buoy, such as overtopping or slamming, are not able to be modelled with linear BEM solvers. Submerged buoys, however, are away from highly nonlinear surface effects, and the outlined method does more closely approximate the nonlinearity of hydrodynamic forces than the simple linear BEM solver about a nominal position. It is commonly thought that the most influential nonlinearity for PA WEC systems is excitation force [2]. However, these results show that while the inclusion of nonlinearities in the excitation force does impact the results, there are more influential nonlinearties for this system not captured.

Linear BEM solvers are not able to fully capture the radiation forces for cylindrical buoys closer to the surface due to the formation of water jets and vortex shedding [26]. It was noticed that in the CFD simulations, significant vorticity was periodically occurring above the cylinder, indicating the presence of some complex resonance effect present in the column of water above the cylinder. Also, poor sampling grid resolution in the pseudo-nonlinear method and higher order nonlinear forces could be the reason for the discrepancy between pseudo-nonlinear and fully nonlinear results. Furthermore, interpreting the CFD results was made difficult due to the limited number of sampled frequencies. These reasons suggest that the proposed pseudo-nonlinear method is suited towards rapid modelling of submerged WEC devices only if additional improvements can be made which incorporate
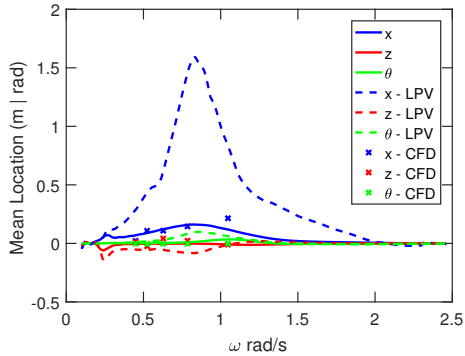
Fig. 12. The mean location for the cylinder at various excitation frequencies when optimal PTO stiffness is used. The linear, pseudo-nonlinear (indicated by LPV), and fully nonlinear CFD results are shown.
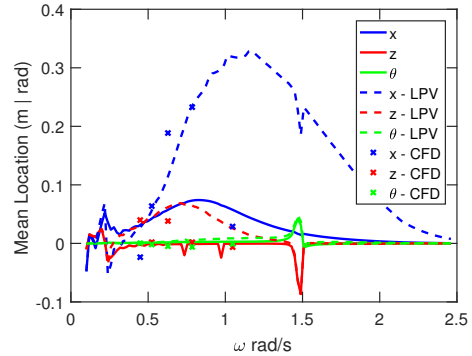

Fig. 13. The mean location for the sphere at various excitation frequencies when optimal PTO stiffness is used. The linear, pseudo-nonlinear (indicated by LPV), and fully nonlinear CFD results are shown.

nonlinear trends as buoys approach the surface. Alternatively, the proposed modelling method may be suited to specific operating conditions, such a sufficient submergence depth, because linear BEM solvers may adequately represent hydrodynamic parameters in particular conditions.

To comprehensively model WEC devices, it is important to accurately model the PTO forces. These forces influence installation cost and power generated. As an indication, the tether forces and power generated for all three modelling methods is provided in Section IV. These results show the pseudo-nonlinear method generally overestimates PTO forces and power generated. It should be emphasised that the viscous drag coefficient for the linear model is held constant and has been shown earlier to be the result of an over-estimated drag coefficient. However, as both the linear and pseudo-nonlinear model overestimate motion at higher frequencies, this is further evidence of the limitation that strong frequency-dependent nonlinearities are not captured using linear BEM solvers. One limitation of this study is that the CFD model was validated only against experimental data of spherical buoys, not cylindrical. Another limitation is that the results present the frequency of maximum oscillation amplitude seen in the response of the WECs when subjected to a regular wave, which does not account for harmonic distortions. Such harmonics were seen in the time domain results of CFD models, and, to a lesser extent, the pseudo-nonlinear model, particularly around natural frequencies.

Though the linear method proposed in this study has significant limitations, there are some benefits to such methods. The primary benefit of the linear and pseudo-nonlinear models is the drastic reduction in simulation time compared to CFD. The pseudo-nonlinear method is marginally more computationally expensive than the linear model. The linear method was able to simulate 2000 seconds in approximately 4 seconds, while the pseudo-nonlinear method took 10–15 seconds, on a standard computer. The CFD model simulated 300 seconds in approximately 2–3 days on a supercomputer. The found results and the potential benefits merit further investigation into the applicability of this modelling technique under a range of operating conditions. If the proposed pseudo-nonlinear

model can be shown to capture significant nonlinearities in hydrodynamic forces, it can greatly speed up development of submerged WEC devices.

Further extensions of this research include improving the modelling method of the drag forces in each direction, which could be made more accurate by including drag coefficients of inclined cylinders rather than decomposing the flow direction into components. Furthermore, the resolution of the sampling grid of different positions and orientations may be increased to more adequately represent nonlinear trends in the hydrodynamic parameters. The model could be extended to explore the effect of larger wave amplitudes on submerged buoys. The CFD model could also be used to acquire results from more excitation frequencies to gain a clearer perspective of nonlinear effects over a broad range of operating conditions. Alternatively, the effect of surface nonlinearities in CFD could be further explored by varying the submergence depth. For submerged devices, this pseudo-nonlinear method presents a potential alternative to greatly improving simulation speed from CFD, while capturing some nonlinear behaviours arising from position dependant hydrodynamic parameters.

VI. Conclusion

In this study a linear, pseudo-nonlinear, and fully nonlinear hydrodynamic parameter model for two point absorbers were developed and the corresponding motion and forces were compared. The linear and pseudo-nonlinear models displayed similar motion amplitudes for a spherical buoy and differing amplitudes for a cylindrical buoy. The pseudo-nonlinear model incorporated position dependence into the hydrodynamic parameters and drag forces. The results showed increased nonlinear behaviour and more closely match the trend in the CFD results compared to linear methods. The proposed model demonstrated the ability to capture some higher order nonlinearities such as drift forces and nonlinear trends in excitation forces. The pseudo-nonlinear model showed only a small increase in computation time over the linear model, but showed some basic nonlinear behaviours noticed in the CFD results and matched the trend of the fully nonlinear results. The significant differences between the pseudo-nonlinear and
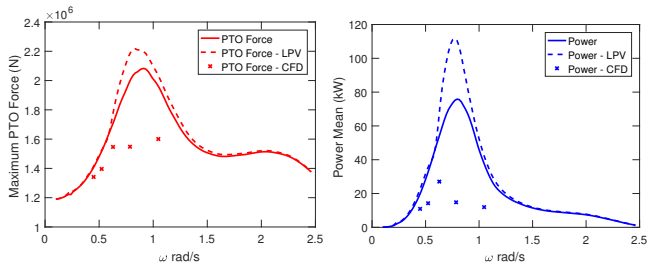
Fig. 14. The maximum PTO force (left) and mean of instantaneous power (right) experienced for each regular wave frequency for the cylindrical buoy.

Fig. 15. The maximum PTO force (left) and mean of instantaneous power (right) experienced for each regular wave frequency for the spherical buoy.

fully nonlinear for the cylindrical buoy results suggest that nonlinearity in the hydrodynamic excitation forces are not the most significant nonlinearity for the buoy dynamics, and that the linear potential flow method for calculating hydrodynamic parameters becomes inadequate close to the surface. For the concept of submerged buoys, the results presented demonstrate the applicability of pseudo-nonlinear modelling for rapid simulation compared to fully nonlinear alternatives, and justify further investigation of this method.

REFERENCES

[1] J. Cruz, *Ocean Wave Energy*, 1st ed. Springer-Verlag Berlin Heidelberg, 2008.

[2] M. Penalba, G. Giorgi, and J. V. Ringwood, "Mathematical modelling of wave energy converters: A review of nonlinear approaches," *Renewable and Sustainable Energy Reviews*, vol. 78, pp. 1188–1207, Oct. 2017.

[3] P. Hardy, B. Cazzolato, B. Ding, and Z. Prime, "A maximum capture width tracking controller for ocean wave energy converters in irregular waves," *Ocean Engineering*, vol. 121, pp. 516 – 529, 2016.

[4] J. Chozas, "International levelised cost of energy for ocean energy technologies an analysis of the development pathway and levelised cost of energy trajectories of wave, tidal and OTEC technologies," Ocean Energy Systems, Tech. Rep., May 2015.

[5] *AQWA User Manual*, ANSYS, Oct. 2012.

[6] *WAMIT USER MANUAL*, 7th ed., WAMIT Inc., 2016.

[7] A. Babarit, *NEMOH User manual*, Ecole Centrale de Nantes, Jan. 2014.

[8] J. Davidson, S. Giorgi, and J. V. Ringwood, "Linear parametric hydrodynamic models for ocean wave energy converters identified from numerical wave tank experiments," *Ocean Engineering*, vol. 103, pp. 31 – 39, 2015.

[9] A. McCabe, G. A. Aggidis, and T. Stallard, "A time-varying parameter model of a body oscillating in pitch," *Applied Ocean Research*, vol. 28, no. 6, pp. 359–370, 2006.

[10] A. Merigaud, J.-C. Gilloteaux, and J. V. Ringwood, "A nonlinear extension for linear boundary element methods in wave energy device modelling," in *Volume 4: Offshore Geotechnics; Ronald W. Yeung Honoring Symposium on Offshore and Ship Hydrodynamics*. ASME, Jul. 2012.

[11] M. Penalba Retes, A. Mérigaud, J.-C. Gilloteaux, and J. Ringwood, "Nonlinear Froude-Krylov force modelling for two heaving wave energy point absorbers," in *Proceedings of the 11th European Wave and Tidal Energy Conference*. European Wave and Tidal Energy Conference 2015, 2015.

[12] F. Meng, A. Rafiee, B. Cazzolato, B. Ding, M. Arjomandi, J. D. Piper, N. Sergiienko, and Q. Hu, "Numerical simulation of a submerged spherical point absorber with asymmetric mass distribution," in *Proceedings of the 11th European Wave and Tidal Energy Conference*, 2017.
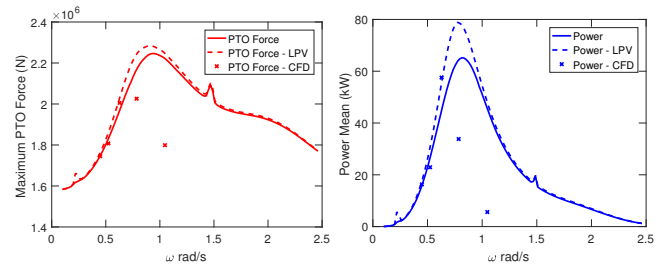
[13] W. Cummins, "The impulse response function and ship motions," David Taylor Model Basin Washington DC, Tech. Rep., 1962.

[14] T. Perez and T. I. Fossen, "A Matlab toolbox for parametric identification of radiation-force models of ships and offshore structures," *Modeling, Identification and Control: A Norwegian Research Bulletin*, vol. 30, no. 1, pp. 1–15, 2009.

[15] R. G. Coe and D. L. Bull, "Nonlinear time-domain performance model for a wave energy converter in three dimensions," in *Oceans-St. John's, 2014*. IEEE, 2014, pp. 1–10.

[16] A. Babarit, J. Hals, M. Muliawan, A. Kurniawan, T. Moan, and J. Krokstad, "Numerical estimation of energy delivery from a selection of wave energy convertersfinal report," *Report, Ecole Centrale de Nantes & Norges Teknisk-Naturvitenskapelige Universitet*, 2011.

[17] J. Falnes, *Ocean waves and oscillating systems: linear interactions including wave-energy extraction*. Cambridge university press, 2002.

[18] F. Meng, B. Cazzolato, B. Ding, and M. Arjomandi, "Modal analysis of a submerged spherical point absorber with asymmetric mass distribution," *submitted to Renewable Energy*, 2017.

[19] R. D. Blevins, "Applied fluid dynamics handbook," *New York, Van Nostrand Reinhold Co., 1984, 568 p.*, 1984.

[20] M. Penalba, T. Kelly, and J. V. Ringwood, "Using NEMOH for modelling wave energy converters: A comparative study with WAMIT," *Centre for Ocean Energy Research (COER), Maynooth University, Co. Kildare, Ireland*, 2017.

[21] N. Y. Sergiienko, B. S. Cazzolato, B. Ding, and M. Arjomandi, "Three-tether axisymmetric wave energy converter: estimation of energy delivery," in *Proceedings of the 3rd Asian Wave and Tidal Energy Conference, Singapore*, 2016, pp. 163–171.

[22] S. Chao Jiang, Y. Gou, B. Teng, and D. Zhi Ning, "Analytical solution of a wave diffraction problem on a submerged cylinder," *Journal of Engineering Mechanics*, vol. 140, no. 1, pp. 225–232, Jan. 2014.

[23] E. Guerber, M. Benoit, S. Grilli, and C. Buvat, "Numerical modeling of fully nonlinear interactions of ocean waves with a submerged moving body," in *Proceedings of the 3rd International Conference on Ocean Energy. Bilbao, Spain*, 2010, pp. 1–6.

[24] L. Letournel, P. Ferrant, A. Babarit, G. Ducrozet, J. C. Harris, M. Benoit, and E. Dombre, "Comparison of fully nonlinear and weakly nonlinear potential flow solvers for the study of wave energy converters undergoing large amplitude motions," in *ASME 2014 33rd International Conference on Ocean, Offshore and Arctic Engineering*. American Society of Mechanical Engineers, 2014, pp. V09BT09A002–V09BT09A002.

[25] L. Letournel, C. Chauvigné, B. Gelly, A. Babarit, G. Ducrozet, and P. Ferrant, "Weakly nonlinear modeling of submerged wave energy converters," *Applied Ocean Research*, vol. 75, pp. 201–222, Jun. 2018.

[26] A. Rafiee and A. Valizadeh, "Nonlinear hydrodynamics of bluff bodies oscillating near freesurface," in *Proceedings of the twenty-eighth International Ocean and Polar Engineering Conference (ISOPE), Sapporo, Hokkaido, Japan*, Jun. 2018.

[27] A. Rafiee and J. Fiévez, "Numerical prediction of extreme loads on the CETO wave energy converter," in *Proceedings of the 11th European Wave and Tidal Energy Conference, Nantes, France*, 2015.

[28] B. W. Kim, S. Y. Hong, and H. G. Sung, "Comparison of drift force calculation methods in time domain analysis of moored bodies," *Ocean Engineering*, vol. 126, pp. 81–91, Nov. 2016.